SAPIENZA
UNIVERSITÀ DI ROMA

Investigation on Internal Solitary Waves Breaking for Geophysical Applications

Dipartimento di Scienze di Base Applicate all'Ingegneria

Dottorato di Ricerca in Modelli Matematici per l'Ingegneria, Elettromagnetismo e Nanoscienze – XXXII Ciclo

Candidate

Davide Cavaliere

ID number 1092754

Thesis Advisor

Dr. Federico Falcini

Co-Advisor

Dr. Giovanni la Forgia

October 2019

Thesis defended on —
in front of a Board of Examiners composed by:

Prof. (chairman)

Prof.

Dr.

Investigation on Internal Solitary Waves Breaking for Geophysical Applications
Ph.D. thesis. Sapienza – University of Rome
ISBN: 000000000-0

This thesis has been typeset by LaTeX and the Sapthesis class.

Author's email: davide.cavaliere@uniroma1.it

Abstract

Nonlinear internal waves are a spectacular phenomenon taking place in many parts of the world ocean. They consist in oscillations that travel along the pycnocline, i.e., the portion of the water column separating the surface layer from relatively more dense underlying fluid. They are mostly generated by the interaction between tidal flow and bottom topography features, such as underwater sills and the continental shelf. Nonlinear internal waves can take the shape of a special waveform called internal solitary wave (ISW), a class of nonsinusoidal waves that has the ability to retain its form over long distances and extended periods of time.
In the present work, we investigate the propagation, shoaling and breaking of ISWs in a two–layer stratified fluid system through analytical and numerical methods. We study the propagation of ISWs over a varying bathymetry through variable coefficients KdV–type equations, which are widely used to model weakly–nonlinear waves in the oceanic context. We study the shoaling and breaking of ISWs along a sloping bathymetry, and we build an anaytical model to derive the ISWs breaking location. Theoretical results are validated by laboratory experiments performed in a wave tank. We then apply KdV–type equations to describe both numerically and analitically the evolution of ISWs generated in the Messina Strait (Mediterranean Sea) propagating northward, towards the frontal slope of a headland, i.e., Capo Vaticano. Finally, we apply our wave–breaking model to predict breaking location of ISWs along this frontal slope. We also focus on the mixing process induced by the ISWs breaking, defining the potential energy, the background potential energy and the available potential energy (APE) of an ISW in a two–layer fluid. Through the Thorpe and Ozmidov length scales we build a theoretical model to predict the values of mixing efficiency involved in ISWs breaking and we validate the model through laboratory experiments.

Contents

1 Introduction **1**
1.1 Internal Solitary Waves 1
1.2 ISWs theoretical models 3
1.2.1 Theoretical modelling of two–dimensional effects 6
1.3 Shoaling and breaking of ISWs. Mixing induced by ISWs breaking. . 9
1.4 Impacts of ISWs propagation and breaking 13
1.5 Thesis outline 16

2 Internal solitary waves: governing equations **19**
2.1 Stability of water masses 19
2.2 Weakly nonlinear internal waves: KdV and eKdV equations 21
2.2.1 Solutions to KdV and eKdV equations: cnoidal and solitary waves 27
2.3 Strongly nonlinear models: MCC and DJL models 30

3 ISWs propagation in a variable environment **35**
3.1 Variable–coefficient extended KdV (veKdV) equation 35
3.2 Adiabatic transformation of ISWs: slowly–varying solution to veKdV equation 41
3.3 Explicit analytic solution for the veKdV solitary wave amplitude . . 47
3.4 Numerical integration of vKdV and veKdV equations 51

4 Shoaling and breaking of ISWs over a sloping bathymetry **55**
4.1 ISWs shoaling and breaking in laboratory experiments 55
4.2 vKdV and veKdV numerical simulations and analytical theory for experimental waves 60
4.3 Wave–breaking description 66
4.4 Experimental results and validation of the wave–breaking model . . 67
4.5 ISWs in the Messina Strait 71
4.6 Numerical simulations and analytic description of ISWs in the Gioia Basin 73
4.7 ISWs breaking location in the Gioia Basin 98
4.8 Discussion of two–dimensional effects 101

5 Mixing induced by ISWs breaking **105**
5.1 Energetics of mixing 105
5.1.1 Available Potential Energy (APE) of ISWs 106

5.2 Thorpe and Ozmidov length scales 107
5.3 Heuristic model for mixing induced by breaking ISWs 110
5.4 Experimental validation of the model 112

6 Conclusions **119**

Appendices **125**

A Surface and interfacial gravity water waves **125**
A.1 Preliminaries 125
A.2 Surface water waves 127
A.2.1 Shallow and deep water waves 128
A.3 Interfacial waves in a two–layer fluid 131
A.3.1 Interfacial waves in infinite–depth fluid 133
A.3.2 Interfacial waves in finite–depth fluid 135
A.3.3 Shallow interfacial waves in rigid–lid approximation 136

B Linear waves in non–uniform media **139**
B.1 Ray theory approach 139
B.2 WKB approach 141
Bibliography 145

Chapter 1

Introduction

1.1 Internal Solitary Waves

Away from well–mixed, vertically homogeneous regions, most of the ocean is stratified, with light water above denser water. A thin, strongly stratified layer, known as *pycnocline*, separates the surface layer from relatively more dense underlying fluid. The pycnocline is the zone where the vertical density gradient is the greatest, indeed it is characterized by a sharp change in density with depth, due to differences in temperature and/or salinity. It represents an extremely stable zone, acting as a barrier for surfaces processes. Below the pycnocline, changes in salinity or temperature are very small [Garrett, 2003]. For completeness we define here the *thermocline* as a zone where density is determined mostly by the rapid temperature variations, and *halocline* where the density variations are controlled mostly by the salinity [Massel, 2015]. Both in freshwater lakes and in oceans, temperature, salinity and pressure change with depth. However, it is mostly the temperature variations, which affect the density change. Thus, a pycnocline is often a thermocline. Depending upon latitude and season, the thermocline region extends downward as far as about 100 m, approximately from 50 to 150 m depth. In the Mediterranean Sea, for instance, the thickness of the surface mixed layer is typically around 100 m, with some peaks and lows that reach ~ 200 m and ~ 30 m, respectively, depending on the season [D'Ortenzio *et al.*, 2005]. During summer, the large density contrast between the warm surface and the cooler deep waters inhibits the vertical mixing: the thermocline results to be shallow and strongly stratified. In winter, instead, the surface cooling leads the thermocline to have weaker stratification and greater thickness [La Forgia, 2016; Sutherland, 2010].

Under the action of the gravitational forces, the heavy fluid can be lowered and the light fluid raised. The interface of two media of different densities is usually unstable and under some forcing impulse wave type disturbances are generated at the interface. A good example of such waves are the ocean surface waves.

In a stratified fluid, gravity waves can propagate through the fluid vertically as well as horizontally. Such gravity waves moving within a continuously stratified fluid are called *internal waves*, while the term *interfacial waves* is used to describe gravity waves moving at the interface between two water layers of different constant densities. As the density difference between water and air is large, the interface

waves are not too high. On the contrary, within the ocean water column, the vertical density gradients are typically very small and small energies are required to move water particles vertically. Therefore, the amplitudes of internal disturbances can be very large [Massel, 2015].
Hump–shaped large undulations of the pycnocline with permanent form are commonly known as Internal Solitary Waves (ISWs) [Sutherland *et al.*, 2013]. The peculiar solitary wave shape results from a balance between nonlinearity, which tends to steepen it, and nonhydrostatic dispersion, which tends to flatten it. These forces act simultaneously and allow the single wave to preserve its shape during motion. They can be generated by river plumes [Nash and Moum, 2005] and by tidal flow over steep topographic features such as underwater sills and the continental shelf [Osborne and Burch, 1980]. In particular, the interaction between barotropic tidal currents and topography can generate internal tides, i.e., internal waves of tidal frequency, that could steepen due to nonlinearity, then disintegrating into a train of much shorter strongly nonlinear internal solitary waves [Gerkema and Zimmerman, 1995; Maxworthy, 1979].
Ocean internal waves typically have wavelengths ranging from hundreds of meters to tens of kilometres and periods from several minutes to several hours. In particular, internal waves with periods anywhere around 12 h are called *semi-diurnal tides*, and internal waves with periods around 24 h are called *diurnal internal tides*. Their amplitudes (peak to trough) often exceed 100 m. Orbital motions of the water particles associated with internal waves have the largest radius at the pycnocline depth, which decreases downward and upward from this depth. Tidally generated internal waves are usually nonlinear and occur often in the form of wave packets. The amplitude and distance between waves in a wave packet decreases from the front to the rear [Dwi Susanto *et al.*, 2005; Massel, 2015].

Historically, John Scott Russell first experimentally observed a surface solitary wave on the Edinburgh–Glasgow Canal in 1834. He called it the "great wave of translation" and then reported his observations at the British Association [Russell, 1844]:

> "I was observing the motion of a boat which was rapidly drawn along a narrow channel by a pair of horses, when the boat suddenly stopped–not so the mass of water in the channel which it had put in motion; it accumulated round the prow of the vessel in a state of violent agitation, then suddenly leaving it behind, rolled forward with great velocity, assuming the form of a large solitary elevation, a rounded, smooth and well–defined heap of water, which continued its course along the channel apparently without change of form or diminution of speed. I followed it on horseback, and overtook it still rolling on at a rate of some eight or nine miles an hour, preserving its figure some thirty feet long and a foot to a foot and a half in height. Its height gradually diminished and after a chase of one or two miles I lost it in the windings of the channel".

The discovery of this remarkable phenomenon inspired him further to conduct a series of extensive laboratory experiments on the generation and propagation of such waves (see Drazin and Johnson [1990]).
Much of the modern interest in large internal waves in oceanography began in the 1960s to 1970s with an interesting confluence of events in ocean instrumentation, applied mathematics, and remote sensing. Most internal wave measurement methods

are based on recording the profiles of temperature and salinity in the water column. The movement of points of equal temperature (*isotherms*) or the movement of points of equal salinity (*isohalines*), as well as the movement of points of equal density (*isopycnals*), are manifestations of the passage of internal waves. The development of fast internally recording vertical arrays ("chains") of thermistors in the 1960s led to observations of large internal waves in the coastal oceans and marginal seas [Helfrich and Melville, 2006]. However, it is only within the last decades that technology has advanced to a point where large numbers of observations become available. Since the launching of the Seasat in 1978 and European Remote Sensing Satellite ERS-1 in 1991 with a Synthetic Aperture Radar (SAR) on board, a large number of data on the surface manifestation of the presence of internal waves has become available. That demonstrated that packets of shoreward-propagating internal waves, separated by tidal periods, were a ubiquitous feature of the coastal oceans [Helfrich and Melville, 2006; Massel, 2015]. Although they propagate along a pycnocline, in the interior of the ocean, nonlinear internal waves alter the sea surface roughness, making them readily detectable in satellite imagery. Currents within a nonlinear internal wave produce convergent and divergent zones on the surface that move in phase with the internal wave's subsurface crests and troughs. These zones cause variations in sea surface roughness that appear as distinctive features in both Synthetic Aperture Radar (SAR) and optical sunglint imagery [Alpers, 1985; Jackson *et al.*, 2013]. In particular, they appear as brighter and darker alternate strips on the image whether the surface waves associated to ISWs propagate in convergent or divergent surface flow zones.

Historically, the Andaman Sea was probably the region where the surface effects of internal waves passage were first observed [Osborne and Burch, 1980]. By satellite photography, internal soliton with crest lengths as long as 150 km and with a separation distance between solitons in a packet as long as 15 km were observed. Packets occurred about every 12 h, indicating a tidal origin for the internal solitons. From then, popular "hot spots" for observation of large amplitude internal solitary waves became the Sulu Sea [Apel *et al.*, 1985], the Gibraltar [Alpers *et al.*, 1996] and Messina Straits [Alpers and Salusti, 1983; Marullo and Santoleri, 1986], the Australian North West Shelf [Holloway, 1984, 1994; Holloway *et al.*, 1997], the Lombok Strait [Dwi Susanto *et al.*, 2000, 2005], the Northern South China Sea [Duda *et al.*, 2004; Lien *et al.*, 2014], and many other sites.

1.2 ISWs theoretical models

More than 60 years after the first observation of Russell, two Dutchmen, D.J. Korteweg and G. de Vries, in 1895, formulated a mathematical model equation to provide an explanation of the solitary wave phenomenon [Korteweg and De Vries, 1895]. The *Korteweg–de Vries* (KdV) equation,

$$\frac{\partial \eta}{\partial t} + c_0 \frac{\partial \eta}{\partial x} + \alpha \eta \frac{\partial \eta}{\partial x} + \beta \frac{\partial^3 \eta}{\partial x^3} = 0\,, \tag{1.1}$$

is, to date, the simplest nonlinear model equation for solitary waves, and it represents the longtime evolution of wave phenomena in which the steepening effect of the

nonlinear term is counterbalanced by linear dispersion. Indeed, the KdV equation arises from an assumption that nonlinearity, scaled by $\varepsilon = a/H$, and nonhydrostatic dispersion, $\delta = (H/l)^2$, are comparable and small: $\delta = O(\varepsilon) \ll 1$. Here, a is a measure of the wave amplitude, H is the vertical scale, and l is a measure of the wavelength. Zabusky and Kruskal [1965] showed the behavior of solitary waves through a numerical approach to the KdV equation: when two or more solitary waves interact, they emerge from the interaction without change of form and amplitude, but with only a small change in their phases [1]. In view of their preservation of shape and the resemblance to the particle–like character of these waves, Kruskal and Zabusky called these solitary waves, *solitons*, like photon, proton, electron, and other terms for elementary particles [Debnath, 2012]. Subsequentely, Gardner *et al.* [1967] constructed exact analytical solutions of the KdV equation through the *Inverse Scattering Transform method* (IST), that provide also the description of the interaction among N solitons.

Despite internal waves are often highly nonlinear, weakly nonlinear KdV–type theories have played the primary role in elucidating the essential features of the observations [Osborne and Burch, 1980; Ostrovsky and Stepanyants, 1989; Stanton and Ostrovsky, 1998]. Furthermore, they allow modelling of unsteady wave evolution under various conditions (e.g., variable environment) [Helfrich and Melville, 2006]. Fully nonlinear theories for solitary waves are available to extend the solitary wave solutions to large amplitudes. However, these models are generally restricted to steady solitary wave.

Derivations of the Korteweg-de Vries equation for the motion in two–layer fluids or continuos stratifications were given by several authors, such as Long [1953] and Benney [1966]. Internal waves may be long with respect to h_1 or h_2, i.e., the depth of one of the two layers, but not to the total depth. In that case, weakly nonlinear theories for infinitely deep fluids, as the *Benjamin–Ono equation* [Benjamin, 1967; Ono, 1975], or intermediate depth [Joseph, 1977; Kubota *et al.*, 1978] are available. An extension of the KdV equation is the *extended KdV* (eKdV) *equation*, known also as *Gardner equation*, including cubic nonlinearity, is [Djorjevic and Redekopp, 1978; Grimshaw *et al.*, 2007; Helfrich and Melville, 1986; Kakutani and Yamasaki, 1978]

$$\frac{\partial \eta}{\partial t} + c_0 \frac{\partial \eta}{\partial x} + \alpha \eta \frac{\partial \eta}{\partial x} + \alpha_1 \eta^2 \frac{\partial \eta}{\partial x} + \beta \frac{\partial^3 \eta}{\partial x^3} = 0\,. \tag{1.2}$$

This equation is particularly useful to describe waves larger than KdV waves, and especially if the wave passes through a turning point $h_1 = h_2$, where $\alpha = 0$. Indeed, in this case we must take into account the cubic nonlinearity. An inversion of solitary

[1] The work of Zabusky and Kruskal [1965] is strictly related to the seminal work of Fermi *et al.* [1955] on a numerical model of a discrete nonlinear mass–spring system. In 1914, Debye suggested that the finite thermal conductivity of an anharmonic lattice is due to the nonlinear forces in the springs. This suggestion led Fermi, Pasta, and Ulam to believe that a smooth initial state would eventually relax to an equipartition of energy among all modes because of nonlinearity. But their study led to the striking conclusion that there is no equipartition of energy among the modes. Although all the energy was initially in the lowest modes, after flowing back and forth among various low–order modes, it eventually returns to the lowest mode, and the end state is a series of recurring states. This remarkable fact has become known as the *Fermi–Pasta–Ulam (FPU) recurrence* phenomenon [Debnath, 2012].

wave polarity can take place when α changes in sign (in fact, if $h_1 < h_2 (h_1 > h_2)$, $\alpha < 0 (\alpha > 0)$), and the wave can trasform from a wave of depression to a wave of elevation or vice versa.
Higher–order KdV–type models have been also investigated, including higher–order nonlinear and dispersive terms [Grimshaw *et al.*, 2002; Koop and Butler, 1981; Lamb and Yan, 1996]. However, if the background stratification gives $\alpha = O(\varepsilon)$, and the balance $\delta = O(\varepsilon^2)$ is satisfied, then the eKdV equation is asymptotically consistent, and it is not necessary to add higher order terms [Helfrich and Melville, 2006]. This occurs, in particular, in the two-layer case when $|h_1 - h_2|/(h_1 + h_2) \ll 1$. A typical KdV solitary wave solution has the so–called "sech^2" waveform [Osborne and Burch, 1980]:

$$\eta(x,t) = A \operatorname{sech}^2 \left(\frac{x - Ut}{L} \right) , \tag{1.3}$$

where A is the wave amplitude, U the solitary wave phase speed, and L the halfwidth. Is easy to check that the amplitudes of the horizontal velocities of the water particles in the upper and lower layer, $u_1(x,t)$ and $u_2(x,t)$, do not decay with depth, but that the velocities in the lower layer are opposite in direction to those in the upper layer [Massel, 2015; Osborne and Burch, 1980]. KdV waves wavelength decreases with increasing amplitude and does not capture the broadening of waves that is often observed. Furthermore, potentially, the amplitude of KdV waves could be infinitely large. In contrast, eKdV solutions can capture the wave broadening when $\alpha_1 < 0$ and they are approaching the limiting amplitude $\eta_{\text{lim}} = -\alpha/\alpha_1$. Thus, eKdV model seems to be more appropriate for internal solitary wave description (see also Small [2001a] for an in–depth discussion).
As observed above, KdV–type models are suitable for the description of unsteady internal solitons. Indeed, it is particularly simple (with respect to other models) to introduce, in the evolution equations, coefficients that can parametrize the variability of the background environment, in time and/or in space. In this way, it is possible to describe the wave transformation along the motion, caused by, for example, varying bathymetry or density. Variable coefficient equations have been developed both for KdV and eKdV equation, and they are usually referred to as *vKdV equation* (variable–coeffcient KdV equation) and *veKdV equation* (variable–coefficient extended KdV equation). Remarkable analytical and numerical studies concerning the vKdV and veKdV equations with oceanographic applications have been carried out by several authors in the last thirty years. In particular, a description of the wave transformation under slowly–varying environmental conditions has been analytically formalized by Grimshaw *et al.* [1998, 1999, 2007, 2010], Grimshaw [2007], and Pelinovsky *et al.* [1994]. Adiabatic solutions to vKdV and veKdV have also been verified with good agreement with numerical simulations [Grimshaw *et al.*, 2004, 2010; Pelinovsky *et al.*, 1994; Small, 2001a] and oceanographic data for several shelves and bathymetries [Holloway *et al.*, 1997, 1999].
Besides weakly nonlinear models, strongly nonlinear and fully nonlinear models have been developed. Miyata, Camassa and Choi derived a two–layer system bounded by a rigid surface (rigid–lid approximation) [Choi and Camassa, 1999; Miyata, 1985] with strong nonlinearity ($\varepsilon = O(1)$) and weak dispersion ($\delta \ll 1$) to describe large–amplitude internal solitary waves. They also developed an equivalent model for

a two–layer system bounded by a free–surface [Choi and Camassa, 1996; Kodaira *et al.*, 2016]. The Miyata–Choi–Camassa (MCC) solitary waves broaden and slow (relative to KdV) with increasing amplitude. Furthermore, the MCC waves have a maximum amplitude that can reach the mid-depth and has infinite wavelength. EKdV and MCC theories agree quite well for $0.4 < h_1/(h_1 + h_2) < 0.6$, where the scaling requirements of eKdV are reasonably met. However, differences grow rapidly outside this range [Helfrich and Melville, 2006]. MCC solitary wave solutions are in good agreement with the laboratory experiments, the full numerical solutions to the Euler equations, and observations over a wide range of relative layer depth [Camassa *et al.*, 2006; Kodaira *et al.*, 2016; Michallet and Barthélemy, 1998; Ostrovsky and Grue, 2003]. Unsteady MCC solitary waves have been studied by Jo and Choi [2002], who considered several examples of MCC waves evolving over slowly–varying bathymetry.

Ostrovsky and Grue [2003] derived a model equivalent to the MCC equations for strongly nonlinear dispersive waves. Using Riemann invariants, they added nonlinear dispersive effects from both the MCC theory and phenomenological considerations to arrive to evolution equations for strongly nonlinear dispersive waves that are generalizations of the KdV and Benjamin-Ono equations [Grue, 2005; Ostrovsky and Grue, 2003]. This model avoids the numerical instability of MCC model at high wave numbers to Kelvin-Helmholtz instability.

Another important model which has acquired great importance in the last two decades is the *DJL model* (Dubreil–Jacotin–Long), which is a fully nonlinear strongly dispersive model [Dubreil-Jacotin, 1937; Long, 1953]. Although DJL solutions are exact solutions of Euler equations, the DJL model can represent only steady–state solitons and must be solved numerically [Lamb, 2002; Stasna and Lamb, 2002; Turkington *et al.*, 1991].

1.2.1 Theoretical modelling of two–dimensional effects

Observations of ISWs [Barale and Gade, 2008, 2019] in the ocean together with numerical simulations (see, e.g., Vlasenko and Stashchuk [2007b]), illustrate that, because of the complicated and essentially two–dimensional bathymetry, wave refraction and diffraction can occur. This indicates that to have a realistic description, horizontal 2D effects are important and in some circumstances cannot be ignored, especially when there are strong variations in the transverse direction [Yuan *et al.*, 2018a]. Among the various KdV–type equations, the *Kadomtsev–Petviashvili equation* (KP) [Kadomtsev and Petviashvili, 1970] represents an important extension from one to two horizontal space dimensions, as it describes weakly–nonlinear, long waves propagating along a predominant direction (say the positive x direction) in a 2D domain [Akylas, 1994; Akylas and Katsis, 1987; Grimshaw and Helfrich, 1989; Johnson, 1980; Kadomtsev and Petviashvili, 1970]:

$$\left(\eta_t + c_0\eta_x + \alpha\eta\eta_x + \beta\eta_{xxx}\right)_x + \frac{\gamma}{2}\eta_{yy} = 0\,, \tag{1.4}$$

where $\eta(x, y, t)$ is the amplitude of the wave; x is chosen to be along the primary wave propagation direction, where the waves have a linear phase speed c_0, while y is the transverse direction where there are weak diffraction effects; α is the nonlinear

coefficient while β and γ are the dispersive coefficients in the x and y directions, respectively. Also in this case it is possible to introduce a nonlinear correction, leading to the so–called *extended Kadomtsev–Petviashvili equation* (eKP), also known as the *(2 + 1) Gardner equation* [Osborne, 2010]:

$$\left(\eta_t + c_0\eta_x + \alpha\eta\eta_x + \alpha_1\eta^2\eta_x + \beta\eta_{xxx}\right)_x + \frac{\gamma}{2}\eta_{yy} = 0\,, \tag{1.5}$$

Both the KP and the eKP equations are integrable by IST method [Osborne, 2010]. To take into account the effects of a variable background (variable bathymetry, background current or density), the KP and the eKP equations can be replaced by their variable coefficients versions, the *vKP* and the *veKP* equations. The vKP equation was first derived by Grimshaw [1981, 1985], while Chen and Liu [1995] considering the effects of rotation, steady background current and varying topography derived and solved a *unified KP equation* for surface and interfacial waves propagating in a channel with sidewalls. The cited KP-type equations are able to take one or some of the effects of rotation, background current, varying topography, and boundary walls into consideration, but nonetheless many of them are based on model density stratifications, such as a two–layered system. Only recently Yuan *et al.* [2018a] derived and applied to some real–field cases a new variable–coefficient KP equation that is based on quite general continuous density stratification and variable 2D topography. In this case, analytical theory, numerical simulations of vKP equation and ISWs simulations through the fully nonlinear, non–hydrostatic MIT general circulation model (MITgcm) are compared with success.

Due to the variable oceanic background, ISWs can undergo refraction and reflection, see Liu and Hsu [2004], Ramp *et al.* [2004], Cai and Xie [2010]. These factors jointly create the possibility that oblique interactions between two or more ISWs can occur. Theoretical investigation of oblique solitary wave–wave interactions in the water wave context began several decades ago with the pioneering work by Miles [1977a,b], who investigated the interaction between two crossing small–amplitude shallow water surface solitary waves, each governed by the KdV equation. It was found that depending on the amplitudes and angles, a Mach stem (that is a resonant phase shift) can arise in the interaction zone [Yuan *et al.*, 2018b]. More recently, Kodama [2010], Kodama *et al.* [2010], Kodama and Yeh [2016] modified the Miles theory and extended its applicability to small but finite incident angles. In this limit the KP equation has emerged as the canonical model for the description of oblique wave–wave interactions. Further applications to surface solitons have been developed, for instance, by Ablowitz and Baldwin [2012] and Chakravarty and Kodama [2013] to ocean surface waves on flat beaches [2]. In the ISWs context, Chen *et al.* [2011], Wang and Pawlowicz [2012], Xue *et al.* [2014] studied different internal wave–wave interaction patterns in different locations, and based their analyses largely on the work of Miles [1977a,b]. Recently, Shimizu and Nakayama [2017] investigated the effects of variable topography and Earth's rotation on the oblique internal solitary-like wave–wave interaction in the Andaman Sea based on the results of three–dimensional MITgcm simulations and the extendend Miles theory (i.e., the Kodama [2010] theory). Currently, to the author's knowledge, one of the most

[2] We highly suggest to the reader to take a look to the beautiful figures and the mathematically reconstructed wave patterns in those articles.

advanced studies is that of Yuan *et al.* [2018b], where the topographic effect on the wave interactions between two oblique internal solitary waves is investigated analytically and numerically through the vKP equation.
Though the KP–type equations framework is well developed, and seems to be the most promising tool to study weakly nonlinear ISWs planar effects, it is possible to investigate refraction, diffraction and spreading phenomena through other practical analytical and numerical tools. In two famous papers, Pierini [1986, 1989] adopted a slightly different version of the KP equation (1.4):

$$\left(\eta_t + c_0\eta_x + \alpha\eta\eta_x - \frac{\beta}{c_0}\eta_{xxt}\right)_x + \frac{c_0}{2}\eta_{yy} = 0\,, \tag{1.6}$$

which is a 2D generalization of the *Peregrine–Benjamin–Bona–Mahony equation* (PBBM) (see also Peregrine [1966] and Benjamin *et al.* [1972]) or *Regularized Long Wave equation* (RLW). In Benjamin *et al.* [1972] it is stressed that the one–dimensional PBBM equation has a dispersion relation which, unlike that of the KdV equation, allows for the presence of spurious short waves in the initial condition without the growth of numerical instabilities. This is also true for (1.6). Equation (1.6) is not exactly integrable by IST and it must be solved numerically; however, its solution exhibits true soliton behavior, really close to the KP solution [Pierini, 1989]. In particular, Pierini [1989] succeded in simulating ISWs in the Alboran Sea (Strait of Gibraltar) under some quite simple assumptions, namely, no background rotation, constant topography, constant interface depth and no background current. Cai and Xie [2010] introduced a variable coefficient version of (1.6) adding also a cubic nonlinear term and effects of bottom friction. The model has been used, in the configuration of a two–layered fluid, to investigate the propagation of ISWs in the northern South China Sea.

Models described above assume, in the evolution equations, the explicit presence of a transverse direction (say the y–direction). However, it is possible to make use of one–dimensional variable coefficients models, such as vKdV and veKdV, including a spreading term. This term naturally arises in the derivation of vKdV and veKdV equations in the context of ray theory (e.g., see Pelinovsky *et al.* [1994]). In particular, Small [2001b] developed a spreading algorithm based on his previous study on ISWs propagation and shoaling (see Small [2001a]), and studied the refraction of a planar wave obliquely incident on a continental slope and over a seamount. In a subsequent study, Small [2003] applied the spreading algorithm to investigate the shoaling and refraction of ISWs in the Malin Sea (United Kingdom). The properties of the simulated ISWs that arose from an idealized initial waveform were close to those obtained from in situ measurements. However, the numerical evolution of waves from a realistic initial condition showed some differences to the observed. These differences were due to neglect of strong nonlinearity and turbulence in the model [Small, 2003]. The spreading algorithm of Small [2001b] with realistic bottom topography, current and stratification, has been adopted by Xie *et al.* [2016] to study the distortion and broadening of an ISW front across the northeastern South China Sea deep basin. The results of simulations showed good agreement with the SAR–observed front. A similar nonlinear refraction model has been used also by Jia *et al.* [2017] to study the refraction and reconnection of ISWs around the Dongsha Atoll in the northern

South China Sea. The results of the simulations agreed with Advanced SAR images captured within 12 h each other.
The application of weakly nonlinear theories (even when modified and extended) to large–amplitude ISWs is under question because of the strong nonlinearity of the latter. For instance, Xie *et al.* [2015], to investigate how the large–amplitude ISWs characteristics in the northeastern South China Sea are perturbed by the oceanic eddies, had to adopt the three–dimensional MITgcm because of the high nonlinearity of those ISWs. Indeed, we observe that, from an analytical point of view, two–dimensional strongly nonlinear ISWs are not studied as much as the weakly nonlinear counterpart. However, a formulation of a two–dimensional MCC model has been recently introduced by Barros and Choi [2013], including also variability in the bottom topography.

1.3 Shoaling and breaking of ISWs. Mixing induced by ISWs breaking.

As internal tides propagate, they steepen due to nonlinearity and disperse into trains of internal solitary waves. Ultimately, these waves interact with the continental or nearshore slope, where they steepen further and eventually break. Prior to breaking, the dynamics of shoaling internal solitary waves are described well by analytical theories. In shallow water, during and after breaking, however, theories break down and non–analytical methods must be used to describe internal wave dynamics [Aghsaee *et al.*, 2010].
In recent years, scientific research has focused on the interaction between ISWs and the continental shelf/slope, studying the particular conditions that cause the breaking of shoaling internal waves and their consequent effects. The continental shelf is a shallow gently sloping region lying between the coast and the shelf break beyond which the water deepens rapidly down the steep continental slope, with an average angle of 2° to 4° (slope 0.03–0.07), to the deep ocean. The shelf break is typically at depths of 100–200 m [Cacchione *et al.*, 2002; Lamb, 2014]. The continental shelf is an important source of food, is a location for industrial activity, and is subject to nutrient, sediment, and pollutants transport from the adjacent land. The breaking and dissipation of internal waves have implications for all [Lamb, 2014].
Although field observations of shoaling and breaking internal waves have been made in the past (e.g.,Davis and Monismith [2011]; Klymak and Moum [2003]; Scotti and Pineda [2004]; Shroyer *et al.* [2009]; Walter *et al.* [2012]), these results are limited by the spatial and temporal resolution of field data. For this reason, much of our knowledge of the breaking of shoaling internal waves comes from laboratory studies and numerical simulations performed with simple geometries and either linear stratifications with constant N or continuous two–layer stratifications.
One of the most famous experiments concerning ISWs over a sloping boundary is that performed by Kao *et al.* [1985]. They studied the transition of ISWs from deep to shallow water in a long wave tank ($\sim$ 9 m) with the slope never intersecting the pycnocline (waves did not pass through a turning point). They evaluated the loss of energy due to shear instabilities and wave–breaking with the pycnocline at

several different depths below the free surface. Using a similar geometry, Helfrich and Melville [1986] studied the transition of ISWs of depression to waves of elevation during shoaling through a turning point onto a shelf. They found that breaking could occur in the neighborhood of the turning point, leading to a volume of mixed fluid that would evolve into a second-mode solitary-like wave propagating shoreward. In a later study, Helfrich [1992] investigated shoaling ISWs of depression in a geometry with a linearly sloping bottom extending to the surface. Thus the interface now intersected the bottom, and breaking occurred in all cases. Helfrich [1992] found that breaking was followed by the formation of waves of elevation (or boluses) containing mixed fluid propagating upslope, as already observed seen by Wallace and Wilkinson [1988] for periodic trains of long internal waves incident on a slope. He perfomed measurements of the *mixing efficiency*, defined in that case as the ratio between the change in potential energy inshore of the breaking point and the net energy into the breaking region

$$\epsilon = \frac{\Delta E_p}{E_{BP} - E_R}\,, \tag{1.7}$$

where E_{BP} is the energy onshore the breaking point and E_R is the reflected energy. In particular, it was found that the energy lost from internal waves, $\epsilon = 15 \pm 5$, was expended in increasing the potential energy of the stratification. In the same study, Helfrich [1992] proposed a criterion for finding the breaking location:

$$\frac{a_m}{H_b - H_m} \geq 0.4\,. \tag{1.8}$$

where a_m is the maximum displacement at the centre of wave, H_b is the water depth at point of wave breaking and H_m is the depth of an undisturbed position of the interface line.
Michallet and Ivey [1999] extended the results obtained by Helfrich [1992] to larger ISWs, finding that mixing efficiency was related to the ratio L_w/L_s, with L_w characteristic horizontal scale of the incident wave and L_s length scale of the slope. They also found a maximum mixing efficiency value of 25%.
Boegman *et al.* [2005] used a tilting tank to create an initial condition with a linearly sloping pycnocline. Thier aim was to reproduce basin-scale seiches that could steepen nonlinearly to form a nonlinear wave train and shoaling on a uniformly sloping bottom placed at one end of the tank. Thus, in a sense, these waves were propagating on a moving pycnocline. Three types of wave breaking were identified: spilling, plunging, and collapsing breakers. However, as reported by Aghsaee *et al.* [2010], the spilling breaker type was erroneously identified. To classify the different types of breaking, they introduced the internal Iribarren number ξ, defined as the ratio of the topographic slope to the square root of the wave slope:

$$\xi = \frac{s}{\sqrt{S_w}}\,, \tag{1.9}$$

where $S_w = S/\lambda$, with S wave surface and $\lambda = S/A$ wavelength. Plunging breakers, in which the rear face of the wave plunges forward (i.e., overturns), were observed for $\xi = 0.45 \div 0.75$, whereas collapsing breakers, in which the rear face of the wave starts to plunge forward but subsequently collapses on itself, were observed for

$\xi > 0.75$ [Boegman *et al.*, 2005; Lamb, 2014]. Boegman *et al.* [2005] modeled the reflection coefficient in terms of the Iribarren number and recast the results obtained by Michallet and Ivey [1999] for ϵ as a function of ξ. They also proposed a breaking point criterion from fit of their experimental data and those of [Helfrich, 1992]:

$$\frac{a_\infty}{h_b} = \frac{0.14}{(\lambda_\infty / L_i)^{0.52}} - 0.03 \tag{1.10}$$

where a_∞ and λ_∞ are the wave amplitude and wave width of the solitary wave in deep water, respectively; h_b is the undisturbed depth of the lower layer at the breaking location (where the rear part of the wave becomes vertical); and L_i is the length of the slope between the breaking location and the toe of the slope.
Sutherland *et al.* [2013] performed laboratory experiments on large amplitude ISWs shoaling on a constant slope with the intent to broaden the parameter range explored in the past in both experiments and simulations. They generated waves with amplitudes up to 3.5 times the shallow layer depth, well beyond the KdV regime. Their analyses focused upon predicting the maximum breaking depth and the consequent upslope propagation of the lower layer as a bolus. They used the Iribarren number (Ir) in order to identify the different breaking regimes: plunging breakers ($\mathrm{Ir} < 0.3$), collapsing breakers ($0.3 < \mathrm{Ir} < 0.7$) and surging breakers ($0.7 < \mathrm{Ir} < 1.5$). The marked difference of the values that identify breaking domains between Boegman *et al.* [2005] and Sutherland *et al.* [2013] is due to the different definition of the wavelength. Indeed, Sutherland *et al.* [2013] defined the wavelength as the halfwidth at the half maximum, while Boegman *et al.* [2005] defined the wavelength as the ratio between the wave surface and the wave amplitude, in accordance with the KdV theory.
In our study, we will consider the results of La Forgia *et al.* [2018a], who investigated large amplitude ISWs by laboratory experiments, broadening further the parameters range explored by Sutherland *et al.* [2013]. One aim of their study was to distinguish the breaking mechanisms by evaluating the parameter $\lambda = S/A$, extensively used in literature to define the ISW wavelength. This allowed to define an experimental set of Ir that have been used to describe breaking mechanisms, merging the numerical/theoretical approaches with the classic experiments on ISW breaking [Boegman *et al.*, 2005; Sutherland *et al.*, 2013]. La Forgia *et al.* [2018a] generated ISWs with wave amplitudes up to 4 times the shallow layers depth, again well beyond the KdV regime. The investigated slope values ranged between 0.15 and 0.95. For this reason, results may be efficiently applied to interpret the physical processes involved in real field observations. They also focused on breaking mechanisms in order to understand how to give rise to a particular type of breaking (i.e., plunging, collapsing and surging). In particular, they obtained a breaking mechanisms classification different from that of Sutherland *et al.* [2013]: for $\mathrm{Ir} < 1$ plunging breakers and for $\mathrm{Ir} = 1 \div 1.5$ collapsing breakers are observed, while plunging–collapsing breakers occur for $\mathrm{Ir} \simeq 1$. Surging breakers occur for $\mathrm{Ir} > 1.5$.
Numerical modelling has been used extensively to study shoaling and breaking internal waves on slopes both at the field [Bourgault *et al.*, 2007; Lamb, 2002; Vlasenko and Stashchuk, 2007a; Walter *et al.*, 2012] and laboratory scales [Aghsaee *et al.*, 2010; Venayagamoorthy and Fringer, 2007; Vlasenko and Hutter, 2002]. Field–scale models are able of capturing realistic wave and slope conditions, but they fail

to resolve the small-scale processes associated with breaking. Conversely, laboratory–scale models begin to resolve breaking processes but fail to capture realistic wave and slope conditions. Several high-resolution three-dimensional modelling studies have examined turbulence and mixing during internal wave generation and breaking on slopes: the direct numerical simulations (DNS) of Gayen and Sarkar [2010] and Arthur and Fringer [2014], and the large-eddy simulations (LES) of Gayen and Sarkar [2011].

Bourgault and Kelley [2007] revisited the laboratory experiments of Michallet and Ivey [1999] using two-dimensional numerical simulations including a parameterization of the effects of side-wall damping. This had a significant effect on the calculation of the reflectance coefficient $R = E_R/E_0$, where E_R and E_0 are the reflected and incident wave energy fluxes, respectively. Side–wall damping between the toe of slope and the breaking site would reduce R. They proposed a parameterization for R as a function of the Iribarren number ξ for laboratory–scale waves without side–wall effects:

$$R \simeq \left(1 - e^{-\xi/\xi_0}\right) , \tag{1.11}$$

with $\xi_0 = 0.78 \pm 0.02$.

Aghsaee *et al.* [2010] investigated the breaking of fully nonlinear internal solitary waves of depression shoaling upon a uniformly sloping boundary in a smoothed two-layer density field using high-resolution two–dimensional simulations. The simulations were performed for the range of boundary slopes $s \in [0.01, 0.3]$, generating internal waves with an amplitude from 0.2 to 2 times the shallow layer depth. They characterized the breaking regimes introducing time scales for each main process involved in the breaking event. They expanded the breakers classification, defining surging, collapsing, plunging and fission breaker types based on several time scales associated with breaking. Including smaller, more realistic slopes ($s \leq 0.05$) allowed to capture fission breakers, which were not included in Boegman *et al.* [2005] classification. During fission, nonlinearity varies gradually, and as the wave passes through the turning point, the rear face separates into a train of solitary waves of elevation that propagate up the slope as boluses. Fission has been observed in the field [Shroyer *et al.*, 2009] and with a two-dimensional field-scale numerical model [Bourgault *et al.*, 2007]. The breaker type was characterized in wave slope $S_w = A/L_w$ versus s space. Aghsaee *et al.* [2010] also evaluated the reflectance coefficient, and they found that the parameterization of [Bourgault and Kelley, 2007] was a good fit to the data. However, a modified parameterization for reflectance at the breaking site was proposed by estimating energy dissipations between the toe of the slope and the breaking location. They also proposed a parameterization for the breaking location

$$\frac{A}{h_{2b}} = \frac{0.14}{(\lambda/L_i)^{0.28}} + 0.13 , \tag{1.12}$$

where h_{2b} is the depth of the lower layer at the breaking location, λ is the width of the solitary wave given by KdV theory, and $L_i = h_2/s$ is the distance from the base of the slope to where the pycnocline intersects the bottom. Vlasenko and Hutter [2002] conducted two–dimensional numerical simulations solving the

Reynolds–averaged equations of ISWs shoaling onto a shelf using three stratifications based on observations in the Andaman Sea. They used a piece–wise linear slope and varied the shelf slope and the shallow-water depth. The simulated wave breaking was of the plunging type. They also proposed a breaking criterion that fits their results:

$$\frac{a_m}{H_b - H_m} \geq \frac{0.8^\circ}{\gamma} + 0.4\,, \tag{1.13}$$

where a_m is the maximum displacement at the centre of wave, H_b is the water depth at point of wave breaking, H_m is the depth of an undisturbed position of the interface line, and γ is the slope angle in the range $0.52^\circ < \gamma < 21.88^\circ$. This criterion is quite different from the more recent criterion proposed by Aghsaee *et al.* [2010]; however, the two were proposed for different shoaling geometries, qualitatively different stratifications, and very different Reynolds numbers [Lamb, 2014].
Arthur and Fringer [2014] using direct numerical simulations (DNS), investigated the structure and energetics of shoaling and breaking ISWs of depression on a sloping three–dimensional idealized domain. In particular, they compared their results for the mixing efficiency ϵ as a function of the Iribarren number ξ with those of Michallet and Ivey [1999] recast by Boegman *et al.* [2005]. Arthur and Fringer [2014] see a minimum mixing efficiency, rather than a maximum, for intermediate Iribarren numbers, and they appear to overestimate mixing efficiency for both the largest and smallest Iribarren number case. The discrepancy between their results and those of Michallet and Ivey [1999] and Boegman *et al.* [2005] can be explained by a Reynolds number (Re_w) effect. While they maintain a constant Re_w in their simulations and vary ξ , Michallet and Ivey [1999] varied Re_w and ξ simultaneously. Although they removed the Re_w effect making their results qualitatively agree with those of Michallet and Ivey [1999], a difference was still present for the lowest Iribarren number case, which has a larger mixing efficiency than the laboratory data. This was likely an effect of dissipation due to sidewall friction on the results, since Michallet and Ivey [1999] did not account for sidewall friction in their calculations, they overestimated the incident wave energy and underestimated the reflected wave energy off the slope [Bourgault and Kelley, 2007]. This led to an overestimation of the total energy lost during breaking, and therefore an underestimation of mixing efficiency.

1.4 Impacts of ISWs propagation and breaking

At the deeper layers of the ocean, surface waves do not play a leading role for the fluid motion. Here, the basic sources of energy are tides, currents and internal waves. Much of the interest in internal wave interaction with bottom topography stems from the claim of Munk and Wunsch [1998] that turbulence due to breaking internal waves at boundaries accounts for a significant sink of energy in the ocean. In particular, they have long been examined as an agent of mixing the ocean to produce the vertical diffusivities needed to maintain the thermoclines in balance with mean vertical advection, contributing to the vertical velocity in the ocean that is required to support the global thermohaline circulation [Arthur and Fringer, 2014;

Massel, 2015].
Many authors have identified large-amplitude ISWs as being of primary importance for mixing on the shelf. On the Scotian shelf, Sandstrom and Elliott [1984] observed that most of the internal tide energy generated at the shelf break was transferred to a few ISWs, which were responsible for the vertical mixing of nutrients. Jeans and Sherwin [2001] observed that water column mixing by ISWs is the prime source of mixing on the Portuguese shelf. St. Laurent [2008] concluded that large-amplitude ISWs make the South China Sea one of the most dissipative shelf regions in the world. It is not clear how often ISWs are a significant factor in driving mixing on the shelf [Lamb, 2014]. For these reasons, the mixing associated with breaking internal waves on slopes has also been an active area of research. As already seen in Sec.1.3, several studies have quantified the mixing efficiency, or the proportion of initial wave energy that contributes to irreversible mixing of the density field. Osborn [1980] estimated the diapycnal diffusivity K_ρ through the Richardson flux number R_f (which represents the ratio of the buoyant destruction of turbulent kinetic energy to the shear production; see Kundu *et al.* [2016] for definition):

$$K_\rho = \frac{R_f}{1 - R_f} \frac{\varepsilon}{N^2} = \Gamma \frac{\varepsilon}{N^2} \tag{1.14}$$

where ε is the turbulent kinetic energy dissipation rate, and Γ is the mixing efficiency representing the fraction of the turbulent dissipation rate ε that goes into raising the potential energy. Citing $R_f = 0.15$ from Ellison [1957], Osborn [1980] treated $\Gamma = 0.2$ as an upper bound. Subsequent usage treated efficiency as constant throughout the ocean. Still today, semi–empirical parametrizations need to assume $\Gamma = 0.2$ (e.g., St. Laurent *et al.* [2002] and Nikurashin and Ferrari [2013]), although it was generally understood that it may vary [3]. Indeed, there is clear consensus from the laboratory and DNS work that Γ is highly variable and changes with mechanism (e.g., see [Gregg *et al.*, 2018]), the evolutionary stage of a turbulent event, and location in the domain (e.g., Barry *et al.* [2001], Shih *et al.* [2005], Smyth *et al.* [2001], Bouffard and Boegman [2013]). From a global perspective, this inconsistency needs to be resolved. Observations show that the oceans are not uniformly and steadily agitated, but rather there is a relatively quiescent interior and turbulent hot spots, often near boundaries. This paradigm is central to global–scale ocean dynamics (e.g., see Wunsch and Ferrari [2004]), and researchers are increasingly focusing their attention on potential hot–spot regions. For example, the mixing

[3] Because of the difficulties in directly measuring R_f in the field and the general complexity of geophysical flows, our current understanding of mixing efficiency is primarily founded upon well–controlled laboratory experiments and DNS (see Sec.1.3). However, even within the context of these simple flows, no single parameterization for R_f in terms of relevant nondimensional parameters has received widespread acceptance [Mater and Venayagamoorthy, 2014b]. This lack of a unified description of mixing efficiency is largely due to certain ambiguities that arise when only a single nondimensional parameter is employed to describe R_f. The most common single–parameter descriptions are based on the gradient Richardson number $Ri = N^2/S^2$ [Karimpour and Venayagamoorthy, 2014], the Froude number $Fr = u/(Nl)$ [Ivey and Imberger, 1991] or the buoyancy Reynolds number Re_b [Shih *et al.*, 2005], but for a complete review on the subject see Gregg *et al.* [2018]. Though unifying multi–parameter frameworks for mixing efficiency description have been proposed (e.g., see Mater and Venayagamoorthy [2014a]), an unambiguous parameterization of mixing efficiency in geophysical flows is still lacking due to an incomplete set of calculable parameters (e.g., the turbulent kinetic energy)[Mater and Venayagamoorthy, 2014b].

efficiency Γ in energetic boundary regions is needed even to close simple energy budget models (e.g., Munk and Wunsch [1998], Wunsch and Ferrari [2004]), and there is a big difference between the model predictions if one uses an efficiency of either 0.2 or 0.02 [Ivey *et al.*, 2008]. Thus, it is important to determine the geography of mixing hot spots and the dynamics responsible for their spatial and temporal distribution.

Turbulent mixing caused by breaking ISWs (or, in general, internal waves) has implications also for nearshore distributions of temperature, nutrients, and larvae, as well as sediment transport and dissolved oxygen variability. ISWs induce bottom stress, which may become sufficient to initiate sediment motion, and near–bed instability can resuspend sediments. For large-amplitude waves over flat bottoms (e.g., Aghsaee and Boegman [2015]) and ISWs incident on steep slopes (as collapsing and plunging breakers), flow separation may occur in the adverse pressure gradient (i.e., a pressure gradient acting to decelerate fluid; in the bottom boundary layer, this can lead to flow separation and vortex formation) wake region behind the waves, driving strong turbulent events and enhanced sediment resuspension [Boegman and Stasna, 2019; Bogucki *et al.*, 1997; Lin *et al.*, 2015]. Smaller waves on gradual slopes will form waves of elevation and boluses [Helfrich, 1992; Sutherland *et al.*, 2013] with instability and resuspension at the wave front. Near–bed instability is, therefore, believed to be the principal mechanism driving ISW-induced sediment resuspension in coastal regions.
Sediments can be redistributed by ISWs through both bed load (i.e., particles in a flowing fluid that are transported along the bottom) transport and resuspension. They are displaced vertically through the water column until background stratification inhibits vertical transport, and then they intrude in the form of nepheloid layers (i.e., a layer of water in the deeper portion of the water column containing significant suspended sediment; see Bourgault *et al.* [2014] and Tian *et al.* [2019]) and form geologic features such as sand waves (e.g., Droghei *et al.* [2016] and Reeder *et al.* [2011]). For a complete review on the subject we suggest Boegman and Stasna [2019].
As ISWs and associated bores arrive into nearshore ecosystems, they bring with them deeper offshore waters. These offshore waters are generally full of nutrients that are largely absent in surface waters. In addition, internal waves and bores move the pycnocline vertically. As the pycnocline impinges into the nearshore because of internal waves, high concentrations of phytoplankton and zooplankton can also be transported into the nearshore [Woodson, 2018]. The transport of larvae to nearshore environments is perhaps the most studied ecological impact of internal waves [Ladah *et al.*, 2005; Pineda, 1991, 1994, 1999]. Internal waves provide a final push into the nearshore after larvae have been transported through other processes [Woodson, 2018]. However, highly nonlinear ISWs or ISWs become propagating bores can transport fluid or propagules embedded within the fluid. Recruitment of larvae to adult habitats by internal waves occurs largely when a propagating bore front accumulates larvae and transports them into adult habitats. Smaller larvae, unable to swim against the propagating front, are kept suspended by the increased turbulence in the bore, and are therefore swept along with it [Pineda, 1994; Woodson, 2018]. Larger larvae, such as late-stage juvenile fishes, may swim with

the wave and surf into a preferred adult habitat [D'Alessandro *et al.*, 2007]. As the bore moves shoreward, it loses energy, and larvae are then deposited in preferred nearshore habitats.

Large–amplitude ISWs can also have strong impact on civil infrastructures and human activities. Indeed, ISWs can cause strong, rapidly varying currents within the water column that are a proven hazard to offshore oil and gas developments in several regions of the world [Jackson *et al.*, 2013]. Osborne *et al.* [1977] describe the engineering impacts of the soliton's currents, which were responsible for a disruption to exploration drilling in the southern Andaman Sea. Subsequently, Osborne and Burch [1980] first linked soliton physics to oceanic nonlinear internal waves. From then, soliton impact on exploration drilling has been noted in many other regions, as Southeast Asia and offshore West Africa. Exploration drilling impacts include large tilts and horizontal displacements of rigs, or excessive mooring line tensions. Beyond exploration, solitons have proven seriously disruptive to other offshore operations, including installation of drilling rigs, offloading from ships to drilling platforms, and vessel maneuvers [Jackson *et al.*, 2013]. The rapid onset of soliton currents has the potential to affect large floating structures in a similar way to strong winds. Furthermore, near–bed currents associated with internal wave breaking present a challenge to pipelines and other seabed infrastructure.
ISWs can also influence undersea navigation and antisubmarine warfare operations [Osborne and Burch, 1980]. The US Navy has been investigating the motion of internal pycnoclines in the ocean because of several losses of modern submarines. These may move along the pycnoclines where detection by surface vessels is avoided, since the pycnocline tends to reflect and refract high–energy sonar pulses. The submarines move vertically according to the motion of the pycnocline since the density is adjusted to that of the surrounding water: neutral buoyancy is attained by flooding or jettisoning sea water from ballast tanks. A well documented loss is the submarine USS Thresher that sank in 1963 with 129 crew members and civilians aboard in the West Atlantic. Thresher had been the most advanced submarine in the world of the time, capable of reaching depths and speeds unimaginable a decade before. According to Pinet [1992] there had been no indication of equipment malfunction or of unusual storm weather. Navy scientists speculate that Thresher was probably cruising along a pycnocline when it encountered a large internal wave that moved the submarine down to a depth below the pressure capacity of the hull. The incident evidently occurred too rapidly for crew members to reduce the submarine's density to arrest their fall [Grue, 2006; Massel, 2015].

1.5 Thesis outline

Though analytical theories have an immediate predictive power, and help us to capture the essential features of physical processes, an analytical or semi–analytical treatment of complex phenomena, as wave breaking or mixing, is ardous. Indeed, studies on fluid flows and wave propagation are often carried out through numerical simulations. The aim of this thesis is to provide some useful analytical tools to study ISWs propagation, shoaling and breaking, so as to partially contribute to fill this gap.

In *Chapter 2*, we give some basic concepts about ISWs models and a brief derivation of the KdV equation for surface and internal waves. We describe the properties of the cnoidal and solitary wave solutions to KdV and eKdV equations. We also dedicate a section to MCC and DJL strongly nonlinear models: in particular, the MCC model will be used as reference model to check and extend the results obtained from KdV–type models.

In *Chapter 3*, we study the propagation of ISWs in non–uniform media, where the stratification or the background flow can vary along a given direction. Here we derive the variable–coefficients KdV (vKdV) and eKdV (veKdV) equations, and their slowly–varying analytical solutions. We examine the possible wave transformations that an ISW could undergo moving on a variable bathymetry and we derive an explicit analytical solution to the veKdV equation. We also describe the numerical algorithms used to perform simulations of vKdV and veKdV equations.

In *Chapter 4*, we study the interaction of ISWs with a sloping bottom. In particular, we examine the propagation and shoaling of ISWs in laboratory experiments, introducing the Iribarren number and classifying the different types of internal wave–breaking. We derive an analytical wave–breaking criterion using eKdV and MCC models, we validate it with experimental results, and we compare it with two empirical criteria developed in the recent years. To understand the behavior of shoaling ISWs we perform direct numerical simulations of vKdV and veKdV equations and we compare the results with the observed experimental waves. We then apply these KdV–type models to observed ISWs propagating northward from the Messina Strait to the frontal slope of Capo Vaticano, predicting breaking location from our wave–breaking model.

In *Chapter 5* we will focus on the mixing processes induced by the ISWs breaking on a sloping bathymetry. We define adiabatic and diabatic processes, potential energy, background potential energy and available potential energy (APE), in line with the theory developed by [Winters *et al.*, 1995]. Then, we dedicate a small section to the calculation of the APE of an ISW in a two–layer system. Finally, we build a theoretical model to predict the values of mixing efficiency involved in ISWs breaking on the basis of initial and final density stratification knowledge only. After a description of the experimental procedure, we validate the model through a comparison with results of laboratory experiments.

Chapter 2

Internal solitary waves: governing equations

In this chapter, we give some basic concepts about internal solitary waves models. Starting from the fundamental equations of motion, the Euler equations, we give a sketch of derivation of the KdV equation for surface and internal waves. Then, we describe the properties of the cnoidal and solitary wave solutions to both KdV and eKdV equations. These properties are of primary importance to understand the structure of the slowly–varying solutions described in Chapter 3. We also dedicate a section to MCC and DJL strongly nonlinear models: in particular, the MCC model will be used as reference model to check and extend the results obtained from KdV–type models.

2.1 Stability of water masses

To understand the physics of internal waves we briefly describe the concept of stability of ocean water. In general, a fluid element can be in one of the following three states:

- **stable case**: it is assumed that water density increases with water depth. The forces acting on an element of water of volume V, density $\rho(z)$ at a level $z = z_1$ are the gravity force W and the buoyancy force. These forces are initially in balance, i.e.

  $$\rho(z_1)gV - W = 0\,.$$

  If we move the element to another level $z = z_2$ (see Fig.2.1a) the weight of the element remains the same but the buoyancy force changes, because of the change of the density of surrounding water. Thus, we have:

  $$\rho(z_2)Vg - \rho(z_1)Vg = (\rho(z_2) - \rho(z_1))\,Vg < 0\,,$$

  since $\rho(z_2) < \rho(z_1)$, and the resulting force is directed downwards and the water element tends to sink back to its original level. If we move the element at level $z = z_3$ the resulting force is directed upwards and the water element tends to rise back to its original level.

- **unstable case**: we assume that the water density decreases with depth. Hence, the balance of forces for the water element moved to level z_2 is:

$$(\rho(z_2) - \rho(z_1))\, V g > 0\,.$$

  Thus, the water element will be pushed up, away from its initial position (Fig.2.1b). When the water element is moved from its initial position to the the level z_3, the buoyancy is not sufficient to balance the element's weight, and the element will sink, moving away from its initial position.

- **neutrally stable case**: the water density remains constant, thus the balance of forces is satisfied at any position. The element will not move if released from rest after being displaced (Fig.2.1c).

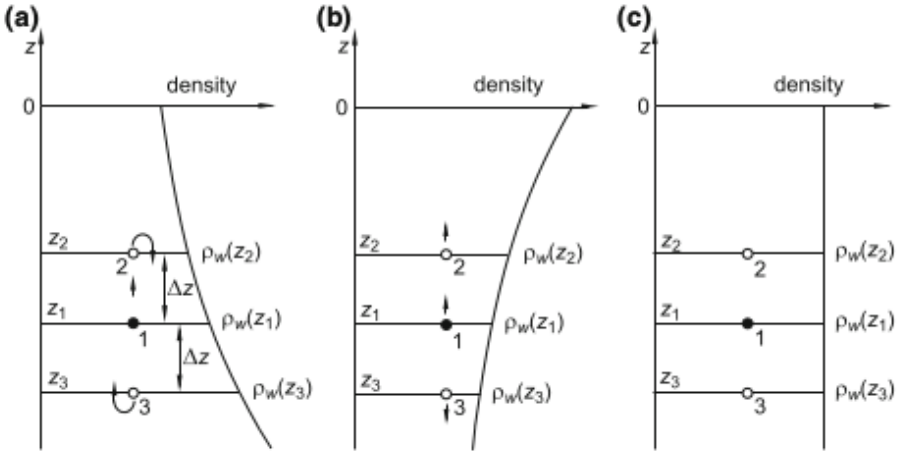

Figure 2.1. Different profiles of water density. (a) stable case: if we move the fluid element upwards (downwards) to the level z_2 (z_3), it tends to sink back (to rise back) to its original level z_1. (b) unstable case: if we move the fluid element upwards (downwards) to the level z_2 (z_3), it will be pushed away from z_1 (it will sink moving away from z_1). (c) neutrally stable: forces are always in balance and the element will not move after being displaced. From Massel [2015].

In reality, density profiles in the ocean may be simultaneously stable and unstable over different ranges of the vertical coordinate. To accommodate this possibility, a local criterion for stability at height z_0 can be determined from Newton's second law for the displaced element using weight and buoyancy (but not friction) forces when the initial vertical displacement ζ is small [Kundu *et al.*, 2016]. Consider a stable profile and assume that the Earth's rotation is ignored, thus when a small amount of water is displaced from its initial position, the resulting force tends to move it back to the initial position. The movement of the water element is restrained by an inertia force, and the resulting balance of force can be expressed as follows:

$$\rho \frac{\mathrm{d}^2\zeta}{\mathrm{d}t^2} + \left(-\frac{g}{\rho}\frac{\mathrm{d}\rho}{\mathrm{d}z}\right)\zeta = 0\,, \tag{2.1}$$

from which

$$\frac{\mathrm{d}^2\zeta}{\mathrm{d}t^2} + N^2(z)\zeta = 0\,,$$

with

$$N(z) = \sqrt{-\frac{g}{\rho}\frac{\mathrm{d}\rho}{\mathrm{d}z}}\,, \tag{2.2}$$

which is called *Brunt–Väisäla frequency*. For the stable static equilibrium in an incompressible fluid $\partial\rho/\partial z < 0$, and $N^2 > 0$. When $\partial\rho/\partial z > 0$, $N^2 < 0$ and the fluid medium is unstable at $z = z_0$: the displaced fluid particle will accelerate away from z_0 after release from $z_0 + \zeta$. When $\partial\rho/\partial z = 0$, $N^2 = 0$, the fluid at $z = z_0$ is neutrally stable and the element will have zero vertical acceleration.

2.2 Weakly nonlinear internal waves: KdV and eKdV equations

Here we shall give a brief outline of the derivation of the KdV equation for surface and internal waves from Euler equations. A more complete discussion can be found in Grimshaw [2002, 2005]. A systematic derivation through multiscale expansions technique for surface waves can be found in Debnath [2012] and Ablowitz [2011]. We consider an inviscid, incompressible fluid bounded above by a free surface and below by a flat rigid boundary of constant depth H (see Fig.2.2). We shall suppose that the flow is two–dimensional and can be described by the horizontal and vertical spatial coordinates x and z, respectively, so that the free surface is $z = \eta$ and the bottom is $z = -H$. The basic equations are then,

$$\rho(u_t + uu_x + wu_z) + p_x = 0\,, \tag{2.3}$$
$$\rho(w_t + uw_x + ww_z) + p_z + g\rho = 0\,, \tag{2.4}$$
$$\rho_t + u\rho_x + w\rho_z = 0\,, \tag{2.5}$$
$$u_x + w_z = 0\,, \tag{2.6}$$

where the first two equations are the Euler equations along the x and z coordinates, while (2.5) and (2.6) are the continuity equation and the incompressibility constraint, respectively. The boundary conditions are

$$w = 0\,, \quad \text{at } z = -H\,,$$
$$p = 0\,, \quad \text{at } z = \eta\,,$$
$$\eta_t + u\eta_x = w\,, \quad \text{at } z = \eta\,.$$

In the basic state the fluid has density $\rho_0(z)$, a corresponding pressure $p_0(z)$ such that $p_{0z} = -gp_0$ describes the basic hydrostatic equilibrium, and a horizontal shear flow $u_0(z)$ in the x–direction. Then, the equations of motion relative to this basic state are:

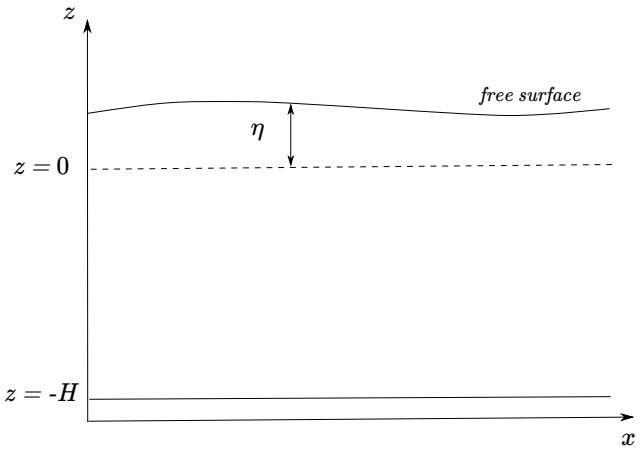

Figure 2.2. Schematic representation of a fluid bounded above by a free surface and below by a flat rigid boundary of constant depth H. The flow is two–dimensional and can be described by the horizontal and vertical spatial coordinates x and z, respectively, so that the free surface is $z = \eta$ and the bottom is $z = -H$.

$$\rho_0(u_t + u_0u_x + wu_{0z}) + p_z = -(\rho_0 + \rho)(uu_x + wu_z) - \rho(u_t + u_0u_x + wu_{0z})\,, \tag{2.7a}$$

$$p_z + g\rho = -(\rho + \rho_0)(w_t + u_0w_x + uw_xww_z)\,, \tag{2.7b}$$

$$g(\rho_t + u_0\rho_x) - \rho_0N^2w = -g(u\rho_x + w\rho_z)\,, \tag{2.7c}$$

$$u_x + w_z = 0\,, \tag{2.7d}$$

where $N(z)$ is the Brunt–Väisäla frequency (see (2.2)) defined as

$$N^2(z) = -\frac{gp_{0z}}{\rho_0}\,, \tag{2.8}$$

and $(u_0 + u, w)$ are the velocity components in the (x, z) directions, $\rho_0 + \rho$ is the density, $p_0 + p$ is the pressure. In this case, the boundary conditions are

$$w = 0\,, \quad \text{at} \;\; z = -H\,, \tag{2.9a}$$

$$p_0 + p = 0\,, \quad \text{at} \;\; z = \eta\,, \tag{2.9b}$$

$$\eta_t + u_0\eta_x + u\eta_x = w\,, \quad \text{at} \;\; z = \eta\,. \tag{2.9c}$$

We now proceed to derive the KdV equation for internal solitary waves, but note that to recover the theory for water waves from this general formulation it is sufficient to put the density $\rho_0(z) = \text{const}$. To describe internal solitary waves we seek solutions whose horizontal length scales are much greater than H, and whose time scales are much greater than N^{-1}. We also assume that the waves have small amplitude. Linear long wave theory is obtained by omitting the right–hand side of equations (2.7), and simultaneously linearizing boundary conditions (2.9b) and (2.9c). Solutions are sought in the form

$$\zeta(x,z,t) = \eta(x - c_0 t)\Phi(z) \tag{2.10}$$

where ζ is the vertical particle displacement relative to the basic state, c_0 is the linear long wave speed and Φ is the modal function defined by the boundary–value problem

$$\Big\{\rho_0(c_0 - u_0)^2\Phi_z\Big\}_z + \rho_0 N^2\Phi = 0\,, \quad \text{for } -H < z < 0\,, \tag{2.11a}$$

$$\Phi(-H) = 0\,, \quad (c_0 - u_0)^2\Phi_z = g\Phi \quad \text{at } z = 0\,. \tag{2.11b}$$

Equation (2.11a) is the long wave limit of the *Taylor–Goldstein equation* (see Kundu *et al.* [2016]; Vallis [2017]), and solved with the boundary conditions (2.11b) determines the modal function and the linear wave speed c_0. The remaining dependent variables are given by

$$u = \eta(c_0 - u_0)\frac{\mathrm{d}\Phi}{\mathrm{d}z}\,, \quad p = \eta\rho_0(c_0 - u_0)^2\frac{\mathrm{d}\Phi}{\mathrm{d}z}\,, \quad \rho = \eta\rho_0 N^2\Phi\,. \tag{2.12}$$

The boundary–value problem (2.11) is a Sturm–Liouville problem, and defines an infinite sequence of modes (eigenfunctions), $\Phi_n^{\pm}(z)$, $n = 0, 1, 2, \ldots$, with corresponding speeds $c_n^{\pm}$ (eigenvalues), where the superscript $\pm$ indicates waves with $c_n^+ > u_M = \max u_0(z)$ and $c_n^- < u_m = \min u_0(z)$ respectively. We shall confine our attention to these regular modes, and consider only stable shear flows. Nevertheless, we note that there may also exist singular modes with $u_m < c < u_M$ for which an analogous theory can be developed [Grimshaw, 2005]. It is useful to let $n = 0$ denote the surface gravity waves for which c scales with $\sqrt{gh}$ and then $n = 1, 2, 3, \ldots$ denotes the internal gravity waves for which c scales with NH. Typically, the surface mode Φ_0 has no extrema in the interior of the fluid and takes its maximum value at the surface $z = 0$, while the internal modes $\Phi_n^{\pm}(z)$, $n = 1, 2, 3, \ldots$, have n extremal points in the interior of the fluid, and vanish near $z = 0$ and $z = -H$ [Grimshaw, 2002, 2005]. For some specific stratifications, as two–layer or exponential stratifications, it is possible to solve the boundary–value problem (2.11) analytically, and for arbitrary stratifications it is possibile to apply a variational approach [Kantorovitch and Krylov, 1962; Massel, 2015]. However, (2.11) can be also solved numerically, especially when one has to deal with values of $N(z)$ determined experimentally (as in the case, for example, of Grimshaw *et al.* [2004]). A numerical approach to (2.11) is given by Fringer and Street [2003], who propose a solution through a second–order centered finite–difference discretization on an arbitrarily spaced mesh.
It can be shown that the solution of the linearized long wave equations can be written as a sum of modes $\Phi_n^{\pm}$ given asymptotically by

$$\zeta \sim \sum_{n=0}^{\infty} \eta_n^{\pm}(x - c_n t)\Phi_n^{\pm}(z)\,, \quad \text{as } t \to \infty\,, \tag{2.13}$$

where the amplitudes $A^{\pm}$ are determined from the initial conditions (see Grimshaw [2005]). Assuming that the speeds $c_n^{\pm}$ of each mode are sufficiently distinct, for large times we can consider just a single mode. Henceforth, we will omit the indices and assume that the mode has speed c, amplitude η and modal function Φ. During time

evolution, the hitherto neglected nonlinear terms begin to have an effect, and cause wave steepening. However, this is opposed by the terms representing linear wave dispersion, also neglected in the linear long wave theory. A balance between these two effects emerges as time increases and the outcome is the KdV equation for the wave amplitude.

We introduce two small parameters, α and ε, respectively characterizing the wave amplitude and dispersion. The KdV balance requires $\alpha = \varepsilon^2$, with a corresponding timescale of ε^{-3}. It is possible to perform an asymptotic analysis defining the scaled variables [Benjamin, 1967; Benney, 1966]

$$T = \epsilon\alpha t\,, \quad X = \epsilon(x - ct)\,,$$

and then putting

$$\zeta = \alpha\eta(X,T)\Phi(z) + \alpha^2\zeta_2 + \cdots\,. \tag{2.14}$$

At leading order, we obtain the linear long wave theory for the modal function $\Phi(z)$ and the speed c, defined by the boundary–value problem (2.11a). Since (2.11a) are homogeneous equations, we can impose a normalization condition on $\Phi(z)$. In particular, we set $\Phi(z_m) = 1$, where $|\Phi(z)|$ assumes a maximum value at $z = z_m$. In this case, the amplitude $\alpha\eta$ is uniquely defined as the amplitude of ζ at the depth z_m (at the leading order, $O(\alpha)$). At the next order, $O(\alpha^2)$ it is possible to obtain a boundary–value problem similar to (2.11a), but of inhomogenous type. From this problem, and its compatibility conditions (see Grimshaw [2005] for all the details), we can get the KdV equation

$$\eta_T + \alpha\eta\eta_X + \beta\eta_{XXX} = 0\,, \tag{2.15}$$

where the coefficients are defined by

$$I\alpha = \int_{-H}^{0} \rho_0(c - u_0)^2\Phi_z^3\,dz\,, \tag{2.16a}$$

$$I\beta = \int_{-H}^{0} \rho_0(c - u_0)^2\Phi^2\,dz\,, \tag{2.16b}$$

$$\text{where} \quad I = 2\int_{-H}^{0} \rho_0(c - u_0)\Phi_z^2\,dz\,. \tag{2.16c}$$

The KdV equation (2.15) has to be solved with the initial condition $\eta(X, T = 0) = \eta_0(X)$, where $\eta_0(X)$ is determined from the linear long wave theory.

A particularly important special case arises when the nonlinear coefficient α defined by the expression (2.16a) is close to zero. In this situation, a cubic nonlinear term is needed, and this can be achieved with a rescaling. The optimal choice is to assume that α is $O(\varepsilon)$, and then replace η with η/ε in (2.14)[Grimshaw *et al.*, 2010]. The outcome is that the KdV equation (2.15) is replaced by the extended KdV equation (eKdV), widely known as the Gardner equation,

$$\eta_T + \alpha\eta\eta_X + \alpha_1\eta^2\eta_X + \beta\eta_{XXX} = 0\,, \tag{2.17}$$

where α_1 can be derived as a function of the eigenfunctions of the boundary–value problem (2.11) and the boundary–value problem for $T(z)$, which is the first nonlinear correction to Φ:

$$\frac{\mathrm{d}}{\mathrm{d}z}\left[(c-u_0)^2\frac{\mathrm{d}T}{\mathrm{d}z}\right] + N^2 T = -\alpha\frac{\mathrm{d}}{\mathrm{d}z}\left[(c-u_0)\frac{\mathrm{d}T}{\mathrm{d}z}\right] + \frac{3}{2}\frac{\mathrm{d}}{\mathrm{d}z}\left[(c-u_0)^2\left(\frac{\mathrm{d}\Phi}{\mathrm{d}z}\right)^2\right] \tag{2.18a}$$

$$T(-H) = 0\,, \quad T(0) = 0\,. \tag{2.18b}$$

To define a unique solution of (2.18) [Grimshaw *et al.*, 2002; Kurkina *et al.*, 2017], we impose the auxiliary normalizing condition the function $T(z)$ so that $T(z_{\max}) = 0$, where $z_{\max}$ is found from $\Phi(z_{\max}) = 1$. Then, α_1 is defined as [Grimshaw *et al.*, 2002, 2004]:

$$\alpha_1 = \frac{\displaystyle\int dz\left\{3(c-u_0)^2\left[3\frac{\mathrm{d}T}{\mathrm{d}z} - 2\left(\frac{\mathrm{d}\Phi}{\mathrm{d}z}\right)^2\right]\left(\frac{\mathrm{d}\Phi}{\mathrm{d}z}\right)^2 - \alpha^2\left(\frac{\mathrm{d}\Phi}{\mathrm{d}z}\right)^2 + \Pi\right\}}{\displaystyle\int (c-u_0)\left(\frac{\mathrm{d}\Phi}{\mathrm{d}z}\right)^2 dz}\,, \tag{2.19a}$$

$$\text{where} \quad \Pi = \alpha(c-u_0)\left[5\left(\frac{\mathrm{d}\Phi}{\mathrm{d}z}\right)^2 - 4\frac{\mathrm{d}T}{\mathrm{d}z}\right]\frac{\mathrm{d}\Phi}{\mathrm{d}z}\,. \tag{2.19b}$$

Moreover, once T is known, it is possible to rewrite the expression for the vertical isopycnal displacement ζ (2.14) up to the first nonlinear correction

$$\zeta(X,z,T) \simeq \eta(X,T)\Phi(z) + \eta^2(X,T)T(z)\,. \tag{2.20}$$

As observed above, it is possible to calculated explicitly the modal function and the coefficients of KdV and eKdV equations in some specific cases. We consider the case of surface waves and interfacial waves.

For surface water waves, we set $\rho_0 = \text{const}$, then $N^2 = 0$. We also assume that there is no background shear. The solution to (2.11a) is [Grimshaw, 2005]

$$\Phi = \frac{z+H}{H}\,, \quad \text{for } -H < z < 0\,, \quad \text{with } c = \sqrt{gh}\,.$$

In this system there are no other modes. The coefficients given by (2.16) then become

$$I = \frac{2\rho_0 c}{H}\,, \quad \alpha = \frac{3c}{2H}\,, \quad \beta = \frac{cH^2}{6}\,. \tag{2.21}$$

Thus, the KdV equation in the original variables (x,t) becomes

$$\zeta_t + c\zeta_x + \frac{3c}{2H}\zeta\zeta_x + \frac{cH^2}{6}\zeta_{xxx} = 0\,, \tag{2.22}$$

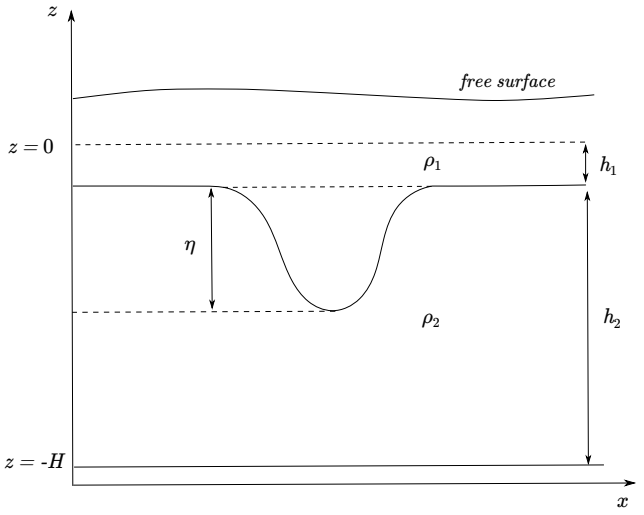

Figure 2.3. Schematic representation of an internal wave of depression in a two–layer fluid system. As upper boundary, at $z = 0$ we find a rigid boundary, which replaces the free surface (rigid–lid approximation). The bottom is situated at $z = -H$. The variable η describes the displacement, with respect to $z = 0$, of the interface between the two fluids with ρ_1 in an upper layer of height h_1 and ρ_2 in the lower layer of height $h_2 = H - h_1$.

which is the form of the equation originally derived by Korteweg and De Vries [1895]. Note that here $z_{\max} = 0$ so we identified η with $\zeta(x, 0, t)$, the free surface displacement, to leading order.

If we now consider a two–layer fluid, waves may occur at the interface between the two fluids with ρ_1 in an upper layer of height h_1 and ρ_2 in the lower layer of height $h_2 = H - h_1$ (see Fig. 2.3). The density in the fluid can be written through the Heaviside function $H(z)$

$$\rho_0(z) = \rho_1 H(z + h_1) + \rho_2 H(-z - h_1)\,, \tag{2.23}$$

and the buoyancy frequency is $N^2 = g((\rho_2 - \rho_1)/\rho_0)\delta(z + h_1)$, where $\delta(z)$ is the Dirac δ-function. For simplicity, we assume that $\rho_1 \simeq \rho_2$ (Boussinesq approximation), the usual situation in the ocean. In this approximation, we can replace the free boundary with a rigid boundary (see Fig.2.3) so that the upper boundary condition for $\Phi(z)$ becomes just $\Phi(0) = 0$. Then, from (2.11) and (2.16), we find

$$\Phi = -\frac{z}{h_1} \quad \text{for } -h_1 < z < 0 \tag{2.24a}$$

$$\Phi = \frac{z + H}{h_2} \quad \text{for } -H < z < -h_1 \tag{2.24b}$$

$$c = \sqrt{\frac{g(\rho_2 - \rho_1)h_1 h_2}{\rho_2(h_1 + h_2)}} \tag{2.24c}$$

$$\alpha = \frac{3}{2}c\frac{h_1 - h_2}{h_1 h_2} \tag{2.24d}$$

$$\beta = \frac{c}{6}h_1 h_2 \tag{2.24e}$$

We note that the nonlinear coefficient α for these interfacial waves is negative (positive) when $h_1 < (>) h_2$ (that is, the when interface is closer to the free surface than to the bottom). If $h_1 > h_2$, the pycnocline is displaced upward, while for $h_1 < h_2$ the pycnocline is displaced downward. In the last case, a wave of depression is observed. During the propagation of an internal wave an inversion of polarity could take place and a wave of elevation would become a wave of depression (or vice versa), and this is associated to a change in sign of the coefficient α [Grimshaw, 2005; Grimshaw *et al.*, 2010; Helfrich and Melville, 2006]. If $h_1 \simeq h_2$, then $\alpha = 0$, and it is necessary to take into account the cubic nonlinear term in equation (2.17). For interfacial waves, solving the problem (2.18) and using (2.19), we get

$$\alpha_1 = \frac{3c_0}{(h_1 h_2)^2}\left[\frac{7}{8}(h_1 - h_2)^2 - \left(\frac{h_1^3 + h_2^3}{h_1 + h_2}\right)\right]. \tag{2.25}$$

2.2.1 Solutions to KdV and eKdV equations: cnoidal and solitary waves

KdV and eKdV equations, i.e., (2.15) and (2.17), respectively, have permanent wave solutions known as solitary waves. Korteweg and De Vries [1895] showed that these waves are the limiting members of a two–parameter family of periodic travelling wave solutions, described by elliptic functions and commonly known as *cnoidal waves* [Grimshaw, 2005, 2007; Massel, 2015]:

$$\zeta(x,t) = \frac{A}{m}\left(1 - \frac{\mathbf{E}(m)}{\mathbf{K}(m)} - m\right) + A\,\mathrm{cn}^2\left[\frac{2\mathbf{K}(m)}{L}(x - Ut)\right], \tag{2.26}$$

where $cn(x,t;m)$ is the cosine–elliptic function of modulus m $(0 < m < 1)$, $\mathbf{K}(m)$ and $\mathbf{E}(m)$ are the elliptic integrals of the first and second kind defined by [Abramowitz and Stegun, 1965]

$$\mathbf{K}(m) = \int_0^{\pi/2} \frac{du}{\sqrt{1 - m\sin^2(u)}}$$
$$\mathbf{E}(m) = \int_0^{\pi/2} \sqrt{1 - m\sin^2(u)}\, du\,,$$

A is the amplitude, L is the wavelength given by

$$L = \frac{48\widehat{\beta}m}{A\widehat{\alpha}}\mathbf{K}(m)\,, \tag{2.27}$$

with $\widehat{\beta} = \beta/c$ and $\widehat{\alpha} = \alpha/c$, which constitutes a transcendetal relationship for the unknown parameter m. The phase speed is given by

$$U = c\left[1 + \frac{\widehat{\alpha}A}{3m}\left(2 - \frac{3\mathbf{E}}{\mathbf{K}} - m\right)\right].$$

The solitary wave solution is obtained from (2.26) for $m \to 1$ (see Fig.2.4), for which we have $\mathbf{K}(1) \to \infty$ and $\mathbf{E} = 1$. Thus, $L \to \infty$ and $cn^2(\cdot) \to \cosh^{-2}(\cdot)$. Since the

ratio $\mathbf{K}/L$ approaches a finite limit (see (2.27)), Eq.(2.26) becomes the KdV solitary wave solution

$$\zeta = A\cosh^{-2}\left(\frac{A\widehat{\alpha}}{12\widehat{\beta}}(x-Ut)\right) = A\,\mathrm{sech}^2\left(K(x-Ut)\right)\,, \tag{2.28}$$

with $U = A\widehat{\alpha}/3 = 4\widehat{\beta}K^2$.

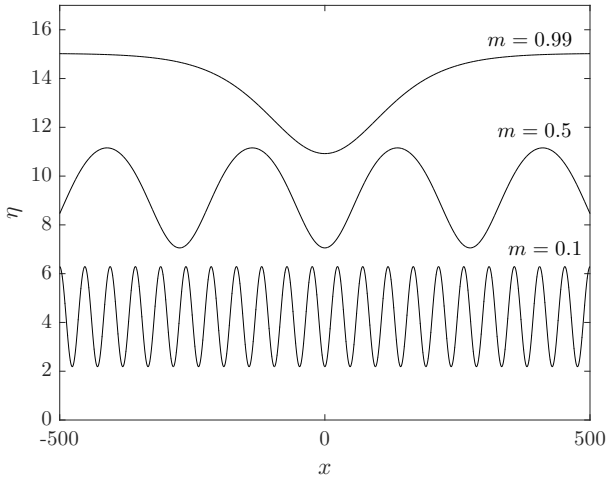

Figure 2.4. Cnoidal solutions of the KdV equation. For $0 < m < 1$, we have cnoidal waves, i.e., periodic waves with permanent form. For $m \to 1$, we get the solitary wave limit, and we see a single travelling wave of permanent form.

The eKdV cnoidal solutions have a more complicated form than that of KdV cnoidal waves, and we refer the reader to Grimshaw [2007](pg.102) to get an idea of it. However, in the limit $m \to 1$ of eKdV cnoidal solutions, it is again possible to recover the solitary wave solution [Grimshaw, 2007], which is

$$\zeta(x,t) = \frac{D}{1 + B\cosh(K(x-Vt))}\,, \tag{2.29}$$

with

$$V = \frac{\alpha D}{6} = \beta K^2\,, \quad B^2 = 1 + \frac{6\alpha_1\beta K^2}{\alpha^2}\,. \tag{2.30}$$

The amplitude of the solitary wave is given by

$$a = \frac{D}{1+B}\,, \tag{2.31}$$

where only the parameter B is arbitrary , and the other parameters depend on it. For $\beta\alpha_1 < 0$, $0 < B < 1$, and the family ranges from small–amplitude waves of KdV–type ("sech^2"–type profile) ($B \to 1$) to flat–topped wave of limiting amplitude $\zeta_{\mathrm{lim}} = -\alpha/\alpha_1$ ($B \to 0$), the so-called "table-top" wave (see Fig.2.5a). For $\beta\alpha_1 > 0$ there are two branches: one branch has $1 < B < \infty$ and ranges from small–amplitude KdV–type waves ($B \to 1$), to large waves with a "sech"–profile ($B \to \infty$).

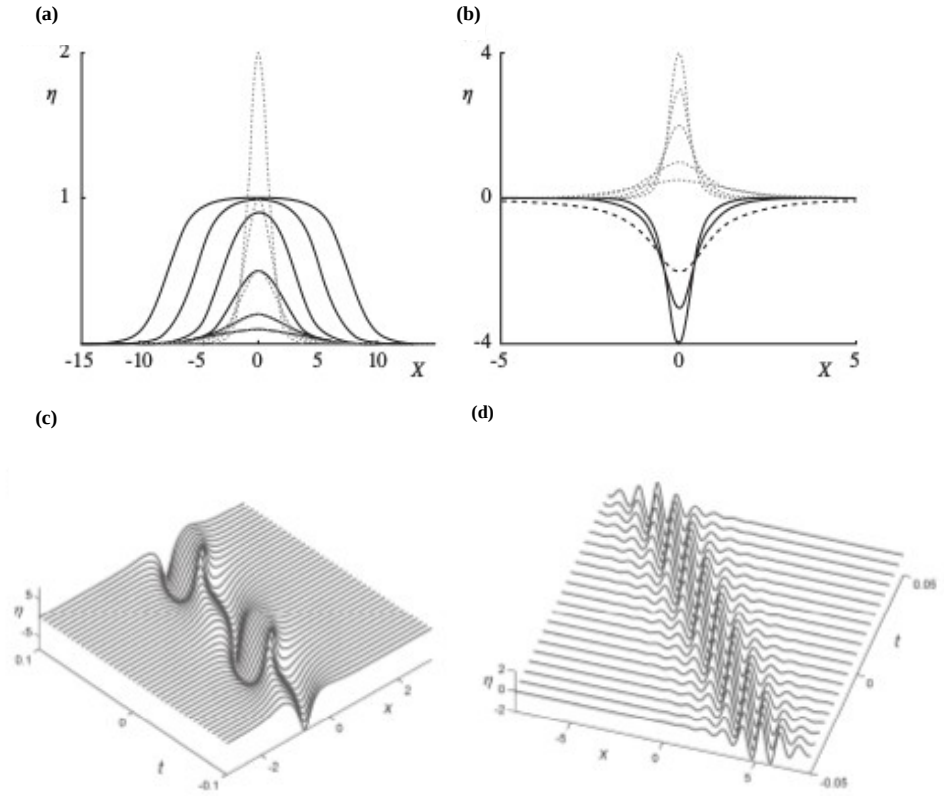

Figure 2.5. Solitary wave solutions of eKdV equation. (a) For $\alpha_1 < 0$ the family ranges from small–amplitude waves of KdV–type to the so-called "table-top" wave with limiting amplitude $\zeta_{\rm lim} = -\alpha/\alpha_1$ (KdV waves, dotted lines; eKdV waves, solid lines). (b) For $\alpha_1 > 0$ there are two branches; one branch (dotted lines) has $1 < B < \infty$ and ranges from small–amplitude KdV–type waves ($B \to 1$), to large waves with a "sech"–profile ($B \to \infty$). The other branch (solid lines) with $-\infty < B < -1$, has the opposite polarity and ranges from large waves with a "sech"–profile when $B \to -\infty$, to a limiting algebraic wave of amplitude $\zeta_{\rm alg} = -2\alpha/\alpha_1$ (dashed line) when $B \to -1$. (c)-(d) Typical breathers of eKdV equation. From Pelinovsky *et al.* [2007].

The other branch with $-\infty < B < -1$, has the opposite polarity and ranges from large waves with a "sech"–profile when $B \to -\infty$, to a limiting algebraic wave of amplitude $\zeta_{\rm alg} = -2\alpha/\alpha_1$ when $B \to -1$ (see Fig.2.5b). Solitary waves with smaller amplitudes cannot exist, and they are replaced by "breathers" [Pelinovsky and Grimshaw, 1997; Pelinovsky *et al.*, 2007]), that is, pulsating solitary waves (see Fig.2.5c-d). A breather may look like the collision of two solitons of opposite polarities, or resemble a localized wave group containing a large number of individual waves. When $\alpha_1 \to 0$, $B \to 1$ and the family reduces to the well–known KdV "sech^2" solitary wave family.

In this thesis, the following form of the KdV equation will be also used in some cases [Helfrich and Melville, 2006; Massel, 2015]:

$$\eta_t + c_0\eta_x + \alpha\eta\eta_x + \beta\eta_{xxx} = 0\,, \tag{2.32}$$

where $\eta(x,t)$ is the pycnocline vertical displacement, c_0 is the phase speed of the associated linear wave. Similarly, for the eKdV equation, we can write

$$\eta_t + (c_0 + \alpha\eta + \alpha_1\eta^2)\eta_x + \beta\eta_{xxx} = 0\,. \tag{2.33}$$

A solution of the eKdV equation is the internal solitary wave:

$$\eta(x,t) = \frac{A}{b + (1-b)\cosh^2\left[\gamma(x - Ut)\right]}\,, \tag{2.34}$$

in which

$$U = c_0 + \frac{A}{3}\left(\alpha + \frac{1}{2}\alpha_1 A\right)\,, \qquad \gamma^2 = \frac{A\left(\alpha + \frac{1}{2}\alpha_1 A\right)}{12\beta}\,, \qquad b = \frac{-A\alpha_1}{2\alpha + \alpha_1 A}\,. \tag{2.35}$$

It is possibile to write the solitary wave solution of the eKdV equation in the form of a "kink–antikink" pair

$$\eta(x,t) = -\frac{\alpha}{\alpha_1}\frac{\nu}{2}\left[\tanh\left(\frac{x - Vt}{\Delta} + \delta\right) - \tanh\left(\frac{x - Vt}{\Delta} - \delta\right)\right]\,, \tag{2.36}$$

where ν is a parameter of nonlinearity that could be varied from 0 (zero nonlinearity, i.e. zero amplitude) to 1 (maximum amplitude), and

$$\delta(\nu) = \frac{1}{4}\ln\left(\frac{1+\nu}{1-\nu}\right)\,, \qquad \Delta = \sqrt{-\frac{24\alpha_1\beta}{\alpha^2\nu^2}}\,, \qquad V = c_0 - \frac{\alpha^2\nu^2}{6\alpha_1}\,. \tag{2.37}$$

where δ is a phase factor, Δ is a width scale and V is the phase speed. The value $2\delta\Delta$ represents the distance between the kink fronts along x [Ostrovsky and Stepanyants, 1989; Small, 2001a; Stanton and Ostrovsky, 1998]. As $\nu \to 1$, the distance tends to infinity ($\delta \to \infty$) and we get the maximum wave amplitude $\eta_{\max} = -\alpha/\alpha_1$. Thus, as already seen, eKdV solitary waves with larger amplitudes have larger widths, and they have a limiting amplitude value.

2.3 Strongly nonlinear models: MCC and DJL models

KdV–type models can fail to describe internal solitary wave profiles of very large amplitude (e.g. $\eta > \eta_{\max}$). Miyata, Camassa and Choi derived a strongly nonlinear weakly dispersive model to describe large–amplitude internal solitary waves for a two–layer system bounded by a rigid surface (rigid–lid approximation) [Choi and Camassa, 1999; Miyata, 1985], which we will denote in the following as *MCC–RL model*. Unlike KdV–type models, there are no smallness assumptions on wave amplitude.

In a two–layer system, with densities and depths given by ρ_1 and h_1 for the upper fluid layer, ρ_2 and h_2 for the lower layer, we define the local layer thicknesses as

$$\eta_1 = h_1 - \zeta\,, \quad \eta_2 = h_2 + \zeta\,, \tag{2.38}$$

where ζ is the elevation of the interface. The MCC–RL model is derived from the continuity equation and the Euler equations for each layer (see Choi and Camassa [1999] for details), and can be written in terms of the unknowns ζ, $\overline{u}_1$, $\overline{u}_2$, P:

$$\eta_{it} + (\eta_i \overline{u}_i)_x = 0 \tag{2.39}$$

$$\overline{u}_{it} + \overline{u}_i \overline{u}_{ix} + g\zeta_x = -\frac{P}{\rho_i} + \frac{1}{\eta_i}\left(\frac{1}{3}\eta_i^3 G_i\right)_x\,, \tag{2.40}$$

with $i = 1, 2$, where P is the pressure at the interface, $\overline{u}_i$ are the depth–averaged horizontal velocities, g the gravitational acceleration and

$$G_i(x,t) = -\frac{(D_i^2 \eta_i)}{\eta_i}\,,$$

with $D_i \equiv \partial_t + \overline{u}_i \partial_x$. To look for travelling wave solutions, i.e. for waves of permanent form propagating with constant speed c, we can write η_i and u_i in the frame of reference moving with the wave as

$$\eta_i = \eta_i(X)\,, \quad \overline{u}_i = \overline{u}_i(X)\,, \quad X = x - ct\,.$$

It is then possible to derive [Choi and Camassa, 1999] the following nonlinear ordinary differential equation for ζ:

$$\zeta_X^2 = \frac{3\zeta^2\left[c^2\left(\rho_1\eta_2 + \rho_2\eta_1\right) - g(\rho_2 - \rho_1)\eta_1\eta_2\right]}{c^2\left(\rho_1 h_1^2 \eta_2 + \rho_2 h_2^2 \eta_1\right)} \tag{2.41}$$

Imposing that $\zeta_X = 0$ when $\zeta = a$ (maximum or minimum of the wave profile), using (2.38), and expliciting with respect to c^2, we get the following relationship between c and a

$$c^2 = \frac{g(h_1 - a)(h_2 + a)(\rho_2 - \rho_1)}{\rho_1 h_2 + a(\rho_1 - \rho_2) + \rho_2 h_1}\,. \tag{2.42}$$

Substituting (2.38) and (2.42) in (2.41), we get the solitary wave profile by numerical integration with the initial condition $\zeta(0) = a$. Integration of (2.41) through separation of variables is also possible, resulting in a wave profile $\zeta(X)$ expressed by an implicit relation $X = X_s(\zeta)$, where X_s is a combination of elliptic integrals [Choi and Camassa, 1999; Miyata, 1985]: wave profiles can be obtained by plotting routines. Integration can be perfomed up to the maximum wave amplitude a_m and its corresponding speed c_m given by [Choi and Camassa, 1999; Kodaira *et al.*, 2016]

$$a_m = \frac{h_1 - h_2\sqrt{\rho_1/\rho_2}}{1 + \sqrt{\rho_1/\rho_2}}\,, \quad c_m^2 = g(h_1 + h_2)\frac{1 - \sqrt{\rho_1/\rho_2}}{1 + \sqrt{\rho_1/\rho_2}}\,.$$

When the upper layer is bounded above by a top free surface located at $z = h_1 + \zeta_1$ and below by the interface located at $z = \zeta_2$, equations (2.39) need some modifications, and we can define a free–surface model, *MCC–FS* (see Choi and Camassa [1996];

Kodaira *et al.* [2016]). In the MCC–FS model, the ratio between the free-surface and interface displacements is given by

$$\frac{\zeta_1}{\zeta_2} = \frac{c_0^2}{c_0^2 - gh_1}\,,$$

and the free surface and the interface are in phase if $\zeta_1/\zeta_2 > 0$ (barotropic mode) while they are out of phase if $\zeta_1/\zeta_2 < 0$ (baroclinic mode). We will not insist on the properties of this model, since it goes beyond our purposes: in fact, in Boussinesq approximation surface displacements are really small and negligible with respect to interface displacements. We refer the reader to Kodaira *et al.* [2016] for details about this model.

We want also to mention here the *DJL model* (Dubreil–Jacotin–Long)[1], which is a fully nonlinear strongly dispersive model [Dubreil-Jacotin, 1937; Long, 1953]. Solitary waves in continuously stratified flows have been explored with numerical solutions [Lamb, 2002; Stasna and Lamb, 2002] of the DJL equation

$$\nabla^2\eta + \frac{N^2(z-\eta)}{c^2}\eta = 0\,, \tag{2.43a}$$

$$\eta = 0 \ \text{ at } z = 0, H \tag{2.43b}$$

$$\eta \to 0 \ \text{ as } \ x \to \pm\infty\,, \tag{2.43c}$$

which is an eigenvalue problem for $\eta(x,z)$, vertical displacement of the streamline passing through (x,z) relative to its far–field height. The equation is solved through a generalization of a variational technique and a numerical algorithm based on the work of Turkington *et al.* [1991]. In contrast with weakly nonlinear theories, which are approximate, solutions found using the variational technique are exact solutions of Euler's equations. On the other hand, DJL solutions can represent only steady–state solitons. Although we recognize the importance of this model, we will not make use of it, since our work is mainly focused on analitycal aspects of both steady–state and varying internal solitary waves.
In conclusion, although the Gardner and KdV equations are approximate and need assumptions of weak nonlinearity and dispersion to be satisfied, they are very simple models and are convenient for investigation since they are integrable. The fully nonlinear MCC–RL model cannot be solved with pure analitycal procedures, but need some numerical calculations. Anyway, it will be used for some comparisons with weakly nonlinear models.

* * *

We summarize the main results of this chapter that will be used in the following. We describe steady–state weakly–nonlinear ISWs through the KdV equation

[1] Marie-Louise Dubreil-Jacotin (1905–1972), born Jacotin, was a French mathematician, the second woman to obtain a doctorate in Pure Mathematics in France, the first woman to become a full professor of Mathematics in France. Paul Dubreil (1904–1994), French mathematician, was her husband.

$$\eta_t + \alpha\eta\eta_x + \beta\eta_{xxx} = 0\,, \tag{2.44}$$

and its second–order extension (in nonlinearity), the eKdV equation

$$\eta_t + \alpha\eta\eta_x + \alpha_1\eta^2\eta_x + \beta\eta_{xxx} = 0\,, \tag{2.45}$$

with coefficients

$$c = \sqrt{\frac{g(\rho_2-\rho_1)h_1h_2}{\rho_2(h_1+h_2)}} \tag{2.46a}$$

$$\alpha = \frac{3}{2}c\frac{h_1-h_2}{h_1h_2} \tag{2.46b}$$

$$\alpha_1 = \frac{3c_0}{(h_1h_2)^2}\left[\frac{7}{8}(h_1-h_2)^2 - \left(\frac{h_1^3+h_2^3}{h_1+h_2}\right)\right] \tag{2.46c}$$

$$\beta = \frac{c}{6}h_1h_2\,. \tag{2.46d}$$

The solution of the KdV equation (2.44) is of the form

$$\eta(x,t) = A\,\mathrm{sech}^2\left(K(x-Ut)\right)\,, \tag{2.47}$$

with $U = A\widehat{\alpha}/3 = 4\widehat{\beta}K^2$, $\widehat{\alpha} = \alpha/c$, $\widehat{\beta} = \beta/c$.
The solution of the eKdV equation (2.45) is of the form

$$\eta(x,t) = \frac{D}{1+B\cosh(K(x-Vt))}\,, \tag{2.48}$$

with

$$V = \frac{\alpha D}{6} = \beta K^2\,, \quad B^2 = 1 + \frac{6\alpha_1\beta K^2}{\alpha^2}\,, \tag{2.49}$$

and the amplitude of the solitary wave given by

$$a = \frac{D}{1+B}\,, \tag{2.50}$$

where only the parameter B is arbitrary , and the other parameters depend on it. Another form of the previous equations is that with the linear term $c_0\eta_x$ not absorbed by a Galileian trasformation. For the KdV equation:

$$\eta_t + c_0\eta_x + \alpha\eta\eta_x + \beta\eta_{xxx} = 0\,, \tag{2.51}$$

where c_0 is the phase speed of the associated linear wave, with the internal solitary wave solution:

$$\eta(x,t) = A\,\mathrm{sech}^2\left(\frac{x-Ut}{L}\right)\,. \tag{2.52}$$

with $L = \sqrt{12\beta/(A\alpha)}$. Similarly, for the eKdV equation, we can write

$$\eta_t + (c_0 + \alpha\eta + \alpha_1\eta^2)\eta_x + \beta\eta_{xxx} = 0\,, \tag{2.53}$$

with the the internal solitary wave solution:

$$\eta(x,t) = \frac{A}{b + (1-b)\cosh^2\left[\gamma(x - Ut)\right]}\,, \tag{2.54}$$

in which

$$U = c_0 + \frac{A}{3}\left(\alpha + \frac{1}{2}\alpha_1 A\right)\,, \qquad \gamma^2 = \frac{A\left(\alpha + \frac{1}{2}\alpha_1 A\right)}{12\beta}\,, \qquad b = \frac{-A\alpha_1}{2\alpha + \alpha_1 A}\,. \tag{2.55}$$

We also report the nonlinear ordinary differential equation for the wave displacement ζ in the MCC strongly nonlinear model:

$$\zeta_X^2 = \frac{3\zeta^2\left[c^2\left(\rho_1\eta_2 + \rho_2\eta_1\right) - g(\rho_2 - \rho_1)\eta_1\eta_2\right]}{c^2\left(\rho_1 h_1^2\eta_2 + \rho_2 h_2^2\eta_1\right)} \tag{2.56}$$

where $\eta_1 = h_1 - \zeta$, $\eta_2 = h_2 + \zeta$. This last equation must be solved numerically. Equations, and related solutions, briefly recalled here will be used and, in some cases, extended to the unsteady–state case in the next chapter.

Chapter 3

ISWs propagation in a variable environment

In this chapter, in order to get suitable mathematical tools for geophysical applications, we examine how waves propagate in media that are non–uniform, in the sense that depth, stratification or background flow can vary along a given direction. For linear waves in non–uniform media, the general treatment through ray theory and WKB method is reported in Appendix B. Here we derive the variable–coefficients KdV (vKdV) and eKdV (veKdV) equations, their slowly–varying analytical solutions and an explicit analytical solution to the veKdV equation. The numerical approach to vKdV and veKdV equations is also shown.

3.1 Variable–coefficient extended KdV (veKdV) equation

We can modify nonlinear equations, such as KdV or eKdV, to deal with variable bathymetry through a heuristic approach as suggested by Pelinovsky *et al.* [1994]. First, we introduce the concept of energy flux. The equation that describes the flow of energy in a fluid under Boussinesq approximation is [Kundu *et al.*, 2016; Massel, 2015]:

$$\frac{\partial}{\partial t}\left[\frac{1}{2}\rho_0(z)\left(u^2+v^2+w^2\right)\right]+g\rho(z)w+\nabla\cdot(p\boldsymbol{u})\,, \tag{3.1}$$

where ρ_0 is the background (unperturbed) density, $\rho(z)$ the perturbation of density due to wave action, p is the water pressure, and $\boldsymbol{u}=(u,v,w)$ is the velocity vector. The first term in (3.1) represents a rate of change of the kinetic energy and the second term can be considered as the rate of change of potential energy. The last term is the net work done by the pressure forces, which can be interpreted as the divergence of the energy flux vector $p\boldsymbol{u}$. Eq.(3.1) describes a balance between the rate of change of energy and energy flux terms[1]. The energy flux vector represents the amount of energy passing across a unit surface area normal to the velocity field

[1]See also Debnath [2012] for an alternative formulation, which leads directly to a conservation law of energy.

$\boldsymbol{u}$ per unit time. Thus, we can define the energy flux, for example in the x–direction, as the instantaneous rate at which work is being done by the dynamic pressure $p = (p_0 + \rho g z)$ per unit width in the direction of wave propagation. The energy flux integrated over water depth H is then given by

$$F = \int_{-H}^{0} pu\, dz\,. \tag{3.2}$$

Along an internal wave ray (see Appendix B for ray theory), the integral of energy flux over depth and wavefront length (equivalently ray tube width) must be conserved [Pelinovsky *et al.*, 1994]. This integrated energy flux is given by

$$F = \int_{\Delta}\int_{-H}^{0} pu\, dz d\Delta\,, \tag{3.3}$$

where $d\Delta$ is the differential wavefront length. Assuming that the waveform is constant along the ray tube (or segment of wave front), we have

$$F = \Delta \int_{-H}^{0} pu\, dz\,. \tag{3.4}$$

Pressure and internal velocity are given by linear theory (see (2.12)) as

$$p = \rho\eta c_0^2 \frac{\mathrm{d}\phi}{\mathrm{d}z}\,, \tag{3.5a}$$

$$u = c_0 \eta \frac{\mathrm{d}\phi}{\mathrm{d}z}\,. \tag{3.5b}$$

Thus, substituting in (3.4),

$$F = \Delta \int_{-H}^{0} \rho c_0^3 \eta^2 \left(\frac{\mathrm{d}\phi}{\mathrm{d}z}\right)^2 dz \tag{3.6}$$

and this must be conserved along a ray, that is, $\partial F/\partial x = 0$, where x is the (horizontal) distance along the ray (it is convenient to designate the space coordinate along the ray as x also):

$$\begin{aligned}\frac{\partial F}{\partial x} = \Delta\eta^2 \int_{-H}^{0} \frac{\partial}{\partial x}\left[\rho c_0^3 \left(\frac{\mathrm{d}\phi}{\mathrm{d}z}\right)^2\right] dz + \\ + 2\Delta\eta\eta_x \int_{-H}^{0} \left[\rho c_0^3 \left(\frac{\mathrm{d}\phi}{\mathrm{d}z}\right)^2\right] dz + \frac{\partial\Delta}{\partial x}\eta^2 \int_{-H}^{0} \left[\rho c_0^3 \left(\frac{\mathrm{d}\phi}{\mathrm{d}z}\right)^2\right] dz = 0\,,\end{aligned} \tag{3.7}$$

where c_0, ρ, ϕ are considered as slowly varying functions with respect to x. Denoting

$$M = \int_{-H}^{0} \left[\rho c_0^3 \left(\frac{\mathrm{d}\phi}{\mathrm{d}z}\right)^2\right] dz\,, \tag{3.8}$$

substituting in (3.7), diving by $2\Delta\eta M$ and explicitating with respect to η_x, we obtain:

$$\frac{\partial\eta}{\partial x} = -\frac{1}{2}\left(\frac{\eta}{M}\frac{\partial M}{\partial x}\right) - \frac{1}{2}\left(\frac{\eta}{\Delta}\frac{\partial\Delta}{\partial x}\right)\,.$$

We note that the change in amplitude along x is dependent on the variation in the modes and phase speed with range (first term) and the change in wavefront length Δ (i.e., the spreading) from the second term. Considering the limit $\delta x/\delta t \to 0$ of

$$\frac{\delta\eta}{\delta t} = -\frac{1}{2}\left(\frac{\eta}{M}\frac{\delta M}{\delta x}\right)\frac{\delta x}{\delta t} - \frac{1}{2}\left(\frac{\eta}{\Delta}\frac{\delta\Delta}{\delta x}\right)\frac{\delta x}{\delta t}\,,$$

we can include the additional terms in the eKdV equation:

$$\frac{\partial\eta}{\partial t} = -c_0\frac{\partial\eta}{\partial x} - \alpha\eta\frac{\partial\eta}{\partial x} - \alpha_1\eta^2\frac{\partial\eta}{\partial x} - \beta\frac{\partial^3\eta}{\partial x^3} - \frac{c_0}{2}\frac{\eta}{M}\frac{\partial M}{\partial x} - \frac{c_0}{2}\frac{\eta}{\Delta}\frac{\partial\Delta}{\partial x}\,, \tag{3.9}$$

that is,

$$\eta_t + c_0(x)\eta_x + \alpha(x)\eta\eta_x + \alpha_1(x)\eta^2\eta_x + \beta(x)\eta_{xxx} + \nu(x)\eta + S(x)\eta = 0\,, \tag{3.10}$$

where

$$\nu(x) = \frac{c_0}{2}\left(\frac{1}{M}\frac{\partial M}{\partial x}\right)\,, \quad S(x) = \frac{c_0}{2}\left(\frac{1}{\Delta}\frac{\partial\Delta}{\partial x}\right)\,,$$

are the shoaling and the spreading coefficients, respectively. Equation (3.10) the *variable–coefficient eKdV equation* (veKdV), in which the effects of a horizontally variable environment is taken into account. In particular, we are interested in the case of a variable bathymetry.
In section 2.2 we have seen that the vertical displacement of the isopycnal surface is given by (2.20), which in this case becomes

$$\zeta(x,z,t) = \eta(x,t)\phi(z) + \eta(x,t)^2 T(z)\,. \tag{3.11}$$

When the water depth and/or the oceanic stratification vary slowly in the horizontal direction, the modal structure of the internal wave also varies slowly, but to the first approximation can be calculated from the Sturm–Liouville problem (2.11) for ϕ [Grimshaw *et al.*, 2004; Small, 2001a], so that

$$\zeta(x,z,t) \simeq \eta(x,t)\phi(z)\,. \tag{3.12}$$

The main effect of higher–order terms is to change the vertical structure of the displacement field by introducing extra vertical modes, but with little effect on the wave variation with range or time. For the two–layer rigid–lid environment, there is only one vertical mode possible (the interfacial mode) and so higher-order terms will not change the vertical structure. For these reasons the approximation (3.12) will be made when describing the displacement of the interface [Small, 2001a]. Noting that the expression for the modal function $\phi(z)$ for the two–layer case is given by (2.24a) and (2.24b), we can calculate the integral (3.8):

$$\begin{aligned} M &= \rho c_0^3 \int_{-H}^{-h_1} \left(\frac{\mathrm{d}\phi}{\mathrm{d}z}\right)^2 dz + \rho c_0^3 \int_{-h_1}^{0} \left(\frac{\mathrm{d}\phi}{\mathrm{d}z}\right)^2 dz \\ &= \rho c_0^3 \left[\int_{-H}^{-h_1} \frac{1}{h_2^2}\,dz + \int_{-h_1}^{0} \frac{1}{h_1^2}\,dz\right] = \rho c_0^3(x)\left(\frac{1}{h_1} + \frac{1}{h_2(x)}\right)\,, \end{aligned}$$

where the assumption is made that as the depth varies, the top layer thickness h_1 remains constant and the bottom layer thickness varies according to $h_2(x) = H(x) - h_1$. We also note that c_0 is a function of x through $h_2(x)$. If we neglect the contribution of the ray width spreading in (3.10), i.e., $S(x)$, we can derive a simple expression for the shoaling term $\nu(x)$ in a two–layer fluid:

$$\begin{aligned}
\nu(x) &= \frac{c_0}{2}\frac{1}{M}\frac{\partial M}{\partial x} = \frac{c_0}{2}\frac{1}{c_0^3(x)\left(\frac{1}{h_1}+\frac{1}{h_2(x)}\right)}\frac{\partial}{\partial x}\left[c_0^3(x)\left(\frac{1}{h_1}+\frac{1}{h_2(x)}\right)\right] \\
&= \frac{3}{2}\frac{\partial c_0(x)}{\partial x} - \frac{c_0(x)}{2}\frac{h_1}{(h_1+h_2(x))h_2(x)}\frac{\partial h_2(x)}{\partial x} \\
&= \frac{3}{4}\left(\frac{h_1+h_2}{g\sigma h_1 h_2}\right)^{\frac{1}{2}}\left[\frac{g\sigma h_1\frac{\partial h_2}{\partial x}(h_1+h_2) - g\sigma h_1 h_2\frac{\partial h_2}{\partial x}}{(h_1+h_2)^2}\right] - \frac{c_0}{2}\frac{\partial h_2}{\partial x}\frac{h_1}{(h_1+h_2)h_2} \\
&= \frac{3}{4}\left\{\left(\frac{g\sigma h_1}{(h_1+h_2)h_2}\right)^{\frac{1}{2}} - \left(\frac{g\sigma h_1 h_2}{h_1+h_2}\right)^{\frac{1}{2}}\frac{1}{h_1+h_2}\frac{\partial h_2}{\partial x}\right\} - \frac{c_0}{2}\frac{\partial h_2}{\partial x}\frac{h_1}{(h_1+h_2)h_2} \\
&= c_0\left[\frac{c_0}{h_2}\frac{\partial h_2}{\partial x} - \frac{c_0}{(h_1+h_2)}\frac{\partial h_2}{\partial x}\right] - \frac{c_0}{2}\frac{\partial h_2}{\partial x}\frac{h_1}{(h_1+h_2)h_2} \\
&= c_0\frac{\partial h_2}{\partial x}\frac{h_1}{(h_1+h_2)h_2}\left(\frac{3}{4}-\frac{1}{2}\right) \\
&= \frac{c_0}{4}\frac{\partial h_2}{\partial x}\frac{h_1}{(h_1+h_2)h_2}\,.
\end{aligned}$$

The veKdV equation (3.10) is often written as

$$\frac{\partial \eta}{\partial t} + c_0(x)\frac{\partial \eta}{\partial x} + \alpha(x)\eta\frac{\partial \eta}{\partial x} + \alpha_1(x)\eta^2\frac{\partial \eta}{\partial x} + \beta(x)\frac{\partial^3 \eta}{\partial x^3} + \frac{c_0(x)}{2}\frac{1}{Q}\frac{\mathrm{d}Q}{\mathrm{d}x}\eta = 0\,, \quad (3.13)$$

in which

$$Q = \Delta M c_0^3(x) \quad M = \int_{-H}^{0}\left(\frac{\mathrm{d}\phi}{\mathrm{d}z}\right)^2 dz\,.$$

Defining the new variables

$$s = \int \frac{dx}{c_0(x)} - t\,, \quad P = \sqrt{\frac{Mc_0\Delta}{(Mc_0\Delta)_0}}\,, \quad \zeta(x,s) = P(x)\eta(x,s)\,,$$

where $(Mc_0\Delta_0)_0$ is the initial value of $Mc_0\Delta_0$ [2]. Substituting in (3.13), we obtain:

$$\frac{\partial \zeta}{\partial x} + \left(\frac{\alpha}{c_0^2 P} + \frac{\alpha_1}{c_0^2 P^2}\right)\frac{\partial \zeta}{\partial s} + \frac{\beta}{c_0^3}\frac{\partial^3 \zeta}{\partial s^3}\,. \quad (3.14)$$

The same result can be obtained from a WKB–wave action flux approach. One of the basic conservation laws for nonlinear dispersive waves is the conservation of wave action density $\mathcal{A} = E/\Omega$ [Dean and Dalrymple, 1991; Debnath, 2012; Massel, 2015; Sutherland, 2010]:

[2] Values with "0" index are the values at any fixed point x_0. It is convenient to use the origin or put $x_0 = 0$ in the initial position of a solitary wave.

$$\frac{\partial}{\partial t}\left(\frac{E}{\Omega}\right)+\frac{\partial}{\partial x}\left(\frac{Ec_g}{\Omega}\right)=0\,, \tag{3.15}$$

where E is the wave energy density (which is a quantity closely related to the square of the wave amplitude, $|A|^2$), Ω is the extrinsic frequency. The quantity Ec_g/Ω is then the wave action flux, with $c_g \simeq c$ if the medium is weakly dispersive. If we look for solutions close to that for a homogeneous medium, we can use a WKB approach (see Appendix B) assuming that the solution has the form

$$\eta \simeq A(x,t)f(t-\tau(x))$$

where $\tau(x)=\int \frac{dx}{c(x)}$ and the phase $t-\tau(x)$ is assumed to vary rapidly compared to the amplitude $A(x.t)$ and the speed $c(x)$. It can be shown that $A(x,t)$ verified the wave–action conservation law (see [Debnath, 2012]).
If we want KdV–type equations to verify the wave–action conservation law in the limit in which nonlinear terms are negligible, we have to add the term $c_0(x)Q_x/(2Q)$, so that the linear wave theory

$$\eta_t+c_0(x)\eta_x+\frac{c_0Q_x}{2Q}\eta=0\,,$$

is transformed into

$$\left(\frac{Q\eta^2}{c_0}\right)_t+\left(Q\eta^2\right)_x=0\,,$$

and $Q\eta^2$ can be interpreted as the wave–action flux. We then have the following veKdV equation:

$$\eta_t+c_0(x)\eta\eta_x+\alpha(x)\eta\eta_x+\alpha_1(x)\eta^2\eta_x+\beta(x)\eta_{xxx}+\frac{c_0(x)Q_x}{2Q}=0\,. \tag{3.16}$$

We perform a change of variable $\xi \sim x/c-t$ (where c is the phase speed) moving to a coordinate system which follows the propagation of the wave. By analogy with the WKB technique, we introduce

$$\tau=\int_0^x \frac{dx'}{c(x')}\,. \tag{3.17}$$

which can be viewed as a mapping of the original spatial coordinate into a time–like coordinate: τ is the travel time between the original position $x=0$ of the wave and its present location. We can also introduce the variable

$$s=\tau(x)-t\,,$$

which represents the time in the system where the coordinates are moving with the phase speed of a long wave, and the scaled amplitude

$$\zeta(\tau,s)=\sqrt{Q(x)}\eta(\tau,s)\,.$$

We then have the following transformations for derivatives

$$\frac{\partial}{\partial t} \longrightarrow -\frac{\partial}{\partial s}$$
$$\frac{\partial}{\partial x} \longrightarrow \frac{1}{c}\frac{\partial}{\partial s} + \frac{1}{c}\frac{\partial}{\partial \tau}\,,$$

but when the background varies vary slowly compared with the size of the wave, it can be demostrated that $\partial/\partial\tau \ll \partial/\partial s$ [Grimshaw, 2005], so that

$$\frac{\partial}{\partial x} \longrightarrow \frac{1}{c}\frac{\partial}{\partial s}$$

which leads to the following equation:

$$\frac{\partial \zeta}{\partial \tau} + \left(\widetilde{\alpha}\zeta + \widetilde{\alpha}_1\zeta^2\right)\frac{\partial \zeta}{\partial s} + \widetilde{\beta}\frac{\partial^3 \zeta}{\partial s^3} = 0\,, \tag{3.18}$$

where

$$\widetilde{\alpha} = \frac{\alpha}{c_0\sqrt{Q}}\,, \quad \widetilde{\alpha}_1 = \frac{\alpha_1}{c_0 Q}\,, \quad \widetilde{\beta} = \frac{\beta}{c_0^3}\,.$$

The linear modification factor Q is given by (see Zhou and Grimshaw [1989])

$$Q = 2\int_{-H}^{0} \rho_0 c_0^3 \left(\frac{\mathrm{d}\phi}{\mathrm{d}z}\right)^2 dz\,. \tag{3.19}$$

For interfacial waves in a two–layer fluid, the density profile is given by (2.23), hence, substituting in (3.19), we get

$$Q = 2g(\rho_2 - \rho_1)c\,.$$

For a two–layer system, we can rewrite the variable $\tau(x)$ as

$$\int_{x_i}^{x} \frac{dx'}{c(x')} = \int_{x_i}^{x} \sqrt{\frac{h_1 + h_2(x')}{g\sigma h_1 h_2(x')}}dx' = \frac{1}{\sqrt{g\sigma h_1}}\int_{x_i}^{x}\sqrt{1 + \frac{h_1}{h_2(x')}}dx'$$
$$= \frac{1}{\sqrt{g\sigma h_1}}\begin{cases} \displaystyle\int_{x_i}^{x}\sqrt{1+\frac{h_1}{h_2}}\,dx'\,, & x_i < x < x_s \\[2ex] \displaystyle\int_{x_i}^{x_s}\sqrt{1+\frac{h_1}{h_2}}\,dx' + \int_{x_s}^{x}\sqrt{1+\frac{h_1}{h_2 - s(x'-x_s)}}\,dx'\,, & x_i < x_s < x < x_f\,, \end{cases}$$

where

$$\int_{x_s}^{x}\sqrt{1 + h_1/\Theta(x')}\,dx'$$
$$= -\frac{1}{s\sqrt{h_1 + \Theta(x')}}\sqrt{1 + \frac{h_1}{\Theta(x')}}\cdot$$
$$\cdot\left[\Theta(x')\sqrt{h_1 + \Theta(x')} + h_1\sqrt{\Theta(x')}\log\left(\sqrt{h_1 + \Theta(x')} + \sqrt{\Theta(x')}\right)\right]\Bigg|_{x_s}^{x}\,,$$

with $\Theta = h_2 - s(x' - x_s)$. This two-layer, analytic formulation allows for fastening numerical integrations that provide temporal evolution of the ISW.

3.2 Adiabatic transformation of ISWs: slowly–varying solution to veKdV equation

For variable oceanic background the solitary wave shape changes, and the wave parameters (amplitude, width, speed) vary, and if the oceanic parameters vary sufficiently slowly, the wave is locally close to the steady–state solitary wave (3.61) (or (2.54)). In this case, we say that the wave transformation is "adiabatic". Thus, when ISWs pass through a variable bathymetry, in some of the shoaling cases the variation in wave amplitude is adiabatic, and the solitary wave is only slowly deformed, while in other cases the change is nonadiabatic, with resultant fission of the solitary wave into a wave packet [Djorjevic and Redekopp, 1978; Small, 2001a]. It is possible to derive a condition for adiabaticity, imposing that the shoaling and the spreading terms in Eq.(3.10) are small compared with the other terms, in particular the nonlinear terms [Small, 2001a]:

$$\frac{\nu(x)}{\alpha(x)} \ll \frac{\partial \eta}{\partial x}\,, \quad \frac{\nu(x)}{\alpha_1(x)} \ll \eta \frac{\partial \eta}{\partial x}\,, \tag{3.20}$$

which can be rewritten as

$$\left|\frac{1}{6}\frac{h_1^2\, s}{(h_1-h_2)(h_1+h_2)}\right| \ll \left|\frac{\eta_0}{l}\right|, \quad \left|\frac{2}{3}\frac{h_1^3 h_2\, s}{(h_1^2+h_2^2+6h_1h_2)(h_1+h_2)}\right| \ll \left|\frac{\eta_0^2}{l}\right|,$$

where η_0 and l are the characteristic scales for the wave amplitude and the halfwidth, respectively.

The slowly–varying solitary wave is an asymptotic solution based on the assumption that the background state varies slowly relative to a typical wavelength. In particular, following Grimshaw [2007], the solitary wave will be considered slowly–varying if the half–width (i.e., the width of the wave at the level of one half of the maximum amplitude) is much smaller than the scale of the variable medium $L = 1/\varepsilon$. We suppose that

$$\alpha = \alpha(\sigma)\,, \quad \alpha_1 = \alpha_1(\sigma)\,, \quad \beta = \beta(\sigma)\,, \quad c = c(\sigma)\,, \quad Q = Q(\sigma)\,, \quad \text{with } \sigma = \varepsilon\tau\,, \ \varepsilon \ll 1\,.$$

Invoking a multiscale asymptotic expansion of the form [Grimshaw, 2007; Grimshaw *et al.*, 2010]

$$\zeta = \zeta_0(\psi,\sigma) + \varepsilon\zeta_1(\psi,\sigma) + \cdots\,, \tag{3.21}$$

where

$$\psi = s - \frac{1}{\varepsilon}\int^{\sigma} V(\sigma)\, d\sigma \tag{3.22}$$

is a temporal variable in a frame moving with the speed V. The variable ζ is defined over the domain $-\infty < \psi < +\infty$, and we will require that ζ remains bounded in the limits $\psi \to \pm\infty$ [Grimshaw *et al.*, 2007]. Substituting (3.21) in (3.18), we get

$$-V\frac{\partial(\zeta_0+\varepsilon\zeta_1)}{\partial\psi} + \widetilde{\alpha}(\zeta_0+\varepsilon\zeta_1)\frac{\partial(\zeta_0+\varepsilon\zeta_1)}{\partial\psi} + \\ + \widetilde{\alpha}_1(\zeta_0+\varepsilon\zeta_1)^2\frac{\partial(\zeta_0+\varepsilon\zeta_1)}{\partial\psi} + \widetilde{\beta}\frac{\partial^3(\zeta_0+\varepsilon\zeta_1)}{\partial\psi^3} = 0\,, \tag{3.23}$$

and expanding all the products and retaining the terms up to the first order in ε, we get the equations

$$O(1): \quad -V\zeta_{0\psi} + \widetilde{\alpha}\zeta_0\zeta_{0\psi} + \widetilde{\alpha}_1{\zeta_0}^2\zeta_{0\psi} + \widetilde{\beta}\zeta_{0\psi\psi\psi} = 0 \quad (3.24)$$

$$O(\varepsilon): \quad -V\zeta_{1\psi} + \widetilde{\alpha}\zeta_0\zeta_{1\psi} + \widetilde{\alpha}\zeta_1\zeta_{0\psi} + \widetilde{\alpha}_1{\zeta_0}^2\zeta_{1\psi} + 2\widetilde{\alpha}_1\zeta_0\zeta_1\zeta_{0\psi} + \widetilde{\beta}\zeta_{1\psi\psi\psi} = -\zeta_{0\sigma}\,. \quad (3.25)$$

If we do not take into account the terms with α_1 (i.e., in the vKdV limit), Eq.(3.24) has a KdV cnoidal solution similar to (2.26) (see Grimshaw [2007]), which, as seen in secton 2.2.1, in the limit $m \to 1$, becomes the solitary wave solution

$$\zeta_0(\psi, \sigma) = A\,\mathrm{sech}^2\,(K\psi)\,, \quad (3.26)$$

where $V = A\widehat{\alpha}/3 = 4\widehat{\beta}K^2$, with $\widehat{\alpha} = \widetilde{\alpha}/c_0$ and $\widehat{\beta} = \widetilde{\beta}/c_0$. All the coefficients depend on σ. The variation of the amplitude $A(\sigma)$, which determines completely the slowly–varying soliton (3.26), is given by [Grimshaw, 2007]:

$$A^3 = \mathrm{const}\frac{\widetilde{\alpha}}{\widetilde{\beta}}\,. \quad (3.27)$$

We do not insist on the derivation of (3.27), since we will briefly derive the variation of the wave–amplitude in section 3.3 as suggested by Small [2001a].
If we take into account the cubic nonlinear term in (3.24), i.e., if we recover the veKdV limit, we obtain the veKdV cnoidal wave solution (see [Grimshaw, 2007]), which in the limit $m \to 1$ leads to the solitary wave solution:

$$\zeta_0 = \frac{D}{1 + B\cosh(K\psi)}\,, \quad (3.28)$$

with

$$D = \frac{6\widetilde{\beta}K^2}{\widetilde{\alpha}}\,, \quad K = \sqrt{\frac{\widetilde{\alpha}^2}{6\widetilde{\alpha}_1\widetilde{\beta}}(B^2-1)}\,, \quad V = \widetilde{\beta}K^2\,. \quad (3.29)$$

The amplitude of the solitary wave is given by

$$a = \frac{D}{1+B}\,, \quad (3.30)$$

where only the parameter B is arbitrary , and the other parameters depend on it. Since we are dealing with a slowly–varying solitary wave, we have $B = B(\sigma)$ and hence $a = D/(1+B) = a(\sigma)$, $V = V(\sigma)$, $K = K(\sigma)$. The determination of how the key parameter B varies with σ is found either by considering the next–order of the expansion (3.25), or equivalently by using the conservation law for momentum

$$\frac{\partial P}{\partial \tau} = 0\,, \quad P = \int_{-\infty}^{+\infty} \zeta^2\, ds\,,$$

which holds at the leading order of ζ [Grimshaw, 2007], i.e.,

$$\frac{\partial P_0}{\partial \sigma} = 0\,, \quad P_0 = \int_{-\infty}^{+\infty} \zeta_0^2\, d\psi = \text{const}\,. \tag{3.31}$$

Substituting the solitary wave (3.61) in (3.31), we impose the conservation of momentum

$$\frac{D^2}{K}\int_{-\infty}^{+\infty} \frac{du}{(1+B\cosh(u))^2} = P_0 = \text{const}\,,$$

where $u = K\psi$. From (3.62),

$$\frac{D^2}{K} = \sqrt{\frac{\widetilde{\beta}\widetilde{\alpha}^2}{\widetilde{\alpha}_1}}(B^2-1)^{3/2}\,.$$

Hence, (3.31) becomes

$$P_0 = \sqrt{\frac{\widetilde{\beta}\widetilde{\alpha}^2}{\widetilde{\alpha}_1}}(B^2-1)^{3/2}\int_{-\infty}^{+\infty} \frac{du}{(1+B\cosh(u))^2}\,,$$

which can be rewritten as

$$G(B) = \sqrt{\frac{\widetilde{\alpha}_1}{\widetilde{\alpha}^2\widetilde{\beta}}}P_0\,, \qquad \text{with } G(B) = (B^2-1)^{3/2}\int_{-\infty}^{+\infty} \frac{du}{(1+B\cosh(u))^2}\,. \tag{3.32}$$

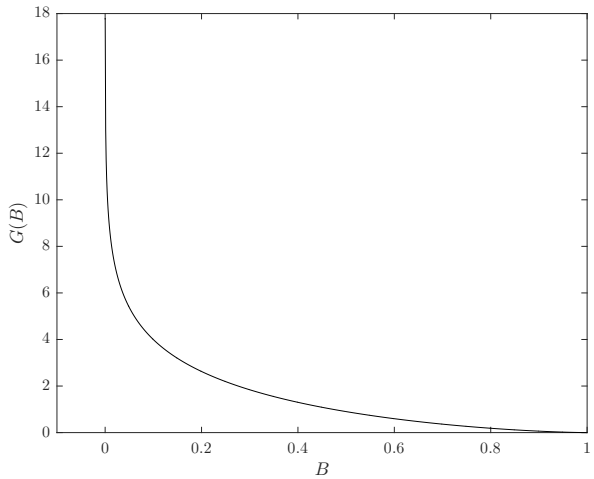

Figure 3.1. Plot of $G(B)$ vs. B for $0 < B < 1$ ($\alpha_1 < 0$, $\alpha < 0$). $G(B)$ is a monotonically decreasing function of B, and we have a soliton of elevation if $\alpha > 0$ or depression if $\alpha < 0$; while, for $\alpha_1 > 0$, B lies between $1 < |B| < \infty$, $G(B)$ is a monotonically increasing function of B, and there are two branches of solitary waves (see also Fig.3.2).

The integral in $G(B)$ can be explicitly evaluated, and the expression is provided by Grimshaw [2007] depending on the choice of the family of the soliton solutions. For $\alpha_1 < 0$ the value of B lies between 0 and 1, $G(B)$ is a monotonically decreasing function of B (Fig.3.1), and we have a soliton of elevation if $\alpha > 0$ or depression if $\alpha < 0$; while, for $\alpha_1 > 0$, B lies between $1 < |B| < \infty$, $G(B)$ is a monotonically

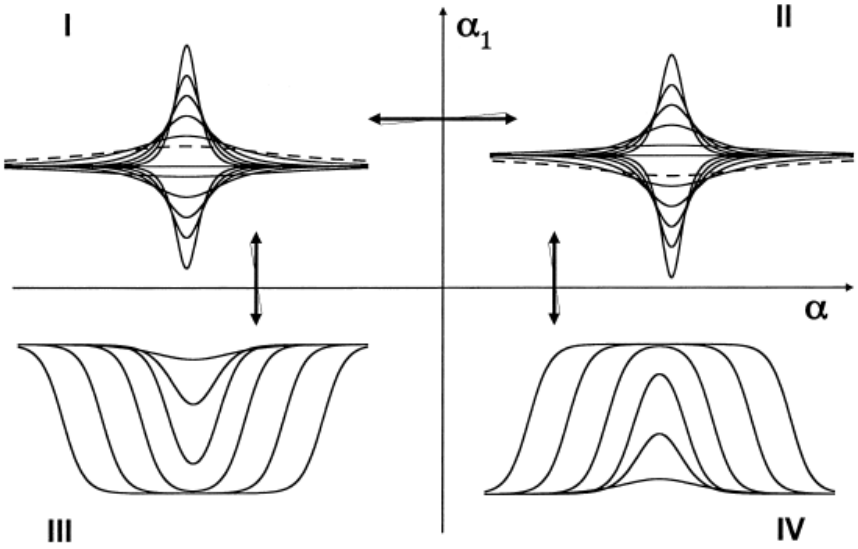

Figure 3.2. Soliton families on plane (α, α_1)(from Grimshaw *et al.* [2004]). The arrows connect the areas of the plane among which transitions are possible. For a complete description of the wave transformation phenomenology see text.

increasing function of B, and there are two branches of solitary waves (see Fig.3.2). Hence, $G(B)$ becomes:

$$B^2 > 1: \; G(B) = 2(B^2-1)^{1/2} \mp 4 \arctan \sqrt{\frac{B-1}{B+1}} \tag{3.33}$$

$$0 < B < 1: \; G(B) = 4 \tanh^{-1} \sqrt{\frac{1-B}{1+B}} - 2(1-B^2)^{1/2}, \tag{3.34}$$

where the alternative signs for $B^2 < 1$ correspond to the cases $B > 1$ or $B < -1$. Equation (3.32) provides an explicit formula for the dependence of B on the basic parameters $\alpha(\sigma)$, $\alpha_1(\sigma)$, $\beta(\sigma)$, $c(\sigma)$, and $Q(\sigma)$, which are calculated from the local hydrology and depth at each point of the wave path. P_0 is a constant determined by the initial conditions, that is through (3.61) with constant coefficients (i.e., the solution of the eKdV equation), which lead to an expression for a and B not dependent on σ:

$$a = \frac{D}{1+B} = \frac{\widetilde{\alpha}}{\widetilde{\alpha}_1}(B-1) = \frac{\alpha\sqrt{Q}}{\alpha_1}(B-1) \quad \Rightarrow \quad B = \frac{a\alpha_1}{\alpha\sqrt{Q}} + 1\,. \tag{3.35}$$

Thus, known the initial value of the amplitude a, (3.35) represents the initial value for B. It is then possible to calculate the initial values for the parameters K, D and V substituting B (Eq. (3.35)) into expressions (3.62) with "frozen" coefficients.
Once the basic parameters and P_0 are evaluated, it is possible to derive $B(\sigma)$ solving

the following trascendental equation[3]:

$$G(B) - \sqrt{\frac{|\widetilde{\alpha}_1|^3}{\widetilde{\alpha}^2\widetilde{\beta}}} P_0 = 0\,. \tag{3.36}$$

Then, $a(\sigma)$ and $\zeta_0(\psi,\sigma)$ are determined, and we have the zero–order solution

$$\zeta_0(\psi,\sigma) = \frac{D(\sigma)}{1 + B(\sigma)\cosh(K(\sigma)\psi)}\,. \tag{3.37}$$

It is possible to verify that the veKdV equation follows the conservation of mass law

$$\frac{\partial M}{\partial \tau} = 0\,, \quad M = \int_{-\infty}^{+\infty} \zeta\, ds\,,$$

but not to the leading order ζ_0 [Grimshaw *et al.*, 2007, 2010]. The remedy is the construction of a trailing shelf $\zeta^{(s)}$ of small amplitude $O(\varepsilon)$ but long length–scale $O(1/\varepsilon)$, which has $O(1)$ mass and $O(\varepsilon)$ momentum. It resides behind the solitary wave, and to leading order is given by $\zeta^{(s)} = \varepsilon\zeta^{(s)}(T)$, where $T = \varepsilon\tau$ for $T < \Psi(\sigma) = \int^{\sigma} V(\sigma)\, d\sigma$. Here $T = \Psi(\sigma)$ is the location of the solitary wave. The leading term ζ_s is determined so that the shelf amplitude is just $\varepsilon D_1(\sigma)$ at the location T of the solitary wave, that is $\zeta^{(s)}(\Psi(\sigma)) = D_1(\sigma)$, where

$$V D_1(\sigma) = -\frac{\partial M_0}{\partial \sigma}\,, \quad \text{with } M_0 = \int_{-\infty}^{+\infty} \zeta_0\, d\psi\,. \tag{3.38}$$

(see [Grimshaw, 2007] for derivation of (3.38)). As reported by Grimshaw [2007], M_0 is given by

$$B^2 > 1:\ M_0 = \pm\sqrt{\Big|\frac{6\widetilde{\beta}}{\widetilde{\alpha}_1}\Big|}\, 4\arctan\sqrt{\frac{B-1}{B+1}}$$
$$0 < B < 1:\ M_0 = \pm\sqrt{\Big|\frac{6\widetilde{\beta}}{\widetilde{\alpha}_1}\Big|}\, 4\tanh^{-1}\sqrt{\frac{1-B}{1+B}}\,,$$

where the alternative signs correspond to the cases $\widetilde{\alpha}B > 0$ or $\widetilde{\alpha}B < 0$.
This is the general theoretical framework for the slowly–varying solution to the veKdV equation.
Following Grimshaw *et al.* [2004], we give a brief general presentation of the wave transformation phenomenology, referring to Fig.3.2.
We begin the analysis looking at the possible failures of the adiabatic approximation. In fact, this approximation can fail for the table solitons that exist for $\alpha_1 < 0$: as one begins to come close to the limiting amplitude, the soliton width greatly increases and becomes comparable to the characteristic scale of the oceanic horizontal

[3]Equivalently, we can write

$$\sqrt{\frac{\widetilde{\beta}\widetilde{\alpha}^2}{\alpha_1}} G(B) = \sqrt{\frac{\widetilde{\beta}_0\widetilde{\alpha}_0^2}{\alpha_{10}}} G(B_0)\,,$$

where the subscript "0" indicates the initial values.

variability. Thus, the adiabatic approximation begins to break down as the solitary wave amplitude tends to the limiting value.
The same situation is realized for the opposite case of a very weak amplitude solitary wave (for $\alpha_1 > 0$ or $\alpha_1 < 0$) of the coefficient of the cubic nonlinear term); its width is large and comparable to the characteristic scale of the oceanic horizontal variability.
A third situation appears for solitary waves with $\alpha_1 > 0$ and amplitude close to that of the algebraic soliton. The algebraic soliton is unstable [Pelinovsky and Grimshaw, 1997], and the soliton breaks down if its amplitude passes through the algebraic value.
Further, there will be possible failures in the adiabatic theory if the coefficients of nonlinearity or dispersion in the eKdV equation pass through a zero value. The dispersion parameter β is always positive for stable flows, but α and α_1 can be zero (independently) for certain conditions of the oceanic environment. In the unlikely event when both nonlinear coefficients become zero simultaneously, the soliton cannot exist and any disturbance evolves into a dispersive wave packet; in this case the soliton–like structure is destroyed.
If α passes through zero, but $\alpha_1 < 0$, the solitary wave is destroyed [Grimshaw *et al.*, 1999]. The soliton amplitude tends to zero at the critical point according to the adiabatic parametrization Eq.(3.34). Secondary solitary waves of the opposite polarity can appear from the tail of the primary soliton, but the primary soliton itself disappears. The impossibility of an adiabatic transformation of a solitary wave in this case is illustrated in Fig.3.2, where there are no connecting arrows between solitary waves between quadrants III and IV. If α_1 is positive, an adiabatic transfer of the solitary wave is possible between quadrants I and II, and formally the soliton amplitude is determined at the critical point according to the adiabatic Eqs.(3.33). But if the soliton amplitude is close to the algebraic value, the adiabatic transformation is impossible, and the soliton–like structure is destroyed.
If α_1 changes its sign, but not α [Nakoulima *et al.*, 2004], the transformation of the solitary wave of the same polarity (negative for $\alpha < 0$ and positive for $\alpha > 0$) can be adiabatic (between quadrants I and III or II and IV), except for the case in which the solitary wave amplitude is close to the amplitude of the table soliton. If the soliton in the upper–half plane (Fig.3.2) has opposite polarity (positive for $\alpha < 0$ and negative for $\alpha > 0$), it is destroyed at the critical point, when α_1 becomes zero. This classification will be used to analyze the data from our numerical simulations of veKdV internal solitary wave transformation.

As last point of this section, we want to alert the reader that in place of (3.18), we will adopt the following form for the veKdV [Grimshaw *et al.*, 2004; Holloway *et al.*, 1997; Talipova *et al.*, 2015]:

$$\frac{\partial \zeta}{\partial x} + \left(\frac{\alpha}{c_0^2 \sqrt{Q}} \zeta + \frac{\alpha_1}{c^2 Q} \zeta^2 \right) \frac{\partial \zeta}{\partial s} + \frac{\beta}{c^4} \frac{\partial^3 \zeta}{\partial s^3} = 0 \,, \tag{3.39}$$

which is obtained by mapping $x \to x$, instead of $x \to \tau$ (with τ given by (3.17)). Eq.(3.58) is the spatial version of the veKdV equation, i.e., the evolution coordinate ("time") is the spatial coordinate, and the initial condition would correspond to

a time series of the wave displacement at the fixed point x_0. This form is more suitable for direct oceanographic applications [Grimshaw, 2002; Grimshaw *et al.*, 2004; Holloway *et al.*, 1997, 1999]. In this case,

$$\widetilde{\alpha} = \frac{\alpha}{c_0^2\sqrt{Q}}\,, \quad \widetilde{\alpha}_1 = \frac{\alpha_1}{c_0^2 Q}\,, \quad \widetilde{\beta} = \frac{\beta}{c_0^4}\,. \tag{3.40}$$

Due to a different scaling used for the horizontal coordinate [Grimshaw, 2002], the expression for Q is slightly modified [Holloway *et al.*, 1997]:

$$Q = \frac{\displaystyle\int_{-H}^{0} c_0^3 \left(\frac{\mathrm{d}\phi}{\mathrm{d}z}\right)^2 dz}{\displaystyle\int_{-H}^{0} c_{00}^3 \left(\frac{\mathrm{d}\phi_0}{\mathrm{d}z}\right)^2 dz}\,, \tag{3.41}$$

where c_{00} and ϕ_0 are the values of c_0 and ϕ at any fixed point x_0 (it is convenient to use the origin and put $x_0 = 0$). The solution at the leading order is

$$\zeta_0(x,s) = \frac{D}{1 + B\cosh(K(s - Vx))}\,,$$

with D, K and V given by (3.62), and a by (3.30), but now depending on x. As before, it is possible to define a trailing shelf which makes the conservation of mass satisfied, i.e.

$$\int_{-\infty}^{+\infty} \zeta_0\, ds + \int_{-\infty}^{\Psi(x)} \zeta^{(s)}\, ds = \text{const}\,.$$

However, to check the evolution of the trailing shelf, we refer directly to the numerical simulations of the vKdV and veKdV equations.

3.3 Explicit analytic solution for the veKdV solitary wave amplitude

In the previous section we have seen that we have to solve the mixed trascendent equation (3.36) to obtain a specific value for the parameter $B(\sigma)$, and this equation must be solved numerically. Furthermore, both vKdV and veKdV require some transformations to be written in their (τ, s)-form (3.18) (or (x, s)-form (3.58)), and the change of variable (3.22) and an asymptotic expansion to be solved at the various order of ε.

We propose here a derivation of an analytic expression for the varying amplitude of the veKdV solitary waves. Although less formal, this derivation is easier than that formulated in the previous section, and provides (under certain conditions) an explicit expression for the amplitude. For the vKdV equation the procedure is quite straightforward and can be found in Small [2001a]. However, we repeat here the argument and we extend the result to the veKdV equation. Consider the variable–coefficient KdV equation

$$\eta_t + c_0(x)\eta_x + \alpha(x)\eta\eta_x + \beta(x)\eta_{xxx} + \frac{c_0(x)M_x}{2M} = 0\,, \tag{3.42}$$

with coefficients given by (2.24), depending slowly on x through $h_2(x)$. The variation of amplitude can be derived from conservation of energy for a solitary wave:

$$E = \int_{-\infty}^{+\infty} \int_{-H}^{0} \rho c_0^2 \left(\frac{\partial \phi}{\partial z}\right)^2 \eta^2 \, dx \, dz \, .$$

If we consider a KdV steady-state soliton, the energy is given by

$$E = \int_{-\infty}^{+\infty} \int_{-H}^{0} \rho c_0^2 \left(\frac{\partial \phi}{\partial z}\right)^2 A^2 \mathrm{sech}^4 \left(\frac{x - Ut}{L}\right) dx \, dz \, .$$

The sech^4 function can be integrated by parts to give [Small, 2001a]

$$\int_{-\infty}^{+\infty} \mathrm{sech}^4 \left(\frac{x - Ut}{L}\right) dx = \frac{4L}{3} \, .$$

Since $L = \sqrt{12\beta/(A\alpha)}$, energy becomes

$$E = \frac{4}{3} A^{3/2} c_0^2 \sqrt{\frac{12\beta}{\alpha}} \mathcal{K} \, ,$$

with

$$\mathcal{K} = \int_{-H}^{0} \rho \left(\frac{\partial \phi}{\partial z}\right)^2 dz \, .$$

As E must be preserved, introducing a slow x-dependence in the coefficients, we impose conservation of energy and we explicit with respect to A, so that:

$$A(x) = \left(\frac{9}{16} \frac{E^2 c_0^2(x) \alpha(x)}{12 \beta(x) M^2(x)} \right)^{\frac{1}{3}} \, , \tag{3.43}$$

since $\mathcal{K}(x) = M(x)/c_0^3$.
We try now to proceed in the same way for the veKdV equation

$$\eta_t + c_0(x)\eta\eta_x + \alpha(x)\eta\eta_x + \alpha_1(x)\eta^2\eta_x + \beta(x)\eta_{xxx} + \frac{c_0(x)M_x}{2M} = 0 \, . \tag{3.44}$$

We have to calculate first the following integral of the steady–state eKdV soliton:

$$
\begin{aligned}
\int_{-\infty}^{+\infty} \eta^2(x,0)\,dx &= \int_{-\infty}^{+\infty} \left(\frac{A}{b+(1-b)\cosh^2(\gamma x)}\right)^2 dx \\
&= \frac{A^2}{2b^{3/2}\gamma}\left[(1+b)\,\mathrm{arctanh}\left(\sqrt{b}\tanh(\gamma x)\right) + \frac{(b-1)\sqrt{b}\sinh(2\gamma x)}{(1+b)+(1-b)\cosh(2\gamma x)}\right]\Bigg|_{-\infty}^{+\infty} \\
&= \frac{A^2}{2b^{3/2}\gamma}\left[(1+b)\,\mathrm{arctanh}\left(\sqrt{b}\tanh(\gamma x)\right) + \frac{(b-1)\sqrt{b}\tanh(2\gamma x)}{(1+b)\,\mathrm{sech}(2\gamma x)+(1-b)}\right]\Bigg|_{-\infty}^{+\infty} \\
&= \frac{A^2}{2b^{3/2}\gamma}\left[(1+b)\,\mathrm{arctanh}(\sqrt{b}) + \frac{(b-1)\sqrt{b}}{(1-b)} - (1+b)\,\mathrm{arctanh}(-\sqrt{b}) + \frac{(b-1)\sqrt{b}}{(1-b)}\right] \\
&= \frac{A^2}{b^{3/2}\gamma}\left[(1+b)\,\mathrm{arctanh}(\sqrt{b}) + \frac{(b-1)\sqrt{b}}{(1-b)}\right] \\
&= \frac{A^2}{b^{3/2}\gamma}\left[(1+b)\,\mathrm{arctanh}(\sqrt{b}) - \sqrt{b}\right],
\end{aligned}
$$

where in the third line we multiplied and divided the second term in the square brackets by $\mathrm{sech}(2\gamma x)$, and in the fifth line we used the simmetry properties of the $\mathrm{arctanh}(\cdot)$ function. Thus, the energy integral becomes:

$$
\begin{aligned}
E &= \frac{A^2}{b^{3/2}\gamma}\left[(1+b)\,\mathrm{arctanh}(\sqrt{b}) - \sqrt{b}\right]\int_{-H}^{0} \rho c_0^2 \left(\frac{\partial\phi}{\partial z}\right)^2 dz \\
&= \frac{A^2}{b^{3/2}\gamma}\left[(1+b)\,\mathrm{arctanh}(\sqrt{b}) - \sqrt{b}\right]\frac{M}{c_0}
\end{aligned}
$$

Since energy must be preserved along the motion, introducing a slow variability from x in the coefficients, we impose energy conservation, so that:

$$
E = \frac{A^2(x)}{b^{3/2}(x)\gamma(x)}\left[(1+b(x))\,\mathrm{arctanh}\left(\sqrt{b(x)}\right) - \sqrt{b(x)}\right]\frac{M(x)}{c_0(x)} \tag{3.45}
$$

Solving explicitly this equation with respect to the amplitude $A(x)$ is not possible (we remark that both b and γ depend on A), being a mixed trascendent equation. However, since the function $\mathrm{arctanh}(x)$ is defined for $|x|<1$, we expand in Taylor series for $\sqrt{b}<1$

$$
\mathrm{arctanh}\left(\sqrt{b}\right) \simeq \sqrt{b} + \frac{b^{3/2}}{3} + \cdots,
$$

hence

$$
(1+b)\,\mathrm{arctanh}\left(\sqrt{b}\right) - \sqrt{b} \simeq (1+b)\left(\sqrt{b} + \frac{b^{3/2}}{3} + \cdots\right) - \sqrt{b} = \frac{4}{3}b^{3/2} + O\left(b^{5/2}\right).
$$

Thus, substituing in (3.45), we get

$$
E \simeq \frac{4}{3}\frac{A^2(x)M(x)}{\gamma(x)c_0(x)}.
$$

Using (2.55), we express all the coefficients in terms of A (we omit the x-dependence for clarity of notation):

$$E \simeq \frac{4A^2M}{3c_0}\sqrt{\frac{12\beta}{A\left(\alpha+\frac{1}{2}\alpha_1 A\right)}}\,,$$

from which

$$A\alpha+\frac{1}{2}A^2\alpha_1 \simeq \frac{64}{3}\frac{\beta A^4M^2}{E^2c_0^2}\,,$$

and finally

$$A^3+\left(-\frac{3E^2c_0^2\alpha_1}{128\beta M^2}\right)A-\frac{3\alpha E^2c_0^2}{64\beta M^2}=0\,. \tag{3.46}$$

We solve this cubic equation through Cardano–Tartaglia formulas. Given the cubic equation in the unknown ξ

$$\xi^3+\Lambda\xi-\Gamma=0\,,$$

the solutions are given by

$$\xi_0 = B_+^{\frac{1}{3}}+B_-^{\frac{1}{3}} \tag{3.47a}$$

$$\xi_\pm = -\frac{1}{2}\left(B_+^{\frac{1}{3}}+B_-^{\frac{1}{3}}\right)\pm i\frac{\sqrt{3}}{2}\left(B_+^{\frac{1}{3}}-B_-^{\frac{1}{3}}\right)\,, \tag{3.47b}$$

with

$$B_\pm = R\pm\sqrt{\Delta}\,,\quad \Delta=R^2+Q^3\,,\quad Q\equiv\frac{\Lambda}{3}\,,\quad R\equiv\frac{\Gamma}{2}\,.$$

Thus, for $\alpha_1<0$ and $\beta>0$, we have

$$\Delta=\left(\frac{3\alpha E^2c_0^2}{128M^2\beta}\right)^2-\left(\frac{E^2c_0^2\alpha_1}{128\beta M^2}\right)^3>0\,, \tag{3.48}$$

and there is one real solution (ξ_0) and two complex solution ($\xi_\pm$). In particular, the real solution will be

$$\begin{aligned}A(x) &\sim \left(R(x)+\sqrt{\Delta(x)}\right)^{\frac{1}{3}}+\left(R(x)-\sqrt{\Delta(x)}\right)^{\frac{1}{3}} \\ &= \left(\frac{3\alpha(x)E^2c_0^2(x)}{128M^2(x)\beta(x)}+\sqrt{\Delta(x)}\right)^{\frac{1}{3}}+\left(\frac{3\alpha(x)E^2c_0^2(x)}{128M^2(x)\beta(x)}-\sqrt{\Delta(x)}\right)^{\frac{1}{3}}\end{aligned} \tag{3.49}$$

We observe that the condition $\sqrt{b}<1$ is consistent with the fact that eKdV solitary waves have a limiting amplitude. Indeed, imposing

$$\sqrt{-\frac{A\alpha_1}{2\alpha+\alpha_1 A}}=1 \quad\Rightarrow\quad A=-\frac{\alpha}{\alpha_1}\,.$$

which is nothing but $\eta_{\max}$. We stress that this condition must be fulfilled to have a good approximation of the solution for $A(x)$ obtained solving the problem numerically by means of (3.45): the smaller $\sqrt{b(x)}$, the better the approximation. We will examine this point in the next chapter in relation to veKdV numerical simulations.

3.4 Numerical integration of vKdV and veKdV equations

As observed in 3.2, to understand the wave transformation process during propagation in a variable environment, it is important to select all possible "nonadiabatic" factors that could make the slowly–varying approximation not valid, even when the horizontal variability of the oceanic parameters may seem slow enough. For this purpose, direct numerical simulations of vKdV and veKdV equations are performed.
In describing the numerical algorithms, we consider the case of the veKdV equation directly, since the case of the vKdV is simply obtained not considering the cubic nonlinear term. We apply an explicit finite difference scheme with the order of approximation $(\Delta X)^2$ and $(\Delta T)^2$, with ΔX and ΔT space and time discrete intervals [Holloway *et al.*, 1997; Obregon and Stepanyants, 2012; Pelinovsky *et al.*, 1994; Small, 2001a; Small *et al.*, 1999; Zabusky and Kruskal, 1965]. Depending on the specific variable considered as "space" or "time", we can write slightly different schemes. In the framework of the theory formulated in section 3.2, we can discretize Eq.(3.58), where the evolution coordinate ("time") is the spatial coordinate x, as [Holloway *et al.*, 1997; Pelinovsky *et al.*, 1994]:

$$\frac{\zeta_j^{n+1}-\zeta_j^{n-1}}{\Delta X}+\frac{\alpha_j}{c_{0j}\sqrt{Q_j}}\zeta_j^n\frac{\zeta_{j+1}^n-\zeta_{j-1}^n}{\Delta T}+\frac{\alpha_{1j}}{c_{0j}^2Q_j}\left(\zeta_j^n\right)^2\frac{\zeta_{j+1}^n-\zeta_{j-1}^n}{\Delta T} + \frac{\beta_j}{c_{0j}^4}\frac{\zeta_{j+2}^n-2\zeta_j^n+2\zeta_{j-1}^n-\zeta_{j-2}^n}{(\Delta T)^3}=0\,, \tag{3.50}$$

where, in this case, n is the space index and j is the time index. For the first step, the first term of (3.50) is replaced by $(\zeta_j^1-\zeta_j^0)/(\Delta X)$, with ζ_j^0 value of the initial waveform. For the solutions of the difference equation to converge to the solutions of equation (3.58), the following numerical stability criterion must be satisfied:

$$\frac{\Delta X}{\Delta T}\left(\alpha\zeta+\frac{3\sqrt{3}\beta}{2(\Delta T)^2}\right)<1\,, \tag{3.51}$$

where the variability of quantities α, β, and ζ during the wave evolution must be taken into account. For small values of ΔT, the condition (3.51) can be simplified as [Holloway *et al.*, 1997]

$$\Delta X<0.384(\Delta T)^3/\beta\,. \tag{3.52}$$

To satisfy this last condition, very fine space discrete intervals are required, especially in deep water, and the algorithm could become very computationally expensive

[Small, 2001a]. Usually, this numerical scheme is solved imposing periodic boundary conditions [Holloway *et al.*, 1997, 1999; Zabusky and Kruskal, 1965],

$$\zeta(s+T,x)=\zeta(s,x)\,.$$

In particular, if one is studying the evolution of an internal tide, it is possible to set $T=2\pi/\omega$, with ω periodic internal tide frequency and $\zeta(s,x_0)=a_0F(\omega s)$, where F is the periodic function, which characterizes the form of the initial wave at the origin x_0. For example the initial wave could be a sinusoidal long wave [Holloway *et al.*, 1999].
We can also use another finite difference scheme, in the natural variables of the problem, i.e, x as space, and t as time. In this case, the reference equation is the standard veKdV equation (3.16), which can be discretized as [Small, 2001a; Zabusky and Kruskal, 1965]

$$\begin{aligned}\frac{\eta_j^{n+1}-\eta_j^{n-1}}{\Delta T}&+c_{0j}\left(\frac{\eta_{j+1}^n-\eta_{j-1}^n}{\Delta X}\right)+\alpha_j\left(\frac{\eta_{j+1}^n+\eta_j^n+\eta_{j-1}^n}{3}\right)\left(\frac{\eta_{j+1}^n-\eta_{j-1}^n}{\Delta X}\right)\\&+\alpha_{1j}\left(\frac{\eta_{j+1}^n+\eta_j^n+\eta_{j-1}^n}{3}\right)^2\left(\frac{\eta_{j+1}^n-\eta_{j-1}^n}{\Delta X}\right)\\&+\beta_j\left(\frac{\eta_{j+2}^n-2\eta_j^n+2\eta_{j-1}^n-\eta_{j-2}^n}{(\Delta X)^3}\right)\\&+\eta_j^nM_j\left(\frac{M_{j+1}-M_{j-1}}{2\Delta X}\right)=0\,,\end{aligned}\tag{3.53}$$

where, in this case, n is the time index and j is the space index. Here a mean value of η over three points is used to help remove noise in the nonlinear term (following Zabusky and Kruskal [1965]). Following Small [2001a], we can assign boundary conditions as

$$\eta_1=\eta_2=\eta_{n_x-1}=\eta_{n_x}=0\,.\tag{3.54}$$

where n_x is the number of spatial points. Provided n_x is large enough, this is not overly restrictive, as generally solitary waveforms are considered, the influence of which decays to zero before the boundaries. The scheme (3.53) can also be written as an implicit difference scheme, which is computationally faster but less precise (see Small [2001a] for details). The stability condition for (3.53) becomes $\Delta T<0.384(\Delta X)^3/\beta$.

* * *

In this chapter, we described the main weakly nonlinear models for ISWs in a variable environment (e.g., variable depth). We describe the evolution of weakly nonlinear ISWs through the vKdV equation

$$\eta_t + c_0(x)\eta_x + \alpha(x)\eta\eta_x + \beta(x)\eta_{xxx} + \frac{c_0(x)Q_x}{2Q} = 0\,, \tag{3.55}$$

or the veKdV equation

$$\eta_t + c_0(x)\eta\eta_x + \alpha(x)\eta\eta_x + \alpha_1(x)\eta^2\eta_x + \beta(x)\eta_{xxx} + \frac{c_0(x)Q_x}{2Q} = 0\,, \tag{3.56}$$

where the coefficients, in the case of a two–layer stratification, are those defined in (2.46), depending slowly on x through $h_2(x)$. Through the transformation $\zeta(x,s) = \sqrt{Q(x)}\eta(x,s)$, it is possible to rewrite (3.55) as

$$\frac{\partial\zeta}{\partial x} + \widetilde{\alpha}\zeta\frac{\partial\zeta}{\partial s} + \widetilde{\beta}\frac{\partial^3\zeta}{\partial s^3} = 0\,, \tag{3.57}$$

and (3.56) as

$$\frac{\partial\zeta}{\partial x} + \left(\widetilde{\alpha}\zeta + \widetilde{\alpha}_1\zeta^2\right)\frac{\partial\zeta}{\partial s} + \widetilde{\beta}\frac{\partial^3\zeta}{\partial s^3} = 0\,, \tag{3.58}$$

where

$$\widetilde{\alpha} = \frac{\alpha}{c_0^2\sqrt{Q}}\,, \quad \widetilde{\alpha}_1 = \frac{\alpha_1}{c_0^2 Q}\,, \quad \widetilde{\beta} = \frac{\beta}{c_0^4}\,. \tag{3.59}$$

Slowly–varying solutions to (3.57) and (3.58) can be found through asymptotic expansions. For vKdV, we obtain

$$\zeta(x,s) = A\,\mathrm{sech}^2\left(K(s - Vx)\right)\,, \tag{3.60}$$

where $V = A\widehat{\alpha}/3 = 4\widehat{\beta}K^2$, with $\widehat{\alpha} = \widetilde{\alpha}/c_0$ and $\widehat{\beta} = \widetilde{\beta}/c_0$.
For veKdV we get

$$\zeta(x,s) = \frac{D}{1 + B\cosh(K(s - Vx)}\,, \tag{3.61}$$

with

$$D = \frac{6\widetilde{\beta}K^2}{\widetilde{\alpha}}\,, \quad K = \sqrt{\frac{\widetilde{\alpha}^2}{6\widetilde{\alpha}_1\widetilde{\beta}}(B^2 - 1)}\,, \quad V = \widetilde{\beta}K^2\,, \tag{3.62}$$

and the amplitude of the solitary wave is given by

$$a(x) = \frac{D(x)}{1 + B(x)}\,. \tag{3.63}$$

The veKdV solutions can transform along the motion changing polarity and structure. The possible transitions are summarized in Fig.3.2. In particular, the transition from quadrant III and IV is prohibited.

The solution to vKdV and veKdV equations can be found also through the procedure illustrated in Sec.3.3, which is easier to carry out and operates directly on equations (3.55) and (3.56) in the natural variables x and t. In particular, it is important to determine the variation of the ISW amplitude, which for vKdV is given by

$$A(x) = \left(\frac{9}{16} \frac{E^2 c_0^2(x) \alpha(x)}{12 \beta(x) M^2(x)} \right)^{\frac{1}{3}} , \tag{3.64}$$

and for veKdV by solving with respect to $A(x)$ the trascendental relationship

$$E = \frac{A^2(x)}{b^{3/2}(x)\gamma(x)} \left[(1 + b(x)) \operatorname{arctanh}\left(\sqrt{b(x)} \right) - \sqrt{b(x)} \right] \frac{M(x)}{c_0(x)} . \tag{3.65}$$

Since (3.65) must be solved numerically, to get an explicit analytic expression for $A(x)$ we found a solution in the approximated regime $\sqrt{b} < 1$, given by

$$A(x) \sim \left(\frac{3\alpha(x) E^2 c_0^2(x)}{128 M^2(x) \beta(x)} + \sqrt{\Delta(x)} \right)^{\frac{1}{3}} + \left(\frac{3\alpha(x) E^2 c_0^2(x)}{128 M^2(x) \beta(x)} - \sqrt{\Delta(x)} \right)^{\frac{1}{3}} , \tag{3.66}$$

with $\Delta(x)$ given by

$$\Delta = \left(\frac{3\alpha E^2 c_0^2}{128 M^2 \beta} \right)^2 - \left(\frac{E^2 c_0^2 \alpha_1}{128 \beta M^2} \right)^3 > 0 . \tag{3.67}$$

We can solve vKdV and veKdV equations also numerically through the finite difference schemes given in Sec.3.4, both in the x–evolution coordinate and t–evolution coordinate.

Chapter 4

Shoaling and breaking of ISWs over a sloping bathymetry

In this chapter, we study the interaction of ISWs with a sloping bottom. In particular, we examine the propagation and shoaling of ISWs in laboratory experiments, and we describe the different types of "breakers", classified through the Iribarren number. For specific types of breaking, we derive an analytical wave–breaking criterion using eKdV and MCC models, we validate it with experimental results, and we compare it with two well–established empirical criteria developed in the recent years. Next, we show a comparison between the propagation and shoaling of the experimental waves and those obtained by direct numerical simulations of vKdV and veKdV ISWs. We then apply these models to describe, both numerically and analitically, the evolution of ISWs generated in the Messina Strait, propagating northward in the Gioia Basin (Tyrrhenian Sea) towards Capo Vaticano. Finally, we apply our wave–breaking model to predict the breaking location of ISWs in the Gioia Basin.

4.1 ISWs shoaling and breaking in laboratory experiments

To study the interaction between ISWs and a sloping boundary, we analyze data of laboratory experiments performed at the Department of Civil Engineering of Roma Tre University [La Forgia *et al.*, 2018a]. In these experiments different types of ISWs have been generated by the lock-release method in a 3.0 m long, 0.2 m wide and 0.3 m deep Perspex tank (Fig. 4.1). In the following, we describe the adopted experimental procedure and the resultant phenomenology.
The entire domain is initially filled with a solution of sodium chloride (NaCl), generating the lower layer of uniform density ρ_2. Over the free surface, we add fresh water of uniform density $\rho_1 < \rho_2$ [La Forgia *et al.*, 2018a]. Then a vertical gate is inserted at a distance x_d from the left wall of the tank (Fig.4.1), making sure that its bottom is few millimeters above the channel bottom. Thus, adding further fresh water on the free surface of the lock, a known volume of brine water flows below the gate, reestablishing the hydrostatic equilibrium. During this phase, the pycnoclines of the two regions form the displacement η_0, which represents the initial setting of the runs. It therefore results a two–layer stratification (Fig.4.1),

composed by a thin, upper layer of fresh water of thickness h_1 and a lower, denser layer of thickness $h_2 > h_1$; the pycnocline is deeper within the lock region, where the thickness of the lighter fluid is $h_1 + \eta_0$. The gravity collapse induced by the gate removal leads to the generation of a single ISW of depression propagating downstream, towards an inclined surface with a uniform slope [La Forgia *et al.*, 2018a]. A digital camera is used to record the flow evolution from the lateral wall of the tank. By the instantaneous pycnocline position inferred by image analysis, the wave amplitude A, the characteristic wavelength λ, the wave surface S and the wave celerity c are estimated.

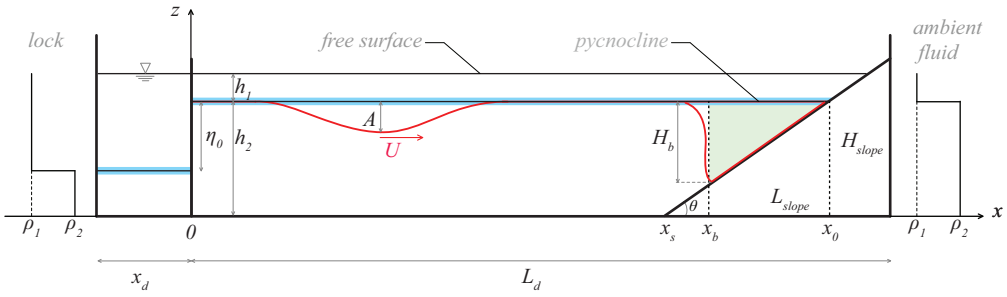

Figure 4.1. Experimental setting: h_1 and h_2 top layer and bottom layer thicknesses; η_0 pycnocline displacement between lock region and ambient region; θ slope angle; H_{slope} and L_{slope} height and length of the slope respectively; x_s abscissa of the toe of slope; x_0 abscissa of the point of intersection between the pycnocline and the slope; x_d length of the lock region; L_d length of the ambient fluid region.

Depending on the ISW geometric features and the slope inclination, the ISW shoaling over the sloping boundary develops differently. Each breaking mechanism is consequently characterized by different effects in terms of mixing, entrainment, and shear stress over the bottom [La Forgia *et al.*, 2018a]. During the wave shoaling along the slope, two processes occur: the steepening of the rear edge of the wave and the downward motion of the volume confined between the leading edge of the wave and the sloping boundary (see Fig.4.2).

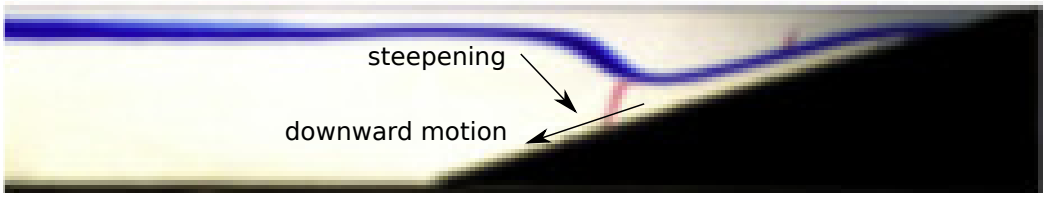

Figure 4.2. Snapshot of a typical shoaling mechanism. Two processes occur: the steepening of the rear edge of the wave and the downward motion of the volume confined between the leading edge of the wave and the sloping boundary.

For plunging breakers a dominant steepening of the trailing edge of the wave takes place, followed by a quick clockwise overturning in the onshore direction, inducing strong local mixing (Fig 4.3). For collapsing breakers, the downward motion of the confined fluid results to be dominant, compared to the trailing edge steepening: the trapped dense fluid leaves its original position with a fast downward motion

in the adverse pressure gradient region. As a result, a turbulent separated bolus forms and quickly dissipates. Then, part of the incident wave is reflected and a gravity current composed of the denser fluid flows up the slope, until hydrostatic conditions are reestablished (Fig 4.3). An intermediate breaking mechanism, i.e., the plunging–collapsing breaker, is observed when the two main shoaling processes occur in the breaking location (Fig 4.4). Finally, in the case of surging breakers, ISWs are not subject to any observable large-scale instability during the shoaling until the wave trough reaches the sloping bottom. The wave is almost reflected by the right wall of the tank (Fig 4.4) [La Forgia *et al.*, 2018b].

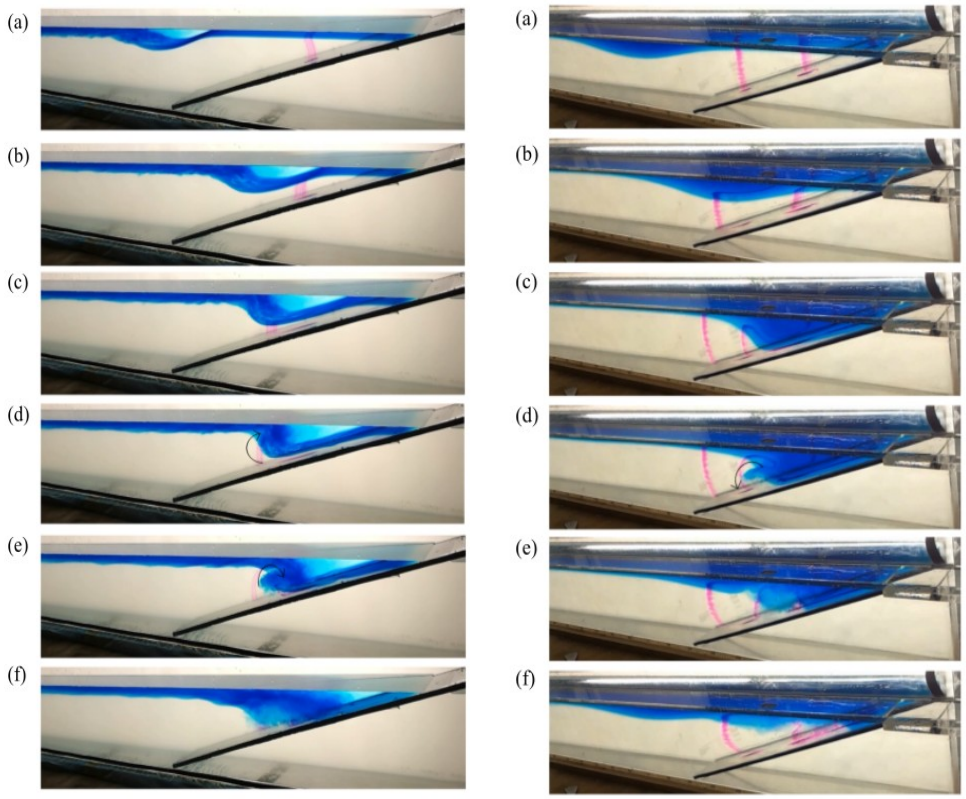

Figure 4.3. Left panel: plunging breaker. The wave reaches the slope (a); the steepening of the trailing edge occurs (b,c); a clockwise vortex forms (d) and reaches the sloping bottom onshore, generating mixing (e,f). Right panel: collapsing breaker. The wave reaches the slope (a); the confined volume beneath the leading edge flows out from this position (b,c); an anti-clockwise vortex forms near the bottom (d); the vortex losing its energy moves onshore (e); the wave is partially reflected (f).

The occurrence of a particular kind of breaking mechanism depends on both geometric characteristics of the incident waves and sloping boundary. Different types of breaking are commonly distinguished introducing the internal Iribarren number [Aghsaee *et al.*, 2010; Boegman *et al.*, 2005; La Forgia *et al.*, 2018a; Sutherland *et al.*, 2013]:

$$\mathrm{Ir} = \frac{s}{\sqrt{S_w}}\,, \tag{4.1}$$

where $s = \tan(\theta)$ is the topographic slope and $S_w = A/\lambda$ is the wave slope. The Iribarren number is a dimensionless parameter originally applied to define surface gravity waves breaker types on beaches [Dean and Dalrymple, 1991]. However, the breaking evolution of surface waves and internal waves are rather different (see Fig.4.5) For $\mathrm{Ir} < 1$ plunging breakers and for $\mathrm{Ir} = 1 \div 1.5$ collapsing breakers are observed, while plunging–collapsing breakers occur for $\mathrm{Ir} \simeq 1$. Surging breakers occur for $\mathrm{Ir} > 1.5$ [La Forgia *et al.*, 2018a] (see Fig.4.6).
In the next section, we will compare the shoaling and breaking processes observed in the laboratory experiments with those reproduced through numerical simulations of vKdV and veKdV equations.

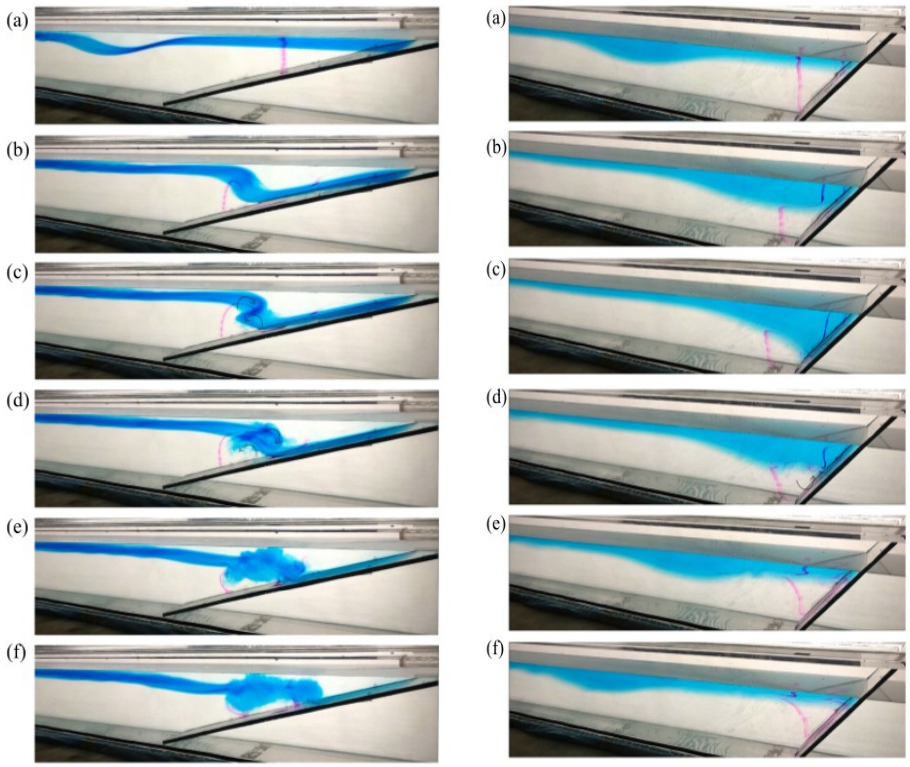

Figure 4.4. Left panel: plunging–collapsing breaker. The wave reaches the slope (a); the steepening of the trailing edge and the downward motion of the confined volume occur (b); a clockwise vortex near the surface and a separation bubble close to the bottom form (c,d); a large amount of mixing occur (e,f). Right panel: surging breaker. The wave reaches the slope (a); the steepening of the trailing edge and the downward motion of the confined volume occur without generating instabilities (b,c); a gravity current forms above the slope (d); most part of the wave is reflected (e,f).

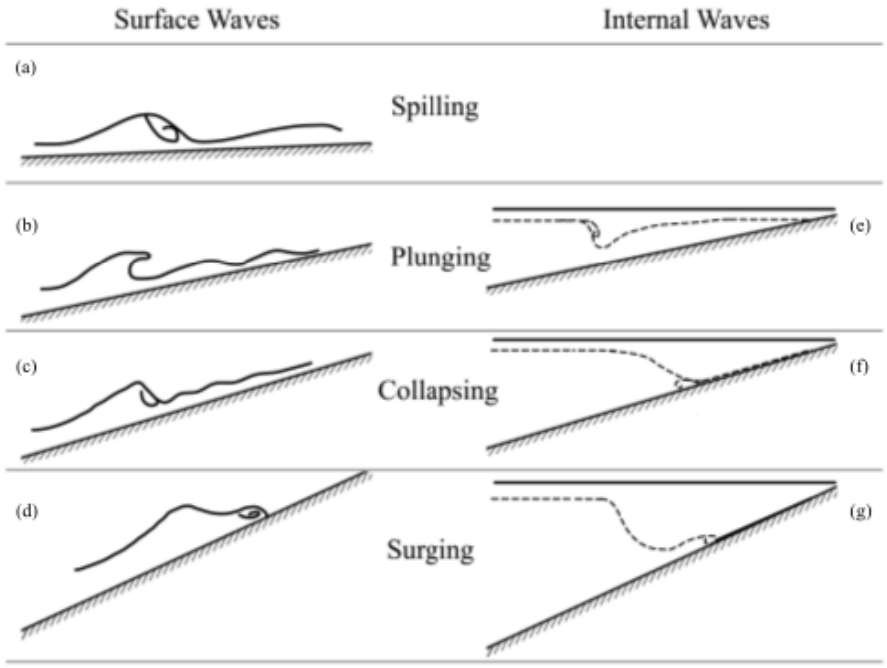

Figure 4.5. Schematization of the different surface (a-d) and internal (e-g) waves breaker types. The scheme considers a single wave interacting with an increasingly inclined sloping boundary. The dashed lines define the pycnocline position. The solid lines over the sloping boundaries indicate the free surfaces.

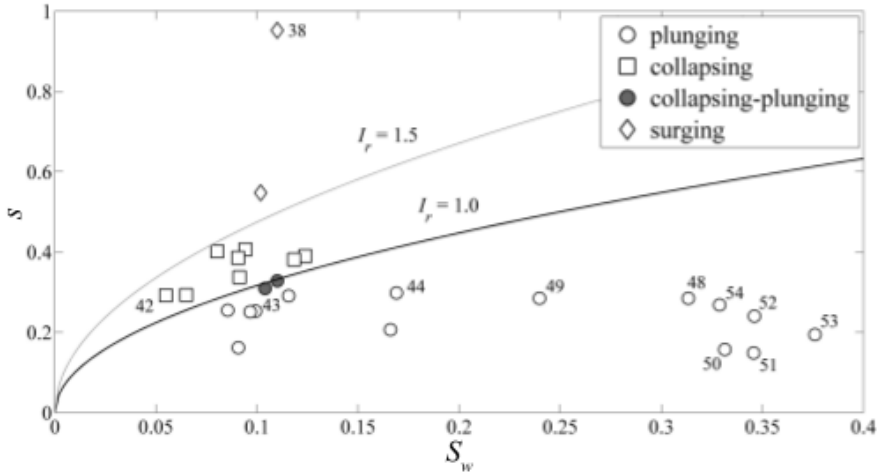

Figure 4.6. Iribarren domains for the experiments performed by La Forgia *et al.* [2018a]. For Ir < 1 plunging breakers and for Ir $= 1 \div 1.5$ collapsing breakers are observed, while plunging–collapsing breakers occur for Ir $\simeq 1$. Surging breakers occur for Ir > 1.5. From La Forgia *et al.* [2018a].

4.2 vKdV and veKdV numerical simulations and analytical theory for experimental waves

In the following we examine the numerical simulations of vKdV and veKdV equations, (3.42) and (3.44),respectively, using the parameters setting of a plunging–collapsing breaker experiment performed by laboratory (see also Sec. 4.4). The simulations are performed making use of the algorithm (3.53), with boundary conditions (3.54). The experimental setting is that of Fig. 4.1 and the specific data are reported in Tab. 4.1(case c). The linear slope is reproduced also in Fig. 4.8g and Fig. 4.10g. Though we selected this type of breaking because its initial amplitude is not too close to the limiting amplitude (so that eKdV soliton can exist), the shoaling and breaking mechanisms reproduced by vKdV and veKdV simulations are practically identical in the three cases examined in the experiments. Thus, one of these experiments will be substantially representative of the others.

The behavior of the coefficients of both vKdV and veKdV equation shows that, along the slope, nonlinear coefficients $\alpha(x)$ and $\alpha_1(x)$ tend to diverge, while the dispersion $\beta(x)$ and the linear veocity $c_0(x)$ tend to zero (i.e., the wave slows down on the slope)(Fig. 4.7). Thus, before the end of the slope we can expect the annihilation of the solitary–wave structure, due to nonlinear effects exceeding dispersion. In general, the significant decrease of the dispersion parameter may lead to the formation of a shock wave with a bore–like structure (dispersive shock wave).

Near the transition point ($h_1 = h_2$), the amplitude of the vKdV wave decreases to zero as $A \simeq -|\alpha|^{1/3}$ (as seen in Sec.3.3), then the mass of the solitary wave increases (in absolute value), while the tail grows to be comparable with the wave itself [Grimshaw *et al.*, 2010]. The adiabatic approximation breaks down as the critical point is approached. Nevertheless, we can infer that the the solitary wave itself is destroyed as the wave passes through the critical point $\alpha = 0$. The structure of the solution beyond this critical point has been examined numerically by Knickerbocker and Newell [1980] and revisited by Grimshaw *et al.* [1998] that the wave tail passes through the critical point as a positive disturbance, which then being in an environment with $\alpha > 0$, can generate a train of solitary waves of positive polarity [Grimshaw *et al.*, 2010].

Furthemore, as the $\alpha(x)$ near the end of the slope changes its sign becoming positive, while $\alpha_1(x)$ remains negative, for veKdV waves there cannot be transitions from quadrants III and IV of the (α_1, α) graph (Fig. 3.2), and the solitary waves loses its identity becoming a dispersive wavetrain of positive polarity.

We focus now on the wave amplitude amplification or reduction during the shoaling. As noticed by Small [2001a], vKdV and veKdV small amplitude waves behave similarly in deep water but differently propagating toward shallow areas. Whereas the vKdV model predicts a steady growth in wave amplitude, the veKdV model predicts a decrease in wave amplitude in shallow water. Actually, this is particularly evident for a large amplitude eKdV initial wave, which evolves into a significantly smaller wave in shallow water, whose amplitude is determined by the limiting amplitude $\eta_{\rm lim} = -\alpha/\alpha_1$. The problem is basically to understand what is the amplitude for an internal solitary wave of given energy and of an initial amplitude A in water depth $H(0)$ of the wave in a different water depth, assuming that energy

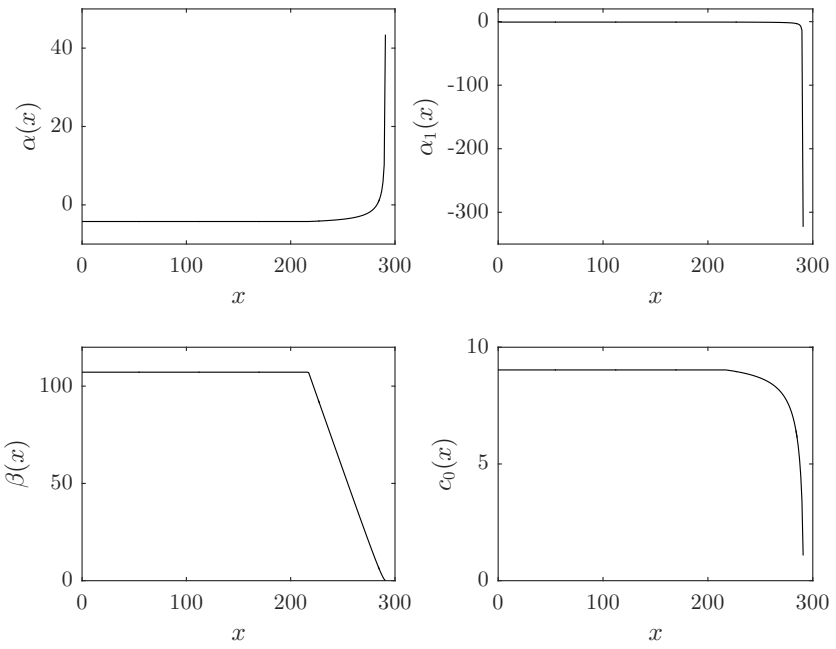

Figure 4.7. Behavior of the vKdV/veKdV coefficients as functions of x for the plunging–collapsing experiment. Along the slope, the nonlinear coefficients $\alpha(x)$ and $\alpha_1(x)$ tend to diverge, while the dispersion $\beta(x)$ and the linear veocity $c_0(x)$ tend to zero (i.e., the wave slows down on the slope). Thus, before the end of the slope we can expect the annihilation of the solitary–wave structure, due to nonlinear effects exceeding dispersion.

is conserved and that the wave adiabatically adjusts to a solitary waveform. Small [2001a] showed that, for a given value of the initial energy, the *wave amplitude of a KdV soliton increases with decreasing depth.* On the contrary, for eKdV waves the energy–amplitude relationships are similar to the corresponding KdV for small wave amplitudes, while for larger (negative) amplitudes the eKdV energies are greater than the KdV wave. The agreement for small amplitudes is to be expected, as the two equations coincide in the small amplitude limit. The divergence at larger amplitudes is due to a property [Michallet and Barthélemy, 1998] of large amplitude eKdV waves growing wider with increasing amplitude, eventually reaching the critical amplitude η_{lim}, where energy and mass go to infinity. Thus, *in shallow waters, to conserve energy the eKdV wave decreases in amplitude, but increases in width.* In particular, the amplitude decreases reducing to its critical value for the *specific depth* the wave is going through in that instant of time.

The propagation and evolution of ISW travelling from shallow to deep water was also investigated by Small [2001a], to see if the shoaling process was reversible. For eKdV solitary waves that were initially small, compared with the critical amplitude η_{lim}, the process was found to be generally reversible. However, for the solitary waves initially close to η_{lim}, the width of the wave was so large that the bathymetry could not be considered slowly varying. As the wave then passed into deeper water where the amplitude was not close to η_{lim}, the wave split in a process similar to KdV

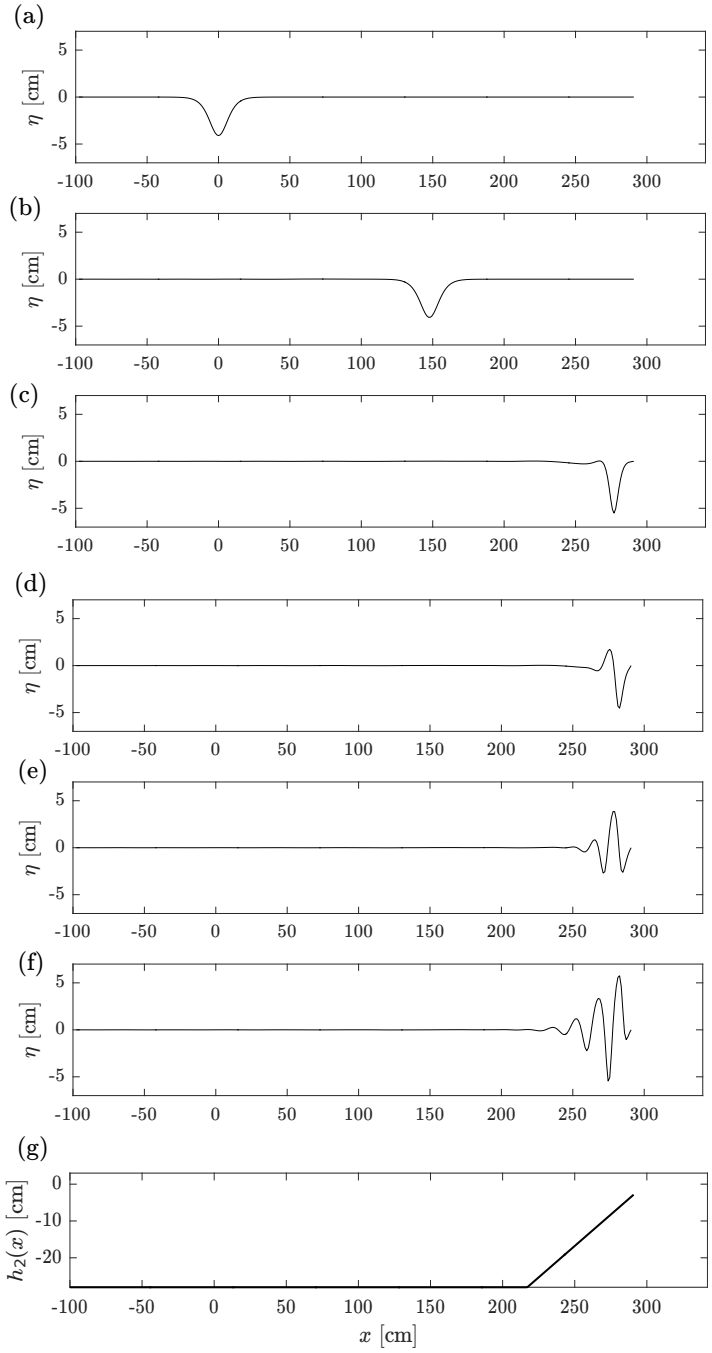

Figure 4.8. vKdV numerical simulation of plunging–collapsing breaker. (a,b,c) Increase in amplitude for vKdV wave. (d) Amplitude reduction (since $\alpha(x) \to 0$), instability becomes visible as a small kink on the rear edge of the wave. (e,f,g) Adiabatic approximation breaks down and the tail becomes larger than the wave itself. The solitary wave is destroyed, but the disturbance survives as a train of waves with positive polarity.

soliton fission. In other words, fission appears to be possible for near–limiting eKdV solitary waves propagating offshelf, as well as for KdV solitons propagating in the opposite direction (i.e., onshelf) [Small, 2001a].
In our numerical simulations we can observe the amplitude amplification for vKdV wave (Fig. 4.8), which starts from $A = -4.1$ cm and arrives to a maximum (in absolute value) of $A \simeq -5.5$ cm retaining its solitary wave shape. Near $x \simeq 280$ cm, begins the amplitude reduction since the coefficient $\alpha(x)$ is approacching zero and, indeed, instability becomes visible as a small kink on the rear edge of the wave (Fig. 4.8d). The adiabatic approximation breaks down and we can see the tail becoming larger than the wave itself (Fig. 4.8e-f). The solitary wave is destroyed, but the disturbance survives as a train of waves with positive polarity until there is no other space for propagation. The behavior of the wave amplitude can be theoretically predicted through (3.43), which is a really good approximation, as can be seen in Fig. 4.9. In particular, it is possibile to observe the amplitude increase (in absolute value) during the shoaling phase and the subsequent rapid reduction near the transition point.

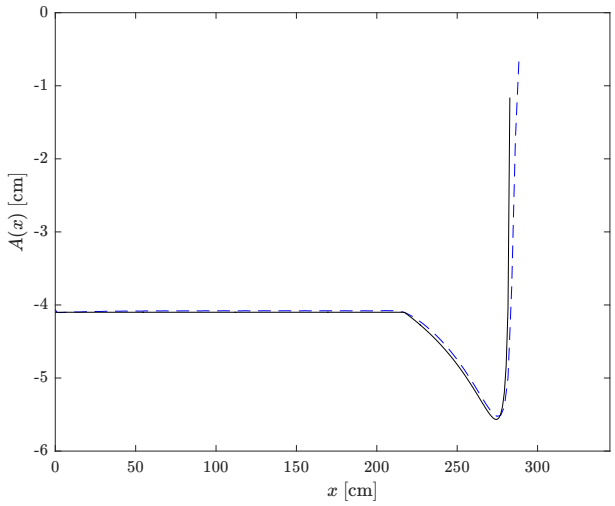

Figure 4.9. Comparison between theoretical (solid black line) and numerical prediction (dashed blue line) of vKdV soliton amplitude. The theoretical prediction given by (3.43) is really good. It is possibile to observe the increase in amplitude (in absolute value) during the shoaling phase and the subsequent rapid reduction near the transition point.

Consider now the numerical simulations of veKdV equation (Fig. 4.10). In this case, the wave undergoes a slight increase of amplitude (almost not perceptible) when it approaches the slope ($x \simeq 217$ cm) and then becomes gradually smaller when $\alpha(x) \to 0$ (Fig. 4.11). Thus, with respect to the vKdV, there is no real increase of amplitude during the shoaling process. When the wave passes $x \simeq 250$ cm, a small kink develops on the rear edge of the wave (Fig. 4.10c-d), and near $x \simeq 280$ cm (where $h_1 \simeq h_2$) the wave loses its identity as a soliton. In the end, once $\alpha(x)$ becomes positive, the solitary wave shape is destroyed and a dispersive tail of positive polarity is generated (Fig. 4.10f). In fact, the solitary wave cannot make any transition from negative to positive polarity when $\alpha_1(x) < 0$.

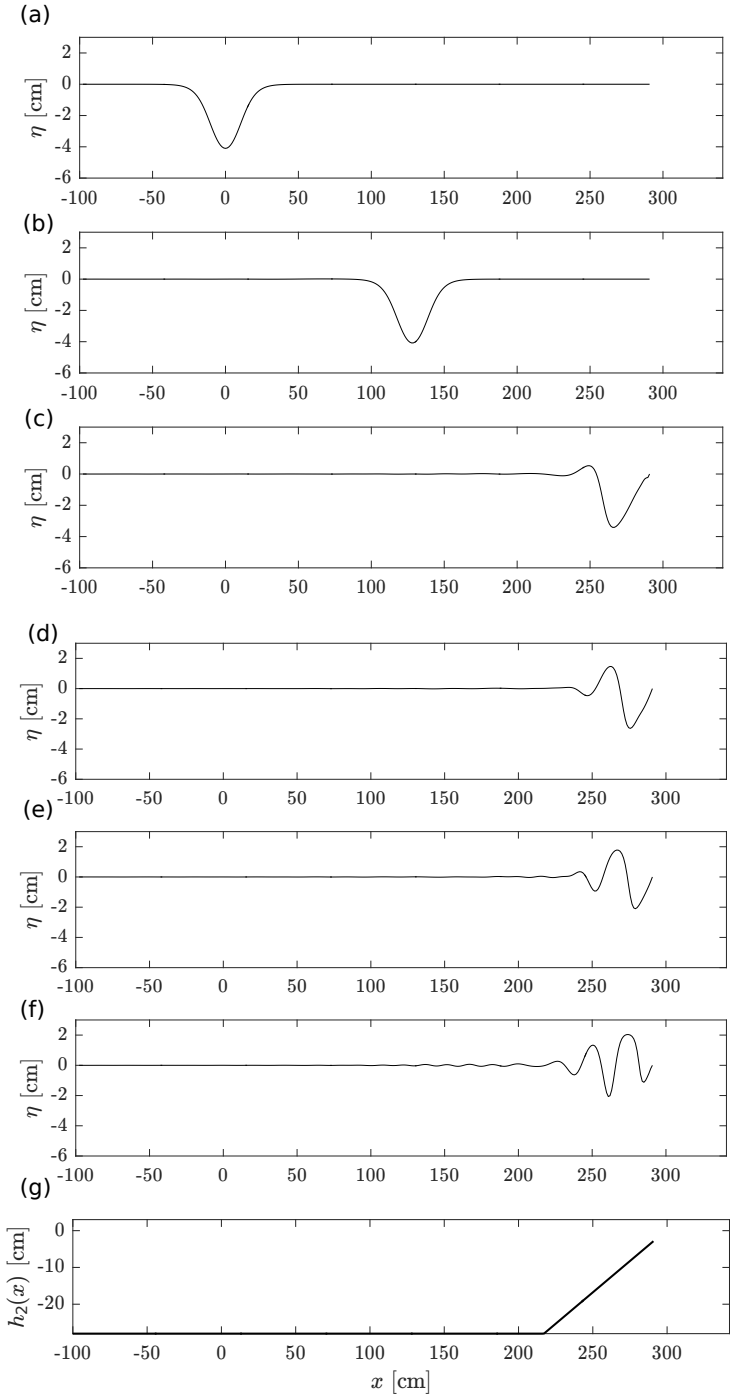

Figure 4.10. veKdV numerical simulation of plunging–collapsing breaker. (a,b,c) The wave becomes gradually smaller as $\alpha(x) \to 0$. There is no real increase of amplitude during the shoaling process. When the wave passes $x \simeq 250$ cm, instability appears as a small kink on the rear edge of the wave (c), and near $x \simeq 280$ cm (where $h_1 \simeq h_2$) the wave loses its identity as a soliton (d). In the end, when $\alpha(x)$ becomes positive, the solitary wave shape is destroyed and a dispersive tail of positive polarity is generated. Indeed, the solitary wave cannot make any transition from negative to positive polarity when $\alpha_1(x) < 0$.

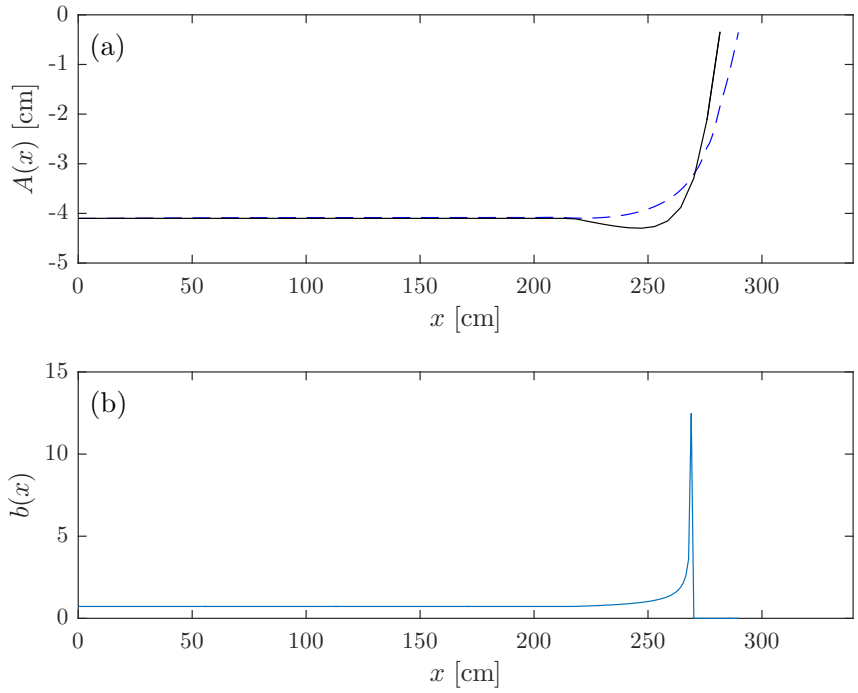

Figure 4.11. (a) Comparison between theoretical (solid black line) and numerical prediction (dashed blue line) of veKdV soliton amplitude. In this case, we used the expression (3.49) as theoretical prediction. (b) The theoretical prediction is affected by the rapid increase of the coefficient $b(x)$.

We can compare the results of the veKdV simulation with the explicit analytic solution (3.49). As already described in Sec. 3.3, we must have $\sqrt{b(x)} < 1$ to get a reasonable approximation of the amplitude evolution. In this case, the condition is not fulfilled exactly near the turning point, where the coefficients $\alpha(x)$ and $\alpha_1(x)$ grow rapidly.

We observe that the process described by the vKdV–veKdV simulations that leads to the wave disintegration is very different from that observed in the real experiments. Comparisons between experiments and numerical simulations of vKdV and veKdV are reported by several authors with good agreement (see, in particular, Helfrich and Melville [1986]). KdV–type equations are derived from Euler equations, and they represent a good approximation to capture some relevant features, as solitary or cnoidal waves formation. However, KdV models cannot describe overtuning and breaking phenomena as they occur in laboratory or in numerical simulations of Euler or Navier–Stokes equations. Thus, the use of KdV–type equations to model wave evolution to breaking is limited, and in recent years a number of fully nonlinear numerical studies of the propagation of internal solitary waves over shoaling topography have been undertaken (see Aghsaee *et al.* [2010]; Arthur and Fringer [2014]; Vlasenko and Hutter [2002]). In the next section we will develop an analytical breaking model so as to partially fill this gap.

4.3 Wave–breaking description

In experiments with plunging, collapsing and, in particular, plunging–collapsing breakers, the solitary wave evolves so that, near the breaking point, the interface between the two fluids is nearly vertical, where it intersects the slope at its point of maximum descent (see Fig.4.1) [Sutherland *et al.*, 2013]. In particular, the wave assumes a right–angled triangular shape in the rightmost corner of the tank, thus the area (volume per width) of the fluid below the initial depth of the interface is

$$A_{\rm tr} \simeq \frac{H_b L_b}{2} = \frac{H_b^2}{2s} \tag{4.2}$$

where s is the slope, $L_b = x_0 - x_b$ is the distance between x_b and the point x_0, i.e. where the slope intersects the unperturbed interface, and H_b is the maximum displacement of the interface (Fig.4.1).
By imposing that the fluid mass, transported by the initial soliton, is approximately the mass that is cointained in the pre–breaking "trianglized" soliton (Fig.4.1), we can equate (4.2) to the area of the soliton at $t = 0$. Hence, we obtain an analytical estimation of the area enclosed by the soliton through eKdV theory:

$$A_{\rm eKdV} = \int_{-\infty}^{+\infty} \frac{A}{b + (1-b)\cosh^2(\gamma x)}\, dx \tag{4.3}$$

By multiplying and dividing the integrand by $\mathrm{sech}^2(\gamma x)$ and remembering that $\mathrm{sech}^2(\gamma x) = 1 - \tanh^2(\gamma x)$, we get

$$A_{\rm eKdV} = 2A \int_0^{+\infty} \frac{\mathrm{sech}^2(\gamma x)}{1 - b\tanh^2(\gamma x)}\, dx\,,$$

which can be integrated via the substitution $t = \tanh(\gamma x)$:

$$A_{\rm eKdV} = \frac{2A}{\gamma}\int_0^1 \frac{dt}{1-bt^2} = \frac{A}{\sqrt{b}\gamma}\log\left(\frac{1+\sqrt{b}t}{1-\sqrt{b}t}\right)\Bigg|_0^1 = \frac{2A\,\tanh^{-1}(\sqrt{b})}{\sqrt{b}\gamma}\,, \tag{4.4}$$

where we used the identity

$$\tanh^{-1}(\sqrt{b}) = \frac{1}{2}\log\left(\frac{1+\sqrt{b}}{1-\sqrt{b}}\right)\,,$$

valid for $|\sqrt{b}| < 1$. By equating (4.2) to (4.4), i.e., $A_{\rm tr} = A_{\rm eKdV}$, we obtain

$$\frac{H_b^2}{2s} = \frac{2A\,\tanh^{-1}(\sqrt{b})}{\sqrt{b}\gamma} \quad \Rightarrow \quad H_{b\rm eKdV} = \sqrt{\frac{4As\,\tanh^{-1}(\sqrt{b})}{\sqrt{b}\gamma}}\,. \tag{4.5}$$

From (4.5) we can derive an expression for the breaking point x_b, evaluated with respect to the toe of slope x_s (i.e., the intersection point between the slope and the horizontal bottom):

$$x_0 - x_b = \frac{H_b}{s} \quad \Rightarrow \quad x_{b\rm eKdV} = x_0 - \frac{H_b}{s} = \frac{h_2}{s} - \sqrt{\frac{4A\,\tanh^{-1}(\sqrt{b})}{s\sqrt{b}\gamma}}\,,$$

where h_2 is the height of the intersection between the slope and the unperturbed interface. If we set the origin of the system in O as in Fig.4.1, we have

$$L_{\text{slope}} = \frac{H_{\text{slope}}}{s}\,,$$

and it is possible to derive x_s as

$$x_s = L_{\text{d}} - L_{\text{slope}} = L_{\text{d}} - \frac{H_{\text{slope}}}{s}\,,$$

where L_{slope} and H_{slope} are respectively the length of the projection of the slope on the x–axis and on the z–axis, and L_{d} is the horizontal extent of ambient fluid region (Fig.4.1). Thus, if we want to evaluate x_b with respect to O, we have to rewrite the breaking point as

$$\widetilde{x_b}_{\text{eKdV}} = x_s + x_{b\text{eKdV}} = x_s + \frac{h_2}{s} - \sqrt{\frac{4A\,\tanh^{-1}(\sqrt{b})}{s\sqrt{b}\gamma}} \tag{4.6}$$

An equivalent estimation can be performed through MCC theory. In fact, once obtained the wave profile $\zeta = \zeta(X)$, we can integrate numerically ζ over a large interval ($\zeta \to 0$ for $X \to \pm\infty$) to get the area enclosed by the soliton, and we can set

$$A_{\text{MCC}} \simeq \frac{H_b^2}{2s}$$

and, proceeding as before, we get

$$H_{b\text{MCC}} = \sqrt{2A_{\text{MCC}}\,s}\,, \quad x_{b\text{MCC}} = \frac{h_2}{s} - \sqrt{\frac{2A_{\text{MCC}}}{s}}\,. \tag{4.7}$$

It is also possible to evaluate the theoretical value for the Iribarren number writing the wavelength λ as

$$\lambda = \frac{S}{A} \quad \Rightarrow \quad \text{Ir} = \frac{s}{\sqrt{A/\lambda}}\,, \tag{4.8}$$

where the wave surface S can be set equal to A_{eKdV} or A_{MCC}, i.e., equation (4.4) and the numerical result from the MCC profile integration, respectively.

4.4 Experimental results and validation of the wave–breaking model

We here compare experimental and theoretical wave profiles during propagation phase in the cases of (a) plunging, (b) collapsing and (c) plunging–collapsing breakers (Fig.4.12). Experimental parameters are reported in Table 4.1. The KdV model, as we expected, does not fit well the experimental data, since the ISWs generated in the tank are strongly nonlinear (see dashed blue line in Fig.4.12a-c). In the case of plunging breakers, in particular, the amplitude of the experimental wave profile exceeds the maximum amplitude admitted for eKdV waves. For cases (b) and (c)

the eKdV profile fits well the experimental ones, although the latter profile appears slightly broader (see yellow dot–dashed lines in Fig.4.12b-c). The MCC strongly nonlinear model provides the best agreement with the experimental waves in all cases (see red lines in Fig.4.12a-c).

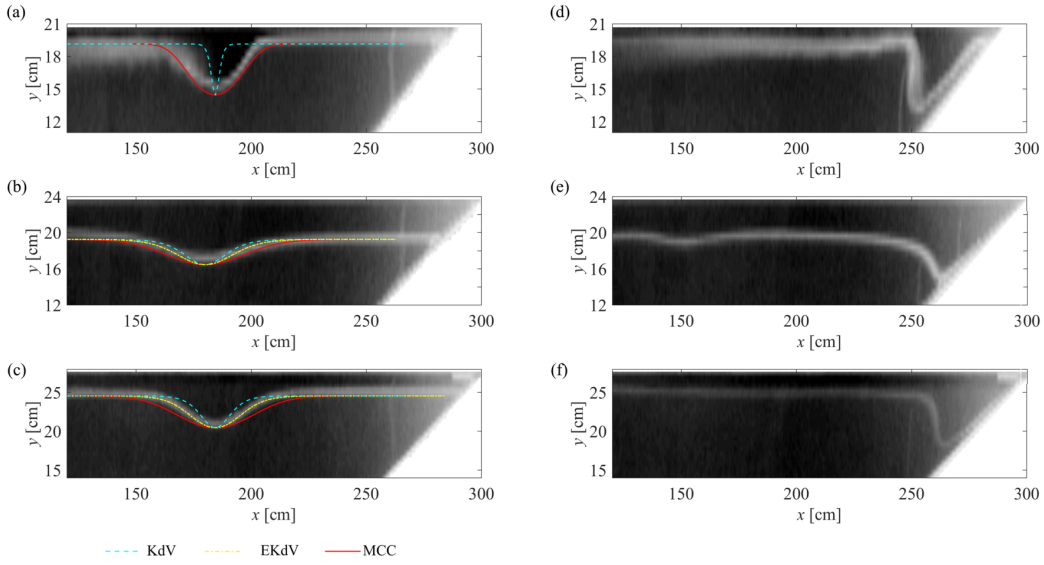

Figure 4.12. Comparison between experimental and theorical wave profiles for (a) plunging breaker, (b) collapsing breaker, (c) plunging–collapsing breaker during free propagation phase. In (d)-(e)-(f) experimental profiles corresponding respectively to cases (a)-(b)-(c) at verticalization instant.

Table 4.1. Experimental parameters and comparison between experimental and theoretical values for $\widetilde{x_b}$, in the case of (a) plunging, (b) collapsing, (c) plunging–collapsing. h_1, h_2, layer thicknesses; $\Delta\rho = \rho_2 - \rho_1$, density difference; A, wave amplitude; λ, wave length; s, topographic slope; Ir, Iribarren number; x_s, toe of slope abscissa; $\widetilde{x_{b\mathrm{exp}}}$, experimental breaking location; $\widetilde{x_{b\mathrm{eKdV}}}$, $\widetilde{x_{b\mathrm{MCC}}}$, theoretical breaking locations from eKdV and MCC theory respectively.

Case	h_1 (cm)	h_2 (cm)	$\Delta\rho$ (g/cm^3)	A (cm)	λ (cm)	s	Ir	x_s (cm)	$\widetilde{x_{b\mathrm{exp}}}$ (cm)	$\widetilde{x_{b\mathrm{eKdV}}}$ (cm)	$\widetilde{x_{b\mathrm{MCC}}}$ (cm)
(a)	0.96	20.40	0.0276	4.7	20.02	0.296	0.61	216.8	249.7	–	256.5
(b)	3.50	20.50	0.0317	2.13	33.03	0.296	1.16	216.2	258.6	263.5	260.4
(c)	2.83	25.17	0.0332	4.1	35.23	0.341	1.00	217.1	260.4	265.5	259.5

Experimental waves are observed to shoal over sloping boundary, leading to the trailing edge steepening. By image analysis we obtain the maximum breaking

depth H_b and the breaking point x_b associated to the trailing edge verticalization (see Fig.4.12d-f). We then apply the model described in Section 4.3 to derive the theoretical values for the breaking location. We report the comparison between the experimental and the theoretically predicted values for $\widetilde{x}_b$ in Table 4.1. The good agreement between the experiments and our theoretical model (Fig.4.12 and Table 4.1) suggests that the adopted geometrical approximations, based on the mass conservation and the observed shoaling evolution, is suitable for predicting breaking location for a given ISW, once the topographic features are known.
Laboratory experiments by Helfrich and Melville [1986] and Helfrich [1992] showed that wave breaking occurs when normalised maximal wave height $a_m/(H_b - H_m)$ exceeds 0.4 and does not depends on the bottom slope, i.e.

$$\frac{a_m}{H_b - H_m} \geq 0.4\,. \tag{4.9}$$

where a_m is the maximum displacement at the centre of wave, H_b is the water depth at point of wave breaking and H_m is the depth of an undisturbed position of the interface line [Massel, 2016].

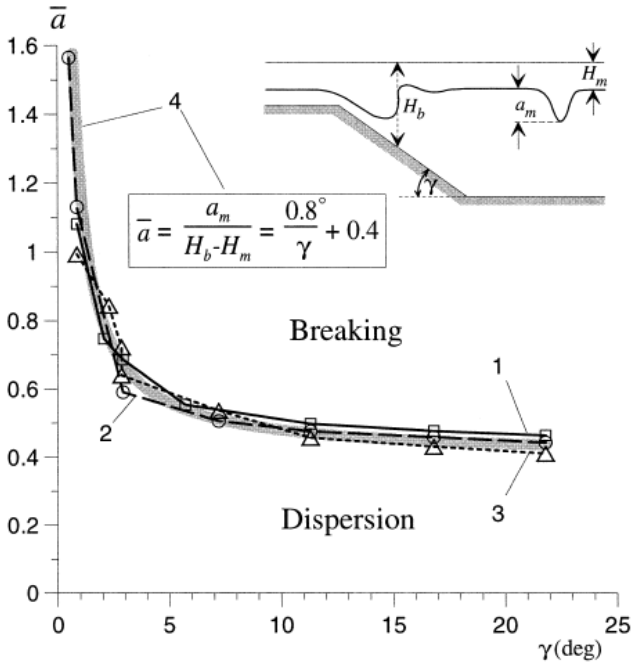

Figure 4.13. Breaking events obtained by Vlasenko and Hutter [2002]. Numbers of curves 1-3 correspond to numerical experiments for different density profiles. The thick shaded line 4 is the best fit for the lines 1-3. It separates the fields of parameters for which internal wave breaking takes place (above the curve), or the wave passes onto the shelf as a dispersive wave train (below the curve). The sketch above explains the parameter used for the breaking criterion.

Observations of Lien *et al.* [2014] on the Dougsha slope (about 0.48) in the northern South China Sea confirmed that convective breaking of the solitary internal waves, with negative displacement, occurs at $a_m/(H_b - H_m) \geq 0.4$, in agreement with the

Table 4.2. Comparisons between our eKdV (4.5) and MCC (4.7) criteria, and the breaking criteria of Helfrich and Vlasenko–Hutter. For a correct comparison, we have defined $\widetilde{H}_b = h_1 + H_b$ for the eKdV and MCC cases.

Case	γ	$\widetilde{H}_{b\text{exp}}$ (cm)	$\widetilde{H}_{b\text{eKdV}}$ (cm)	$\widetilde{H}_{b\text{MCC}}$ (cm)	$H_{b\text{Helfrich}}$ (cm)	$H_{b\text{VH}}$ (cm)
(a)	16.5°	8.56	-	9.60	12.71	11.44
(b)	16.5°	9.40	9.06	10.92	8.82	8.25
(c)	18.8°	10.29	11.64	13.53	13.08	12.09

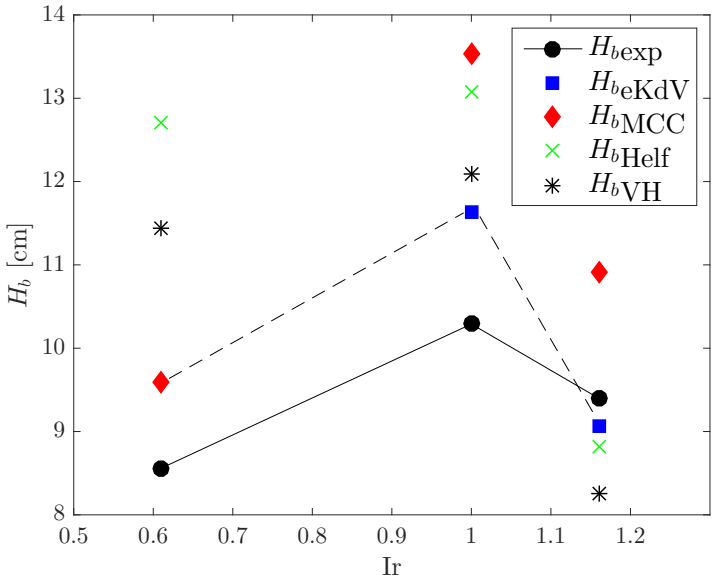

Figure 4.14. Comparison between our analytical prediction of the breaking depths and the criteria of Helfrich (4.9) and Vlasenko–Hutter (4.10) with respect to experimental data. The analytical model (dashed line) seems to reproduce the experimental values for H_b (–•–) better than the previous criteria (at least for this range of values of the Iribarren number) using eKdV predictions for collapsing and plunging–collapsing breakers (blue squares), and MCC model (red diamonds) for plunging breakers.

Helfrich's laboratory results.

Numerical calculations by Vlasenko and Hutter [2002] showed that the kinematic instability is responsible for mechanism of strong wave breaking rather than a shearing instability. They considered a two-layer system with a vertical fluid stratification. Amplitudes of waves and the bottom parameters were chosen to be close to those observed in the Andaman and Sulu Seas. A proposed breaking criterion for the internal solitary waves (see Fig.4.13) for sea bottom slope in the range $0.52° < \gamma <$

21.88° is:

$$\frac{a_m}{H_b - H_m} \geq \frac{0.8^\circ}{\gamma} + 0.4\,. \tag{4.10}$$

If the water depth on the shelf is less than H_b , a solitary wave breaks before it and penetrates into the shallow water zone, otherwise it passes into the shelf without breaking.
In Tab. 4.2 and Fig. 4.14, we propose a comparison between our analytical breaking model and the breaking criteria of Helfrich and Vlasenko–Hutter using our experimental data. We observe that our analytical model can predict the breaking depths better than the previous criteria if we consider eKdV predictions for collapsing and plunging–collapsing breakers, and MCC model for plunging breakers.

4.5 ISWs in the Messina Strait

In this section, we give a description of the physical features of the ISWs generated in the Messina Strait by tidal forces.
The Strait of Messina is a narrow channel separating Sicily from the Italian peninsula and connecting the Tyrrhenian Sea in the north and the Ionian Sea in the south (Fig.4.15). The center of the Strait is about 80 m; the sea bottom slopes gradually down approximately 1300 m toward the Ionian Sea while the bathymetry on the northern side slopes down 300-600 m in the Tyrrhenian Sea (i.e., in the Gioia Basin, Fig.4.15), remaining almost flat before the Capo Vaticano frontal slope [Alpers and Salusti, 1983; Longhitano, 2018].
The Strait constitutes a submarine barrier for the water flowing through the channel. In particular, it represents an amphidromic point for the semi-diurnal tides of the two adjacent sub-basins [Alpers and Salusti, 1983; Brandt *et al.*, 1999; Sapia and Salusti, 1987]. During the southward tidal flow the Tyrrhenian Surface Water (TSW) spills into the Ionian Sea; vice versa during the northward tidal flow the denser Intermediate Levantine Water (LIW) overflowing the sill, spreads under the lighter TSW (see Fig.4.16a). The phase opposition of these tides generates very strong tidal currents (up to 3 m/s) at the sill region [Longhitano, 2018; Vercelli, 1925].
These tidal effects along with the presence of the two different water masses give rise to nonlinear internal solitary waves (ISWs) of depression at the interface between LIW and TSW (see Fig.4.16b). These solitons propagate at about 1 m/s [Alpers *et al.*, 2008] from the Strait towards the northern and the southern mouth of the Strait alternately (approximately with a 6 hours period). ISWs off the Strait were frequently observed by using both in situ [Brandt *et al.*, 1999; Sapia and Salusti, 1987] and remote sensing measurements [Alpers and Salusti, 1983; Artale *et al.*, 1990]. Sea surface manifestations of internal waves can be detected, indeed, from Synthetic Aperture Radar (SAR) images [Alpers, 1985]: they appear as brighter and darker alternate strips on the image whether the surface waves associated to ISWs propagate in convergent or divergent surface flow zones.
Propagating northward, nonlinear internal waves are supposed to break when approaching Capo Vaticano frontal slope. Although never observerd directly, this is revealed by indirect observations [Marullo and Santoleri, 1986]: *i*) the presence of a

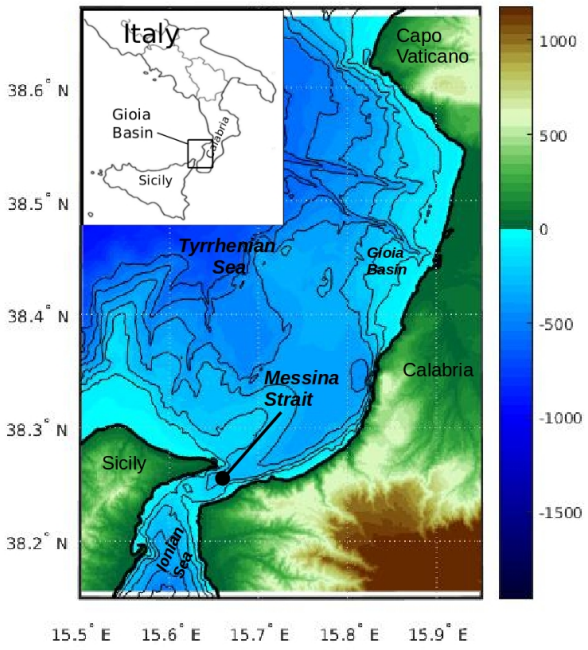

Figure 4.15. Map of the Gioia Basin (area of Italy indicated in the insert). The Messina Strait is the narrow channel separating Sicily from the Italian peninsula and connecting the Tyrrhenian Sea in the north and the Ionian Sea in the south. At the northernmost point we find the Capo Vaticano promontory.

thermal front of colder water on the sea surface due to mixing processes induced by breaking; *ii*) SAR images show a dark grey area widespread 10 km southward Capo Vaticano, associated to the presence of biofilms likely produced by plankton that mark deep water spun up by mixing; *iii*) the presence of warm and salty water (T $\sim$ 14°C; S $\sim$ 37.8–38.6) in this zone, that indicates mixing between LIW and TSW.

Laboratory experiments described in section 4.1 validate our wave–breaking model in the case of plunging, collapsing and plunging–collapsing breakers. However, to apply our results to the case of the Messina Strait, we have to know first how far the ISWs generated at the Messina Strait sill can travel retaining their solitary wave structure and if, consequentely, they will break at the Capo Vaticano frontal slope. For this reason, in the next section, we will perform numerical simulations of the veKdV equation over the bathymetry all along the Gioia Basin, so to understand the possible wave evolution during the propagation and the shoaling phases before breaking.

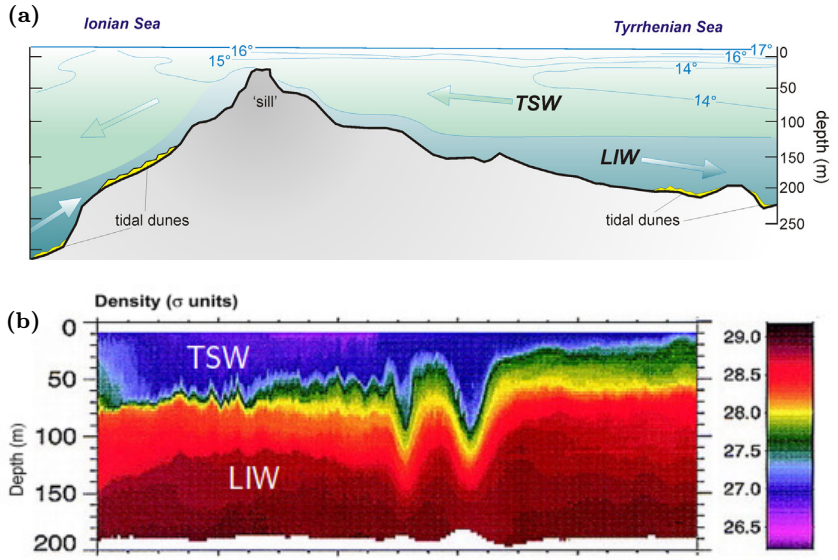

Figure 4.16. (a) Conceptual representation of the water masses superimposition and inversion between TSW and LIW. The sill in the Messina Strait constitutes a submarine barrier for the water flowing through the channel. During the southward tidal flow the Tyrrhenian Surface Water (TSW) spills into the Ionian Sea; vice versa during the northward tidal flow the denser Intermediate Levantine Water (LIW) overflowing the sill, spreads under the lighter TSW. From Longhitano [2018]. (b) Density distribution measured by Brandt *et al.* [1999] with a CTD chain north of the Messina Strait, showing the propagation of a large amplitude ISW at the interface between TSW and LIW.

4.6 Numerical simulations and analytic description of ISWs in the Gioia Basin

We now study numerically and analitically the evolution of ISWs all along the Gioia Basin, focusing on a representative bathymetry which connects the Messina Strait to Capo Vaticano. As seen in section 3.2, oceanic shelves may contain wave paths along which the parameters do not vary sufficiently slowly, and they may also include several critical points. In this case an internal solitary wave transforms with loss of its identity as a soliton, and so we may say the soliton–like wave has a finite lifetime. Thus, to consider nonadiabatic effects of wave transformation, and to estimate the soliton life–time, we solve numerically the veKdV equation using the finite–difference scheme (3.50) with periodic boundary condition, an eKdV typical solitary wave as initial condition, and with coefficients calculated for a two–layer system. The two–layer system represents a good approximation when the pycnocline is sharp with respect to the total depth. When the pycnocline is rather broad or we want to consider experimental data for the oceanic stratification, it is possible to use general formulas for the coefficients of the veKdV equation (see [Grimshaw *et al.*, 2004]).

We consider the bathymetry reported in Fig. 4.17, which extends from the Messina Strait to Capo Vaticano. The main features of the bathymetry are indicated: the highest seamound ($x \simeq 2 \div 10$ km), two canyons and the Capo Vaticano frontal slope. As we will see in the following, these are the most important sections of the

bathymetry for the wave transformation.

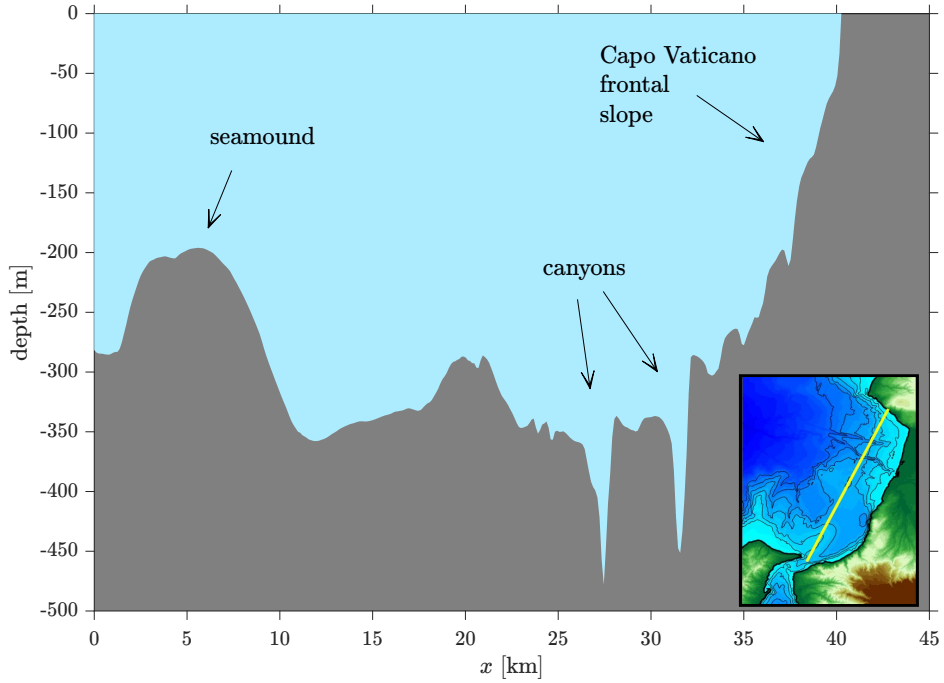

Figure 4.17. Bathymetry considered for numerical simulations of veKdV equation. It extends from the Messina Strait to Capo Vaticano (see yellow line in the insert). Main features of the bathymetry are indicated: the highest seamound ($x \simeq 2 \div 10$ km), the two canyons and the Capo Vaticano frontal slope.

Table 4.3. Limiting amplitude values for eKdV waves, $\eta_{\max} = -\alpha/\alpha_1$, calculated at the first point of the bathymetry, $x = 0$ (where $h_2 \simeq 300$ m).

h_1 (m)	$\eta_{\lim}$ (m)
10	-31.52
30	-61.10
50	-66.95
70	-60.54

We choose the upper layer density and the lower layer densities equal to $\rho_1 = 1026$ kg/m^3, $\rho_2 = 1029$ kg/m^3, respectively, i.e. similar to the mean densities found in the Gioia Basin ([La Forgia *et al.*, 2018a]). We consider as the only variable oceanic parameter the depth of the lower layer $h_2(x)$, while we keep the depth of the upper layer h_1 constant. For $h_1 = 10, 30, 70$ m fixed, we perform runs at different amplitudes, $A = -10, -30, -50$ m. In the case $h_1 = 10$ m, we perform only the simulation at $A = -10$ m, since the limiting amplitude value is $\eta_{\lim} \simeq -31$ m (see Table 4.3).

To get an idea of the adiabaticity of the wave–evolution, the behavior of the coefficients of the veKdV equation must be examined, with particular attention to the nonlinear coefficients α and α_1.
In Fig. 4.18 an example of evolution of the coefficients (3.59) of the veKdV equation (3.58) along the bathymetry is shown. As we can see, at the beginning the nonlinear coefficients $\widetilde{\alpha}(x)$ and $\widetilde{\alpha}_1(x)$ are negative, and change their sign only near the Capo Vaticano slope ($x \sim 35 \div 40$ km), where $h_2(x) \to h_1$. We observe that the quadratic nonlinear coefficient $\widetilde{\alpha}$ is initially greater than $\widetilde{\alpha}_1$, hence the cubic nonlinearity is, at this stage, irrelevant. The cubic nonlinear term becomes gradually important near the frontal slope, where it grows more rapidly than $\widetilde{\alpha}$, becoming more and more negative, and governing the nonlinear dynamics until breaking. On the contrary, $\widetilde{\alpha}$ becomes large but positive. As explained in 3.2, if $\widetilde{\alpha}$ passes through zero, but $\widetilde{\alpha}_1 < 0$, the solitary wave is destroyed (no connecting arrows between solitary waves of quadrants III and IV of Fig. 3.2). Secondary solitary waves of the opposite polarity can appear from the tail of the primary soliton, but the primary soliton itself disappears.

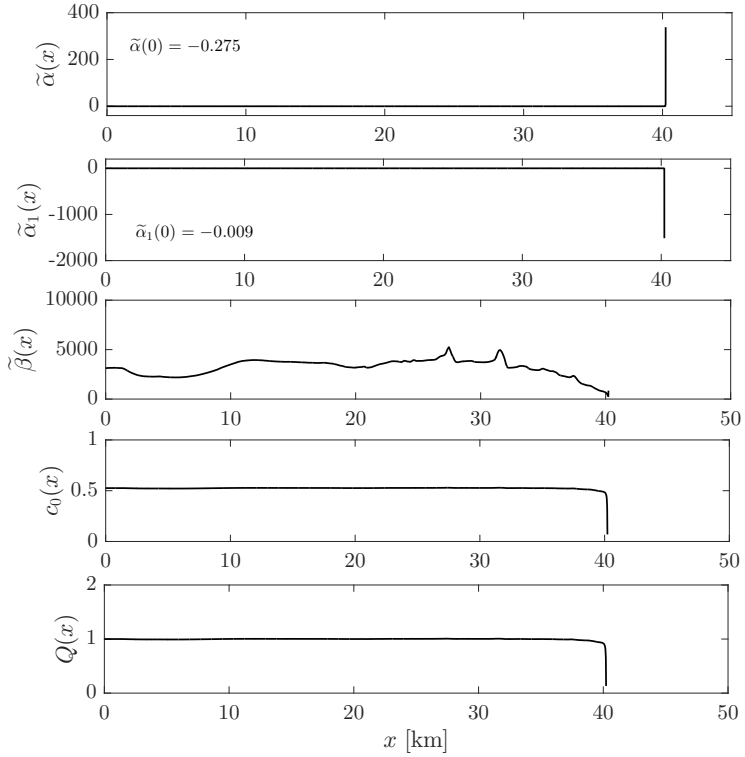

Figure 4.18. Evolution of the coefficients (3.59) of the veKdV equation (3.58) (case $h_1 = 10$ m , $A = -10$ m). $\widetilde{\alpha}(x)$ and $\widetilde{\alpha}_1(x)$ change their sign only near the Capo Vaticano frontal slope ($x \sim 35 \div 40$ km), where $h_2(x) \to h_1$. The cubic nonlinear term becomes more and more negative, governing the nonlinear dynamics until breaking. On the contrary, $\widetilde{\alpha}$ becomes large but positive. This configuration leads to solitary wave destruction.

We can examine the adiabaticity of the transformations in detail using several methodologies. Probably, the best one is simply to compare the simulations with the veKdV adiabatic theory (as done below). However, other criteria can help us to

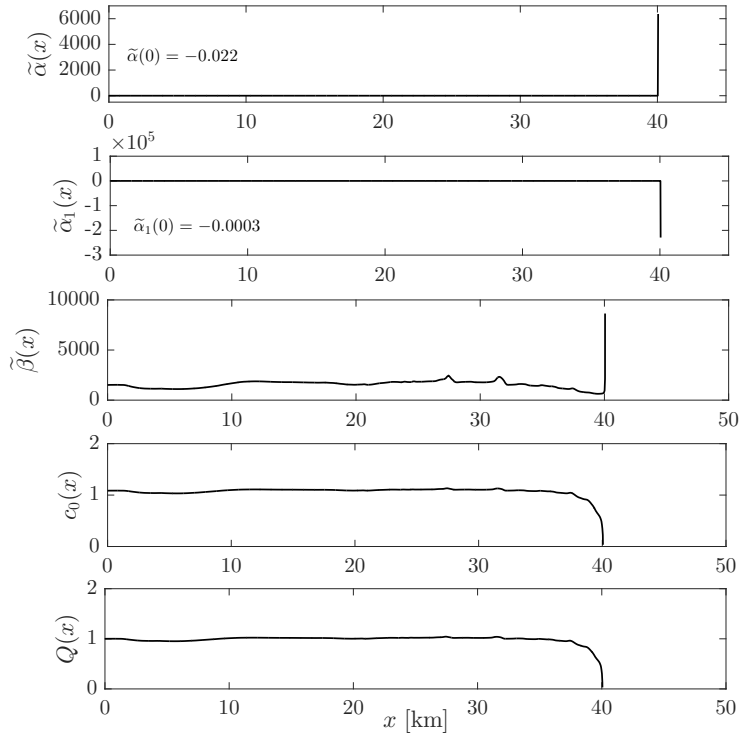

Figure 4.19. Evolution of the coefficients (3.59) of the veKdV equation (3.58) (case $h_1 = 50$ m, $A = -50$ m).

understand what are the nonadiabatic factors during the wave evolution. A criterion has been presented in section 3.2, and it consists in the comparison of the ratio of the shoaling term and the nonlinear terms of veKdV equation with the ratio of the amplitude and halfwidth scales:

$$\left|\frac{\nu(x)}{\alpha(x)}\right| \ll \left|\frac{\eta_0}{l}\right|, \quad \left|\frac{\nu(x)}{\alpha_1(x)}\right| \ll \left|\frac{\eta_0^2}{l}\right|. \tag{4.11}$$

We compare values of $\nu(x)/\alpha(x)$ and $\nu(x)/\alpha_1(x)$ for some h_1 and A along all the slope with the relative scales (Fig. 4.20). These two ratios exceed the reference scale values along the first (highest) seamound, the canyons and the frontal slope, which then represent the main features of the bathymetry affecting the wave evolution. In some cases, the values along the seamound are lower than the reference scales values (see, for example, Fig. 4.20(a)-(b)), and the evolution in these area results, in fact, to be quite regular. Clearly, in the cases with large amplitudes (30-50 m), the transformation along these bathymetric sections generate a strong growth of the rear tail and solitary wave fission (see Fig. 4.34 and Fig. 4.37).

A second procedure to evaluate the adiabaticity of the wave transformation is suggested by Small [2001a] and it consists in estimating the parameter

$$R = \left|\frac{A}{Ls}\right|, \tag{4.12}$$

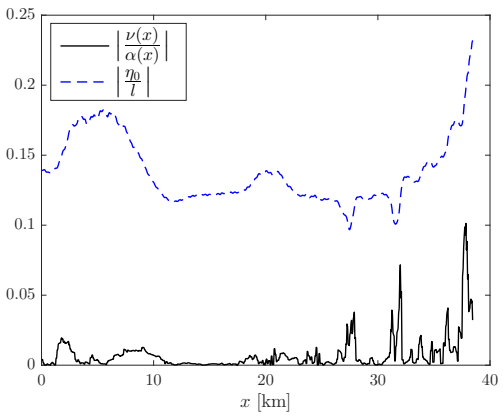

(a) $h_1 = 10$ m, $A = -10$ m

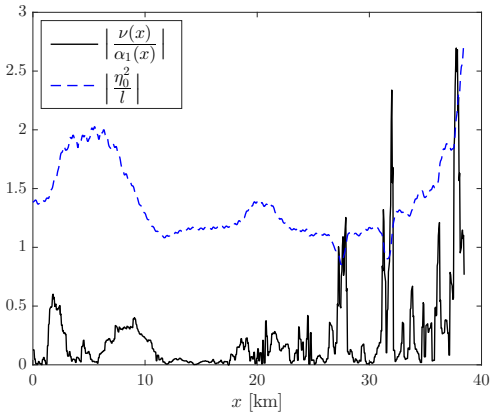

(b) $h_1 = 10$ m, $A = -10$ m

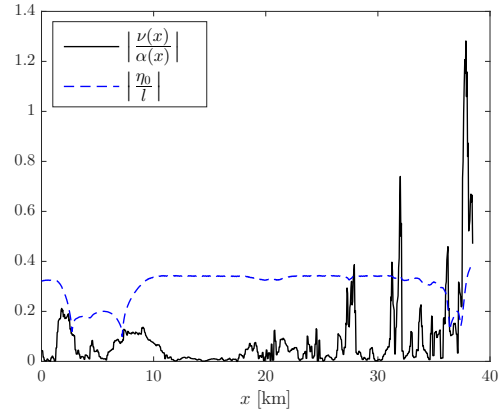

(c) $h_1 = 30$ m, $A = -50$ m

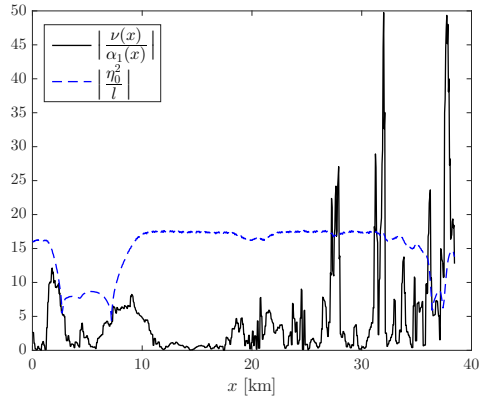

(d) $h_1 = 30$ m, $A = -50$ m

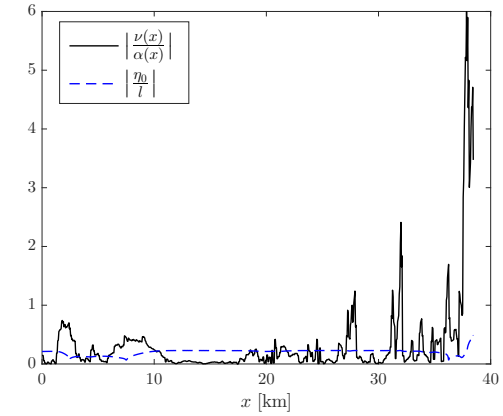

(e) $h_1 = 50$ m, $A = -50$ m

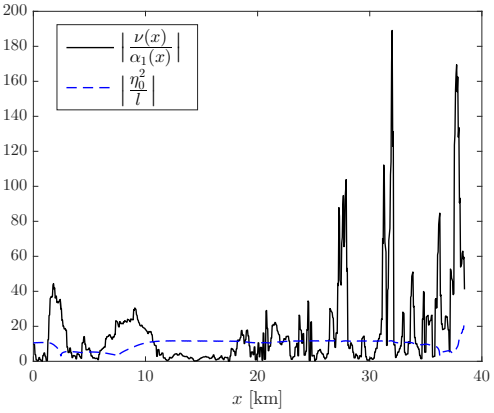

(f) $h_1 = 50$ m, $A = -50$ m

Figure 4.20. Some comparisons between nonlinear coefficients and shoaling coefficient, with reference to (4.11). When the ratio $|\nu(x)/\alpha(x)|$ or $|\nu(x)/\alpha_1(x)|$ (black solid lines) exceed their respective adiabaticity scales $|\eta_0/l|$ or $|\eta_0^2/l|$ (blue dashed lines), the adiabaticity is broken.

where L is the halfwidth, A/L is the wave steepness, and s is the bathymetric slope. In general, if $R > 1$ the adiabatic approximation holds, while for $R < 1$ the evolution results to be not adiabatic. This means that when the wave is steeper than the slope, the wave will be not particulary affected by the interaction with the bathymetry, while a steep slope can induce a fast transformation of the wave, also leading in some cases to its destruction or fission. It is possible to consider some sections of the bathymetry and evaluate the parameter r. In particular, we can select the intervals reported in Tab 4.4.

Table 4.4. Bathymetry sections for adiabaticity evaluation along the Gioia Basin. x_1 and x_2 are the abscissae of each section boundaries, and z_1 and z_2 their respective depths. s is the value of the slopes (roughly) calculated as $s = |z_2 - z_1|/|x_2 - x_1|$. Sections 1 and 2 are located along the first seamound. Sections 3 and 4 along the first canyon, while sections 5 and 6 along the second canyon. Section 7 corresponds (roughly) to the Capo Vaticano frontal slope zone.

section	x_1 (m)	z_1 (m)	x_2 (m)	z_2 (m)	s
1	1292	-282.3	2836	-210.6	0.046
2	6696	-205	10780	-345.3	0.034
3	26310	-360.6	27640	-476.2	0.087
4	27640	-476.2	28020	-339.8	0.359
5	31010	-353.4	31510	-449.3	0.19
6	31510	-449.3	32169	-287.5	0.249
7	35000	-277	40200	-17.63	0.05

We estimate the wavelength as [Michallet and Barthélemy, 1998]:

$$\lambda = \frac{\int_{-\infty}^{+\infty} \eta(x)\, dx}{A}\,, \tag{4.13}$$

and the halfwidth as $L = \lambda/2$. Thus for every h_1 and A we have different values of L along x (e.g., see Fig. 4.21). We can study the behavior of R along x in the different sections characterized by different values of s . For example, considering the case $h_1 = 10$, $A = -10$, since section 1 has slope $s_1 = 0.046$, we can look at zone 1 (i.e., in the interval $x \in [1292 : 2836]$, $z \in [-282.3 : -210.6]$) in Fig. 4.22a, and determine if $R > 1$ or $R < 1$. For all of the seven cases, we obtain that for small and large amplitudes, shallow and deep pycnoclines, the most critical cases are s_4, s_5, s_6, i.e. near the two canyons, for which $R < 1$ (see Fig. 4.22 and Fig. 4.23) and then we expect a nonadiabatic behavior in the respective intervals defined in Tab. 4.4. We observe that the quantity R is conceptually similar to the Iribarren number, thus one could think to use the Iribarren number also as an indicator of the adiabaticity of the wave evolution.

Another way to evaluate the adiabaticity is to compare the wavelength to the length scale of the variable environment (L_s) [Grimshaw *et al.*, 2004], i.e. we should verify that $\lambda \ll L_s$. This is not a stringent criterion, but it can give a first indication on the

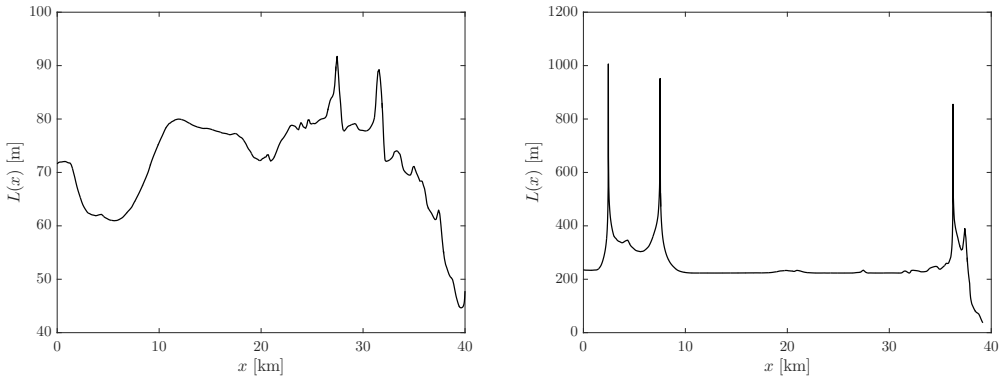

(a) **(b)**

Figure 4.21. Evolution of the halfwidth $L = \lambda/2$ (see (4.13)) along the bathymetry for (a)$h_1 = 10$ m, $A = -10$ m, (b) $h_1 = 30$ m, $A = -50$ m.

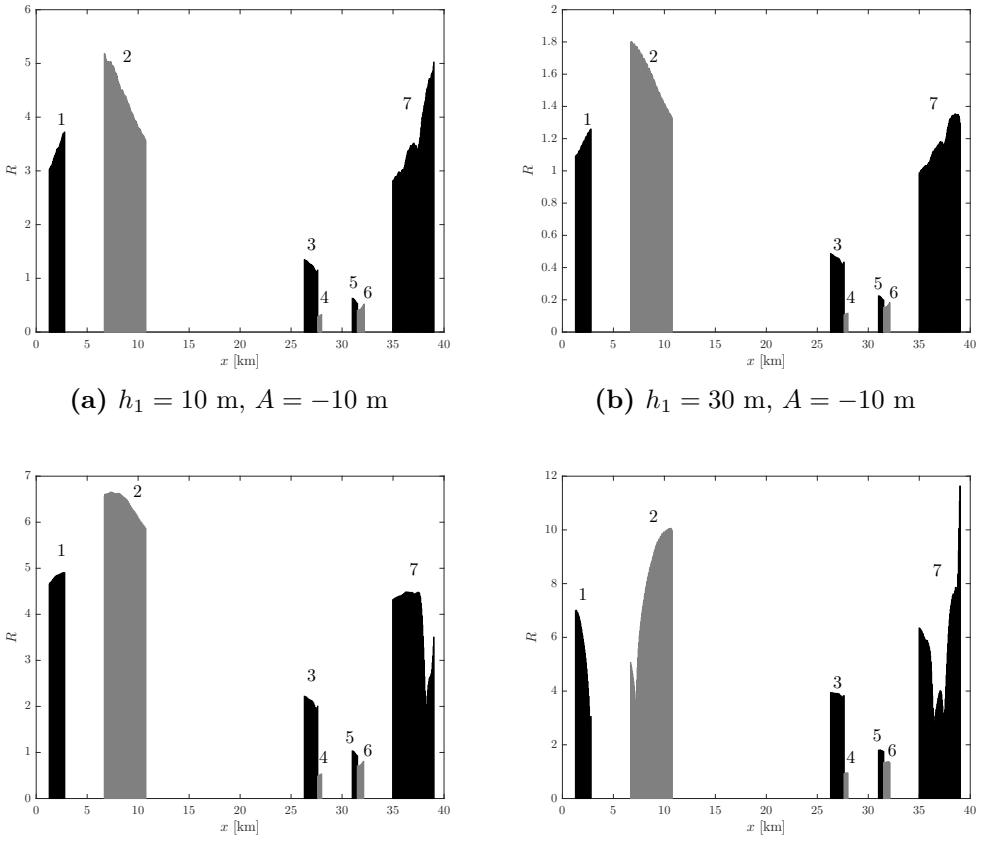

(a) $h_1 = 10$ m, $A = -10$ m **(b)** $h_1 = 30$ m, $A = -10$ m

(c) $h_1 = 30$ m, $A = -30$ m **(d)** $h_1 = 30$ m, $A = -50$ m

Figure 4.22. Ratio R in the different sections, characterized by different values of s: if $R > 1 (< 1)$ (see (4.12)) the evolution is adiabatic (nonadiabatic).

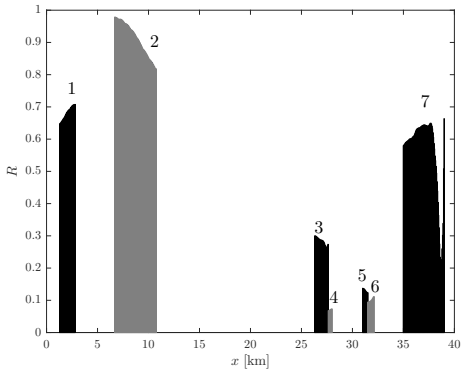

(a) $h_1 = 50$ m, $A = -10$ m

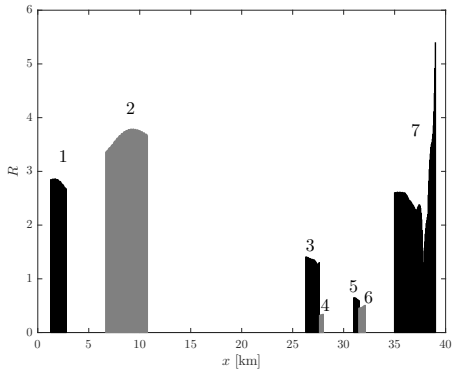

(b) $h_1 = 50$ m, $A = -30$ m

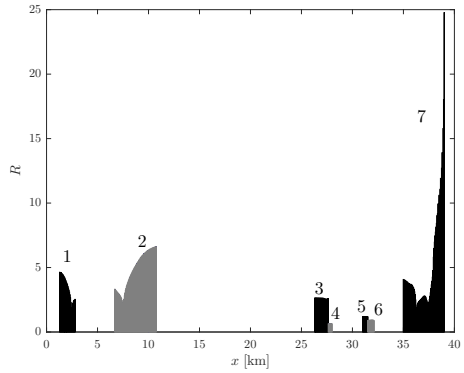

(c) $h_1 = 50$ m, $A = -50$ m

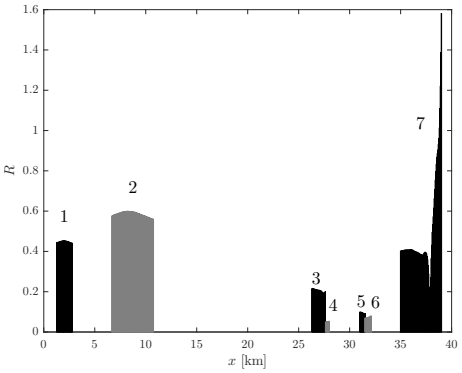

(d) $h_1 = 70$ m, $A = -10$ m

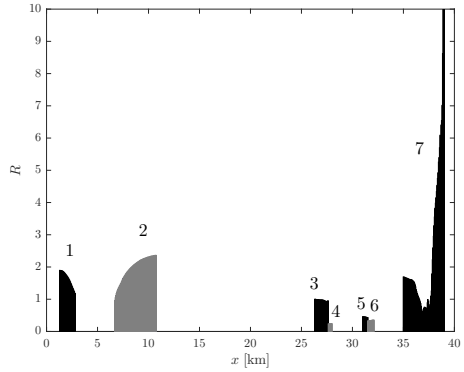

(e) $h_1 = 70$ m, $A = -30$ m

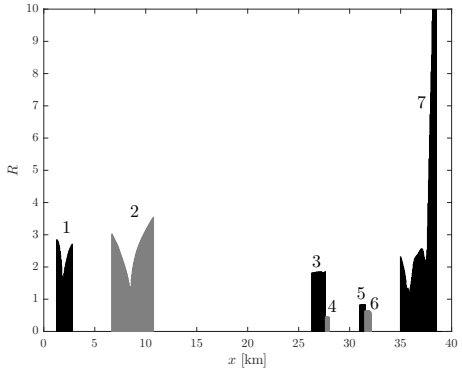

(f) $h_1 = 70$ m, $A = -50$ m

Figure 4.23. Ratio R in the different sections, characterized by different values of s: if $R > 1 (< 1)$ (see (4.12)), the evolution is adiabatic (nonadiabatic).

adiabaticity of the transformation. Considering the differences $|x_2 - x_1|$ of the values in Tab. 4.4 we have an approximate estimation of the length scale of variability of the relevant features of the bathymetry. If we consider, for example, $h_1 = 10$ m and $A = -10$ m, at $x = 1292$ m, we have $\lambda \simeq 143$ m. Thus, considering the first

section (left side of the highest seamound), we have $\lambda/L_s \simeq 0.1$, and the wave can be supposed to vary slowly. We choose as threshold value for adiabaticity $\lambda/L_s = 1/10$ (at least one order of magnitude between λ and L_s), and proceeding as before for the different sections, we can observe that the nonadiabatic areas ($\lambda/L_s > 0.1$) are sections 4, 5 and 6 (Fig. 4.24a) for shallow pycnoclines and small wave amplitudes. For large amplitudes and deep pycnoclines all sections except section 7 result to be nonadiabatic zones (Fig. 4.25c or Fig. 4.25f). For shallow pycnoclines and large amplitudes (Fig. 4.24d), in sections 2 and 7 adiabatic transformations are predicted. For deep pycnoclines and small amplitudes (Fig. 4.25a or Fig. 4.25d), only in section 7 we can have adiabaticity (and maybe in section 2).

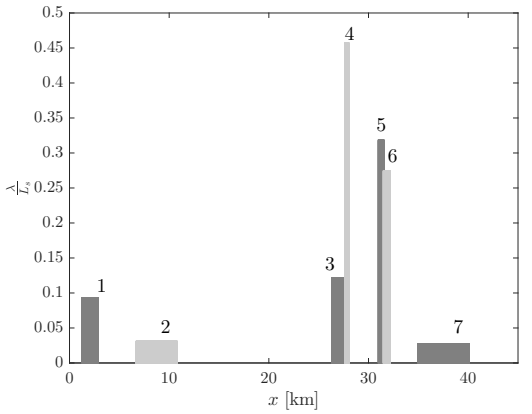

(a) $h_1 = 10$ m, $A = -10$ m

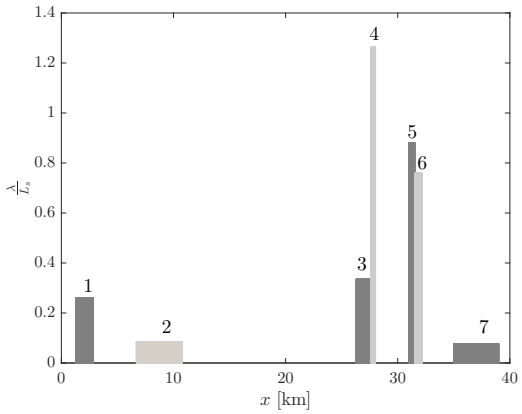

(b) $h_1 = 30$ m, $A = -10$ m

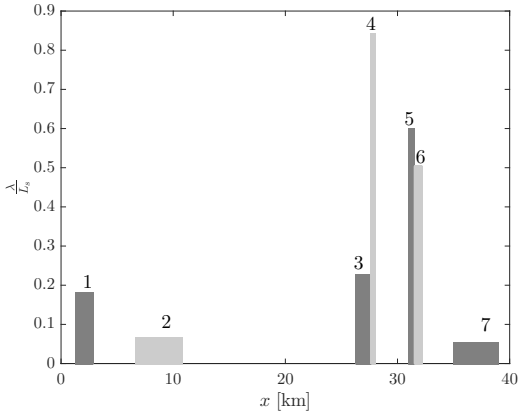

(c) $h_1 = 30$ m, $A = -30$ m

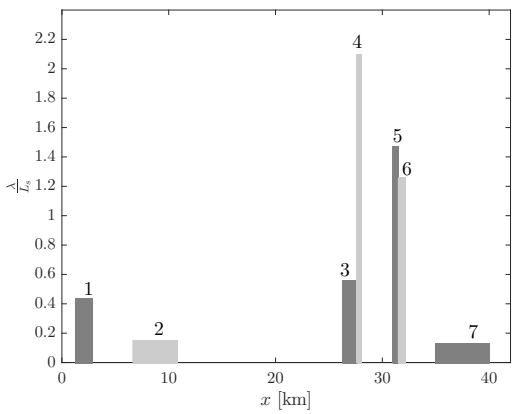

(d) $h_1 = 30$ m, $A = -50$ m

Figure 4.24. Comparisons between the wavelength and the horizontal scale of variability for the different section of the bathymetry of the Gioia Basin. The threshold value for adiabaticity has been chosen as $\lambda/L_s = 0.1$.

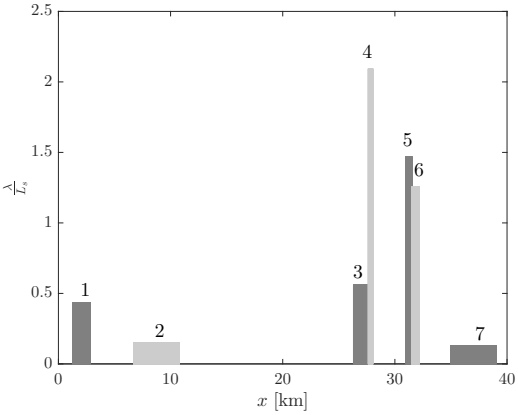

(a) $h_1 = 50$ m, $A = -10$ m

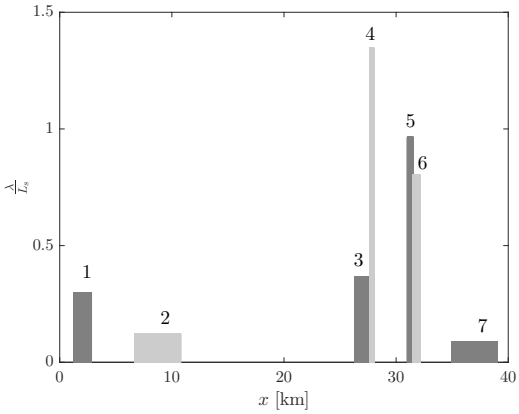

(b) $h_1 = 50$ m, $A = -30$ m

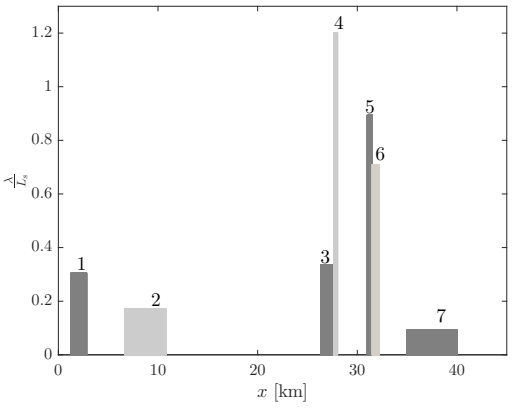

(c) $h_1 = 50$ m, $A = -50$ m

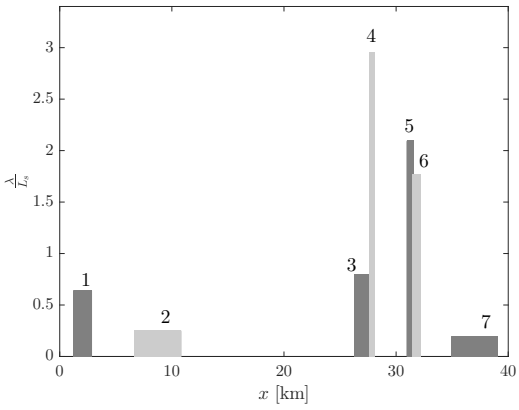

(d) $h_1 = 70$ m, $A = -10$ m

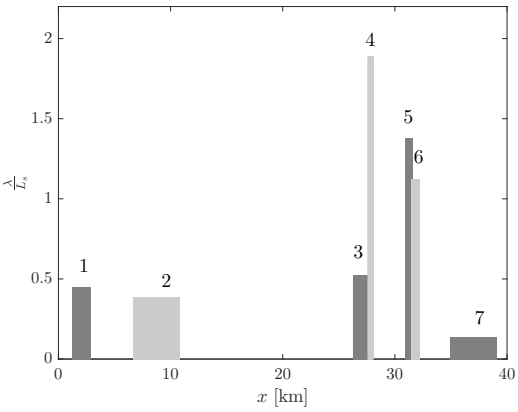

(e) $h_1 = 70$ m, $A = -30$ m

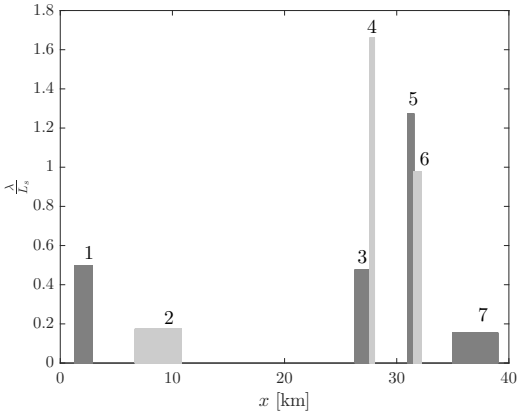

(f) $h_1 = 70$ m, $A = -50$ m

Figure 4.25. Comparisons between the wavelength and the horizontal scale of variability for the different section of the bathymetry of the Gioia Basin. The threshold value for adiabaticity has been chosen as $\lambda/L_s = 0.1$.

The wave evolution in the Messina Strait at several distances from the initial point is presented in Figs. 4.28-4.37, where the time in all figures is the time in a shifted system of coordinates.

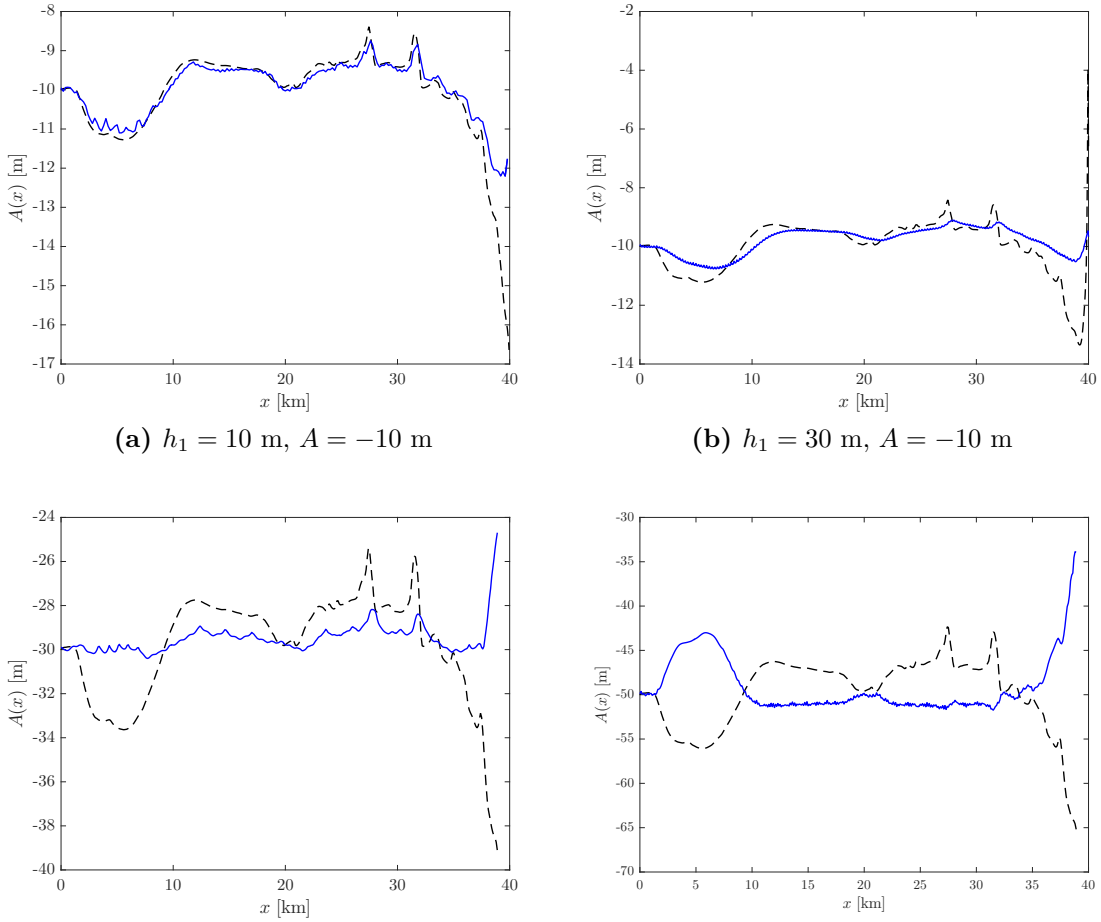

(a) $h_1 = 10$ m, $A = -10$ m **(b)** $h_1 = 30$ m, $A = -10$ m

(c) $h_1 = 30$ m, $A = -30$ m **(d)** $h_1 = 30$ m, $A = -50$ m

Figure 4.26. Comparisons between amplitudes from vKdV analytical theory (see Eq.(3.43))(dashed black line) and veKdV simulations (solid blue line). We can notice the divergence of the behavior of the two curves with the increase of amplitude and pycnocline depth: the "inversion of polarity" of the veKdV simulation with respect to the vKdV theory curve is an indication of the transition to a shallow water eKdV behavior, i.e., decreasing (increasing) amplitude at decreasing (increasing) depth (as explained in Sec.3.4).

The first simulation, for $h_1 = 10$ m and $A = -10$ m, shows a quite regular behavior of the solitary wave (see Fig. 4.28). The initial ISW has a negative polarity ($\alpha < 0$ and $\alpha_1 < 0$), and the wave retains its soliton–like shape for a distance of about 40 km. The curves of the veKdV simulation (solid blue line), the adiabatic solution of Grimshaw (red dashed line) et al. and the explicit solution (black dash–dotted line) are really close. The explicit solution is regular all along the bathymetry since $\sqrt{b(x)}$ (Fig 4.29c) is always lesser than 1,increasing rapidly only near the frontal slope. The

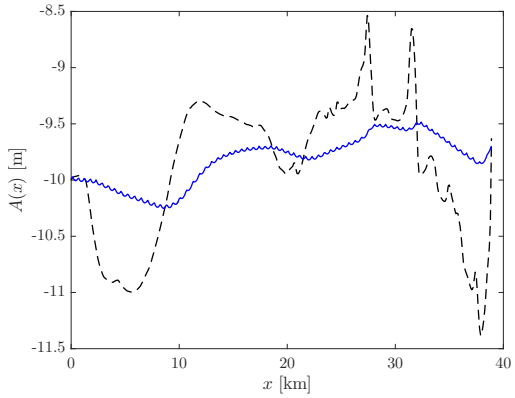

(a) $h_1 = 50$ m, $A = -10$ m

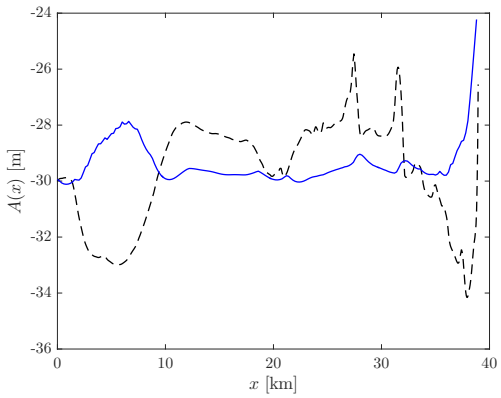

(b) $h_1 = 50$ m, $A = -30$ m

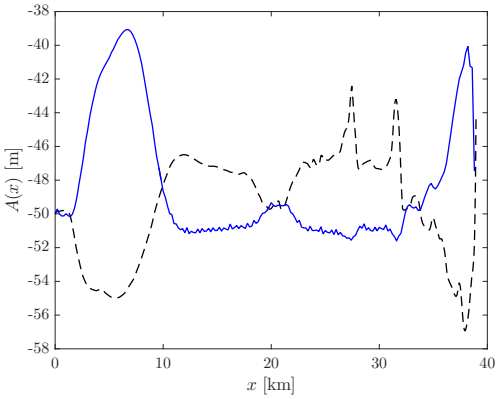

(c) $h_1 = 50$ m, $A = -50$ m

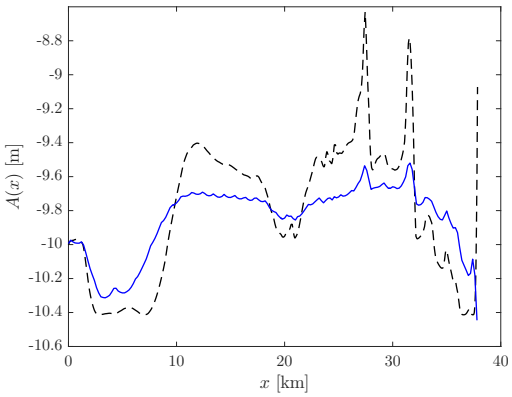

(d) $h_1 = 70$ m, $A = -10$ m

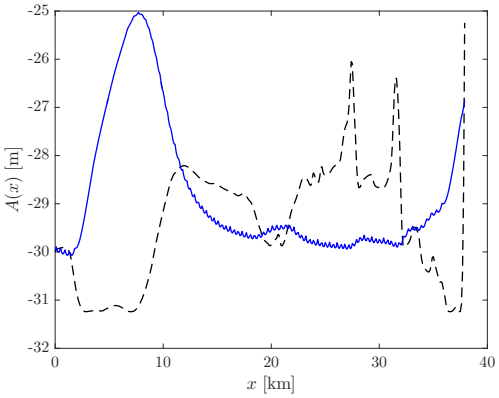

(e) $h_1 = 70$ m, $A = -30$ m

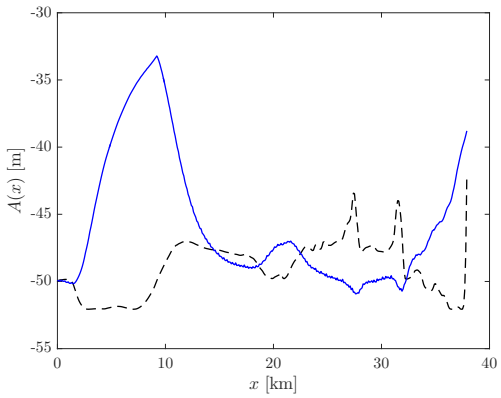

(f) $h_1 = 70$ m, $A = -50$ m

Figure 4.27. Comparisons between amplitudes from vKdV analytical theory (see Eq.(3.43))(dashed black line) and veKdV simulations (solid blue line). In Fig. (b,c,e,f) we observe a shallow water eKdV behavior, i.e., decreasing (increasing) amplitude at decreasing (increasing) depth (see Sec.3.4).

influence of the bathymetry is revealed by the presence of a radiating tail that begins to form clearly at about $x = 5$ km. This feature has been already examined in section 3.2 and is due to the fact that the soliton does not conserve the mass (though it does conserve energy) at the leading order of the asymptotic expansion of ζ, and the tail compensates for this. The variations in amplitude follow in a specular way the depth variations (see Fig.4.29), i.e. amplitude decreases (increases) for increasing (decreasing) values of depth. Indeed, before the Capo Vaticano frontal slope, the depth variations range in $200 \div 500$ m, thus being $A/H \simeq 0.02 \div 0.05$ we are in a small–amplitude regime, and we can expect this KdV behavior (for vKdV–veKdV amplitude comparisons see Fig. 4.26 and Fig. 4.27), as already explained in Sec.4.2. However, along the frontal slope, differently from a KdV soliton, the wave starts to reduce its amplitude (see Fig. 4.29d), as expected for an eKdV wave in shallow water, and for $x \simeq 40.2$ km, since $\alpha(x) \to 0$, the wave is destroyed (no transitions between quadrants III and IV of Fig.3.2).
The second set of simulations has been perfomed for the parameters choice $h_1 = 30$ m and $A = -10, -30, -50$ m. For $A = -10$ m, we have a KdV behavior again along almost all the bathymetry, with an eKdV typical wave amplitude reduction at the frontal slope (Fig.4.26b). The pertubations generated by the interaction with the bathymetry are now more pronounced and begin already along the first two sections of the seabed (i.e. along the seamound). In this case, these areas do not represent adiabatic transition zones, and this can be easily argued from Fig. 4.30, where we can observe wave deformations appearing between 0 and 14 km. In Fig. 4.33a, we can see that the adiabatic explicit theory and the theory of Grimshaw et al. reproduce less well the simulation in all bathymetry sections. Indeed, the ratio λ/L_s results to be lesser than 0.1 only in sections 2 and 7, but after the wave passed areas of nonadiabatic transition, the wave arrives to the end of the bathymetry already distorted, before the complete destruction past $x = 40$ km. In the case $A = -30$ m, the transitions are less pronounced, in fact the values of λ/L_s are smaller than those for $A = -10$ m. The adiabatic solution of Grimshaw et al.("GRa", from here on) in this case seems to work fine over the entire bathymetry (Fig. 4.31), with a lower precision near the canyons (sections 4, 5, 6), where the adiabaticity is not guaranteed. The explicit solution has the right eKdV structure, but the amplitude now is not so small and this affects the coefficient $b(x)$, which becomes too large, in particular in sections 1 and 7 (seamound and frontal slope). The case $A = -50$ m presents adiabaticity (or quasi–adiabaticity) in sections 1, 2, 3 and 7. However, the adiabatic solution of GRa approximates well the behavior of the wave amplitude in all zones (Fig. 4.32). Furthemore, we can notice the "inversion of polarity" of the simulation and adiabatic theory curves along the entire bathymetry with respect to the previous cases, which is an indication of a shallow water eKdV behavior, i.e., decreasing (increasing) amplitude at decreasing (increasing) depth. Indeed, in this case the initial wavelength ($\lambda \simeq 310$ m) is comparable to the total fluid depth, and during the evolution is, at some depths, much greater (up to 1200 m)(see Fig.4.21b).
The third set of numerical experiments has been performed for $h_1 = 50$ m and $A = -10, -30, -50$ m. This set of simulations is quite similar to the previous one, but now the analytical theories perform a little worse than before. Adiabaticity is reduced in all sections (see Fig. 4.23 and Fig. 4.25), and even the GRa theory cannot reproduce well the numerical data. Being less precise than the numerical solution to

the transcendental problem (3.45) or (3.36), the explicit solution does not work fine, especially in cases $A = -30$ m and $A = -50$ m (large waves). We observe that for $A = -50$ m becomes evident the generation of a secondary solitary wave, maybe through a fission mechanism. However, the ratio λ/L_s is even smaller than that of the case $h_1 = 30$ m (see, for example, Fig. 4.25c-d) in all the seven sections, and in that case we did not observe particular fission phenomena. This may appear as a contradiction. This is why, though its effectiveness, the ratio λ/L_s is good only as first indicator of adiabaticity. If we look at Fig. 4.20e-f, we can see $\nu(x)/\alpha$ and $\nu(x)/\alpha_1$ exceeding their respective adiabaticity reference scales (see (4.11)) along every bathymetry section. This means that the shoaling term is becoming more important than the other terms in the veKdV equation. This induces nonadiabatic transformations which may lead to fission.

The fourth set of simulations is for $h_1 = 70$ m and $A = -10, -30, -50$ m (Fig. 4.36). For $A = -10$ m we have a KdV behavior along all the bathymetry, but with a strongly reduced amplitude with respect to the vKdV amplitude evolution (Fig. 4.27d). For $A = -30, -50$ m, we have instead a pure eKdV behavior, and the difference with the vKdV amplitude evolution is impressive (Fig. 4.27e-f). However, the adiabatic approximation does not hold. This can be argued from criterion (4.11), from the study of the ratio λ/L_s (which, however, also in this case is not too indicative), from the snapshots of wave evolutions (see in particular Fig. 4.37), and from the comparison with the adiabatic theory (Fig. 4.38). Indeed, the wave evolution, especially in the case $h_1 = 70$ m and $A = -50$ m (Fig. 4.38), shows instabilities in the waveform starting from the second section, where a set of secondary solitary waves and an energetic (large) dispersive tail begin to form, later growing and separating from the initial wave, till up the wave destruction along the frontal slope. The adiabatic theory of GRa does not perform well for any of the examined wave amplitudes.

In conclusion, simulations of ISWs travelling northward of the Messina Strait show that small or large waves can resist to transformations along the Gioia Basin, reaching the Capo Vaticano frontal slope. The interaction with the varying bathymetry does not alter the soliton–like shape along almost all the bathymetry for small–amplitude waves, and at least along the seamound for large amplitude waves. However, the wave evolution leads to the generation of a dispersive tail and, in case of large amplitudes, also of a set of secondary solitary waves. The development of a kink in the rear part of the waveform represents the first stage of the wave annihilation. Since the coefficient α_1 does not change sign during the propagation, near the transition zone $\alpha = 0$ the wave is simply destroyed, becoming a dispersive wavetrain.

As already shown in Sec.4.2 the wave–breaking phenomenon described by vKdV and veKdV simulations is not that expected in a laboratory experiment or in a typical oceanic situation. To get information about wave–breaking, in the next section we will apply our wave–breaking model (see Sec.4.3) to the case of the Messina Strait.

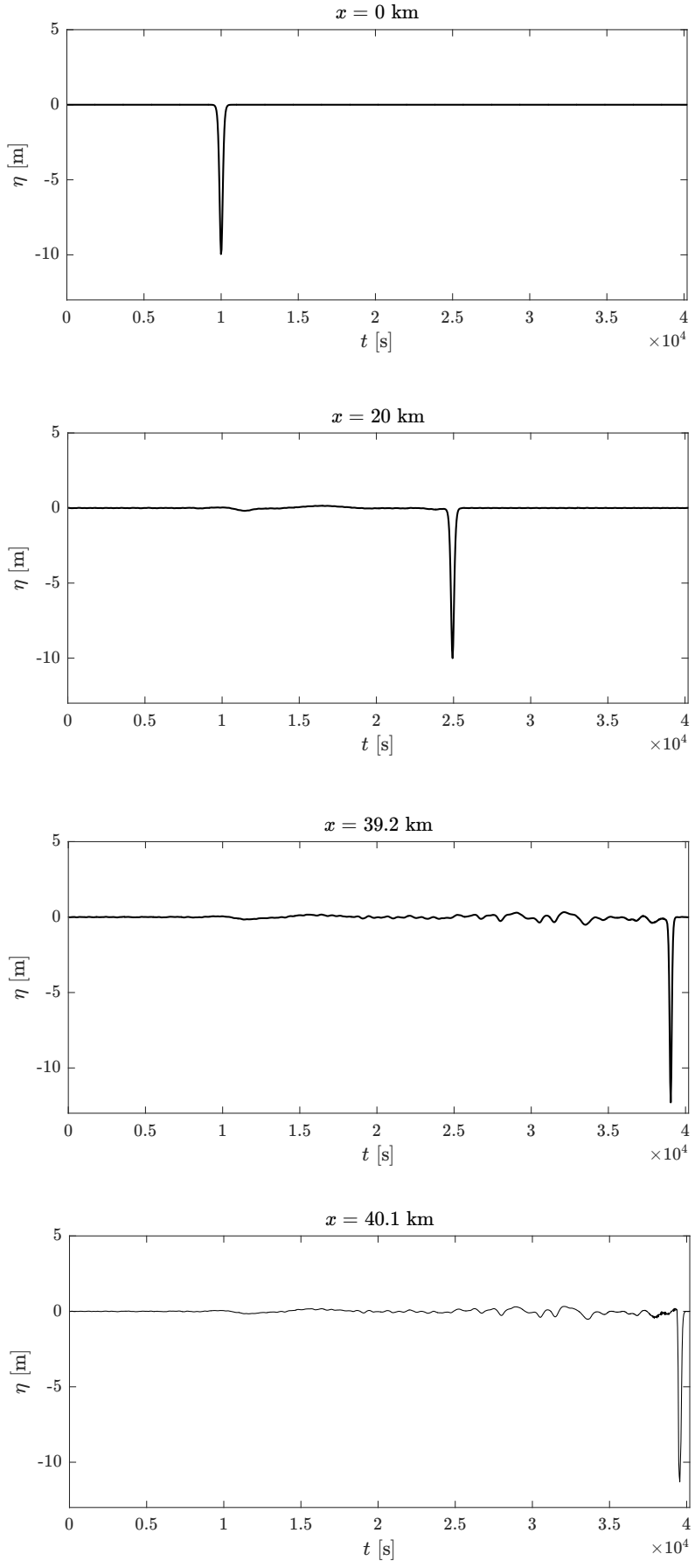

Figure 4.28. veKdV solitary wave evolution in the Gioia Basin with $h_1 = 10$ m, $A = -10$ m. See text or caption in Fig.4.29 for general explanation.

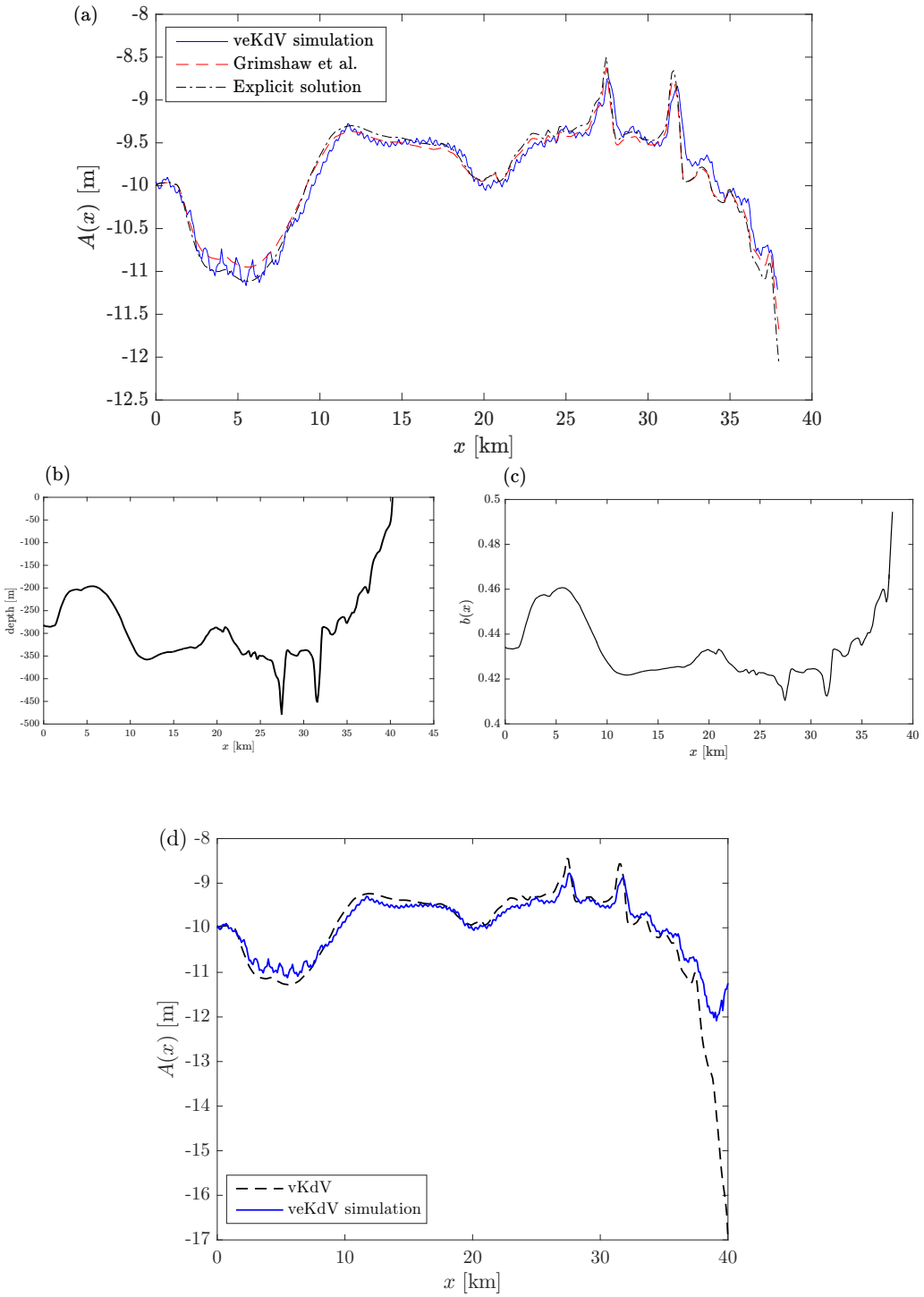

Figure 4.29. (a)Comparison between simulation and theoretical prediction of amplitude evolution along the Gioia Basin with $h_1 = 10$ m, $A = -10$ m. The amplitude follows the variations of the bathymetry (Fig.(b)) in a specular way, i.e. it decreases (increases) for increasing (decreasing) values of depth. The curves of the veKdV simulation (solid blue line), the adiabatic solution of Grimshaw (red dashed line) et al. and the explicit solution (black dash–dotted line) are really close. The explicit solution is regular all along the bathymetry since $\sqrt{b(x)}$ (Fig.(c)) is always lesser than 1,increasing rapidly only near the frontal slope, where the wave is expected to break. (d) Comparison between vKdV varying amplitude (analitycal theory) and veKdV simulations. The behavior of the two models in shallow water (near the frontal slope, $x \geq 35$ km) is different: veKdV wave reduces its amplitude before being destroyed, while vKdV increases its amplitude more than veKdV before collapsing to zero (not shown) at the end of the bathymetry.

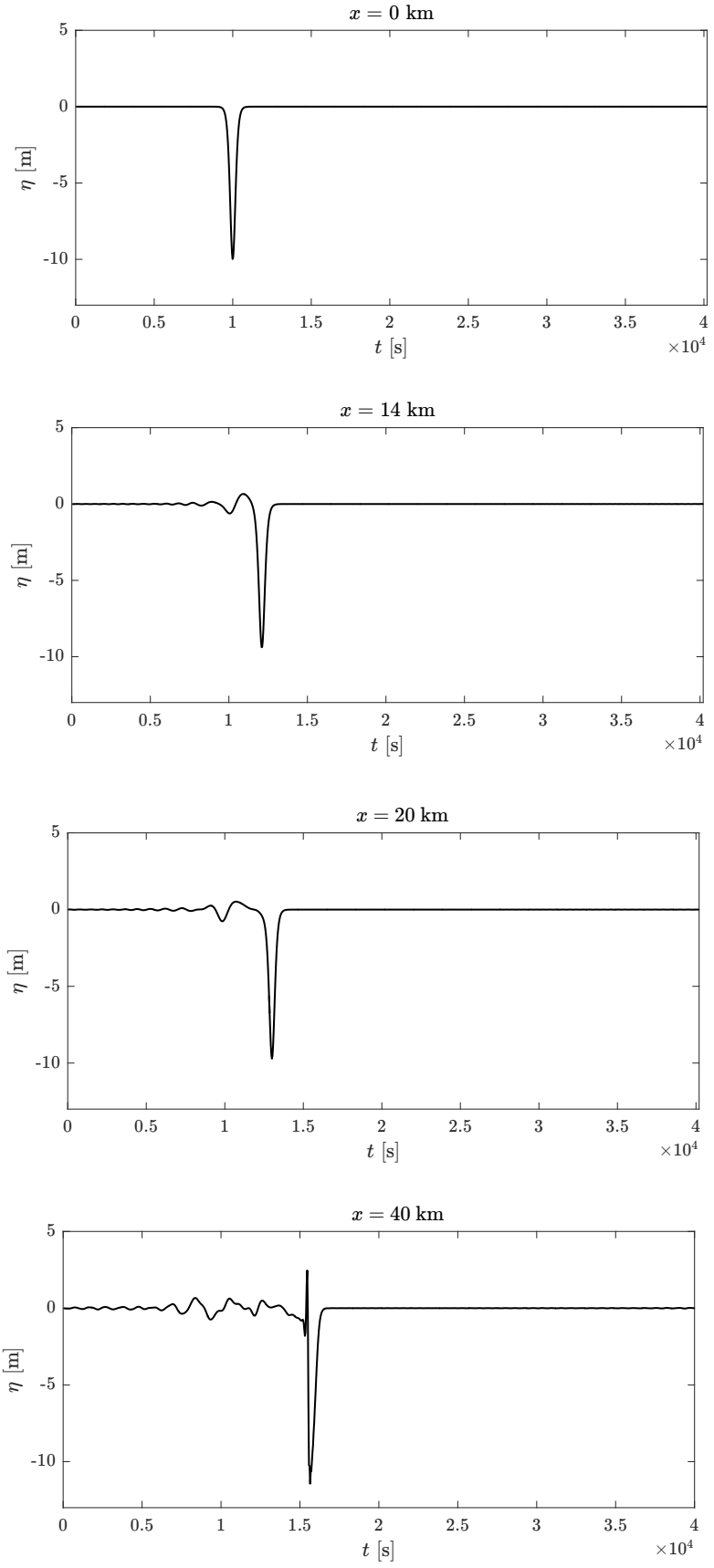

Figure 4.30. veKdV solitary wave evolution in the Gioia Basin with $h_1 = 30$ m, $A = -10$ m. See text or caption in Fig.4.33 for general explanation.

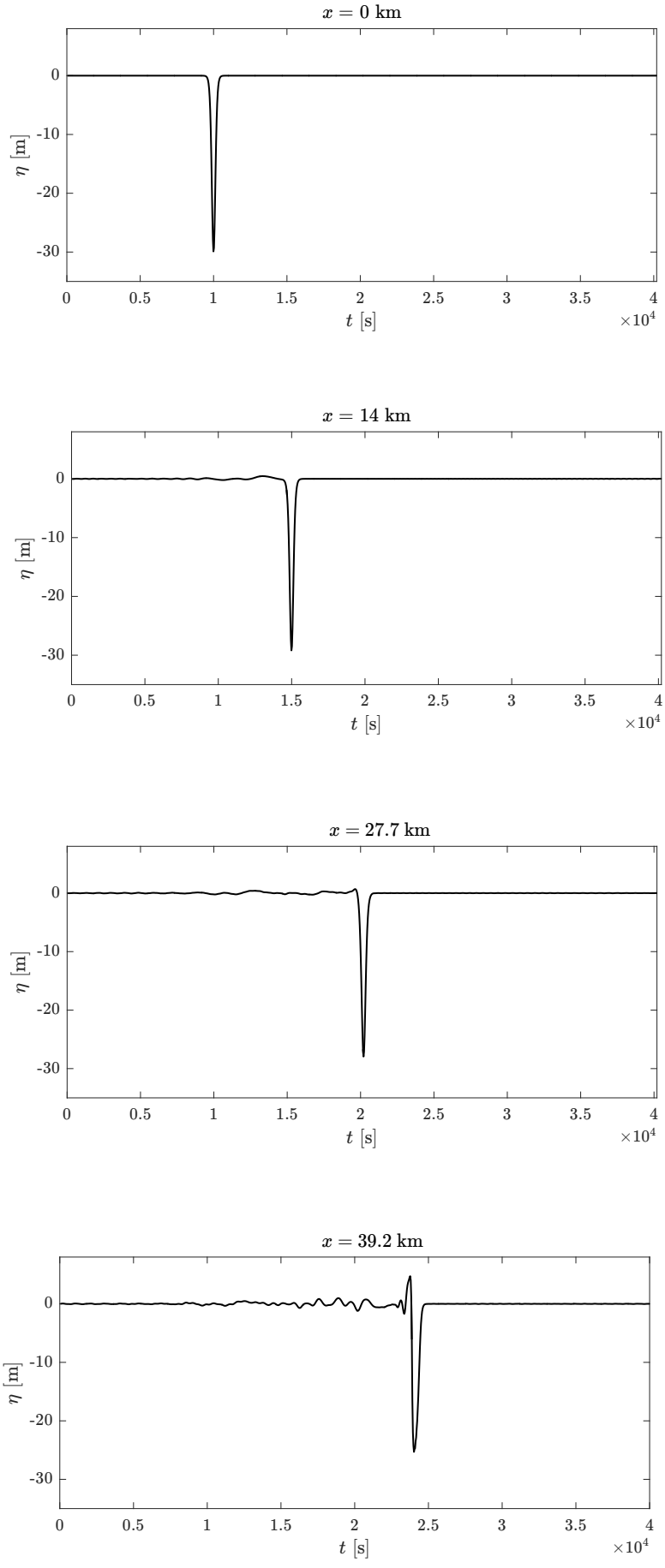

Figure 4.31. veKdV solitary wave evolution in the Gioia Basin with $h_1 = 30$ m, $A = -30$ m. See text or caption in Fig.4.33 for general explanation.

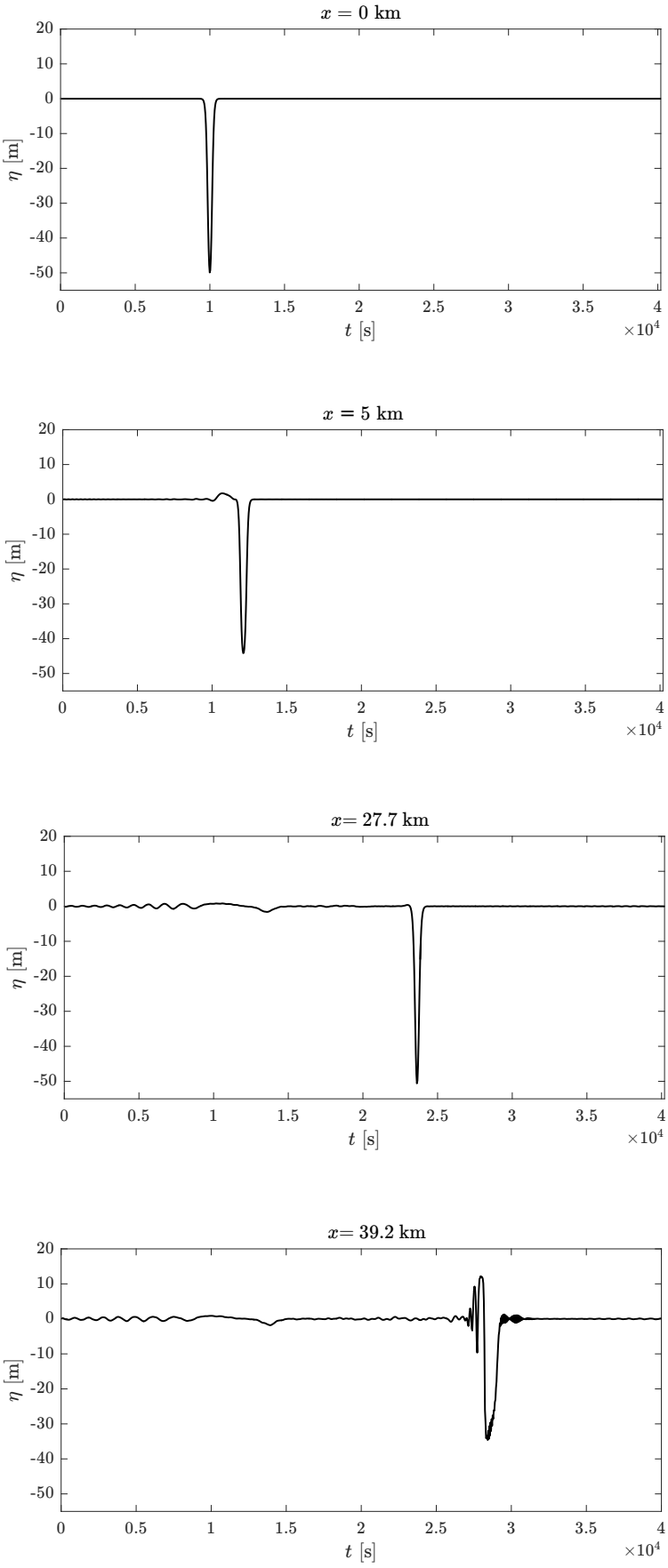

Figure 4.32. veKdV solitary wave evolution in the Gioia Basin with $h_1 = 30$ m, $A = -50$ m. See text or caption in Fig.4.33 for general explanation.

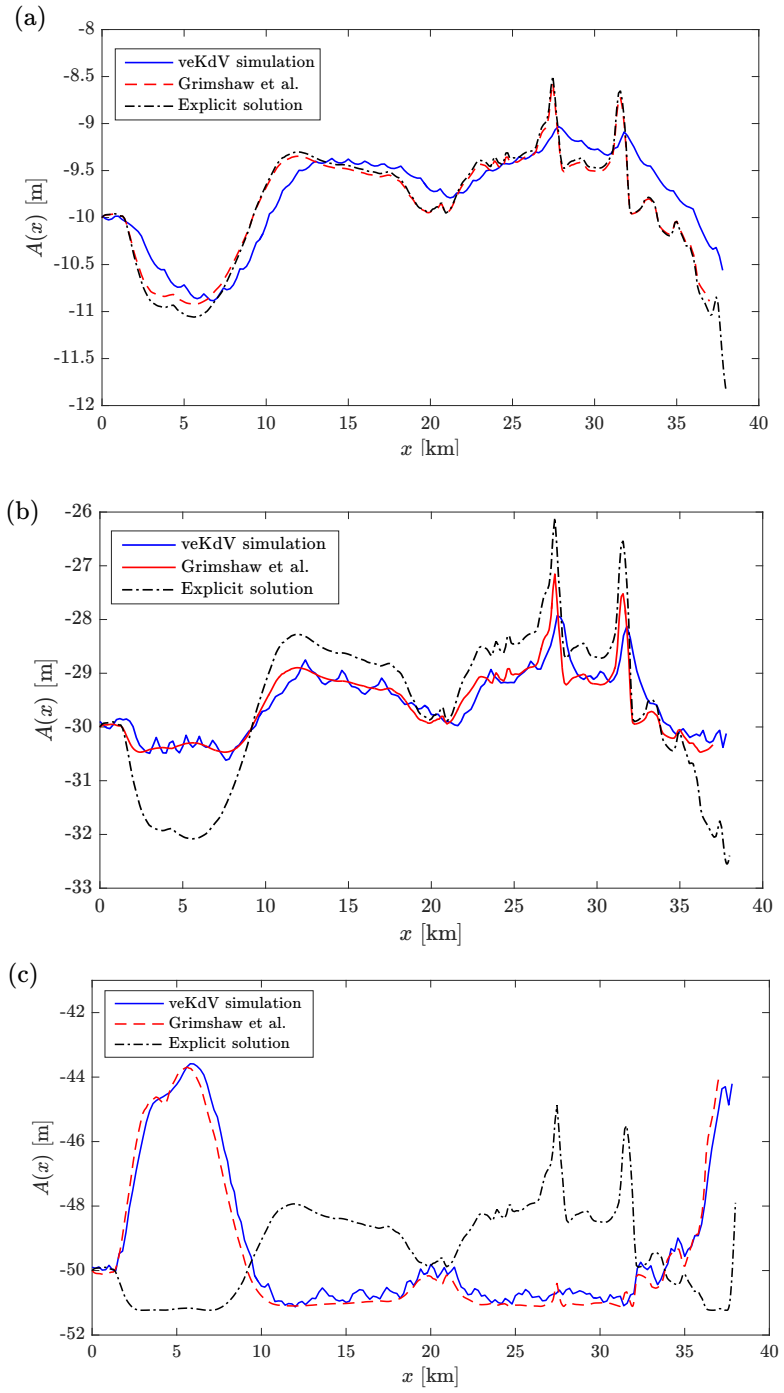

Figure 4.33. Comparison of amplitude evolutions along the Gioia Basin with $h_1 = 30$ m, $A = -10, -30, -50$ m. (a) $A = -10$ m. We have a KdV behavior along almost all the bathymetry, with an eKdV typical wave amplitude reduction at the frontal slope (not shown here, see Fig.4.26b). The GRa theory does not reproduce well the simulation in all bathymetry sections, since the wave passes through nonadiabatic areas. (b) $A = -30$ m. The GRa adiabatic solution works fine over the entire bathymetry (Fig. 4.31), with a lower precision near the canyons (sections 4, 5, 6; see Tab. 4.4). The explicit solution has the right eKdV structure, but the amplitude now is not so small and this affects the coefficient $b(x)$. (c) $A = -50$ m. There is adiabaticity (or quasi–adiabaticity) in sections 1, 2, 3 and 7 (see Tab. 4.4). The GRa theory works fine in all zones (Fig. 4.32). veKdV simulations have a shallow water eKdV behavior. Indeed, in this case the initial wavelength ($\lambda \simeq 310$ m) is comparable to the total fluid depth, and during the evolution is, at some depths, much greater (up to 1200 m)(see Fig.4.21b).

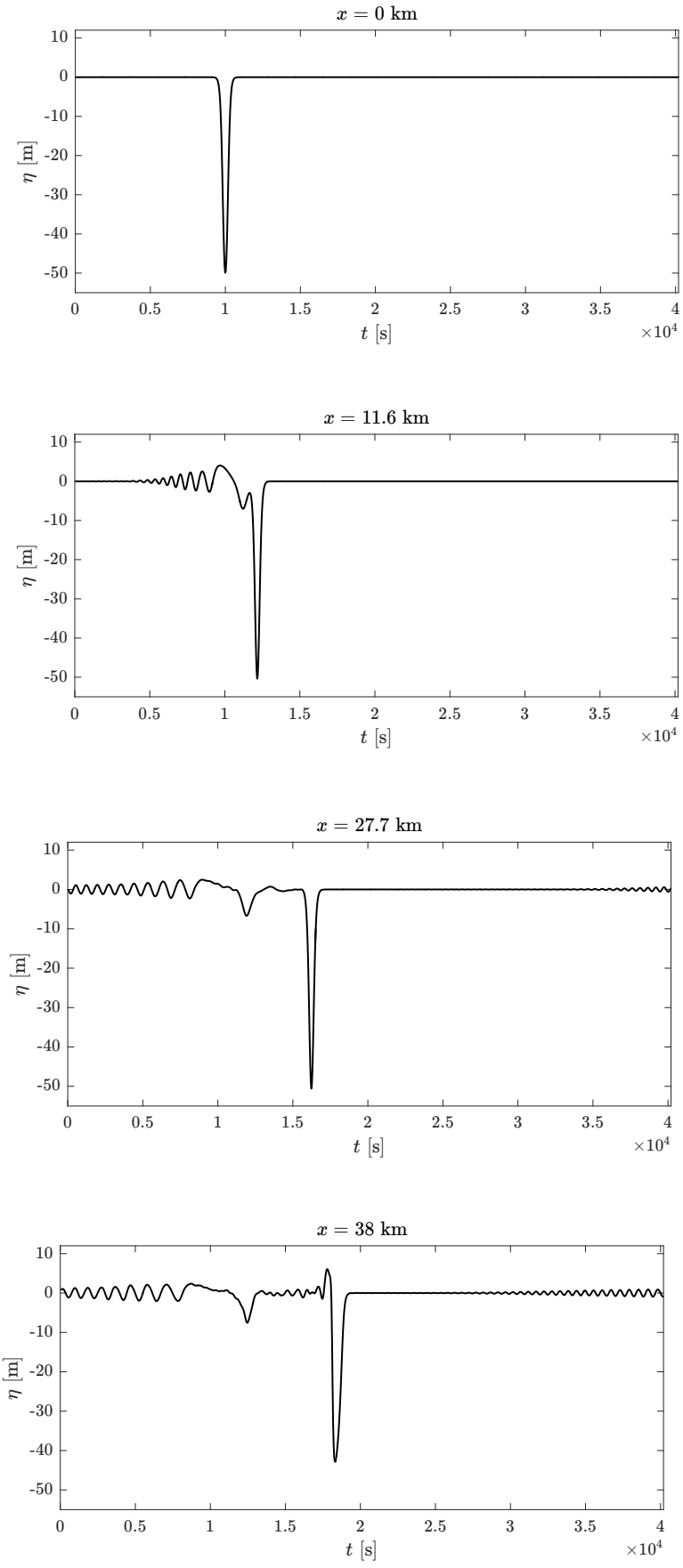

Figure 4.34. veKdV solitary wave evolution in the Gioia Basin with $h_1 = 50$ m, $A = -50$ m. See text or caption in Fig.4.35 for general explanation.

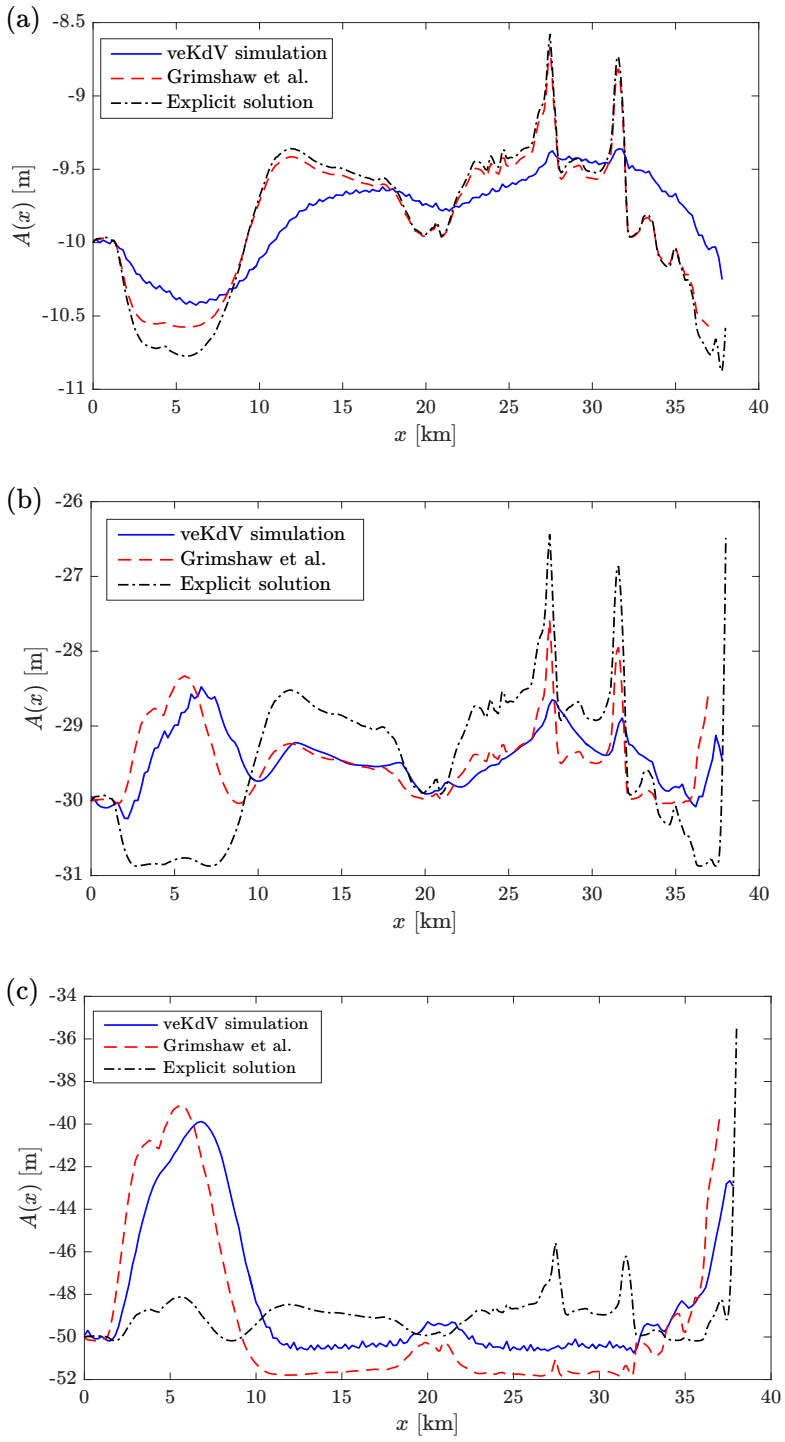

Figure 4.35. Comparison of amplitude evolutions along the Gioia Basin with $h_1 = 50$ m, $A = -10, -30, -50$ m. Adiabaticity is reduced in all sections (see Fig. 4.23 and Fig. 4.25), and even the GRa theory cannot reproduce well the numerical data. Being less precise than the numerical solution to the transcendental problem (3.45) or (3.36), the explicit solution does not work fine, especially in cases (b) $A = -30$ m and (c) $A = -50$ m (large waves). We observe that for $A = -50$ m (see Fig. 4.34) becomes evident the generation of a secondary solitary wave, maybe through a fission mechanism. Indeed, $\nu(x)/\alpha$ and $\nu(x)/\alpha_1$ (see (4.11)) exceed their respective adiabaticity reference scales (see Fig. 4.20e-f) along every bathymetry section. This induces nonadiabatic transformations which may lead to fission.

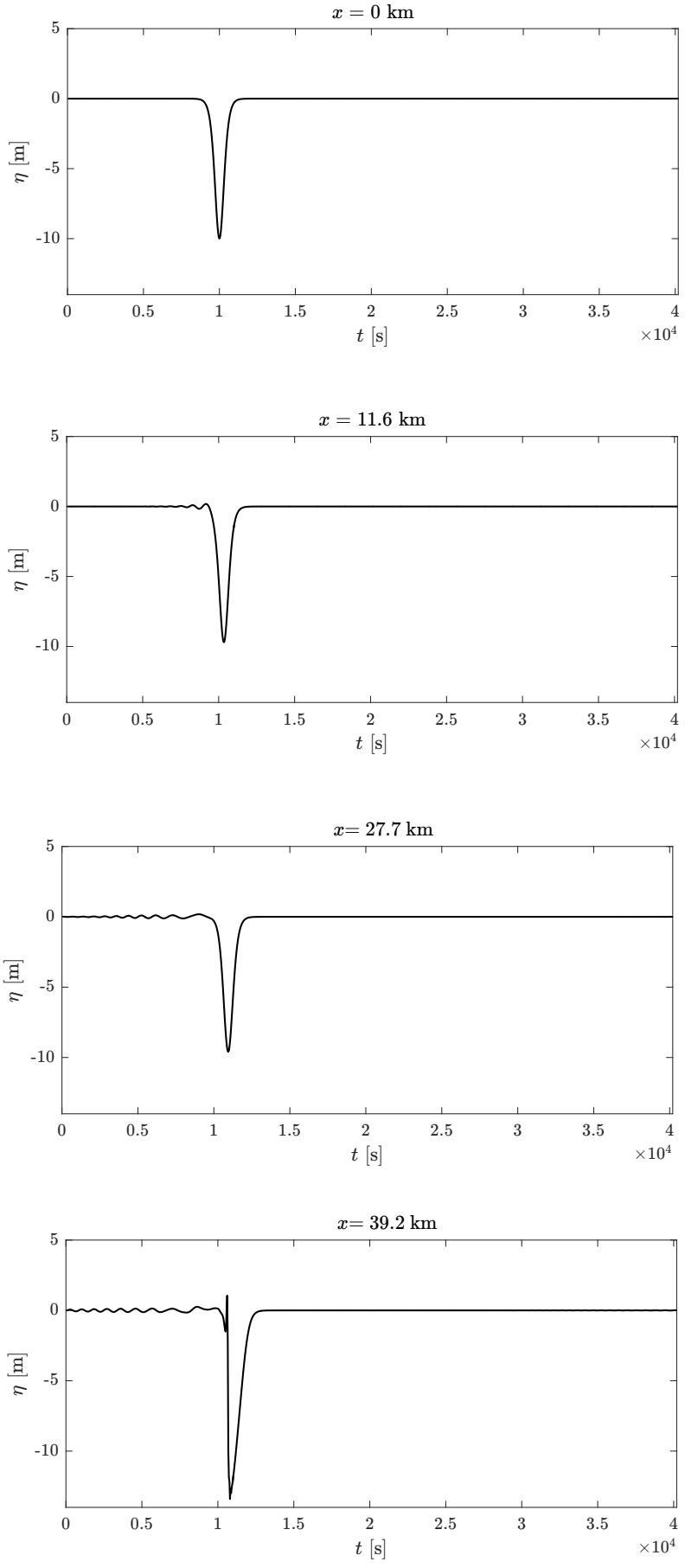

Figure 4.36. veKdV solitary wave evolution in the Gioia Basin with $h_1 = 70$ m, $A = -10$ m. See text or caption in Fig.4.38 for general explanation.

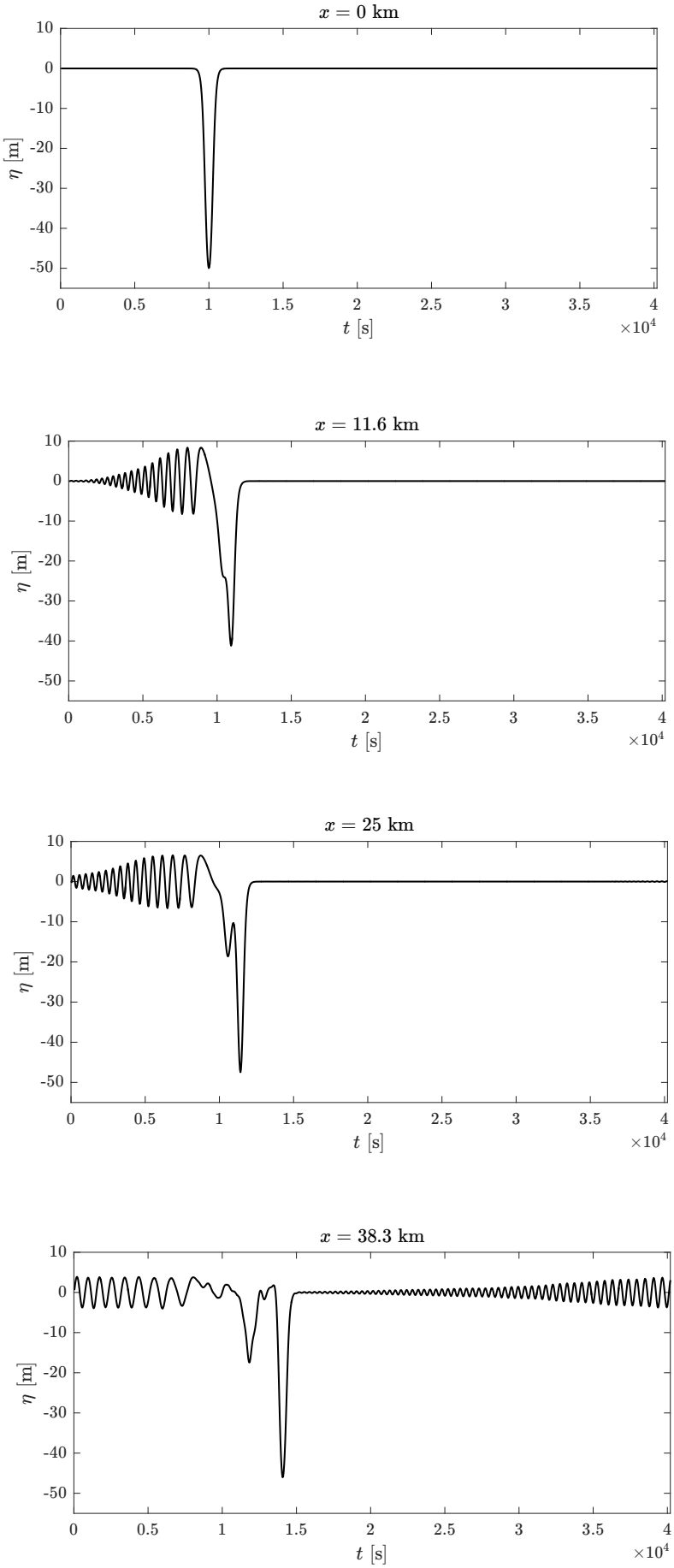

Figure 4.37. veKdV solitary wave evolution in the Gioia Basin with $h_1 = 70$ m, $A = -50$ m. See text or caption in Fig.4.38 for general explanation.

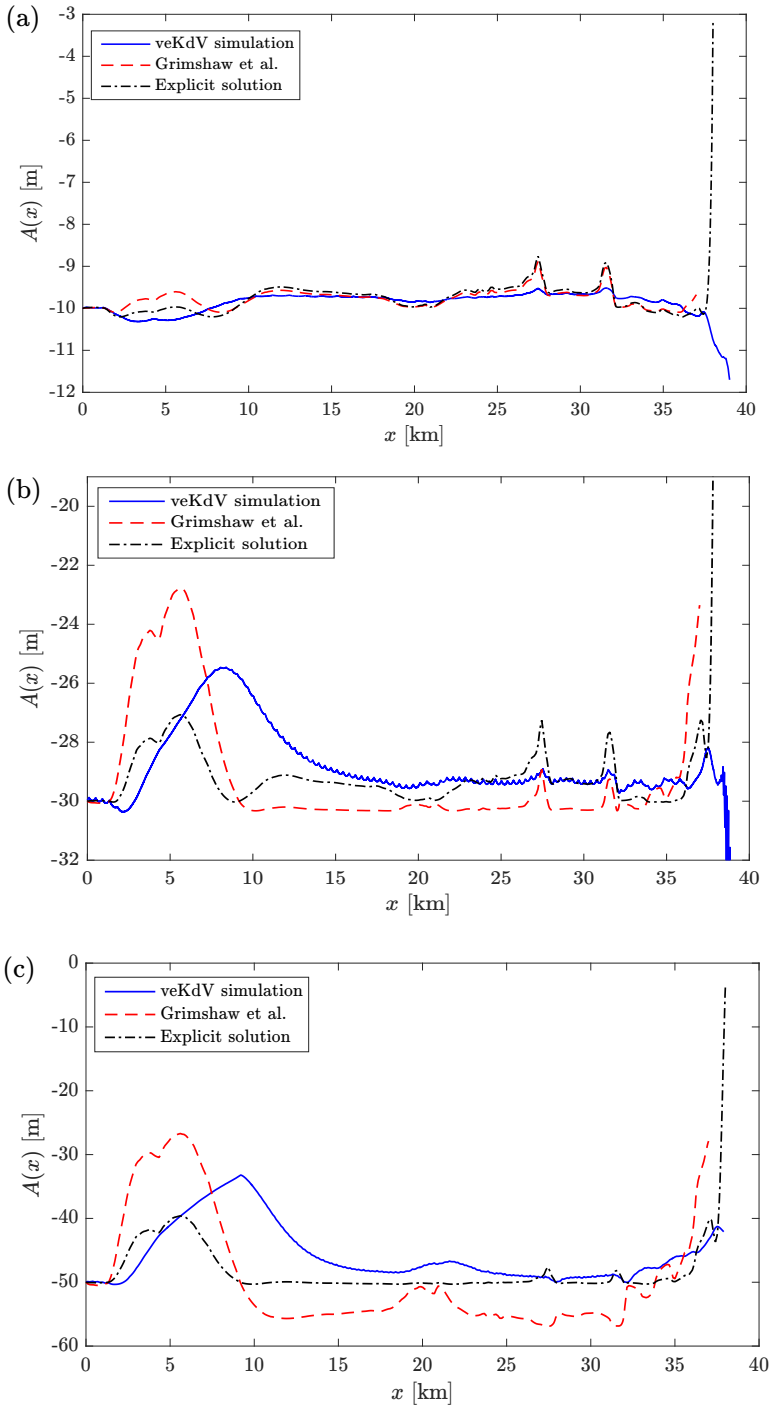

Figure 4.38. Comparison of amplitude evolutions along the Gioia Basin with $h_1 = 70$ m, $A = -10, -30, -50$ m. (a) $A = -10$ m. We have a KdV behavior along all the bathymetry, but with a strongly reduced amplitude with respect to the vKdV amplitude evolution (see Fig. 4.27d). For (b) $A = -30$ m and (c) $A = -50$ m, we have instead a pure eKdV behavior, and the difference with the vKdV amplitude evolution is impressive (see Fig. 4.27e-f). However, the adiabatic approximation does not hold. Indeed, the wave evolution, especially in the case $h_1 = 70$ m and $A = -50$ m (see Fig. 4.37), shows instabilities in the waveform starting from the second section, where a set of secondary solitary waves and an energetic (large) dispersive tail begin to form, later growing and separating from the initial wave, till up the wave destruction along the frontal slope. The adiabatic theory of GRa does not perform well for any of the examined wave amplitudes.

4.7 ISWs breaking location in the Gioia Basin

ISWs produced at the sill of the Messina Strait undergo a series of trasformations propagating by interacting with bathymetric constraints. SAR images allow us to visualize path of solitary wave trains (Fig. 4.39). Surface manifestations, captured by satellite, reveal the presence of ISWs packets propagating northward from the Messina Strait. We observe, in particular, three different ISWs packets, produced at the sill every 12 hours (F1-F3 in Fig.4.39), and wave refraction phenomena close to topographic mounds and coastlines (see F1-F2 in Fig.4.39), which tend to deflect wave trajectories toward shallow areas (as argued by Droghei *et al.* [2016], see Fig. 4.40).

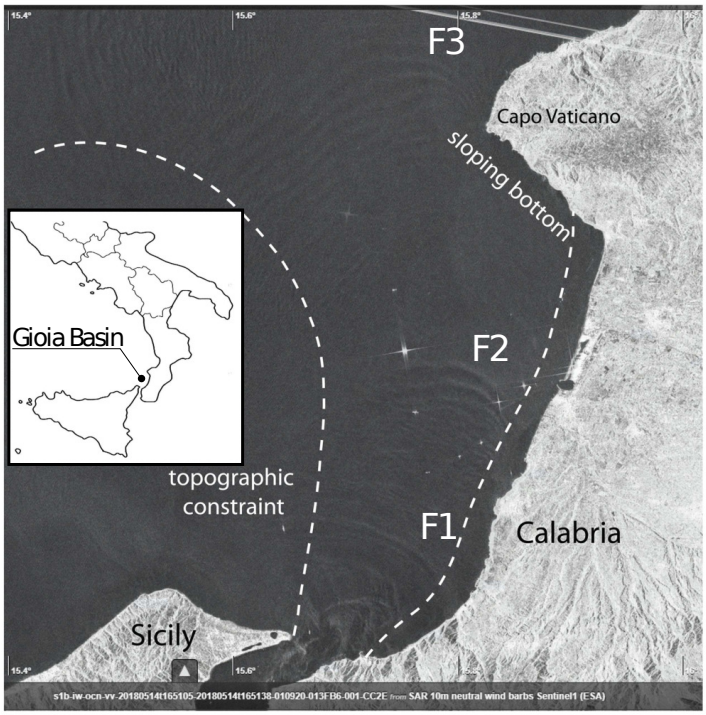

Figure 4.39. SAR image showing ISWs packets propagating northward from the Messina Strait toward Capo Vaticano promontory on 14 May 2018 [W. Alpers, personal communication]. We observe, in particular, three different ISWs packets, produced at the sill every 12 hours. The distance between the first two fronts is about 16 km, thus the propagation speed is approximately 0.4 m/s. This value is lower than those measured in previous oceanographic campaigns (about 1 m/s [Alpers *et al.*, 2008]). For this reason, within the same SAR image three successive wave packets are visible. One can suppose that this special occurence results from the particular stratification conditions expected in late spring (i.e. weaker pycnocline). ISWs deflect near the topographic constraint on the left constituted by a seamound (see fronts F1–F2). The same refractive phenomenon is present along the Calabrian coastline on the right. Thus, the waves propagate inside the white dashed lines towards Capo Vaticano promontory.

Interestingly, south of Capo Vaticano coastline, no surface manifestation of ISWs is visible, while the ISWs packet F3 keeps propagating westward (Fig.4.39). This

suggests an interaction between the northward-propagating ISWs and the Capo Vaticano bathymetric constraint, which induces wave breaking, as marked by observation of the thermal front and the dark grey area southward of Capo Vaticano discussed in Section 4.5 [Marullo and Santoleri, 1986].

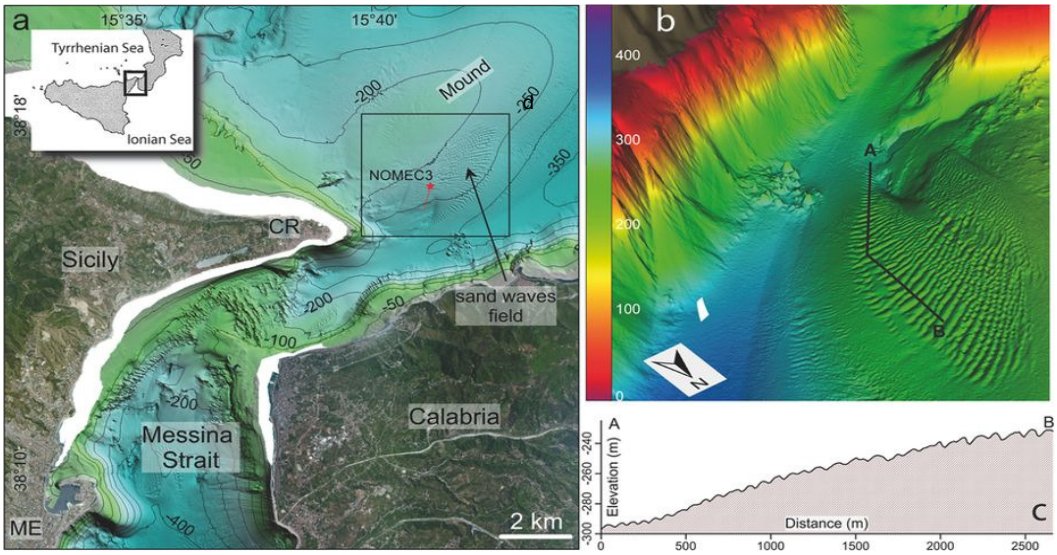

Figure 4.40. (a) Bathymetric map of the Messina Strait. The box shows the sand–wave field over the topographic seamound also indicated in Fig. 4.17. In plan-view, sand-waves have linear or slightly sinuous crest–lines that are mostly oriented obliquely to the isobaths; their crest–lines are laterally continuous southward (close to the Messina Strait), whereas they become more discontinuous northwards. (b) 3D zoom of the sand-wave field. The black line indicates the bathymetric section in (c). (c) Bathymetric section of sand-wave crests. The sand–wave field indicates the presence of wave refraction phenomena, which tend to deflect wave trajectories toward shallow areas (see F1-F2 in Fig. 4.39). From Droghei *et al.* [2016].

To apply our theoretical approach for predicting breaking location on real field, we consider ISWs arriving (almost) orthogonal to isobaths over the steeper slope south of Capo Vaticano (Fig.4.42). We then set in Equations (2.53) and (2.41) the stratification conditions that define the pycnocline position at $h_1 = 30$ m [Alpers and Salusti, 1983; Sapia and Salusti, 1987] and $h_1 = 70$ m [Brandt *et al.*, 1999] depending on seasonal effects, $H = h_1 + h_2 = 400$ m, $\rho_1 = 1026$ kg/m^3, $\rho_2 = 1029$ kg/m^3. By considering ISWs amplitudes ranging from $A = -40$ m to $A = -70$ m [Brandt *et al.*, 1999], we estimate the breaking depths H_b and the theoretical values for the Iribarren number for each case (Fig.4.42). The Iribarren numbers are in the range Ir $\simeq 0.15 \div 0.80$, consistent with a plunging breaking mechanism. For each incoming wave and slope direction we evaluate the coordinates of the breaking position. Thus, we identify a breaking region where ISWs are expected to verticalize (Fig.4.42). The breaking depth values are in the range $H_b \simeq 50 \div 200$ m and the distance from the coastline varies approximately from 2 to 4 km. The trailing edge verticalization is associated to the larger offshore bottom velocities, induced by the downslope flow of the denser water beneath the leading edge [La Forgia *et al.*, 2018a]. In this strip we then expect to observe phenomenona that are related to the

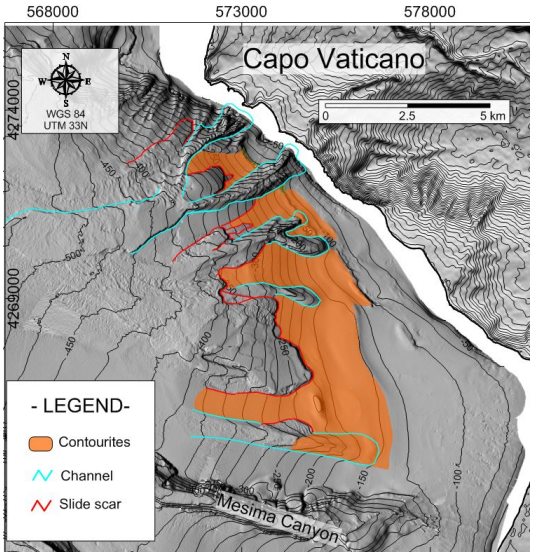

Figure 4.41. Morphobathymetric features southward Capo Vaticano promontory; the contourites area, channels and slide scars are highlighted.

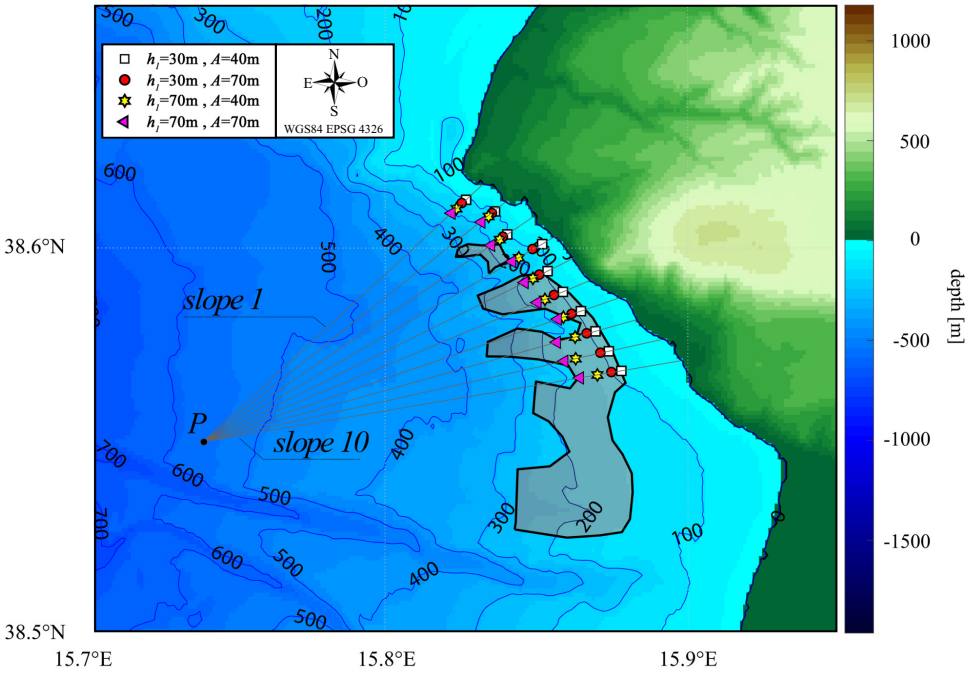

Figure 4.42. Breaking positions (symbols) and related depths along each slope from MCC theory. Breaking points from eKdV (not showed) are located really close to the respective MCC points. ISWs amplitudes ranging from $A = 40$ m to $A = 70$ m and pycnocline positions at $h_1 = 30$ m and $h_1 = 70$ m have been considered. Slopes have been linearized in $0 \div 300$ m depth range. The identified breaking depth results to be in the range $H_b \simeq 50 \div 200$ m and the distance from the coastline varies approximately from 2 to 4 km. Lines represent the pathways over the steeper slopes south of Capo Vaticano.

effect of the shoaling and breaking of ISWs. Interestingly, the area southward Capo Vaticano is characterized by a very narrow shelf and a steep continental slope, where morpho-bathymetric features, such as canyons, channels, landslides and contourite drifts, determine a complex seabed morphology (see Fig.4.41) [Martorelli *et al.*, 2016]. In particular, several slide events affects the elongated sedimentary drifts in the upper continental slope, giving rise to the Capo Vaticano slide complex, which is composed of several intersecting slide scars and overlapping deposits and displays a large spatial coverage between 200 m and 500 m depth [Martorelli *et al.*, 2016]. ISWs breaking might trigger the formation of a large variety of morphological structures, as contourite–related landslides, located exactly in that area [Martorelli *et al.*, 2016]. In particular, during the shoaling process large-scale resuspension can erode seafloor sediments and generate nepheloid layers, intruding offshore [Bourgault *et al.*, 2014]. In our case, resuspension may represent a favorable factor for formation of contourite deposits and may contribute to net downslope sediment flux, eventually promoting the triggering of turbidity currents. In Fig.4.42 it is possible to observe the overlap between the breaking points and the conturites region (shaded area), and this may represent an indirect evidence of ISWs breaking processes southward of Capo Vaticano.

In conclusion, we proposed a semi–quantitative method to derive the breaking location of internal solitary waves interacting with a sloping bathymetry. We found that our theoretical model, based on KdV–type models, MCC theory, mass conservation and shoaling evolution observations, agrees very well with the laboratory experimental data for the breaking location. In the real–field case of the Messina Strait, SAR images confirms that ISWs interact with the Capo Vaticano frontal slope and, indeed, through the theoretical model, we can identify an area where ISWs should break and the effects of water mixing should be more intense and visible.

4.8 Discussion of two–dimensional effects

As reported in Sec.1.2.1, a realistic description of ISWs should include two–dimensional effects as wave refraction, reflection, diffraction or oblique interactions. However, concepts developed in this thesis are mainly related to one–dimensional wave phenomena. The aim of the thesis is, indeed, to give a theoretical framework to breaking and mixing processes by taking advantage of ISWs that were simulated in a wave tank. These experiments were performed in a 3 m long, 20 cm wide and 30 cm deep tank, thus the propagation and breaking processes were essentially one–dimensional, with a wave profile given by $\eta(x,t)$. In a 20 cm wide tank it is not possible to observe clear two–dimensional effects because of the presence of the sidewalls that affect the wave lateral motion. Moreover, from a theoretical point of view, one–dimensional models have been the first tool to explore properties of ISWs, and despite two–dimensional models have been studied since '70s, 1D models are still largely employed today (e.g., see the cited literature in Sec.1.2) with success, since they are simpler to handle but really effective in unveiling the main properties of wave propagation and shoaling. Indeed, most of these properties are then found also in two–dimensional processes (e.g., see Yuan *et al.* [2018a] or Small [2001b]). Thus, one–dimensional models remain a primary tool to explore new features of ISWs at a fundamental level and, as already

discussed in Sec.1.2.1, further extensions to two–dimensional waves can be applied in a second step.
In Sec.1.2.1 we mentioned the possibility to insert a spreading term in vKdV and veKdV equations as done by Small [2001b], making a one–dimensional model two–dimensional to all effects. In the following we give a sketch of this methodology in view of future applications. We want to solve Eq.(3.10), that we report here for convenience:

$$\eta_t + c_0(x)\eta_x + \alpha(x)\eta\eta_x + \alpha_1(x)\eta^2\eta_x + \beta(x)\eta_{xxx} + \nu(x)\eta + S(x)\eta = 0\,, \qquad (4.14)$$

where

$$\nu(x) = \frac{c_0}{2}\left(\frac{1}{M}\frac{\partial M}{\partial x}\right)\,, \quad S(x) = \frac{c_0}{2}\left(\frac{1}{\Delta}\frac{\partial \Delta}{\partial x}\right)\,,$$

are the shoaling and the spreading coefficients, respectively. A set of points on the initial wave front denoting the positions of the ISWs is chosen to specify the different rays. Their propagation directions (as well as the ray directions) are all normal to the wavefront. At the same time, the initial ISWs are assumed to have an eKdV waveform. For each radial the veKdV equation with $S(x) = 0$ is used to predict the wave evolution. The model is run over a period of n time steps, and the phase speed c of the leading wave is used to project the previous wave front forward by a distance $cn\delta t$, along each ray (c varies between the rays due to the cylindrically asymmetrical bathymetry), at the initial ray direction. At the end of n steps, the new distance between the wave front on one ray and that on the next ray is noted. It is possible to calculate $S(x)$ for interior rays through a centered difference, using the linear segments either side of a reference point (say, P):

$$S(x) = \frac{c_0}{2}\left(\frac{1}{\Delta}\frac{\partial \Delta}{\partial x}\right) \sim \frac{c_0}{2}\left(\frac{1}{\Delta_i + \Delta_{i+1}}\frac{\partial(\Delta_i + \Delta_{i+1})}{\partial x}\right) \qquad (4.15)$$

$$\sim \frac{c_0}{2}\left(\frac{1}{(\Delta_i + \Delta_{i+1})_J}\frac{(\Delta_i + \Delta_{i+1})_J - \Delta_i + \Delta_{i+1})_{J-1}}{D_i}\right) \qquad (4.16)$$

where Δ_{i+1} denotes the ray separation between point P on ray i and its adjacent point on the next ray $i+1$, and Δ_i the ray separation between P on ray i and another adjacent point on ray $i-1$; subscripts J and $J-1$ denote the variables at the current time and the previous time, respectively. The propagation distance along ray i for time step δt is given as $D = c\delta t$, in which the phase speed is $c = c_0 + \frac{A}{3}\left(\alpha + \frac{1}{2}\alpha_1 A\right)$, where A is the wave amplitude. Except for at the initial time, the ray direction is calculated after n time steps separately for the internal and boundary points. For an internal point, the ray direction is along the radius of a circle, determined by the point and its two adjacent points, as well depicted by Small [2001b]. For the boundary points, the ray is set perpendicular to the wavefront.
The spreading term $S(x)$ is numerically implemented into the wave evolution equation as follows. If $\eta(x)$ is the output from the veKdV evolution along the ith ray, with no spreading, then the new waveform with spreading taken into account, $\eta_s(x)$, is given by

$$\frac{\partial \eta}{\partial t} = -S(x)\eta \quad \Rightarrow \quad \frac{\eta_s(x) - \eta(x)}{T} = -S(x)\eta(x) \tag{4.17}$$

where T is the time between implementations of the spreading algorithm. The above steps can be then entirely repeated. This algorithm can describe a planar wave evolution with spreading and refraction effects, but as the veKdV model with $S(x) = 0$ (and also the vKP model), it cannot describe the wave–breaking as seen in laboratory experiments or real field. To implement this feature in the algorithm an idea could be to apply a generalized form of our wave–breaking criterion along each wave ray:

$$\int_{-\infty}^{+\infty} \eta(x)\, dx \simeq \frac{h_2^2(x)}{2h_2'(x)}\,, \tag{4.18}$$

where $h_2'(x) = \partial h_2(x)/\partial x$ must be taken positive (it is the equivalent of the slope value s). Once the criterion is satisfied, in that point along that ray wave–breaking it is supposed to occur. Repeating the procedure for each wave ray, we should obtain the shape of the breaking wavefront. However, we stress that the entire procedure, including the wave–breaking implementation, must be performed numerically, and the only way to verify its validity is by fully nonlinear nonhydrostatic numerical simulations (e.g., MITgcm simulations).

* * *

In this chapter we investigated the propagation and shoaling of ISWs over a sloping bottom. First, we examined the propagation and shoaling processes in a wave tank through numerical simulations of vKdV and veKdV equations, using the parameters setting of a real plunging–breaking experiment. The numerical simulations cannot reproduce the breaking and overturning mechanism, but give us some information about the behavior of the two models. As already observed by other authors (e.g., Small [2001a]) the vKdV and the veKdV models behave very differently depending on whether the wave is propagating towards shallower or deeper water.
We also built a semi–analytical model for predicting the wave–breaking location. The model is derived under the mass conservation assumption and through geometrical approximations only. It predicts the breaking location of waves obtained in laboratory experiments with good agreement, and it seems to provide results comparable to or better than previous empirical criteria. In this case, we modelled larger waves with the MCC model, since eKdV waves cannot exist if their limiting amplitude is exceeded.
Then, we applied the analytical and numerical tools discussed in the preceding chapters to the real–field case of the Messina Strait. We performed numerical simulations of ISWs propagating from the Messina Strait to the Capo Vaticano frontal slope. The wave amplitude undergoes several variations along the 40 km bathymetry examined, and the solitary wave structure is retained or not depending on the adiabaticity of the transformation, which has been evaluated through three different methodologies. However, we could observe that the wave retains part of its identity as a soliton until the wave shoals on the Capo Vaticano frontal slope. In that area, the veKdV model ceases to give reliable information since the wave begins

a transition from a soliton with $\alpha_1 < 0$ and $\alpha < 0$ to a soliton with $\alpha_1 < 0$ and $\alpha > 0$ (III–IV quadrant transition of Fig.3.2), which is not allowed: the wave transforms in a dispersive wavetrain, losing completely its identity. The most critical cases are those with large amplitudes and deep pycnoclines, since the waves strongly interact with the bathymetry, and they can even fission in nonadiabatic transition zones. We compared the veKdV simulation results with Grimshaw [2007] analytical theory and our explicit analytical solution. As expected the theory of Grimshaw [2007] works fine in almost all the examined cases, reproducing quite well the simulation results. Our explicit solution for the wave amplitude (3.66) seems to work fine only for small or intermediate amplitudes, reproducing the general trend of the simulation results and the adiabatic theory of Grimshaw [2007]. Thus, our explicit solution seems to have a limited range of application.

Lastly, we applied our wave–breaking model to the case of ISWs propagating along the Gioia Basin and interacting with the Capo Vaticano slope. We identified a "breaking strip", where breaking could take place, on the Capo Vaticano frontal slope. This result is confirmed by the observations of Marullo and Santoleri [1986], the phenomenology observed through SAR imagery and could be linked to the formation of morphobathymetric features present along the Gioia Basin and the Capo Vaticano promontory.

Chapter 5

Mixing induced by ISWs breaking

In this chapter, we will focus on the mixing processes induced by the ISWs breaking on a sloping bathymetry. We will make use of the theory of Winters *et al.* [1995] to study the adiabatic and diabatic processes involved in mixing. Useful definitions of potential energy, background potential energy and available potential energy (APE) will be introduced. In particular, we will calculate the APE of an ISW. Through the Thorpe and Ozmidov length scales we will build a theoretical model to predict the values of mixing efficiency involved in ISWs breaking and we will validate the model through laboratory experiments.

5.1 Energetics of mixing

To mix a stably stratified fluid, energy is required. In a homogeneous fluid, the supply of energy is only that necesssary to overcome mechanical friction. In a stratified fluid, work must be done to raise heavy fluid elements and lower light elements. With their pioneering work, Winters *et al.* [1995] have introduced a conceptual framework that allows the energetics of stratified fluid flows to be described in a unified and systematic manner. Their analysis is based on the notion that, for closed fluid systems, only irreversible, diabatic processes can change the probability density function (p.d.f.) of density. Winters *et al.* [1995] define as *adiabatic* a process in which there is no heat or molecular mass transfer, and simply define as *diabatic* a process that is not adiabatic. To properly quantify the energetics of mixing, Winters *et al.* [1995] partition the changes in potential energy due to diabatic mixing from changes due to adiabatic processes. Assuming that the state of the flow is known within a fixed volume V, the instantaneous potential and kinetic energies of a fluid are defined as

$$E_p(t) = g \int_V \rho(x, y, z, t) z \, dV \,, \tag{5.1}$$

$$E_k(t) = \frac{\rho_0}{2} \int_V \left(u^2 + v^2 + w^2 \right) \, dV \,, \tag{5.2}$$

where ρ is the local instantaneous density field, ρ_0 is a constant reference density, z is the vertical spatial coordinate, u, v, w are the velocities in the x, y, z directions respectively. For adiabatic processes, changes in the fluid potential energy result from the switching of the kinetic energy into potential energy without any diffusive mixing (i.e., no heat or mass transfer occurs). Otherwise, diabatic processes produce the change of the total potential energy of the fluid induced by irreversible molecular diffusion. The instantaneous volume–integrated *background potential energy* is defined as

$$E_b(t) = g \int_V \rho^*(x, y, z, t) z \, dV \,, \tag{5.3}$$

where $\rho^*(x, y, z, t)$ is the density field in the configuration of the minimum potential energy, obtained by sorting the fluid parcels by an adiabatic volume-conserving rearrangement. The background potential energy is evaluated for the density field in the configuration of the minimum potential energy, obtained by sorting the fluid parcels through an adiabatic volume–conserving redistribution of ρ. For this reason, it uniquely depends on the p.d.f. of density and thus it is not affected by the instantaneous spatial distribution of density in the flow domain. Changes in the background potential energy are thus associated with the energy consumed in mixing the fluid and can be used to characterize this process.

The difference between the total potential energy and the background potential energy quantifies the amount of potential energy released in the adiabatic transition from $\rho(x, y, z, t)$ to $\rho^*(x, y, z, t)$ without altering the p.d.f. of density. This amount of energy is called *available potential energy*, since it represents the amount of potential energy stored in the fluid when it is not in gravitational equilibrium [Lorenz, 1955]. It is defined as:

$$E_a(t) = E_p(t) - E_b(t) \,. \tag{5.4}$$

5.1.1 Available Potential Energy (APE) of ISWs

Hebert [1988] and, recently, Lamb [2008] considered that in order to get the correct estimate of the APE of an isolated feature of the flow, one need to assume that the density structure outside the feature extents to infinity. Using symmetric density fields they suggest that the APE of the isolated feature is asymptotically reaching the constant "true" APE value when the domain is extended to infinity. We will calculate APE with and without the spreading out the extents of the domain for the case of ISWs in two-layer fluid. We assume that the wave of amplitude A is propagating in a two–layer fluid with depths of the top layer h_1 and the bottom layer h_2 and densities ρ_1 and ρ_2 (with $\rho_2 > \rho_1$), respectively. The horizontal extents occupied by the wave is $2L_0$. Let us place the coordinate system at the interface between layers. The sorted background state for this system will be the system of two horizontal homogeneous layers. It can be shown that, for such coordinate system, centers of mass of each layer in the reference state are located at half–depths and thus the background potential energy (5.3) is

$$E_b = \int_{-L_0}^{L_0} dx \int_{-h_2}^{0} g\rho_2 z dz + \int_{-L_0}^{L_0} dx \int_{0}^{h_1} g\rho_1 z dz = \frac{1}{2}\left(\rho_1 h_1^2 - \rho_2 h_2^2\right) 2L_0 \,. \quad (5.5)$$

The potential energy E_p of the ISW calculated by (5.1) is

$$E_p = \int_{-L_0}^{L_0} dx \int_{-h_2}^{\eta(x)} g\rho_2 z dz + \int_{-L_0}^{L_0} dx \int_{\eta(x)}^{h_1} g\rho_1 z dz = g\frac{(\rho_2 - \rho_1)}{2} \int_{-L_0}^{L_0} \eta^2(x)\, dx + E_b \,. \quad (5.6)$$

Thus, the avalaible potential energy of the ISW is

$$E_a = \frac{g\Delta\rho}{2} \int_{-L_0}^{L_0} \eta^2(x)\, dx \,. \quad (5.7)$$

If we consider, for example, a KdV solitary wave, with $\eta(x) = A\mathrm{sech}^2\left[(x - c_0 t)/L\right]$, in the limit $L_0 \to \infty$ we get the well–known formula for the half the total energy E_0 of a KdV solitary wave [Bogucki and Garrett, 1993; Bourgault and Kelley, 2003],

$$E_a = \frac{4}{3}\Delta\rho g A^2 L = \frac{E_0}{2} \,. \quad (5.8)$$

We remark that this calculation assumes that the symmetric density structure on both sides of the feature is exactly the same. This condition is unlikely to be fulfilled in practice and thus the method should be used with care for real life situations. In practice, it is more likely that some distant density profile that can be associated with the reference background field will be used for APE calculations.

5.2 Thorpe and Ozmidov length scales

The concept of available potential energy as the potential energy released if the fluid were to be adiabatically rearranged to the state of minimum potential energy was initially introduced by Lorenz [1955]. Lorenz's idea was first applied by Thorpe [1977] for the one–dimensional density profile in lakes. Thorpe's method for empirically estimating the length scales of turbulent overturning in a stratified turbulent flow is useful for the analysis of vertical density profiles when the flow is homogeneous in the horizontal and density inversions are the result of turbulent stirring. The method consists of rearranging or ordering an observed potential density profile, which may contain inversions, into a stable monotonic profile which contains no inversions (see Fig. 5.1). Consider a density profile consisting of n samples of density ρ_n, each of which was observed at depth z_n. If the sample at depth z_n must be moved to depth z_m to generate the stable profile (see Fig. 5.1), the Thorpe displacement is $d_n = z_m - z_n$ [Dillon, 1982]. The *Thorpe length scale* is the root mean square value of the distances d_n:

$$L_T = \langle d^2 \rangle^{1/2} \quad (5.9)$$

The length L_T, can be estimated from fine–scale measurements of density from a free–fall instrument or slowly lowered CTD probe (Galbraith and Kelley [1996];

Gargett and Garner [2008]; Park *et al.* [2014]) by use of a reordering routine or "sorting algorithm" that converts the observed profile into one in which density increases downwards everywhere [Thorpe, 2005].

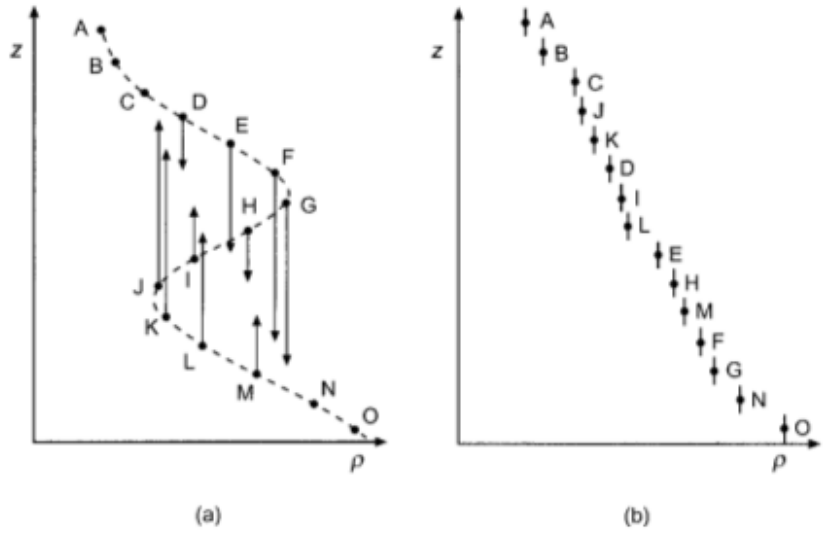

Figure 5.1. The Thorpe's sorting algorithm. This is used to create a stable profile of density with $\mathrm{d}\rho/\mathrm{d}z \leq 0$ shown in (b) from the observed profile, (a), in which there is a statically unstable region where $\mathrm{d}\rho/\mathrm{d}z > 0$. The points, A–O, represent the discrete measured values of density at their respective levels, z. Those between C and N are statically unstable in the sense that, because of the density inversion, there is denser fluid above or less dense below them even though the density only decreases with depth between G and J. The vertical lines and arrows show the displacements in z required to re–sort the observed density profile into the statically stable order shown in (b). The vertical lines in (b) show the depth increments that are represented by the measured density values. From Thorpe [2005].

It is often assumed that temperature can be used as a surrogate to infer density, in freshwater lakes or at temperatures 4°C in the ocean if the relation of temperature to density is monotonic (see Fig. 5.2) [Dillon, 1982; Thorpe, 2005].
Strictly related to the Thorpe scale is the *Ozmidov length scale*, defined as [Dillon, 1982; Lumley, 1964; Ozmidov, 1965; Thorpe, 2005]

$$L_O = \left(\frac{\varepsilon}{N^3}\right)^{1/2}, \tag{5.10}$$

where ε is the turbulent dissipation rate and N is the buoyancy frequency. L_O provides a measure of the vertical size of the largest eddies which may overturn in stably stratified water. The Ozmidov scale can be derived on dimensional grounds provided that the scale of the motion is supposed to be so large that viscosity is negligible, so that ε and N are the only dimensional quantities characterizing the eddies [Dillon, 1982; Osborn, 1980; Ozmidov, 1965; Thorpe, 2005]. Dillon [1982] suggested a linear relationship between L_T and L_O (see Fig.5.3), such that [Park *et al.*, 2014]

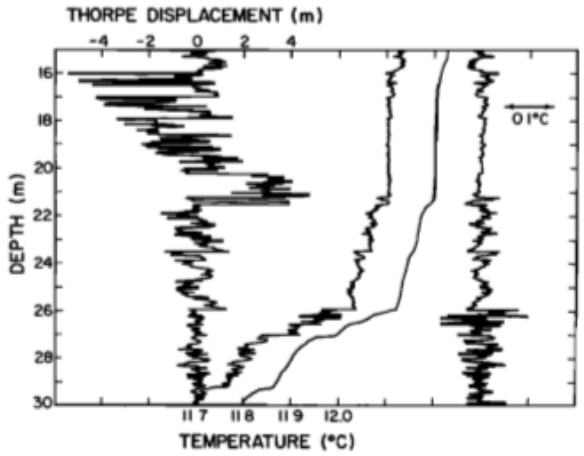

Figure 5.2. From left to right: Thorpe displacements, observed temperature, ordered temperature, and temperature fluctuations (defined as the difference between the ordered and unordered temperature) for a temperature cast from Dillon [1982]. The Thorpe displacement structure has sharp edges and the shape of a reversed z, resembling an overturning eddy. In the interior of the disturbance are fluctuations with displacements nearly as large as the structure; the Thorpe scale for this event is 2.0 m, and the size of the structure is 5 m. The distinctive sharp edges of the displacement suggest that overturning is occurring at the edges of the large feature between 16 and 22 m. From Dillon [1982].

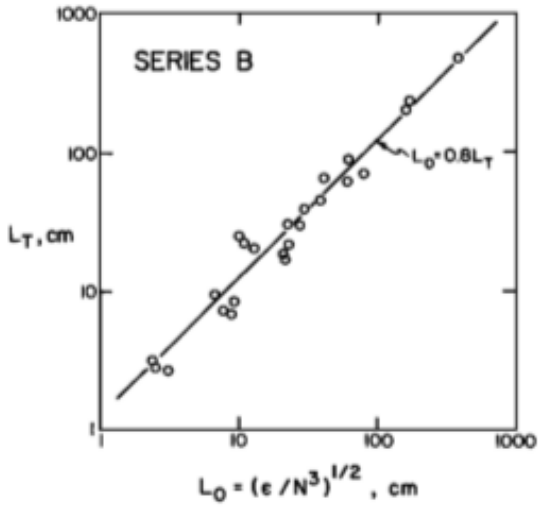

Figure 5.3. The Thorpe scale plotted against the Ozmidov scale for a series of high-wind oceanic casts of Dillon [1982]. The line drawn represents the equation $L_O = 0.8 L_T$. A striking correlation between L_O and L_T is seen over nearly three decades. From Dillon [1982].

$$L_O = 0.8(\pm 0.4) L_T \,. \tag{5.11}$$

We give also some information about another fundamental length scale: the *Kolmogorov length scale*. On dimensional grounds, the scale of the turbulent motions at which viscous dissipation becomes significant must depend on the turbulent dissipation rate ε, i.e. the rate at which kinetic energy is supplied to the smallest eddies, which characterizes the turbulent motion, and the kinematic viscosity ν, which characterizes viscous effects and smears out the velocity gradients of the smallest eddies; no other dimensional and relevant quantities are available to characterize the length scale. Therefore, to have the dimensions of a length, this scale must be proportional to $(\nu^3/\varepsilon)^{1/4}$ [Thorpe, 2005]. Note, in fact, that ε has dimensions L^2 T^{-3} and ν has dimensions L^2 T^{-1}. The coefficient of proportionality is about unity and the scale is known as the Kolmogorov length scale

$$L_K = \left(\frac{\nu^3}{\varepsilon}\right)^{1/4} \tag{5.12}$$

The oceanic values of ε lead to a range of L_K from about $6 \cdot 10^{-5}$ m in very turbulent regions to 0.01 m in the abyss [Thorpe, 2005]. The following relationship between the size of L_K relative to the large–eddy length scale l can be determined (see Kundu *et al.* [2016])

$$L_K \sim \mathrm{Re}_l^{-3/4}\, l\,. \tag{5.13}$$

with $\mathrm{Re}_l = Ul/\nu$ outer scale Reynolds number. Thus, we can infer that the sizes of the largest and smallest eddies in high Reynolds number turbulence potentially differ by many orders of magnitude.

5.3 Heuristic model for mixing induced by breaking ISWs

As already seen in Sec.1.3, for mixing processes induced by ISWs breaking, Michallet and Ivey [1999] and Helfrich [1992] give the following definition (in their notation):

$$\epsilon = \frac{\Delta E_p}{E_0 - E_R} = \frac{\Delta E_p / E_0}{1 - R}\,, \tag{5.14}$$

where ΔE_p is the difference between the final and the initial potential energy, E_0 is the wave incident energy and E_R is the energy of reflected wave, and $R = E_R/E_0$ is the reflectance coefficient. Michallet and Ivey [1999] calculated ΔE_p through the formula

$$E_p = \int_{-H}^{0} \rho g z B(z) dz\,, \tag{5.15}$$

evaluated for final and initial density profiles, and with $B(z) = L + L_s(1 + z/H)$, which represents the trapezoidal region at depth z, where L is the length of the tank before the start of the slope, H is the total water depth $L_s = H/s$ is the horizontal extent of the sloping boundary, and s is the slope. An analogous definition has been used by Helfrich [1992], who isolated only the triangular region at depth z starting from the toe of slope, given by $B(z) = L_s(1 + z/H)$. Since, ΔE_p represents the

increase in the irreversible potential energy caused by wave breaking on the slope [Bourgault and Kelley, 2007], we will indicate it as ΔE_b, i.e., the change in the background potential energy, in view of what explained in Sec. 5.1. Michallet and Ivey [1999] calculate the incident wave energy E_0 as

$$E_0 = c_0 g \Delta\rho \int_{t_0}^{t_1} \eta^2(t)\, dt\,, \tag{5.16}$$

where t_0 and t_1 are appropriate times chosen to compute the wave energy. (5.16) can be rewritten through a change of variable as

$$E_0 = g\Delta\rho \int_{x_1}^{x_2} \eta^2(x)\, dx \simeq g\Delta\rho \int_{-\infty}^{+\infty} \eta^2(x)\, dx\,. \tag{5.17}$$

Although both Bourgault and Kelley [2007] and Aghsaee *et al.* [2010] give a parametrization for the reflectance coefficient (see Sec.1.3), here, for simplicity, we suppose that $E_R \ll E_0$, and we write

$$\epsilon \simeq \frac{\Delta E_b}{E_0} = \frac{\Delta E_b}{2E_a} = \frac{\Delta E_b}{g\Delta\rho \displaystyle\int_{-\infty}^{+\infty} \eta^2(x)\, dx}\,,$$

where we used the relation (5.7) (or (5.17)). This is good formulation for ϵ when $E_R \ll E_0$, but forces us to stay in a specific model framework, such as KdV, eKdV, MCC, or so, because of the necessity to evaluate theoretically the wave profile, and it needs the specification of initial and final density profiles to evaluate ΔE_b. We want to make a step further trying to estimate the mixing efficiency starting from the initial and final density profile only.
Since the Kolmogorov length scale is defined as in (5.12), using the definition of the Ozmidov scale (5.10), we can write:

$$L_\mathrm{K} \sim \left(\frac{\nu^3}{\varepsilon}\right)^{1/4} \sim \left(\frac{\nu^3}{L_0^2 N^3}\right)^{1/4} \sim \mathrm{Re}^{-3/4} l\,.$$

Thus,

$$\left(\frac{\nu^3}{L_O^2 N^3}\right)^{1/4} \sim \mathrm{Re}^{-3/4} l \quad \Rightarrow \quad L_O^2 \sim \frac{\nu^3 \mathrm{Re}^3}{L_O^4 N^3} = \frac{\nu^3 \dfrac{c_0^3 L_O^3}{\nu^3}}{N^3 L_O^4} = \frac{c_0^3}{N^3 L_O}\,,$$

since $l = L_O$, and we average the buoyancy frequency over the fluid depth so as to have a reference value to work with:

$$\langle N \rangle = \frac{1}{H} \int_{-H}^{0} \sqrt{-\frac{g}{\rho_2} \frac{\mathrm{d}\rho(z)}{\mathrm{d}z}}\, dz\,.$$

Therefore, we write the Ozmidov scale as

$$L_O = \frac{c_0}{\langle N \rangle}\,.$$

The available potential energy of an overturn can be defined as ([Chalamalla and Sarkar, 2015; Ivey and Imberger, 1991])

$$E_a \propto \Delta\rho g L_T \propto g\frac{\mathrm{d}\rho}{\mathrm{d}z}L_T^2 \propto N^2 L_T^2\,,$$

but, since $L_O = 0.8(\pm 0.4)L_T$, E_a can be thought as the APE expended to generate the largest eddies which may overturn in stably stratified water. If we suppose that the incident wave energy is completely expended to generate an overturn, i.e. $E_0 = 2E_a \propto 2N^2(L_O^2/0.64)$, we rewrite the mixing efficiency as

$$\epsilon \propto \frac{\Delta E_b}{2\langle N\rangle^2 L_T^2} = \frac{\Delta E_b}{2\langle N\rangle^2 (L_O/0.8)^2} = \frac{\Delta E_b\, 0.64}{2c_0^2}\,. \tag{5.18}$$

Comparing the expression in (5.18) with the data for ϵ obtained from laboratory experiments (see next section), we expect to find a close relation between the theoretical and the experimental results for the mixing efficiency.

5.4 Experimental validation of the model

Mixing caused by breaking ISWs can be quantified by the energy budget method of Winters et al., which has been widely used in the literature (see, e.g., Fragoso *et al.* [2013]; La Forgia *et al.* [2018b]; Ottolenghi *et al.* [2016a,b]).
The energy lost for irreversible mixing can be evaluated by calculating the change in background potential energy between successive states of the system. However, though the rate of change of the background potential energy can be thought as a direct measure of mixing [Winters *et al.*, 1995], the mixing efficiency can more effectively represent the amount of mixing since it quantifies the fraction of energy consumed by irreversible diabatic mixing related to the amount of energy available to support this process. Following the approach of Michallet and Ivey [1999], we evaluate the mixing efficiency through the relation (5.14) with ΔE_b in place of ΔE_p:

$$\epsilon = \frac{\Delta E_b}{E_0 - E_R}\,. \tag{5.19}$$

We performed a series of laboratory experiments (see Tab. 5.1), in which the density fields are evaluated using dye as tracer. In each experiment, a constant value of 30 kg/m^3 is used as density difference between the two layers in the ambient fluid region. Thus the reduced gravity g' is similar to the values measured in real field conditions (e.g., Marullo and Santoleri [1986]). Following the same method used by Theiler and Franca [2016] and La Forgia *et al.* [2018a], at the end of each experiment, we acquired several images characterized by a known concentration of dye. Then, for each pixel of the image, we obtained a relation between the amount of the uniformly distributed dye in the tank, and the grey scale values. The ratio between the maximum range of density and the grey scale levels (i.e., approximately 0.1 kg/m^3) can be considered a measure of the error associated to the evaluation of the instantaneous density fields. In this way, we derived the initial and the final (after wave–breaking) density stratifications (see Fig 5.4a and Fig 5.4b) for each experiment. Comparing Fig 5.4a and Fig 5.4b, it is easy to see that the pycnocline interface has become thicker after

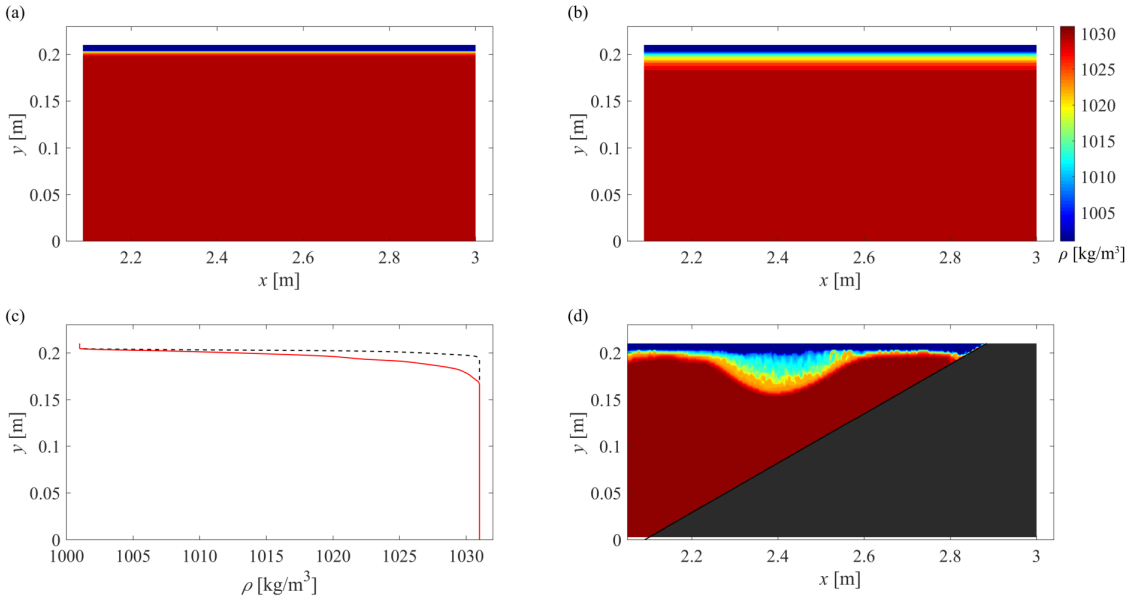

Figure 5.4. (a) Initial and (b) final (after wave–breaking) density stratifications. Comparing (a) and (b), it is easy to see that the pycnocline interface has become thicker after the wave–breaking. An intermediate–density layer between the upper layer 1 and the bottom layer 2 has been created. (c) Initial and final density profiles. The initial profile (black dashed line) is really sharp (almost two–layer stratification), while the final profile is smoother, indicating the presence of new intermediate values of density between ρ_1 and ρ_2. (d) Sample of wave propagation over the slope in our experiments seen through image analysis. For the geometrical properties of the wave and the two layers, see also Tab.5.1

the wave–breaking. Indeed, a fraction of the lighter fluid with density ρ_1 has been mixed with a fraction of the heavier fluid with density ρ_2 by the breaking process, and an intermediate–density layer between the upper layer 1 and the bottom layer 2 has been created. This can be argued also from the density profiles in Fig. 5.4c, where we can see the initial, sharp stratification (almost two–layer stratification), and the final, "smoothed" density profile, indicating the presence of new intermediate values of density between ρ_1 and ρ_2.

Analyzing the profiles of the incident waves, we extracted the information in Tab. 5.1 about layers depth, amplitudes, and wavelengths. From these parameters, for a given slope value s, it is possibile to derive the Iribarren number (Tab. 5.1). Furthemore, analyzing both incident and reflected wave profiles and applying relation (5.17), we can derive the energies E_0 and E_R, respectively. The change in background potential energy ΔE_b has been evaluated through the sorting method of Winters *et al.* [1995] described in Sec.5.1, for each experiment.

This procedure allowed us to derive experimental values of the mixing efficiency, ϵ_{exp}, reported in Fig. 5.5 as a function of the Iribarren number. In the same plot, the results of Michallet and Ivey [1999] and Arthur and Fringer [2014] are also reported. Our results seem to be in good agreement with those of Michallet and Ivey [1999] (here we did not consider the large errorbars present in the original plot of Michallet

Table 5.1. Parameters of the laboratory experiments. h_1 upper layer thickness, h_2 bottom thickness, $|A|$ absolute value of the wave amplitude, λ wavelength, s slope value, Ir Iribarren number.

Exp.	h_1 (cm)	h_2 (cm)	$\|A\|$ (cm)	λ (cm)	s	Ir
1	1.10	19.90	3.87	24.73	0.29	0.73
2	1.46	19.54	1.75	14.64	0.29	0.84
3	0.54	12.19	2.71	23.49	0.17	0.46
4	1.15	11.84	2.60	20.91	0.16	0.40
5	0.85	12.15	2.26	17.58	0.25	0.62
6	0.87	12.13	2.60	19.65	0.19	0.48
7	0.87	12.13	2.60	19.48	0.27	0.66

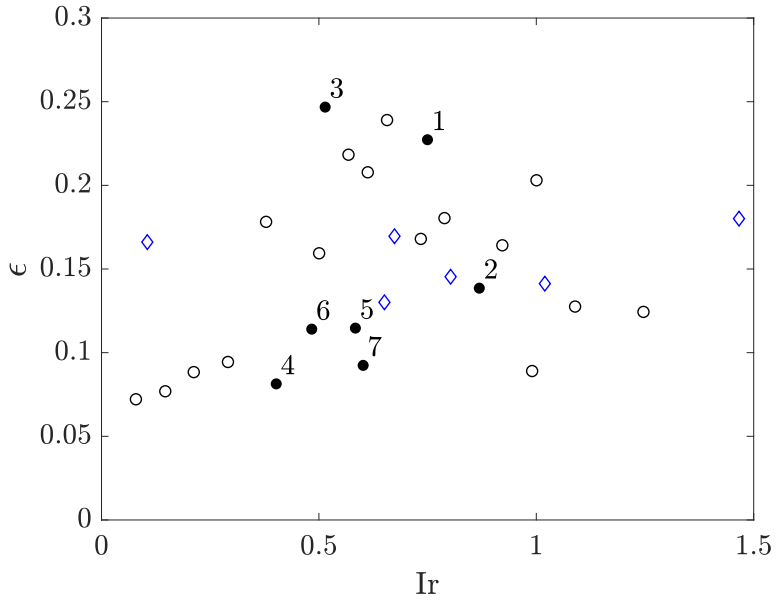

Figure 5.5. Comparison between our experimental results for ϵ (black numbered filled dots) and those from experiments of Michallet and Ivey [1999] (empty circles) and numerical simulations of Arthur and Fringer [2014] (diamonds). Our values for ϵ have been calculated by (5.19), re–sorting the density profiles (through Winters'method) to evaluate E_b.

and Ivey [1999]), though a definite data trend cannot be actually argued. What we can infer from these results is that the mixing efficiency peaks around $\epsilon \simeq 0.25$, for Ir $\simeq 0.8$ in Michallet and Ivey [1999] and for Ir $\simeq 0.5$ in our experimental data. For Ir < 0.8 our results and those of Michallet and Ivey [1999] show a similar trend, with ϵ increasing for increasing values of Ir. For Ir > 0.8, a part for our points 5 and 7, the general trend is in relative agreement with that of Michallet and Ivey [1999]. However, the large point dispersion in the Michallet and Ivey [1999] dataset prevent us from making objective observations.
As already observed by Boegman *et al.* [2005] the plunging breaker (Ir < 1) area seems to be the zone with the highest values of mixing efficiency. This is probably due to the fact that for low values of Ir, the wave slope is steep relative to s and the wave propagation over the slope approaches that of a wave in a fluid of constant depth, thus $R \to 0$ and viscosity dominates with minimal wave energy converted to an increase in the potential energy of the system through diapycnal mixing. Conversely, for waves with very large Ir, the time scale of wave–slope interaction is small, $R \to 1$, and the collapsing breakers again induce minimal mixing. The inertia of these waves appears unable to overcome the stabilizing effect due to buoyancy. Intermediate to these extremes, plunging breakers develop with gravitational instabilities that drive mixing efficiencies, peaking near 25% [Boegman *et al.*, 2005]. We reported the data of Arthur and Fringer [2014] simulations for completeness only, since they show a really different behavior from our experimental data and those of Michallet and Ivey [1999]. We refer the reader to the paper of Arthur and Fringer [2014] for further details about these discrepancies.
Since our data seem to be in good agreement with those of Michallet and Ivey [1999], we can use them to validate our theoretical model, described in Sec.5.3. To look for some proportionality relatioships, the experimental results, ϵ_{exp}, are plotted (with a x–log scale) against the theoretical values, ϵ_o (obtained using the Ozmidov length scale) in Fig. 5.6a. As we can see, there is a linear relationship (in a semilog scale) between ϵ_o and ϵ_{exp} (Fig.5.6b-c). Only for the experiment 2 we find a discrepancy. Actually, this is correct, since the experiment 2 has an Iribarren number value of 0.8, thus the breaking process will be closer to a collapsing than to a plunging mechanism. This means that the maximum overturning lengthscale (the Ozmidov scale) will be not reached, and the relationship between ϵ_o and ϵ_{exp} breaks down. Thus, now we can derive an empirical law that connects the ϵ_o and the ϵ_{exp} through an exponential fit (linear fit in a semilog scale), as reported in Fig.5.6b-c, and we obtain:

$$\epsilon_o = a e^{b\epsilon_{\text{exp}}} \quad \Rightarrow \quad \epsilon_{\text{exp}} = \frac{\log(\epsilon_o/a)}{b}\,, \tag{5.20}$$

with $a = 1.84 \cdot 10^{-6}$ and $b = 10.21$.
Hence, in the end, we found that a non–linear relationship can directly connect the mixing efficiency evaluated only knowing the initial and final density stratification and the mixing efficiency obtained through laboratory experiments of shoaling and breaking ISWs. Furthermore, the theoretical expression (5.18) is strictly related to the Thorpe length which is a quantity easily measureable through CTD casts in the ocean.

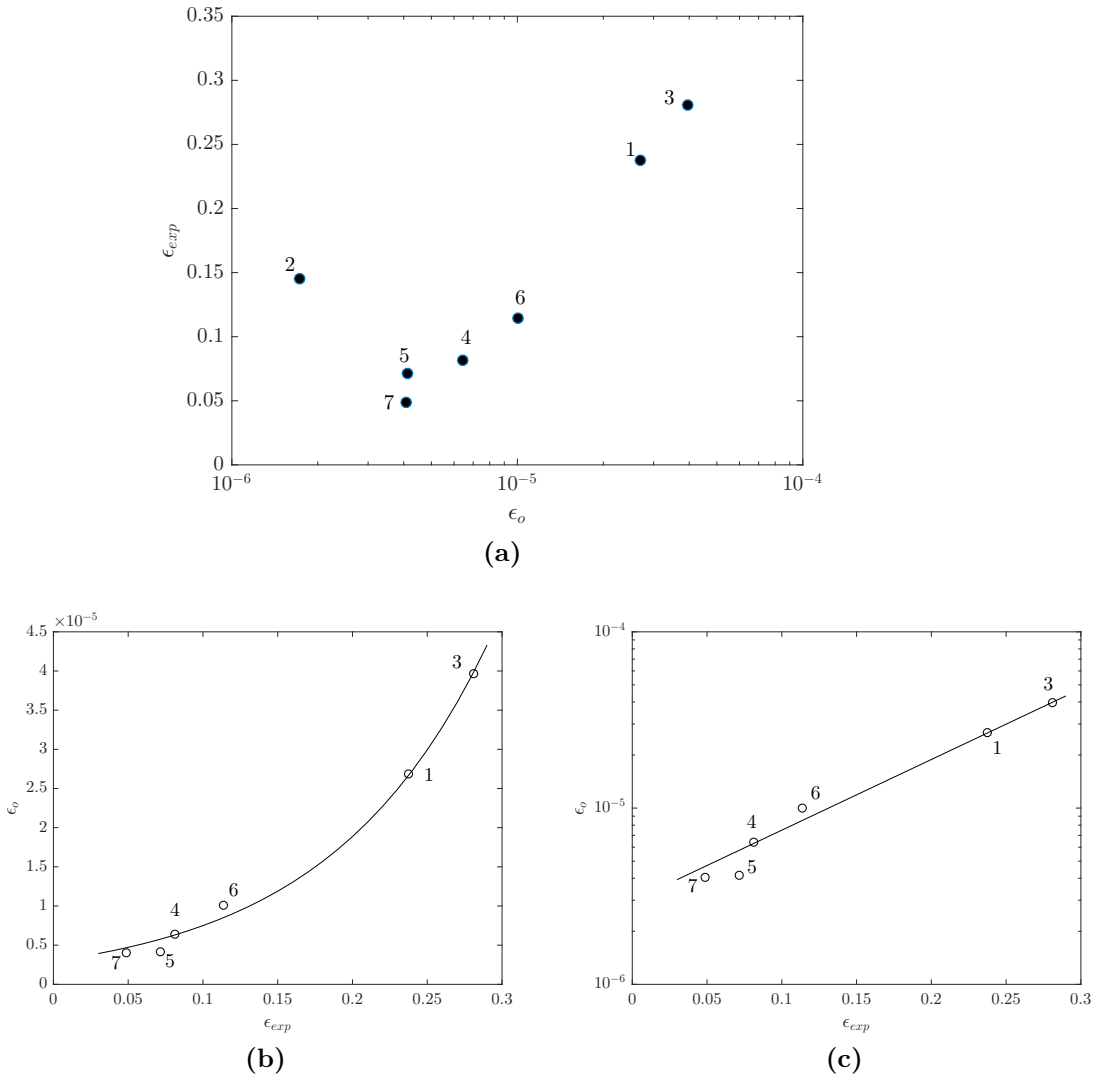

Figure 5.6. (a) Plot of data from image analysis of laboratory experiments and theoretical values (Eq.(5.18)) for the mixing efficiency. Experiment 2 has an Iribarren number value of 0.8, thus the breaking process will be closer to a collapsing than to a plunging mechanism. This means that the maximum overturning lengthscale (the Ozmidov scale) will be not reached, and the relationship between ϵ_o and ϵ_{exp} breaks down. (b) Exponential fit $\epsilon_o = ae^{b\epsilon_{\text{exp}}}$, with $a = 1.84 \cdot 10^{-6}$ and $b = 10.21$, for experiments in (a) (experiment 2 excluded). (c) y–log scaled version of (b). From (b) and (c) we can see the striking exponential relationship that exists between ϵ_o and ϵ_{exp}.

* * *

In this chapter, we studied the mixing processes induced by ISWs breaking. We used the theoretical framework of Winters *et al.* [1995] to describe the energetics of a stratified fluid flow, introducing the concepts of potential energy, background potential energy and available potential energy. In particular, the available potential energy (APE) represents the amount of energy stored in the system when it is not in gravitational equilibrium. We calculated the APE of an ISW of depression in a two–layer system, assuming that the symmetric density structure on both sides of the feature is exactly the same. We built an heuristic model to derive mixing efficiency (ϵ) values related to ISWs breaking in laboratory experiments starting from the definition of ϵ given by Michallet and Ivey [1999],

$$\epsilon = \frac{\Delta E_b}{E_0 - E_R}. \tag{5.21}$$

The formula derived for ϵ,

$$\epsilon \simeq \frac{\Delta E_b}{g\Delta\rho \displaystyle\int_{-\infty}^{+\infty} \eta^2(x)\, dx}\,, \tag{5.22}$$

represents a good formulation when the reflected wave energy is negligible with respect to the incident wave energy ($E_R \ll E_0$). However, this representation requires to assume a reference wave model (such as KdV, eKdV, MCC or DJL), and to have prior knowledge of the initial and final density profiles to evaluate ΔE_b. To avoid this, we derived a theoretical bulk formula for ϵ by means of the Thorpe and Ozmidov length scales. We compared the results for the mixing efficiency calculated through the definition of Michallet and Ivey [1999] from laboratory experimental data with those evaluated through our mixing efficiency formula, and we obtained a striking exponential correlation. From an exponential fit we extracted the parameters to write an empirical relation that connects this last formulation to (5.21):

$$\epsilon_o = a e^{b\epsilon_{\exp}} \tag{5.23}$$

This allows us to evaluate the mixing efficiency in ISWs breaking phenomena knowing the initial and final density stratification only.

Chapter 6

Conclusions

In the present thesis, we studied the propagation, the shoaling and the breaking of internal solitary waves (ISWs) over a varying bathymetry through analytical and numerical methods. We examined the evolution of the ISWs in the framework of the vKdV (Eq.(3.55)) and veKdV (Eq.(3.56)) weakly–nonlinear models, since they are suitable for the description of unsteady internal solitons. After a description of the steady–state KdV (Eq.(2.51)) and eKdV (Eq.(2.53)) models for a two–layer environment, we briefly derived the slowly–varying solutions to vKdV and veKdV equations, (3.60) and (3.61), respectively. In particular, we followed the asymptotic expansions approach of Grimshaw [2007] to derive the adiabatic solution to the veKdV equation, which allows to define the possible transitions between different ISW structures. In fact, the sign of the coefficients $\alpha(x)$ and $\alpha_1(x)$ of the veKdV equation determines four soliton families in the (α, α_1) plane. In particular, for solitons with $\alpha_1 < 0$, the transition between states with $\alpha < 0$ and $\alpha > 0$ is not allowed, leading to the wave annihilation in a train of dispersive waves. Since the solution of Grimshaw [2007] has to be calculated solving numerically the trascendental relationship (3.36) for the parameter B (which is strictly related to the other parameters of the equation), we derived an explicit slowly–varying solution for the veKdV equation (Eq.(3.66)). This solution comes from a Taylor series expansion for $|\sqrt{b}(x)| < 1$ of the trascendental relationship (3.65) for the wave amplitude equivalent to that of Grimshaw [2007], but derived through an easier procedure.

Then, we investigated the propagation and shoaling of ISWs in a wave tank through numerical simulations of vKdV and veKdV equations, using the parameters setting of a real plunging–breaking experiment. The numerical simulations cannot reproduce the breaking and overturning mechanism, but give us some information about the behavior of the two models. As already observed by other authors (e.g., Small [2001a]) the vKdV and the veKdV models behave very differently depending on whether the wave is propagating towards shallower or deeper water.

We also built a semi–analytical model for predicting the wave–breaking location. This model is quite simple, since it is derived under the mass conservation assumption and through geometrical approximations only. However, it predicts the breaking location of waves obtained in laboratory experiments with good agreement, and it seems to provide results comparable to or better than previous empirical criteria. In this case, we modelled larger waves with the MCC model, since eKdV waves cannot

exist if their limiting amplitude is exceeded.
The analytical and numerical tools discussed in the first part of this thesis, have been then applied to the real–field case of the Messina Strait. We performed numerical simulations of ISWs propagating from the Messina Strait to the Capo Vaticano frontal slope. The wave amplitude undergoes several variations, and the solitary wave structure is retained or not depending on the adiabaticity of the transformation, which has been evaluated through three different methodologies. We observed that, despite the simulated wave travels for about 40 km along the bathymetry, it survives to the bathymetric variations almost unaltered. In general, we could observe that the wave retains part of its identity as a soliton until the wave shoals on the Capo Vaticano frontal slope. In that area, the veKdV model ceases to give reliable information since the wave begins a transition from a soliton with $\alpha_1 < 0$ and $\alpha < 0$ to a soliton with $\alpha_1 < 0$ and $\alpha > 0$, which is not allowed. Thus, we observe the wave transforming in a dispersive wavetrain, losing completely its identity. The most critical cases are those with large amplitudes and deep pycnoclines, since the wave strongly interact with the bathymetry, and it can even fission in nonadiabatic transition zones. We compared the veKdV simulation results with Grimshaw [2007] analytical theory and our explicit analytical solution (3.66). As expected the theory of Grimshaw [2007] works fine in almost all the examined cases, reproducing quite well the simulation results. Our explicit solution seems to work fine only for small or intermediate amplitudes, reproducing the general trend of the simulation results and the adiabatic theory of Grimshaw [2007]. Thus, our explicit solution seems to have a limited range of application.
We applied our wave–breaking model to the case of ISWs propagating along the Gioia Basin and interacting with the Capo Vaticano slope. We identified a "breaking strip", where breaking could take place, on the Capo Vaticano frontal slope. This result is confirmed by the observations of Marullo and Santoleri [1986] and the phenomenology observed through SAR imagery.
Finally, we studied the mixing processes induced by ISWs breaking. We used the theoretical framework of Winters *et al.* [1995] to describe the energetics of a stratified fluid flow, introducing the concepts of potential energy, background potential energy and available potential energy. Changes in the background potential energy are associated with the energy consumed in mixing the fluid and can be used to characterize this process. The available potential energy (APE) represents the amount of energy stored in the system when it is not in gravitational equilibrium. We calculated the APE of an ISW of depression in a two–layer system, assuming that the symmetric density structure on both sides of the feature is exactly the same. In this way, the APE converges to a constant value considering the domain extending to infinity. We built an heuristic model to derive mixing efficiency (ϵ) values involved in ISWs breaking starting from the definition of ϵ (5.21) given by Michallet and Ivey [1999]. Through some approximation, we derived the formula (5.22) for ϵ (not too different from that of Michallet and Ivey [1999]), that represents a good formulation when $E_R \ll E_0$, i.e., when the reflected wave energy is negligible with respect to the incident wave energy. However, this representation forces us to stay in a specific model framework, such as KdV, eKdV, MCC, and to know both initial and final density profiles to evaluate ΔE_b. Defining the Thorpe and Ozmidov length scales we derived a theoretical bulk formula for ϵ. We compared the results

for the mixing efficiency calculated through the definition of Michallet and Ivey [1999] from laboratory experimental data with those evaluated through our mixing efficiency formula, and we obtained a striking exponential correlation (Eq.(5.23)). From an exponential fit we extracted the parameters to write an empirical relation that connects the two formulations. This allows us to evaluate the mixing efficiency in ISWs breaking phenomena knowing the initial and final density stratification only.

Appendices

Appendix A

Surface and interfacial gravity water waves

A.1 Preliminaries

The equations of motion for a fluid particle can be obtained on the basis of Newton's law of conservation of momentum, considering the effect of a pressure force and of a body force (such as gravity) acting on a fluid element (see Stoker [1957], **?** or Kundu *et al.* [2016]) . What we get are the well-known *Euler equations*:

$$\boldsymbol{u}_t + \boldsymbol{u} \cdot \nabla \boldsymbol{u} = -\frac{\nabla p}{\rho} + \boldsymbol{g} \tag{A.1}$$

where $\boldsymbol{u} = (u, v, w)$ is the velocity field, and $\boldsymbol{g} = (0, 0, -g)$ is the gravity force. If viscous effects are not negligible, which is commonly true near the boundaries of the flow field, we have to add a friction term $\nu\Delta\boldsymbol{u}$, obtaining the *Navier–Stokes equations*

$$\frac{\mathrm{D}\boldsymbol{u}}{\mathrm{D}t} = -\frac{\nabla p}{\rho} + \boldsymbol{g} + \nu\Delta\boldsymbol{u} \tag{A.2}$$

where

$$\frac{\mathrm{D}}{\mathrm{D}t} \equiv \partial_t + \boldsymbol{u} \cdot \nabla$$

is the *material derivative*, $\Delta \equiv \nabla^2$ is the *Laplacian operator* and ν is the *kinematic viscosity coefficient*.
In the Navier–Stokes equations too many unknown variables are involved: we have three scalar equations versus five scalar unknowns. Thus, we introduce two other equations:

$$\rho_t + \nabla \cdot (\rho \boldsymbol{v}) = 0\,, \tag{A.3}$$

$$p = p(\rho, S)\,, \tag{A.4}$$

which are, respectively, the *continuity equation* and the *equation of state*. The first one states the conservation of mass and the second one is a thermodynamic relation among the pressure p, the density ρ and the entropy S.

Let us consider an incompressible fluid, i.e. with $\rho \simeq$ const, which is the case of water. Using eq.(A.3) we have:

$$\nabla \cdot \boldsymbol{u} = 0\,. \tag{A.5}$$

For

$$(\boldsymbol{u} \cdot \nabla)\boldsymbol{u} = \frac{1}{2}\nabla|\boldsymbol{u}|^2 - \boldsymbol{u} \times (\nabla \times \boldsymbol{u})\ , \tag{A.6}$$

we can write the rotor of the Euler equations as

$$(\nabla \times \boldsymbol{u})_t - \nabla \times (\boldsymbol{u} \times \boldsymbol{\omega}) = 0\,, \tag{A.7}$$

where $\boldsymbol{\omega} = \nabla \times \boldsymbol{u}$ is known as *vorticity*. Then,

$$\boldsymbol{\omega}_t = \nabla \times (\boldsymbol{u} \times \boldsymbol{\omega})\ . \tag{A.8}$$

Thus, we notice that if $\boldsymbol{\omega} = 0$ at $t = 0$, we have that

$$\boldsymbol{\omega}_t = 0 \ \ \Rightarrow \ \ \boldsymbol{\omega} = 0 \ \ \forall t\,,$$

that is, there is no vorticity along all the motion.
Let us now study hydrodynamic phenomena with zero vorticity. In this situation, we can express the velocity field as the gradient of a scalar *velocity potential* ϕ. In fact, if the domain is simply connected, we have:

$$\boldsymbol{\omega} = \nabla \times \boldsymbol{u} = 0 \ \ \Rightarrow \ \ \exists \phi \ : \boldsymbol{u} = \nabla\phi\,.$$

Hence, for the incompressibility condition,

$$\nabla \cdot \boldsymbol{u} = 0 \ \ \Rightarrow \ \ \nabla \cdot \nabla\phi = 0 \ \ \Rightarrow \ \ \Delta\phi = 0\,,$$

that is, ϕ is a harmonic function.
We now write the Euler equations in terms of ϕ:

$$(\nabla\phi)_t + \frac{1}{2}\nabla|\nabla\phi|^2 - \frac{\boldsymbol{g}}{\rho} + \frac{\nabla p}{\rho} = 0\,.$$

Integrating over the spatial variables and setting the integration constant equal to zero[1], we obtain

$$\phi_t + \frac{1}{2}|\nabla\phi|^2 + gz + \frac{p}{\rho} = 0 \tag{A.9}$$

which is known as *Bernoulli equation*. This equation represents a simplified version of the Euler equations because we are now dealing with only one scalar object (ϕ), instead of the three scalar components of $\boldsymbol{u}$.

[1] This can be done by means of a gauge transformation on ϕ or absorbing the constant into the potential ϕ. See Stoker [1957] or **?** for details.

A.2 Surface water waves

Let us now consider an incompressible fluid with a free surface and a flat bottom that obeys the Euler equation (A.1) and the mass continuity equation (A.5). The free surface at the top of the fluid is at $z = \eta(x, y, t)$, where η is the *surface elevation*, the mean position of the free surface is at $z = 0$ and the bottom of the fluid, assumed flat, is at $z = -H$. We write the following equation for the free surface

$$z - \eta(x, y, t) \doteq \zeta(x, y, z, t) = 0\,. \tag{A.10}$$

The free surface separates the fluid from some other medium (e.g. air) and has the property that any particle which is once on it remains on it. Roughly, particles can't leave the fluid going from water to air. If we differentiate ζ with respect to t:

$$\frac{\mathrm{D}\zeta}{\mathrm{D}t} = \zeta_t + \boldsymbol{u} \cdot \nabla\zeta = 0\,,$$

which becomes

$$\zeta_t + \nabla\phi \cdot \nabla\zeta = 0\,,$$

and for (A.10) we have

$$-\eta_t - \phi_x\eta_x - \phi_y\eta_y + \phi_z = 0\,,$$

and finally

$$\phi_z = \eta_t + \phi_x\eta_x + \phi_y\eta_y\,.$$

On the free surface the Bernoulli equation must hold, that is

$$\phi_t + \frac{1}{2}\left(\phi_x^2 + \phi_y^2 + \phi_z^2\right) + \frac{p}{\rho} + g\eta = 0\,,$$

The potential ϕ satisfies the irrotationality condition in the interior of the fluid:

$$\Delta\phi = 0\,, \quad -H \le z \le \eta\,.$$

Furthermore, we impose the bottom impermeability:

$$\phi_z = 0\,, \quad z = -H\,.$$

To summarize, the following equations describe the surface water waves problem:

$$\begin{aligned}
\phi_z &= \eta_t + \phi_x\eta_x + \phi_y\eta_y\,, && z = \eta(x, y, t)\\
\phi_t + \frac{1}{2}\left(\phi_x^2 + \phi_y^2 + \phi_z^2\right) + \frac{p}{\rho} + g\eta &= 0\,, && z = \eta(x, y, t)\\
\Delta\phi &= 0\,, && -H \le z \le \eta\\
\phi_z &= 0\,, && z = -H\,.
\end{aligned}$$

A.2.1 Shallow and deep water waves

We choose the x–axis in the direction of wave propagation with the z–axis vertical so that the motion is two–dimensional in the x–z plane. Let $\eta(x,t)$ denote the surface elevation from its undisturbed location $z=0$.
Our water waves equations become

$$\phi_z = \eta_t + \phi_x \eta_x \,, \qquad z = \eta(x,t) \tag{A.11}$$

$$\phi_t + \frac{1}{2}\left(\phi_x^2 + \phi_z^2\right) + \frac{p}{\rho} + g\eta = 0 \,, \qquad z = \eta(x,t) \tag{A.12}$$

$$\Delta\phi = \phi_{xx} + \phi_{zz} = 0 \,, \qquad -H \le z \le \eta \tag{A.13}$$

$$\phi_z = 0 \,, \qquad z = -H \,. \tag{A.14}$$

Usually, p along the free surface is a constant atmospheric pressure, which is taken as zero: $p_{|z=\eta} = 0$. Thus, (A.12) becomes

$$\phi_t + \frac{1}{2}\left(\phi_x^2 + \phi_z^2\right) + g\eta = 0 \,, \tag{A.15}$$

We notice that an exact analytic solution of the linear partial differential equation (A.13) with the nonlinear surface boundary conditions (A.15) and (A.11) is generally impossible, although approximate solutions can be found in special limits. If the amplitude of the wave is small with the horizontal scale, then the boundary conditions become linear partial differential equations. Furthermore, if the bottom of the domain is horizontal, then explicit analytic solutions can be found Sutherland [2010].
Following the approach of Stoker [1957], we assume that the amplitude of the surface elevation $z=\eta(x,t)$, the velocity potential ϕ, and their derivatives are small. Thus, η and ϕ can be expanded in power series with respect to a small parameter ε (which represents the small wave amplitude). It is also possible to follow the approach of **?** or Sutherland [2010], expanding the functions of $z=\eta(x,t)$ at $z=0$ (a known location), with η small, by Taylor series:

$$f(\eta) \simeq f(0) + \eta f'(0) + \cdots \,,$$

which ensures the same results of the first method.
Substituting in (A.11) and in (A.15) the expansions for η and ϕ

$$\eta(x,t) = \eta_0(x,t) + \varepsilon\eta_1(x,t) + \varepsilon^2\eta_2(x,t) + \cdots$$

$$\phi(x,z,t) = \phi_0(x,z,t) + \varepsilon\phi_1(x,z,t) + \varepsilon^2\phi_2(x,z,t) + \cdots \,,$$

keeping only the linear terms, and neglecting the products of η and ϕ smaller than the linear terms, we can write the *linearized water waves equations*

$$\phi_z = \eta_t\,, \quad z = 0 \tag{A.16a}$$
$$\phi_t + g\eta = 0\,, \quad z = 0 \tag{A.16b}$$
$$\phi_{xx} + \phi_{zz} = 0\,, \quad -H \le z \le 0 \tag{A.16c}$$
$$\phi_z = 0\,, \quad z = -H\,. \tag{A.16d}$$

Assuming the domain has infinite horizontal extent, the equations are simplified by seeking plane wave solutions that are periodic in time with frequency ω and are horizontally periodic in space with horizontal wavenumber k (which is the first component of the wavevector $\boldsymbol{k} = (k, l, m)$). Because the domain is bounded above and below we cannot assume a plane wave structure in z. Instead, using the method of separation of variables, we seek for a solution with the z–dependent part of the wave structure separable from the x and t dependent parts. Thus, we write the velocity potential as

$$\phi(x, z, t) = \mathrm{Re}\left(\widetilde{\phi}(z) e^{i(kx - \omega t)}\right)$$

and the surface displacement as

$$\eta(x, t) = A e^{i(kx - \omega t)}\,.$$

Substituting these expressions in the linearized water waves equations (i.e. in a two-dimensional Laplace equation and in the necessary boundary conditions), after some calculations (see [**?**] or Kundu *et al.* [2016]), we obtain

$$\phi(x, z, t) = \frac{A\omega}{k \sinh(kH)} \cosh\left[k\,(z + H)\right] \sin\left(kx - \omega t\right)\,. \tag{A.17}$$

If we differentiate (A.16b) with respect to t, we have

$$\phi_{tt} + g\eta_t = \phi_{tt} + g\phi_z = 0\,,$$

Thus, substituting in the latter the solution (A.17), and calculating for $z = 0$, we have

$$-\omega^2 \cosh\left(kH\right) + gk \sinh\left(kH\right) = 0\,,$$

hence

$$\omega^2 = gk \tanh\left(kH\right)\,. \tag{A.18}$$

This is known as *dispersion relation*. It shows that surface waves are *dispersive*, because their (rightward[2]) propagation speed

$$c = \frac{\omega}{k} = \sqrt{\frac{g}{k} \tanh(kH)} \tag{A.19}$$

[2]In fact, for each k there are two waves propagating in opposite directions, parallel and antiparallel to the wave vector, because

$$\omega = \pm\sqrt{gk \tanh\left(kH\right)} \;\;\Rightarrow\;\; c = \pm\sqrt{\frac{g}{k} \tanh(kH)}\,.$$

depends on wave number, with lower k (longer $\lambda = 2\pi/k$) waves traveling faster. Thus, a concentrated wave packet made up of many wavelengths (or frequencies) will not maintain a constant waveform or shape. Instead, it will disperse or spread out as it travels. The longer wavelength components will travel faster than the shorter wavelength ones, so that an initial impulse evolves into a wide wave train[3] (Kundu *et al.* [2016],Pedlosky [2003]).

We now examine the *shallow water* (or *long wave*) and the *deep water* (or *short wave*) limits.

Shallow water limit. In this case we consider waves with wavelength long compared to the depth, $H/\lambda \ll 1$, i.e. $kH \ll 1$. Thus, $\tanh(kH) \sim kH$, and

$$\omega \sim \sqrt{gH}k\,.$$

Our (phase) speed of propagation becomes

$$c = \sqrt{gH}\,,$$

which is independent of the wavenumber k. This means that shallow water waves are *nondispersive*. A good physical example of a long water wave is a *tsunami*, which is a very long gravity wave generated by tidal forces or earthquakes. In fact, for tsunamis we have $\lambda \sim 100\,\text{km}$ and $\eta \sim 1\,\text{m}$. In the open ocean, $H \sim 4 \div 6\,\text{km}$ (e.g. in the Pacific Ocean), thus $H/\lambda \ll 1$. The propagation speed will be $c = \sqrt{gH} \sim 870\,\text{km/h}$ (almost the speed of an airplane).
The pressure change below the liquid surface from an undisturbed state produced by surface waves is given by

$$p' = p + \rho g z\,. \tag{A.20}$$

We can evaluate p from the linearized Bernoulli equation, i.e.

$$\frac{\partial\phi}{\partial t} + \frac{p}{\rho} + gz \simeq 0 \quad \Rightarrow \quad p = -\rho\frac{\partial\phi}{\partial t} - \rho g z\,. \tag{A.21}$$

We can insert the time derivative of (A.17)

$$\frac{\partial\phi}{\partial t} = -\frac{A\omega^2}{k}\cosh\left[k\left(z+H\right)\right]\cos\left(kx-\omega t\right)\,,$$

into (A.21), and making use of the shallow water approximation $kH \ll 1$, we obtain:

$$\begin{aligned} p' &= \rho\frac{\partial\phi}{\partial t} = \rho\frac{A\omega^2}{k}\cosh\left[k\left(z+H\right)\right]\cos\left(kx-\omega t\right) \\ &\simeq \rho\frac{A\omega^2}{k}\frac{1}{kH}\cos(kx-\omega t) \\ &= \rho g A\cos(kx-\omega t) \\ &= \rho g\eta\,, \end{aligned}$$

[3]This is precisely what happens when an object is dropped onto the surface of a quiescent pond. The radial extent of the circular waves increases with time, and the longest wavelengths appear farthest from the point of impact while the shortest wavelengths are seen closest to the point of impact Kundu *et al.* [2016].

where we used the fact that the $\omega^2 \simeq gk^2H$, then $g \simeq \omega^2/k^2H$, and that $\eta = A\cos(kx - \omega t)$. This shows that the pressure change is indipendent of depth in any point, and equals the hydrostatic increase of pressure due to the surface elevation change η. *The pressure field is therefore completely hydrostatic in shallow water waves.* For this reason, shallow water waves are also called *hydrostatic waves*Kundu *et al.* [2016].

Deep water limit. In this case we are dealing with waves such that $H/\lambda \gg 1$, i.e. $kH \gg 1$. Thus, for $kH \to \infty$, $\tanh(kH) \to 1$, and

$$\omega \sim \sqrt{gk}\,. \tag{A.22}$$

It is clear that deep water waves are *dispersive*, because the phase speed

$$c = \sqrt{\frac{g}{k}}\,,$$

depends on the wavenumber k. Wind-generated surface waves represent a good physical example of short waves, because typically $\lambda \sim 100\,\mathrm{m}$, $\eta \sim 2\,\mathrm{m}$, thus in the open ocean $H \gg \lambda$. Actually, this is true even over the continental shelf, where $H \sim 100\,\mathrm{m}$. Thus, the dominant wind waves in the ocean act as deep water waves and do not feel the effects of the ocean bottom until they arrive near the coastline (Kundu *et al.* [2016], Pedlosky [2003]).

A.3 Interfacial waves in a two–layer fluid

We now consider waves that propagate along the interface between two layers of immiscible fluid having different densities. Interfacial waves can be thought as internal waves at a density jump discontinuity. For example, these could represent undulations of the thermocline in the ocean.

The basic situation can be idealized by considering a lighter fluid of density ρ_1 lying over a heavier fluid of density ρ_2. We assume that both the upper and the lower layer have uniform densities and the thickness of the interface between them is so small compared with the horizontal wavelength of the interfacial waves that it can be treated as infinitesimally thin. Although one could consider two miscible layers, we will neglect heat and salt diffusion so that the density discontinuity at the interface persists for all time (Kundu *et al.* [2016], Sutherland [2010]).

Consider a horizontally unbounded two–layer fluid which can be unbounded vertically or which can have horizontal upper and lower boundaries. In the absence of waves, this fluid is characterized by the ambient density profile

$$\bar{\rho}(z) = \begin{cases} \rho_1 & z \geq \eta \\ \rho_2 & z < \eta\,, \end{cases}$$

with $\rho_1 < \rho_2$. To determine the equations of motion for interfacial waves, the Laplace equation for the velocity potential must be solved in both fluids above and below the interface. Clearly, this requires the fluid to be irrotational and incompressibile in both layers. Defining velocity potential ϕ_1 and ϕ_2, we therefore have

$$\Delta\phi_1 = \phi_{1_{xx}} + \phi_{1_{zz}} = 0 \quad z > \eta$$
$$\Delta\phi_2 = \phi_{2_{xx}} + \phi_{2_{zz}} = 0 \quad z < \eta\,.$$

These are coupled with the nonlinear dynamical interface conditions that require continuity of pressure via Bernoulli's law (A.15) evaluated at the interface:

$$\rho_1 \left[\frac{\partial\phi_1}{\partial t} + \frac{1}{2}\left(\left(\frac{\partial\phi_1}{\partial x}\right)^2 + \left(\frac{\partial\phi_1}{\partial z}\right)^2 \right) + gz \right] \Bigg|_{z=\eta} = \\ = \rho_2 \left[\frac{\partial\phi_2}{\partial t} + \frac{1}{2}\left(\left(\frac{\partial\phi_2}{\partial x}\right)^2 + \left(\frac{\partial\phi_2}{\partial z}\right)^2 \right) + gz \right] \Bigg|_{z=\eta}, \quad \text{(A.23)}$$

where we used the expanded notation for the derivatives so as to be clearer. For the vertical velocity we have the kinematic conditions

$$\frac{\mathrm{D}\eta}{\mathrm{D}t} = \left.\frac{\partial\phi_1}{\partial z}\right|_{z=\eta} = \left.\frac{\partial\phi_2}{\partial z}\right|_{z=\eta}$$

What remains to specify are the upper and the lower boundary conditions. If the fluid is *vertically unbounded*, we assume that the velocity potentials vanish far from $z = 0$:

$$\phi_1 \to 0 \quad \text{as} \quad z \to \infty$$
$$\phi_2 \to 0 \quad \text{as} \quad z \to -\infty\,.$$

However, if the fluid is *vertically bounded* we require that there is no normal flow across the rigid boundaries above and/or below the interface, i.e.

$$\left.\frac{\partial\phi_1}{\partial z}\right|_{z=H_1} = \left.\frac{\partial\phi_2}{\partial z}\right|_{z=-H_2} = 0\,,$$

where H_1 and H_2 are the depths of the two layers.

In the *small–amplitude approximation*, we have to linearize the interface conditions around $z = 0$ substituting the power series expansions

$$\eta(x,t) = \eta_0(x,t) + \varepsilon\eta_1(x,t) + \varepsilon^2\eta_2(x,t) + \cdots\,,$$

$$\phi_1(x,z,t) = \phi_1^{(0)}(x,z,t) + \varepsilon\phi_1^{(1)}(x,z,t) + \varepsilon^2\phi_1^{(2)}(x,z,t) + \cdots\,,$$

$$\phi_2(x,z,t) = \phi_2^{(0)}(x,z,t) + \varepsilon\phi_2^{(1)}(x,z,t) + \varepsilon^2\phi_2^{(2)}(x,z,t) + \cdots\,,$$

and neglecting terms higher than the linear ones. Hence, what we obtain for the dynamic and kinematic conditions is

$$\rho_1 \left(\left. \frac{\partial \phi_1^{(1)}}{\partial t} \right|_{z=0} + g\eta^{(1)} \right) = \rho_2 \left(\left. \frac{\partial \phi_2^{(1)}}{\partial t} \right|_{z=0} + g\eta^{(1)} \right)$$

$$\frac{\partial \eta^{(1)}}{\partial t} = \left. \frac{\partial \phi_1^{(1)}}{\partial z} \right|_{z=0} = \left. \frac{\partial \phi_2^{(1)}}{\partial z} \right|_{z=0} .$$

Omitting the superscripts and defining the *reduced gravity*

$$g' \equiv g \, \frac{(\rho_2 - \rho_1)}{\rho_2} \, ,$$

we have

$$\rho_1 \frac{\partial \phi_1}{\partial t} = \rho_2 \frac{\partial \phi_2}{\partial t} + \rho_2 g' \eta \quad \text{at} \;\; z = 0$$

$$\frac{\partial \eta}{\partial t} = \frac{\partial \phi_1}{\partial z} = \frac{\partial \phi_2}{\partial z} \quad \text{at} \;\; z = 0 \, .$$

In the limit in which the upper layer has a density much smaller that the lower one (as for water-air interface), $\rho_1 \ll \rho_2$, then $g' \simeq g$ and the motion is governed by the dynamics of the lower layer alone, i.e. by equations (A.16).
If the density difference between the layers is small, then $g' \ll g$. For this reason g' is referred as 'reduced gravity'.

A.3.1 Interfacial waves in infinite–depth fluid

Let us focus now on the solution of the system

$$\Delta \phi_1 = 0 \quad \text{at} \;\; z > \eta \tag{A.24a}$$
$$\Delta \phi_2 = 0 \quad \text{at} \;\; z < \eta \tag{A.24b}$$
$$\phi_1 \to 0 \quad \text{as} \;\; z \to \infty \tag{A.24c}$$
$$\phi_2 \to 0 \quad \text{as} \;\; z \to -\infty \tag{A.24d}$$
$$\rho_1 \frac{\partial \phi_1}{\partial t} = \rho_2 \frac{\partial \phi_2}{\partial t} + \rho_2 g' \eta \quad \text{at} \;\; z = 0 \tag{A.24e}$$
$$\frac{\partial \eta}{\partial t} = \frac{\partial \phi_1}{\partial z} = \frac{\partial \phi_2}{\partial z} \quad \text{at} \;\; z = 0 \, , \tag{A.24f}$$

which describes small–amplitude interfacial waves in an unbounded (above and below) fluid, i.e. an infinite–depth fluid.
As we did in the case of the linearized water waves equations, we seek for plane wave solutions for η and ϕ, with waves moving only in the x–direction:

$$\eta(x,t) = ae^{i(kx-\omega t)} \tag{A.25}$$
$$\phi_1(x,z,t) = \widetilde{\phi_1}(z)e^{i(kx-\omega t)} \tag{A.26}$$
$$\phi_2(x,z,t) = \widetilde{\phi_2}(z)e^{i(kx-\omega t)}\,. \tag{A.27}$$

In this specific case, (A.24c) and (A.24d) require that the velocity potentials must be of the form

$$\phi_1(x,z,t) = Ae^{-kz}e^{(kx-\omega t)} \tag{A.28}$$
$$\phi_2(x,z,t) = Be^{kz}e^{(kx-\omega t)} \tag{A.29}$$

so that the ϕ_1 and ϕ_2 result to be bounded for increasing (decreasing) values of z in the upper (lower) layer. Here, the amplitudes A and B can be complex and they can be determined from the kinematic boundary conditions (A.24f). We obtain

$$A = -B = \frac{i\omega a}{k}$$

The dynamic boundary condition (A.24e) then leads to the dispersion relation for interfacial waves in an infinitely deep two–layer fluid:

$$\omega^2 = gk\left(\frac{\rho_2-\rho_1}{\rho_2+\rho_1}\right) = g'k\frac{\rho_2}{\rho_1+\rho_2}\,, \tag{A.30}$$

where we used $\rho_2 g' = g(\rho_2-\rho_1)$. If we set $\varepsilon^2 \equiv (\rho_2-\rho_1)/(\rho_2+\rho_1)$, we have

$$\omega = \varepsilon\sqrt{gk}\,,$$

and since ε is a small number if the density difference between the two liquids is small, the last equation shows that waves at the interface between two fluids of infinite thickness travel like deep water surface waves, but with at a frequency ω that is smaller by a factor ε. Being $c = \sqrt{\omega/k}$, we have that, in general, *internal waves have a lower frequency and slower phase speed than surface waves with the same wavenumber.*
As expected, in the limit $\rho_1 \ll \rho_2$, we recover the dispersion relation for deep water waves at a water-air interface (A.22).

We can now write the solution for our potentials

$$\phi_1(x,z,t) = \mathrm{Re}\left\{i\frac{\omega}{k}ae^{-kz}e^{i(kx-\omega t)}\right\} = -\frac{\omega}{k}ae^{-kz}\sin(kx-\omega t)$$
$$\phi_2(x,z,t) = \mathrm{Re}\left\{i\frac{\omega}{k}ae^{kz}e^{i(kx-\omega t)}\right\} = \frac{\omega}{k}ae^{kz}\sin(kx-\omega t)$$

in which we have taken the real part to get physical solutions. These expressions allow us to write the horizontal velocity components in the two layers

$$u_1 = \frac{\partial\phi_1}{\partial x} = -\omega ae^{-kz}\sin(kx-\omega t)$$
$$u_2 = \frac{\partial\phi_2}{\partial x} = \omega ae^{kz}\sin(kx-\omega t)$$

which are clearly opposed directed. This means that the interface acts like a time–dependent *vortex sheet* because the tangential velocity is discontinuous across it, and there is infinite shear that periodically changes sign between crest and troughs[4].

A.3.2 Interfacial waves in finite–depth fluid

Now consider a two–layer fluid the a semi–infinite upper–layer fluid and a finite–depth lower–layer fluid [5]. This is sometimes referred to as a 'one–and–a–half–layer–fluid'. To analyze this situation, let the origin $z = 0$ be placed at the mean position of the free surface, and let be the lower layer bounded by a free-slip horizontal plane at $z = -H$. The governing equations are:

$$\Delta\phi_1 = 0 \quad \text{at} \quad z > \eta \tag{A.31a}$$

$$\Delta\phi_2 = 0 \quad \text{at} \quad z < \eta \tag{A.31b}$$

$$\phi_1 \to 0 \quad \text{as} \quad z \to \infty \tag{A.31c}$$

$$\rho_1 \frac{\partial \phi_1}{\partial t} = \rho_2 \frac{\partial \phi_2}{\partial t} + \rho_2 g' \eta \quad \text{at} \quad z = 0 \tag{A.31d}$$

$$\frac{\partial \eta}{\partial t} = \frac{\partial \phi_1}{\partial z} = \frac{\partial \phi_2}{\partial z} \quad \text{at} \quad z = 0 \tag{A.31e}$$

$$\frac{\partial \phi_2}{\partial z} = 0 \quad \text{at} \quad z = -H\,, \tag{A.31f}$$

where in (A.31f) we costrained the vertical velocity of the lower–layer fluid to be zero at the bottom boundary. Again, we are seeking solutions in the form of plane waves, i.e. as in (A.25).
To satisfy the bottom boundary condition, in the lower–layer it must be

$$\phi_2 = A \cosh\left[k(z + H)\right] e^{i(kx - \omega t)} \quad -H < z < 0\,.$$

Applying the linearized form of the interface conditions (A.31d) and (A.31e), we can get the dispersion relation

$$\omega^2 = g' k \frac{\rho_2 \sinh(kH)}{\rho_1 \sinh(kH) + \rho_2 \cosh(kH)} = g' k \frac{\rho_2}{\rho_1 + \rho_2 \coth(kH)}\,. \tag{A.32}$$

In the limit $\rho_1 \to 0$ the previous one reduces to the dispersion relation for surface waves. In the limit of short waves, $kH \gg 1$, $\coth(kH) \to 1$. Hence, (A.32) reduces to the dispersion relation for an infinitely deep two–layer fluid (A.30).

As we will see in the next subsection, we can also consider the case in which depths H_1 and H_2 of the upper and lower layer fluids are sufficientely small compared with the wavelength. This means that neither the upper nor the lower layer can be treated as infinitely large. This situation can describe also an interfacial wave in

[4]The existence of vorticity does not contradict the assumption that each layer is irrotational, because the vorticity predicted by the model is confined to the interface and does not extend into the interior of each layerSutherland [2010].

[5]See Kundu *et al.* [2016]; Lamb [1932]; Sutherland [2010]

which the upper boundary is a free suface. In fact, the displacement of the surface due to interfacial waves is typically so small that a rigid surface boundary condition can be reasonably assumed Sutherland [2010]. We call this simplification *rigid–lid approximation*. This approximation provides the same results of the case of an interfacial wave in a three–layer fluid, in which the upper layer has immediately above a fluid with density comparable to that of air, and of the case (in specific limits) of an interfacial wave in a three–layer fluid unbounded above and below.

A.3.3 Shallow interfacial waves in rigid–lid approximation

The shallow water (or long wave) case, in which the wavelength is much longer than the depth of one or both layers of fluid, is representative of many geophysical situations, e.g. the undulations of the thermocline with a long horizontal scale compared to the mixed–layer depth but with short horizontal scale compared to the depth of the ocean Sutherland [2010]. Let us treat the case of long waves in a two–layer *Boussinesq fluid*, which means that between ρ_1 and ρ_2 there is only a small difference[6]. The depths H_1 and H_2 of the upper and lower layer are sufficientely small compared to the wavelength. For this case we will explicitly make calculations following the approach suggested in the previous subsection. These are our equations:

$$\Delta\phi_1 = 0 \quad \text{at} \quad z > \eta \tag{A.33a}$$

$$\Delta\phi_2 = 0 \quad \text{at} \quad z < \eta \tag{A.33b}$$

$$\rho_1 \frac{\partial \phi_1}{\partial t} = \rho_2 \frac{\partial \phi_2}{\partial t} + \rho_2 g' \eta \quad \text{at} \quad z = 0 \tag{A.33c}$$

$$\frac{\partial \eta}{\partial t} = \frac{\partial \phi_1}{\partial z} = \frac{\partial \phi_2}{\partial z} \quad \text{at} \quad z = 0 \tag{A.33d}$$

$$\frac{\partial \phi_1}{\partial z} = 0 \quad \text{at} \quad z = H_1\,, \tag{A.33e}$$

$$\frac{\partial \phi_2}{\partial z} = 0 \quad \text{at} \quad z = -H_2\,. \tag{A.33f}$$

We seek again for plane wave solutions like:

$$\begin{aligned} \eta(x,t) &= a e^{i(kx-\omega t)} \\ \phi_1(x,z,t) &= \widetilde{\phi_1}(z) e^{i(kx-\omega t)} \\ \phi_2(x,z,t) &= \widetilde{\phi_2}(z) e^{i(kx-\omega t)}\,. \end{aligned}$$

Substituting $\phi_{1,2}$ in (A.33a) and (A.33b), we have

$$\frac{\partial^2 \phi_{1,2}}{\partial x^2} + \frac{\partial^2 \phi_{1,2}}{\partial z^2} = 0 \quad \Rightarrow \quad \frac{\mathrm{d}^2 \widetilde{\phi_{1,2}}(z)}{\mathrm{d}z^2} - k^2 \widetilde{\phi_{1,2}}(z) = 0\,,$$

thus the solutions will be of the form:

[6] In general, the Boussinesq approximation assumes that the density varies vertically by a relatively small amount, as in the ocean.

$$\widetilde{\phi_1}(z) = Ae^{kz} + Be^{-kz}$$
$$\widetilde{\phi_2}(z) = Ce^{kz} + De^{-kz}$$

Let us impose conditions (A.33e) and (A.33f):

$$\left.\frac{\partial \phi_1}{\partial z}\right|_{z=H_1} = k\left(Ae^{kH_1} - Be^{-kH_1}\right)e^{i(kx-\omega t)} = 0 \quad \Rightarrow \quad A = Be^{-2kH_1}$$
$$\left.\frac{\partial \phi_2}{\partial z}\right|_{z=-H_2} = k\left(Ce^{-kH_2} - De^{kH_2}\right)e^{i(kx-\omega t)} = 0 \quad \Rightarrow \quad D = Ce^{-2kH_2}$$

We now impose (A.33d):

$$\frac{\partial \eta}{\partial t} = -a\omega i e^{i(kx-\omega t)} \stackrel{!}{=} \left.\frac{\partial \phi_1}{\partial t}\right|_{z=0} = k(A-B)e^{i(kx-\omega t)} = k\left(Be^{-2kH_1} - B\right)e^{i(kx-\omega t)}$$
$$\stackrel{!}{=} \left.\frac{\partial \phi_2}{\partial t}\right|_{z=0} = k(C-D)e^{i(kx-\omega t)} = k\left(C - Ce^{-2kh_2}\right)e^{i(kx-\omega t)},$$

thus:

$$-\frac{a\omega i}{k} = B\left(e^{-2kH_1} - 1\right) = C\left(1 - e^{-2kH_2}\right)$$

which means:

$$B = \frac{a\omega i}{k\left(1 - e^{-2kH_1}\right)}, \qquad C = -\frac{a\omega i}{k\left(1 - e^{-2kH_2}\right)}.$$

We can now write the expression for ϕ_1:

$$\phi_1(x,z,t) = \left(Ae^{kz} + Be^{-kz}\right)e^{i(kx-\omega t)} = B\left(e^{-2kH_1}e^{kz} + e^{-kz}\right)e^{i(kx-\omega t)}$$

$$= \frac{a\omega i}{k}\,\frac{e^{-2kH_1}e^{kz} + e^{-kz}}{(1 - e^{-2kH_1})}e^{i(kx-\omega t)} = \frac{a\omega i}{k}\,\frac{e^{-kH_1}e^{kz} + e^{-kz}e^{kH_1}}{(e^{kH_1} - e^{kH_1})}e^{i(kx-\omega t)}$$

$$= \frac{a\omega i}{k}\,\frac{\cosh(k(z-H_1))}{\sinh(kH_1)}e^{i(kx-\omega t)},$$

and taking the real part we have:

$$\phi_1(x,z,t) = -\frac{a\omega}{k}\frac{\cosh(k(z-H_1))}{\sinh(kH_1)}\sin(kx-\omega t),$$

A similar procedure for ϕ_2 leads to

$$\phi_2(x,z,t) = \frac{a\omega}{k}\frac{\cosh(k(z+H_2))}{\sinh(kH_2)}\sin(kx-\omega t)\,.$$

Let us impose the last condition (A.33c), i.e.

$$\rho_1\frac{\omega^2 a}{k}\frac{\cosh(k(z-H_1))}{\sinh(kH_1)}\bigg|_{z=0}\cos(kx-\omega t) = \\ -\rho_2\frac{\omega^2 a}{k}\frac{\cosh(k(z+H_2))}{\sinh(kH_2)}\bigg|_{z=0}\cos(kx-\omega t) + \rho_2 g' a\cos(kx-\omega t)\,, \quad \text{(A.34)}$$

which becomes:

$$\rho_1\frac{\omega^2 a}{k}\frac{\cosh(-kH_1)}{\sinh(kH_1)} = -\rho_2\frac{\omega^2 a}{k}\frac{\cosh(kH_2)}{\sinh(kH_2)} + \rho_2 g'\,.$$

The hyperbolic cosine is an even function, thus $\cosh(-kH_1) = \cosh(kH_1)$, and the previous equation becomes

$$\rho_1\coth(kH_1) + \rho_2\coth(kH_2) = \rho_2 g'\frac{k}{\omega^2}\,,$$

which leads to

$$\omega^2 = g'k\frac{\rho_2}{\rho_1\coth(kH_1) + \rho_2\coth(kH_2)}\,.$$

In the Boussinesq approximation we have $\rho_1 \simeq \rho_2$, then we can find the dispersion relation

$$\omega^2 = g'k\frac{1}{\coth(kH_1) + \coth(kH_2)}$$

and taking the limits $kH_1 \ll 1$ and $kH_2 \ll 1$, we have $\coth(kH_{1,2}) \simeq 1/kH_{1,2}$, thus

$$\omega \simeq k\sqrt{g'\frac{H_1H_2}{H_1+H_2}}\,.$$

The waves, as expected, are nondispersive, being $\omega = \pm ck$ with

$$c = \sqrt{g'\frac{H_1H_2}{H_1+H_2}}\,. \quad \text{(A.35)}$$

Thus, the waves move as a one–layer fluid with reduced gravity g' and depth

$$\bar{H} \equiv \frac{H_1H_2}{H_1+H_2}$$

which is the *harmonic mean* of H_1 and H_2. We notice that for $H_1 \gg H_2$, (A.35) becomes $c = \sqrt{g'H_2}$, and for $H_1 \ll H_2$, it becomes $c = \sqrt{g'H_1}$. Thus, small–amplitude interfacial waves in a shallow upper layer behave the same as interfacial waves in a shallow lower layer. This is expected in the Boussinesq approximation, whose equations are invariant upon reflection on z (see Sutherland [2010] and Vallis [2017]).

Appendix B

Linear waves in non–uniform media

B.1 Ray theory approach

The general treatment of small–amplitude wave propagation in non–uniform, but slowly varying media is known as ray theory. We assume that any local property of the wavetrain can be specified by the function

$$\eta(\boldsymbol{x},t) = A(\boldsymbol{x},t)e^{i\varphi(\boldsymbol{x},t)} \tag{B.1}$$

where $A(\boldsymbol{x},t)$ is a slowly–varying function of space and time, compared with the wavelength and period of waves, and $\varphi(\boldsymbol{x},t)$ is a rapidly oscillatory phase function. The local wavenumber and frequency are defined by

$$\boldsymbol{k} = \nabla\varphi\,, \quad \omega = -\frac{\partial\varphi}{\partial t}\,, \tag{B.2}$$

and from the first expression it follows that $\nabla\times\boldsymbol{k} = 0$, i.e., the local wavenumber vector is irrotational. We suppose that the amplitude A varies slowly over a wavelength and a period; that is, $|\Delta A|/|A|$ is small over the length $1/k$ and the period $1/\omega$, or

$$\frac{1}{A}\Big|\frac{\partial A}{\partial x}\Big| \ll k\,, \quad \frac{1}{A}\Big|\frac{\partial A}{\partial t}\Big| \ll \omega$$

and similarly in the other directions. We will assume that the wavenumber and frequency as defined by (B.2) are the same as those that would arise if the medium were homogeneous and a were a constant. Thus, we may obtain a local dispersion relation from the governing equation by keeping the spatially (and possibly temporally) varying parameters fixed, and obtain

$$\omega = \Omega(\boldsymbol{k},\boldsymbol{x},t) \tag{B.3}$$

and then allow $\boldsymbol{x}$ and t to vary, albeit slowly [Vallis, 2017]. Eliminating φ from (B.2) we get

$$\frac{\partial k_i}{\partial t} + \frac{\partial\omega}{\partial x_i} = 0\,,$$

which is equivalent to

$$\frac{\partial \boldsymbol{k}}{\partial t} + \nabla_{\boldsymbol{k}}\Omega \cdot \nabla \boldsymbol{k} = -\nabla\Omega\,. \tag{B.4}$$

Being the group velocity

$$\boldsymbol{c_g} = \frac{\partial \Omega}{\partial \boldsymbol{k}}\,,$$

we can rewrite (B.4) as

$$\frac{\partial \boldsymbol{k}}{\partial t} + \boldsymbol{c_g} \cdot \nabla \boldsymbol{k} = -\nabla\Omega\,. \tag{B.5}$$

From (B.3), we can find a similar expression for the time-evolution of ω [Vallis, 2017]:

$$\frac{\partial \omega}{\partial t} + \boldsymbol{c_g} \cdot \nabla \omega = \frac{\partial \Omega}{\partial t}\,. \tag{B.6}$$

The left-hand side of (B.5) and (B.6) is similar to an advective derivative, but uses the group velocity. Evidently, if the dispersion relation (B.3) for frequency is not an explicit function of space then the wavevector is propagated at the group velocity. If the dispersion relation is not a function of time, the frequency also propagates at the group velocity.

Thus, we define a *ray* as the trajectory traced by the group velocity, and we see that if the function Ω *is not an explicit function of space or time, then both the wavevector and the frequency* [1] *are constant along a ray* [Vallis, 2017].

Consider a group of waves at the initial position $\boldsymbol{x}_0$, for which the amplitude and wavenumber vary slowly with position, and the dispersion relation $\omega = \Omega(\boldsymbol{k}, \boldsymbol{x}, t)$ is known. If we denote the advective derivative as

$$\frac{\mathrm{d}}{\mathrm{dt}} \equiv \frac{\partial}{\partial t} + \boldsymbol{c_g} \cdot \nabla\,,$$

from (B.5) and (B.6) we get the following ordinary differential equations:

$$\frac{\mathrm{d}\boldsymbol{k}}{\mathrm{dt}} = -\nabla\Omega\,, \tag{B.7a}$$

$$\frac{\mathrm{d}\omega}{\mathrm{dt}} = \frac{\partial \Omega}{\partial t}\,. \tag{B.7b}$$

Thus, ray theory strongly simplified our problem: we can track a group of waves from one location to another solving ordinary differential equations (ODEs) rather than the full wave equations of motion.

[1] When describing waves in an ambient flow moving at velocity $\boldsymbol{U}$, it is important to distinguish between the definitions of the frequencies given by ω and Ω. Generally, it is assumed that the observer is stationary and records the frequency ω as the waves are advected by the background flow. This is called the *intrinsic frequency*. Conversely, an observer moving with the background flow records waves with frequency Ω, called the *extrinsic frequency* [Sutherland, 2010]. Thus, when the medium itself is moving with velocity $\boldsymbol{U}$, the frequency of waves passing a fixed point is

$$\omega = \Omega + \boldsymbol{k} \cdot \boldsymbol{U}\,,$$

in which the extrinsic frequency $\Omega = \Omega(\boldsymbol{k}, \boldsymbol{x})$ satisfies the dispersion relation for waves in a stationary ambient [Massel, 2015; Sutherland, 2010].

These ODEs are solvable provided we know the right-hand sides, that is, provided we know the space and time location at which the dispersion relation $\omega = \Omega(\boldsymbol{k}, \boldsymbol{x}, t)$ is to be evaluated. If we move to a frame of reference in which we continually track the wavepacket that is moving at its group velocity, then we can derive the location because the position $\boldsymbol{x}$ changes in time as

$$\frac{\mathrm{d}\boldsymbol{x}}{\mathrm{d}t} = \boldsymbol{c_g}\,, \tag{B.8}$$

with $\boldsymbol{c_g} = \partial\Omega/\partial\boldsymbol{k}|_{\boldsymbol{x},t}$. Thus, equation (B.7a) can be rewritten as the coupled system

$$\frac{\mathrm{d}k_i}{\mathrm{dt}} = -\frac{\partial\Omega}{\partial x_i}\,, \tag{B.9a}$$

$$\frac{\mathrm{d}x_i}{\mathrm{dt}} = \frac{\partial\Omega}{\partial k_i}\,, \tag{B.9b}$$

which forms a set of Hamilton's equations [Debnath, 2012; Sutherland, 2010; Whitham, 1974], with Hamiltonian Ω, referred to as *canonical ray equations* [2]. Equations (B.9) can be solved to give the trajectory of a wave packet or collection of wave packets as illustrated in Fig.B.1. If the medium or the wavepacket amplitude is not slowly varying ray theory will fail, and this happens if two wave packets collide.

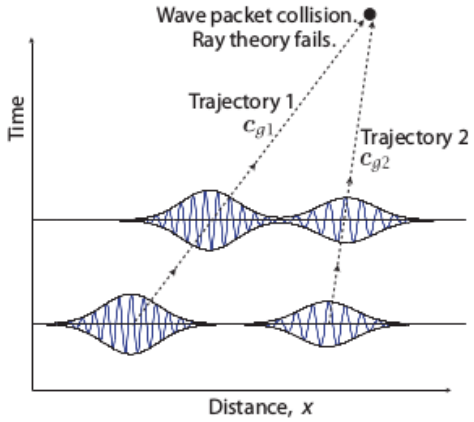

Figure B.1. Wave packets collision. Equations (B.9) can be solved to give the trajectory of a wave packet or collection of wave packets. If the medium or the wavepacket amplitude is not slowly varying, wave packets collide and ray theory fails. From Vallis [2017].

B.2 WKB approach

The WKB method (Wentzel, Kramers and Brillouin) is, in general, a way of finding approximate solutions to certain linear differential equations in which the term with

[2] Indeed, the analogy between Hamilton's equations and the wavepacket evolution equations is more explicit when compared with the Hamiltonian representation of quantum mechanics. The energy and momentum of a free "wave-particle" are $H = \hbar\omega$ and $p = \hbar k$, respectively. Substituting these in Hamilton's equations, cancelling Planck's constant, and letting $q = x$, we recover (B.9) [Sutherland, 2010].

the highest derivative is multiplied by a small parameter. However, in our case, we are interested in using the WKB method to solve linear differential equations in which the coefficients vary slowly in space or time. Consider the following equation [Kundu *et al.*, 2016; Vallis, 2017]:

$$\frac{\mathrm{d}^2\xi}{\mathrm{d}z^2} + m^2(z)\xi = 0\,. \tag{B.10}$$

If $m^2(z)$ is constant and positive, the equation has wavelike solutions of the harmonic form

$$\xi = \mathrm{Re}\, A_0\, \mathrm{e}^{imz}\,, \tag{B.11}$$

where A_0 is a complex constant. If m varies only slowly with z, i.e. the variations in m only occur on a scale much longer than $1/m$, we expect that the harmonic solution (B.11) would provide a good first approximation; that is, we expect the solution to locally look like a plane wave with local wavenumber $m(z)$. However, we might also expect that the solution would not be exactly of the form $\mathrm{e}^{im(z)\,z}$, because the phase of ξ is $\theta(z) = mz$, so that $\mathrm{d}\theta/\mathrm{d}z = m + z\,\mathrm{d}m/\mathrm{d}z \neq m$. Thus, in (B.11) m is not the wavenumber unless m is constant.
The derive the WKB approximate solution, we seek solutions to (B.10) in the form

$$\xi = A(z)\mathrm{e}^{i\theta(z)}\,. \tag{B.12}$$

Substituting (B.12) in (B.10), we get

$$i\left[2\frac{\mathrm{d}A}{\mathrm{d}z}\frac{\mathrm{d}\theta}{\mathrm{d}z} + A\frac{\mathrm{d}^2\theta}{\mathrm{d}z^2}\right] + \left[A\left(\frac{\mathrm{d}\theta}{\mathrm{d}z}\right)^2 - \frac{\mathrm{d}^2A}{\mathrm{d}z^2} - m^2A\right] = 0\,, \tag{B.13}$$

and the terms in the square brackets must be zero. The WKB approximation consists in assuming that the amplitude $A(z)$ varies sufficiently slowly that

$$\left|\frac{1}{A}\frac{\mathrm{d}^2A}{\mathrm{d}z^2}\right| \ll m^2\,,$$

(this condition will generally be satisfied if variations in the background state, or in the medium, occur on a scale much longer than the wavelength) and hence the term $\mathrm{d}^2A/\mathrm{d}z^2$ in (B.13) can be neglected. Thus, separating the real and the imaginary part in (B.13), we obtain the following equations:

$$\left(\frac{\mathrm{d}\theta}{\mathrm{d}z}\right)^2 = m^2 \tag{B.14}$$

$$2\frac{\mathrm{d}A}{\mathrm{d}z}\frac{\mathrm{d}\theta}{\mathrm{d}z} + A\frac{\mathrm{d}^2\theta}{\mathrm{d}z^2} = 0\,. \tag{B.15}$$

The solution to (B.14) is

$$\theta = \pm\int^z m(z')\,dz'\,, \tag{B.16}$$

Substituting (B.16) in (B.15), we obtain

$$2\frac{\mathrm{d}A}{\mathrm{d}z}\frac{\mathrm{d}\theta}{\mathrm{d}z} + A\frac{\mathrm{d}m}{\mathrm{d}z} = 0\,,$$

with solution [Kundu *et al.*, 2016; Vallis, 2017]

$$A(z) = \frac{A_0}{\sqrt{m(z)}}\,.$$

Thus, the WKB solution to (B.10) is

$$\xi(z) = \frac{A_0}{\sqrt{m(z)}}\mathrm{e}^{\pm i\left(\int^z m(z')\,dz'\right)}\,. \tag{B.17}$$

Bibliography

Ablowitz, M. (2011). *Nonlinear Dispersive Waves: Asymptotic Analysis and Solitons*. Cambridge.

Ablowitz, M. J. and Baldwin, D. E. (2012). Nonlinear shallow ocean-wave soliton interactions on flat beaches. *Physical Review E*, **86**.

Abramowitz, M. and Stegun, I. A. (1965). *Handbook of mathematical functions*. Dover Publications.

Aghsaee, P. and Boegman, L. (2015). Experimental investigation of sediment resuspension beneathinternal solitary waves of depression. *Journal of Geophysical Research: Oceans*, **120**, 3301–3314.

Aghsaee, P., Boegman, L., and Lamb, K. G. (2010). Breaking of shoaling internal solitary waves. *Journal of Fluid Mechanics*, **659**, 289–317.

Akylas, T. R. (1994). Three–dimensional long water–wave phenomena. *Annual Review of Fluid Mechanics*, **26**, 191–210.

Akylas, T. R. and Katsis, C. (1987). On the excitation of long nonlinear water waves by a moving pressure distribution. Part 2. Three- dimensional effects. *Journal of Fluid Mechanics*, **177**, 49–65.

Alpers, W. (1985). Theory of radar imaging of internal waves. *Nature*, **314**, 245–247.

Alpers, W. and Salusti, E. (1983). Scylla and Charybdis observed from space. *Journal of Geophysical Research: Oceans*, **88**(C3), 1800–1808.

Alpers, W., Brandt, P., Rubino, A., and Backhaus, J. O. (1996). Recent contributions of remote sensing to the study of internal waves in the Straits of Gibraltar and Messina. *Bulletin - Institut Oceanographique Monaco-Numero Special* -, pages 21–40.

Alpers, W., Brandt, P., and Rubino, A. (2008). Internal waves generated in the straits of gibraltar and messina: Observations from space. *Barale, V. and Gade. M.(eds.), Remote Sensing of the European Seas. Dordrecht, the Netherlands: Springer*, pages 319–330.

Apel, J. R., Holbrook, J. R., Liu, A. K., and Tsai, J. J. (1985). The Sulu Sea Internal Soliton Experiment. *Journal of Physical Oceanography*, **15**, 1625–1651.

Artale, V., Levi, D., Marullo, S., and Santoleri, R. (1990). Analysis of nonlinear internal waves observed by Landsat thematic mapper. *Journal of Geophysical Research: Oceans*, **95**(C9), 16065–16073.

Arthur, R. S. and Fringer, O. B. (2014). The dynamics of breaking internal solitary waves on slopes. *Journal of Fluid Mechanics*, **761**, 360–398.

Barale, V. and Gade, M. E. (2008). *Remote Sensing in the European Seas*. Springer.

Barale, V. and Gade, M. E. (2019). *Remote Sensing in the Asian Seas*. Springer.

Barros, R. and Choi, W. (2013). On regularizing the strongly nonlinear model for two-dimensional internal waves. *Physica D*, **264**, 27–34.

Barry, M., Ivey, G. N., Winters, K., and Imberger, J. (2001). Measurements of diapycnal di usivities instrati ed fluids. *Journal of Fluid Mechanics*, **442**, 267–291.

Benjamin, T. B. (1967). Internal waves of permanent form in fluids of great depth. *Journal of Fluid Mechanics*, **29**, 559–592.

Benjamin, T. B., Bona, J. L., and Mahony, J. J. (1972). Model equations for long waves in nonlinear dispersive systems. *Phys. Trans. Roy. Soc. London*, **278A**, 555–604.

Benney, D. J. (1966). Long Nonlinear Waves in Fluid Flows. *Journal of Mathematics and Physics*, **45**, 52–63.

Boegman, L. and Stasna, M. (2019). Sediment Resuspension and Transport by Internal Solitary Waves. *Annual Reviews of Fluid Mechanics*, **51**, 129–154.

Boegman, L., Ivey, G., and Imberger, J. (2005). The degeneration of internal waves in lakes with sloping topography. *Limnology and oceanography*, **50**(5), 1620–1637.

Bogucki, D. and Garrett, C. (1993). A Simple Model for the Shear–Induced Decay of Internal Solitary Waves. *Journal of Physical Oceanography*, **23**, 1767–1776.

Bogucki, D., Dickey, T., and Redekopp, L. G. (1997). Sediment resuspension and mixing by resonantly generated internal solitary waves. *Journal of Physical Oceanography*, **27**(7), 1181–1196.

Bouffard, D. and Boegman, L. (2013). A diapycnal diffusivity model for stratified environmental flows. *Dynamics of Atmospheres and Oceans*, **61–62**, 14–34.

Bourgault, D. and Kelley, D. E. (2003). Wave-induced boundary mixing in a partially mixed estuary. *Journal of Marine Research*, **61**(5), 553– 576,.

Bourgault, D. and Kelley, D. E. (2007). On the reflectance of uniform slopes for normally incident interfacial solitary waves. *Journal of Physical Oceanography*, **37**, 1156–1162.

Bourgault, D., Blokhina, M. D., Mirshak, R., and Kelley, D. E. (2007). Evolution of a shoaling internal solitary wavetrain. *Geophysical Research Letters*, **34**, L03601.

Bourgault, D., Morsilli, M., Richards, C., Neumeier, U., and Kelley, D. E. (2014). Sediment resuspension and nepheloid layers induced by long internal solitary waves shoaling orthogonally on uniform slopes. *Continental Shelf Research*, **72**, 21–33.

Brandt, P., Rubino, A., Quadfasel, D., Alpers, W., Sellschopp, J., and Fiekas, H.-V. (1999). Evidence for the influence of Atlantic–Ionian stream fluctuations on the tidally induced internal dynamics in the Strait of Messina. *Journal of physical oceanography*, **29**(5), 1071–1080.

Cacchione, D. A., Pratson, L. F., and Ogston, A. S. (2002). The shaping of continental slopes by internal tides. *Science*, **296**, 724–727.

Cai, S. and Xie, J. (2010). A propagation model for the internal solitary waves in the northern South China Sea. *Journal of Geophysical Research*, **115**(C12), C12074.

Camassa, R., Choi, W., Michallet, H., Rusås, P.-O., and Sveen, J. K. (2006). On the realm of validity of strongly nonlinear asymptotic approximations for internal wavesin a two-fluid system. *Journal of Fluid Mechanics*, **549**, 1–23.

Chakravarty, S. and Kodama, Y. (2013). Construction of KP solitons from wave patterns. *Journal of Physics A*, **47**(2e).

Chalamalla, V. K. and Sarkar, S. (2015). Mixing, Dissipation Rate, and Their Overturn-Based Estimates in a Near-Bottom Turbulent Flow Driven by Internal Tides. *Journal of Physical Oceanography*, **45**, 1969–1987.

Chen, G.-Y., Liu, C.-T., Wang, Y.-H., and Hsu, M.-K. (2011). Interaction and generation of long-crested internal solitary waves in the South China Sea. *Journal of Geophysical Research*, **116**(C6).

Chen, Y. and Liu, P. L.-F. (1995). The unified Kadomtsev– Petviashvili equation for interfacial waves. *Journal of Fluid Mechanics*, **288**, 383–408.

Choi, W. and Camassa, R. (1996). Weakly nonlinear internal waves in a two-fluid system. *Journal of Fluid Mechanics*, **313**, 83–108.

Choi, W. and Camassa, R. (1999). Fully nonlinear internal waves in a two–layer fluid system. *Journal of Fluid Mechanics*, **396**, 1–36.

Davis, K. A. and Monismith, S. G. (2011). The modification of bottom boundary layer turbulence and mixing by internal waves shoaling on a barrier reef. *Journal of Physical Oceanography*, **41**(11), 2223–2241.

Dean, R. and Dalrymple, R. (1991). *Water Waves Mechanics for Engineers and Scientists*. World Scientific.

Debnath, L. (2012). *Nonlinear Partial Differential Equations for Scientists and Engineers*. Birkhäuser.

Dillon, T. M. (1982). Vertical Overturns: A Comparison of Thorpe and Ozmidov Length Scales. *Journal of Geophysical Research*, **87**(C12), 9601–9613.

Djorjevic, V. D. and Redekopp, L. G. (1978). The Fission and Disintegration of Internal Solitary Waves Moving over a Two–Dimensional Topography. *Journal of Physical Oceanography*, **8**, 1016–1024.

D'Ortenzio, F., Iudicone, D., de Boyer Montegut, C., Testor, P., Antoine, D., Marullo, S., Santoleri, R., and Madec, G. (2005). Seasonal variability of the mixed layer depth in the Mediterranean Sea as derived from in situ profiles. *Geophysical Research Letters*, **32**(12).

Drazin, P. and Johnson, R. (1990). *Solitons: An Introduction*. Cambridge University Press.

Droghei, R., Falcini, F., Casalbore, D., Martorelli, E., Mosetti, R., Sannino, G., Santoleri, R., and Chiocci, F. (2016). The role of Internal Solitary Waves on deep-water sedimentary processes: the case of up-slope migrating sediment waves off the Messina Strait. *Scientific reports*, **6**, 36376.

Dubreil-Jacotin, M. L. (1937). Sur les theoremes d'existence relatifs aux ondes permanentes periodiques a deux dimensions dans les liquides heterogenes. *J. Math. Pures Appl.*, **16**, 43–67.

Duda, T. F., Lynch, J. F., Irish, J. D., Beardsley, R. C., Ramp, S. R., Chiu, C.-S., Tang, T. Y., and Yang, Y.-J. (2004). Internal Tide and Nonlinear Internal Wave Behavior at the Continental Slope in the Northern South China Sea. *IEEE Journal of Oceanic Engineering*, **29**(4), 1105–1130.

Dwi Susanto, R., Gordon, A. L., Sprintall, J., and Herunadi, B. (2000). Interseasonal variability and tides in Makassar Strait. *Geophysical Reaserch Letters*, **27**(10), 1499–1502.

Dwi Susanto, R., Mitnik, L., and Zheng, Q. (2005). Ocean internal waves observed in the Lombok Strait. *Oceanography*, **18**(4), 81–87.

D'Alessandro, E., Sponaugle, S., and Lee, T. (2007). Patterns and processes of larval fish supply to the coral reefs of the upper Florida Keys. *Marine Ecology Progress Series*, **331**, 85–100.

Ellison, T. (1957). Turbulent transport of heat and momentum from an infinite rough plane. *Journal of Fluid Mechanics*, **2**, 456–466.

Fermi, E., Pasta, J., and Ulam, S. (1955). Studies of nonlinear problems. I. *Los Alamos report (LA-1940)*.

Fragoso, A., Patterson, M., and J.S. Wettlaufer, J. (2013). Mixing in gravity currents. *J. Fluid Mech.*, **734**, Art–No.

Fringer, O. B. and Street, R. L. (2003). The dynamics of breaking progressive interfacial waves. *Journal of Fluid Mechanics*, **494**, 319–353.

Galbraith, P. S. and Kelley, D. E. (1996). Identifying Overturns in CTD Profiles. *Journal of Atmospheric and Oceanic Technology*, **13**, 688–701.

Gardner, C., Green, J., Kruskal, M., and Miura, R. (1967). Method For Solving the Korteweg–de Vries Equation. *Physical Review Letters*, **19**, 1095.

Gargett, A. and Garner, T. (2008). Determining Thorpe Scale from Ship–Lowered CTD Density Profiles. *Journal of Atmospheric and Oceanic Technology*, **25**, 1657–1670.

Garrett, C. (2003). Internal Tides and Ocean Mixing. *Science*, **301**(5641), 1858–1859.

Gayen, B. and Sarkar, S. (2010). Turbulence during the generation of internal tide on a critical slope. *Phys. Rev. Lett.*, **104**(21), 218502.

Gayen, B. and Sarkar, S. (2011). Boundary mixing by density overturns in an internal tidal beam. *Geophysical Research Letters*, **38**(14), L14608.

Gerkema, T. and Zimmerman, J. T. F. (1995). Generation of Nonlinear Internal Tides and Solitary Waves. *Journal of Physical Oceanography*, **25**, 1081–1094.

Gregg, M., D'Asaro, E. A., Riley, J. J., and Kunze, E. (2018). Mixing Efficiency in the Ocean. *Annual Review of Marine Science*, **10**, 443–473.

Grimshaw, R. (1981). Evolution equations for long, nonlinear internal waves in stratified shear flows. *Stud. Appl. Math*, **65**, 159–188.

Grimshaw, R. (1985). Evolution equations for long, nonlinear internal waves in a rotating fluid. *Stud. Appl. Math*, **73**, 1–33.

Grimshaw, R. (2002). *Environmental stratified flows*. Kluwer Academic Publishers.

Grimshaw, R. (2005). *Nonlinear Waves in Fluids: Recent Advances and Modern Applications*. SpringerWienNewYork.

Grimshaw, R. (2007). Internal solitary waves in a variable medium. *Gesellschaft fur Angewandte Mathematik*, **30**, 96–107.

Grimshaw, R. and Helfrich, W. K. (1989). On the derivation of the modified Kadomtsev–Petviashvili equation. *Stud. Appl. Math*, **80**, 183–202.

Grimshaw, R., Pelinovsky, E., and Talipova, T. (1998). Solitary Wave Transformation Due to a Change in Polarity. *Studies in Applied Mathematics*, **101**, 357–388.

Grimshaw, R., Pelinovsky, E., and Talipova, T. (1999). Solitary wave transformation in a medium with sign-variable quadratic nonlinearity and cubic nonlinearity. *Physica D*, **132**, 40–62.

Grimshaw, R., Pelinovsky, E., and Poloukhina, O. (2002). Higher–order Korteweg-de Vries models for internal solitary waves in a stratified shear flow with a free surface. *Nonlinear Processes in Geophysics*, **9**, 221–235.

Grimshaw, R., Pelinovsky, E., Talipova, T., and Kurkin, A. (2004). Simulation of the Transformation of Internal Solitary Waves on Oceanic Shelves. *Journal of Physical Oceanography*, **34**, 2774–2791.

Grimshaw, R., Pelinovsky, E., and Talipova, T. (2007). Modelling Internal Solitary Waves in the Coastal Ocean. *Surveys in Geophysics*, **28**, 273–298.

Grimshaw, R., Pelinovsky, E., Talipova, T., and Kurkina, O. (2010). Internal solitary waves: propagation, deformation, disintegration. *Nonlinear Processes in Geophysics*, **17**, 633–649.

Grue, J. (2005). Generation, propagation, and breaking of internal solitary waves. *Chaos*, **15**, 037110.

Grue, J. (2006). Very large internal waves in the ocean - observations and nonlinear models. In J. Grue and K. Trulsen, editors, *Waves in Geophysical Fluids: Tsunamis, Rogue Waves, Internal Waves and Internal Tides*, pages 205–270. SpringerWienNewYork.

Hebert, D. (1988). The Available Potential Energy of An Isolated Feature. *Journal of Geophysical Research*, **93**(C1), 556–564.

Helfrich, K. and Melville, W. (2006). Long Nonlinear Waves. *Annual Review of Fluid Mechanics*, **38**, 395–425.

Helfrich, K. R. (1992). Internal solitary wave breaking and run-up on a uniform slope. *Journal of Fluid Mechanics*, **243**, 133–154.

Helfrich, K. R. and Melville, W. (1986). On long nonlinear internal waves over slope-shelf topography. *Journal of Fluid Mechanics*, **167**, 285–308.

Holloway, P. E. (1984). On the semi-diurnal internal tide at a shelf-break region on the Australian North West Shelf. *Journal of Physical Oceanography*, **14**, 1778–1790.

Holloway, P. E. (1994). Observations of internal tide propagation on the Australian North West Shelf. *Journal of Physical Oceanography*, **24**, 1706–1716.

Holloway, P. E., Pelinovsky, E., Talipova, T., and Barnes, B. (1997). A Nonlinear Model of Internal Tide Transformation on the Australian North West Shelf. *Journal of Physical Oceanography*, **27**, 871–896.

Holloway, P. E., Pelinovsky, E., and Talipova, T. (1999). A generalized Korteweg-de Vries model of internal tide transformation in the coastal zone. *Journal of Geophysical Research*, **108**, 18 333–18 350.

Ivey, G., Winters, K., and Koseff, J. (2008). Density Stratification, Turbulence, but How Much Mixing? *Annual Reviews of Fluid Dynamics*, **40**, 169–184.

Ivey, G. N. and Imberger, J. (1991). On the Nature of Turbulence in a Stratified Fluid. Part I: The Energetics of Mixing. *Journal of Physical Oceanography*, **21**, 650–658.

Jackson, C. R., Da Silva, J. C. B., Jeans, G., Alpers, W., and Caruso, M. J. (2013). Nonlinear Internal Waves in Synthetic Aperture Radar Imagery. *Oceanography*, **26**(2), 68–79.

Jeans, D. and Sherwin, T. (2001). The evolution and energetics of large amplitude nonlinear internal waves on the Portuguese shelf. *Journal of Marine Research*, **59**, 327–353.

Jia, T., Liang, J. J., Li, X.-M., and Sha, J. (2017). SAR Observation and Numerical Simulation of Internal Solitary Wave Refraction and Reconnection Behind the Dongsha Atoll. *Journal of Geophysical Research*, **123**.

Jo, T.-C. and Choi, W. (2002). Dynamics of strongly nonlinear internal solitary waves in shallow water. *Stud. Appl. Math.*, **109**, 205–227.

Johnson, R. S. (1980). Water waves and Korteweg–de Vries equations. *Journal of Fluid Mechanics*, **97**, 701–719.

Joseph, R. I. (1977). Solitary waves in a finite depth fluid. *J. Phys. A.: Math. Gen.*, **10**(12), 225–227.

Kadomtsev, B. B. and Petviashvili, V. I. (1970). On the stability of solitary waves in weakly dispersing media. *Sov. Phys. Dokl.*, **15**, 539–541.

Kakutani, T. and Yamasaki, N. (1978). Solitary Waves in a Two–Layer Fluid. *Journal of the Physical Society of Japan*, **45**(2), 674–679.

Kantorovitch, L. V. and Krylov, V. I. (1962). *Approximate methods of advanced analysis*. Gos Izd Fiz-Math Lit.

Kao, T. W., Pan, F.-S., and Renouard, D. (1985). Internal solitons on the pycnocline: generation, propagation, and shoaling and breaking over a slope. *Journal of Fluid Mechanics*, **159**, 19–53.

Karimpour, F. and Venayagamoorthy, S. (2014). A simple turbulence model for stably stratified wall-boundedflows. *Journal of Geophysical Research: Oceans*, **119**(2), 870–880.

Klymak, J. M. and Moum, J. N. (2003). Internal solitary waves of elevation advancing on a shoaling shelf. *Geophysical Research Letters*, **30**(20), 2045.

Knickerbocker, C. J. and Newell, A. (1980). Shelves and the Korteweg–de Vries equation. *Journal of Fluid Mechanics*, **8**, 803–818.

Kodaira, T., Waseda, T., Miyata, M., and Choi, W. (2016). Internal solitary waves in a two–fluid system with a free surface. *Journal of Fluid Mechanics*, **804**, 201–223.

Kodama, Y. (2010). KP solitons in shallow water. *Journal of Physics A*, **43**(43).

Kodama, Y. and Yeh, H. (2016). The KP theory and Mach reflection. *Journal of Fluid Mechanics*, **800**, 766–786.

Kodama, Y., Li, W., and Yeh, H. (2010). Mach reflection and KP solitons in shallow water. *Eur. Phys. J.*, **185**, 97–111.

Koop, C. G. and Butler, C. (1981). An investigation of internal solitary waves in a two-fluid system. *Journal of Fluid Mechanics*, **112**, 225–251.

Korteweg, D. J. and De Vries, G. (1895). XLI. On the change of form of long waves advancing in a rectangular canal, and on a new type of long stationary waves. *The London, Edinburgh, and Dublin Philosophical Magazine and Journal of Science*, **39**(240), 422–443.

Kubota, T., Ko, D. R. S., and Dobbs, L. D. (1978). Weakly–Nonlinear, Long Internal Gravity Waves in Stratified Fluids of Finite Depth. *Journal of Hydronautics*, **12**(4), 157–165.

Kundu, P., Cohen, I., and Dowling, D. a. (2016). *Fluid Mechanics*. Academic Press, 6th ed.

Kurkina, O., Rouvinskaya, E., Talipova, T., and Soomere, T. (2017). Propagation regimes and populations of internal waves in the Mediterranean Sea basin. *Estuarine, Coastal and Shelf Science*, **185**, 44–54.

La Forgia, G. (2016). *Shoaling and breaking internal solitary waves*. Ph.D. thesis, Roma Tre University.

La Forgia, G., Adduce, C., and Falcini, F. (2018a). Laboratory investigation on internal solitary waves interacting with a uniform slope. *Advances in Water Resources*, **120**, 4–18.

La Forgia, G., Tokyay, T., Adduce, C., and Constantinescu, G. (2018b). Numerical investigation of breaking internal solitary waves. *Physical Review Fluids*, **3**(10), 104801.

Ladah, L., Tapia, F., J., P., and Lopez, M. (2005). Spatially heterogeneous, synchronous settlement of Chthamalus spp. larvae in northern Baja California. *Marine Ecology Progress Series*, **302**, 177–185.

Lamb, H. (1932). *Hydrodynamics*. Cambridge University Press, 6th ed.

Lamb, K. G. (2002). A numerical investigation of solitary internal waves with trapped cores formed via shoaling. *Journal of Fluid Mechanics*, **451**, 109–144.

Lamb, K. G. (2008). On the calculation of the available potential energy of an isolated perturbation in a density-stratified fluid. *Journal of Fluid Mechanics*, **597**, 415–427.

Lamb, K. G. (2014). Internal Wave Breaking and Dissipation Mechanisms on the Continental Slope/Shelf. *Annu. Rev. Fluid Mech.*, **46**, 231–254.

Lamb, K. G. and Yan, L. (1996). The evolution of internal wave undular bores: comparison of a fully–nonlinear numerical model with weakly nonlinear theories. *Journal of Physical Oceanography*, **26**, 2712–2734.

Lien, R.-C., Henyey, F., and Barry, M. (2014). Large-Amplitude Internal Solitary Waves Observed in the Northern South China Sea: Properties and Energetics. *Journal of Physical Oceanography*, **132**, 1095–1115.

Lin, C., Yu, S.-M., Yeh, P.-H., Yu, M.-H., Tsai, C.-P., Hsieh, S.-C., and et al. (2015). Characteristics of boundary layer flow induced by solitary wave propagating over horizontal bottom. *Journal of Marine Science and Technology*, **23**(6), 909–922.

Liu, A. K. and Hsu, M.-K. (2004). Internal wave study in the South China Sea using synthetic aperture radar (SAR). *Intl. J.Remote Sens.*, **25**, 1261–1264.

Long, R. R. (1953). Some Aspects of the Flow of Stratified Fluids: I. A Theoretical Investigation. *Tellus*, **5**(1), 42–58.

Longhitano, S. (2018). Between Scylla and Charybdis (part 1): the sedimentary dynamics of the modern Messina Strait (central Mediterranean) as analogue to interpret the past. *Earth Science Reviews*, **185**, 259–287.

Lorenz, E. N. (1955). Available potential energy and the maintenance of the general circulation. *Tellus*, **7**, 157–167.

Lumley, R. V. (1964). The spectrum of nearly inertial turbulence in a stably stratified fluid. *Journal of Atmospheric Science*, **21**, 99–102.

Martorelli, E., Bosman, A., Casalbore, D., and Falcini, F. (2016). Interaction of down-slope and along-slope processes off Capo Vaticano (southern Tyrrhenian Sea, Italy), with particular reference to contourite-related landslides. *Marine Geology*, **378**, 43–55.

Marullo, S. and Santoleri, R. (1986). Fronts and internal currents at the northern mouth of the Strait of Messina. *Il Nuovo Cimento C*, **9**(3), 701–713.

Massel, S. (2015). *Internal Gravity Waves in the Shallow Seas*. Springer.

Massel, S. (2016). On the nonlinear internal waves propagating in an inhomogeneous shallow sea. *Oceanologia*, **58**, 59–70.

Mater, B. D. and Venayagamoorthy, S. (2014a). A unifying framework for parameterizing stably stratified shear-flow turbulence. *Physics of Fluids*, **26**(036601).

Mater, B. D. and Venayagamoorthy, S. (2014b). The quest for an unambiguous parameterization of mixing efficiency in stably stratified geophysical flows. *Geophysical Reasearch Letters*, **41**(13), 4646–4653.

Maxworthy, T. (1979). A note on the internal solitary waves produced by tidal flow over a three-dimensional ridge. *Journal of Geophysical Research: Oceans*, **84**(C1), 338–346.

Michallet, H. and Barthélemy, E. (1998). Experimental study of interfacial solitary waves. *Journal of Fluid Mechanics*, **366**, 159–177.

Michallet, H. and Ivey, G. (1999). Experiments on mixing due to internal solitary waves breaking on uniform slopes. *Journal of Geophysical Research: Oceans*, **104**(C6), 13467–13477.

Miles, J. W. (1977a). Obliquely interacting solitary waves. *Journal of Fluid Mechanics*, **79**, 157–169.

Miles, J. W. (1977b). Resonantly interacting solitary waves. *Journal of Fluid Mechanics*, **79**, 171–179.

Miyata, M. (1985). An internal solitary wave of large amplitude. *La mer*, **23**, 43–48.

Munk, W. and Wunsch, C. (1998). Abyssal recipes II: energetics of tidal and wind mixing. *Deep Sea Research*, **45**(12).

Nakoulima, O., Zahiboa, N., Pelinovsky, E., Talipova, T., Slunyaev, A., and Kurkinc, A. (2004). Analytical and numerical studies of the variable-coefficient Gardner equation. *Applied Mathematics and Computation*, **152**, 449–471.

Nash, J. D. and Moum, J. N. (2005). River plumes as a source of large-amplitude internal waves in the coastal ocean. *Nature*, **437**(5641), 400–403.

Nikurashin, M. and Ferrari, R. (2013). Overturning circulation driven by breaking internal waves in the deep ocean. *Geophysical Research Letters*, **40**, 3133–3137.

Obregon, M. and Stepanyants, Y. (2012). On numerical solution of the Gardner–Ostrovsky equation. *Mathematical Modelling of Natural Phenomena*, **7**(2), 113–130.

Ono, H. (1975). Algebraic Solitary Waves in Stratified Fluids. *Journal of the Physical Society of Japan*, **39**(4), 1082–1091.

Osborn, T. R. (1980). Estimates of the local rate of vertical diffusion from dissipation measurements. *Journal of Physical Oceanography*, **10**, 83–89.

Osborne, A. and Burch, T. (1980). Internal solitons in the andaman sea. *Science*, **208**(4443), 451–460.

Osborne, A., Brown, J., Burch, T., and Scarlet, R. (1977). The influence of internal waves on deepwater drilling operations. *Paper presented at the Offshore Technology Conference, May 2–5, 1977,*.

Osborne, A. R. (2010). *Nonlinear Ocean Waves and the Inverse Scattering Transform*. Associated Press.

Ostrovsky, L. and Stepanyants, Y. A. (1989). Do internal solitons exist in the ocean? *Reviews of Geophysics*, **27**, 293–310.

Ostrovsky, L. A. and Grue, J. (2003). Evolution equations for strongly nonlinear internal waves. *Physics of Fluids*, **15**(10), 2934–2948.

Ottolenghi, L., Adduce, C., Inghilesi, R., Armenio, V., and Roman, F. (2016a). Entrainment and mixing in unsteady gravity currents. *J. Hydraul. Res.*, **54**(5), 541–557.

Ottolenghi, L., Adduce, C., Inghilesi, R., Roman, F., and Armenio, V. (2016b). Mixing in lock-release gravity currents propagating up a slope. *Phys. Fluids*, **28**(5), 056604.

Ozmidov, R. V. (1965). On the turbulent exchange in a stably stratified ocean. *Bull. Acad. Sci. U.S.S.R.*, **1**, 493–497.

Park, Y.-H., Lee, J.-H., Durand, L., and Hong, C.-S. (2014). Validation of Thorpe–scale–derived vertical diffusivities against microstructure measurements in the Kerguelen region. *Biogeosciences*, **11**, 6927–6937.

Pedlosky, J. (2003). *Waves in the Ocean and Atmosphere: Introduction to Wave Dynamics*. Springer.

Pelinovsky, D. E. and Grimshaw, R. (1997). Structural transformation of eigenvalues for a perturbed algebraic soliton potential. *Physics Letters A*, **229**(3), 165–172.

Pelinovsky, E., Stepanyants, Y., and Talipova, T. (1994). Simulation of nonlinear internal wave propagation in horizontalally inhomogeneous ocean. *Atmospheric and Ocean Physics*, **30**, 77–83.

Pelinovsky, E., Polukhina, O., Slunyaev, A., and Talipova, T. (2007). Internal solitary saves. In book: Solitary Waves in Fluids, Chapter 4. , **29**, 85–110.

Peregrine, D. H. (1966). Calculations of the development of an undular bore. *Journal of Fluid Mechanics*, **25**(2), 321–330.

Pierini, S. (1986). Solitons in a channel emerging from a three–dimensional initial wave. *Nuovo Cimento*, **9C**, 1045–1061.

Pierini, S. (1989). A model for the Alboran Sea internal solitary waves. *Journal of Physical Oceanography*, **19**, 755–772.

Pineda, J. (1991). Predictable upwelling and the shoreward transport of planktonic larvae by internal tidal bores. *Science*, **253**(103191), 548–549.

Pineda, J. (1994). Internal tidal bores in the nearshore: warm-water fronts, seaward gravity currents and the onshore transport of neustonic larvae. *Journal of Marine Research*, **52**, 427–458.

Pineda, J. (1999). Circulation and larval distribution in internal tidal bore warm fronts. *Limnology and Oceanography*, **44**, 1400–1414.

Pinet, P. (1992). *Oceanography: an introduction to the planet oceans*. West Publishing Company.

Ramp, S. R., Tang, T. Y., Duda, T. F., Lynch, J. F., Liu, A. K., Chiu, C.-S., Bahr, F. L. Kim, H.-R., and Yang, Y.-J. (2004). Internal solitons in the northeastern South China Sea. Part I. Sources and deep water propagation. *IEEE J. Ocean. Engng*, **29**, 1157–1181.

Reeder, D. B., Ma, B. B., and Yang, Y. J. (2011). Very large subaqueous sand dunes on the upper continental slope in the South ChinaSea generated by episodic, shoaling deep-water internal solitary waves. *Marine Geology*, **279**, 12–18.

Russell, J. S. (1844). Report on waves. In *14th meeting of the British Association for the Advancement of Science*, pages 311–319.

Sandstrom, H. and Elliott, J. (1984). Internal tide and solitons on the Scotian Shelf: A nutrient pump at work. *Journal of Geophysical Research*, **89**, 6415–6426.

Sapia, A. and Salusti, E. (1987). Observation of nonlinear internal solitary wave trains at the northern and southern mouths of the Strait of Messina. *Deep Sea Research Part A. Oceanographic Research Papers*, **34**(7), 1081–1092.

Scotti, A. and Pineda, J. (2004). Observation of very large and steep internal waves of elevation near the Massachusetts coast. *Geophysical Research Letters*, **31**(22), L22307.

Shih, L. H., Koseff, J. R., Ivey, G. N., and Ferziger, J. H. (2005). Parameterization of turbulent fluxes and scales using homogeneous sheared stably stratified turbulence simulations. *Journal of Fluid Mechanics*, **525**, 193–214.

Shimizu, K. and Nakayama, K. (2017). Effects of topography and Earth's rotation on the oblique interaction of internal solitary-like waves in the Andaman Sea. *Journal of Geophysical Research*, **122**, 7449–7465.

Shroyer, E. L., Moum, J. N., and Nash, J. D. (2009). Observations of polarity reversal in shoaling nonlinear internal waves. *Journal of Physical Oceanography*, **39**(3), 691–701.

Small, J. (2001a). A Nonlinear Model of the Shoaling and Refraction of Interfacial Solitary Waves in the Ocean. Part I: Development of the Model and Investigations of the Shoaling Effect. *Journal of Physical Oceanography*, **31.11**, 3163–3183.

Small, J. (2001b). A Nonlinear Model of the Shoaling and Refraction of Interfacial Solitary Waves in the Ocean. Part II: Oblique Refraction across a Continental Slope and Propagation over a Seamount. *Journal of Physical Oceanography*, **31**, 3184–3199.

Small, J. (2003). Refraction and Shoaling of Nonlinear Internal Waves at the Malin Shelf Break. *Journal of Physical Oceanography*, **33**, 2657–2674.

Small, J., Sawyer, T. C., and Scott, J. C. (1999). The evolution of an internal bore at the Malin shelf break. *Annales Geophysicae*, **17**, 547–565.

Smyth, W., Moum, J., and Caldwell, D. (2001). The efficiency of mixing in turbulent patches: inferences from direct simulations and microstructure observations. *Journal of Physical Oceanography*, **31**, 1969–1692.

St. Laurent, L. (2008). Turbulent dissipation on the margins of the South China Sea. *Geophysical Research Letters*, **35**(L23615).

St. Laurent, L. C., Simmons, H., and Jayne, S. (2002). Estimating tidally driven mixing in the deep ocean. *Geophysical Research Letters*, **29**(23).

Stanton, T. and Ostrovsky, L. (1998). Observations of highly nonlinear internal solitons over the Continental Shelf. *Geophysical Research Letters*, **25**, 2695–2698.

Stasna, M. and Lamb, K. G. (2002). Large fully nonlinear internal solitary waves: The effect of background current. *Physics of Fluids*, **14**(9), 2987–2999.

Stoker, J. J. (1957). *Water Waves: The Mathematical Theory with Applications*. Interscience Publishers.

Sutherland, B. (2010). *Internal Gravity Waves*. Cambridge University Press.

Sutherland, B., Barrett, K., and Ivey, G. (2013). Shoaling internal solitary waves. *Journal of Geophysical Research*.

Talipova, T., Kurkina, O. E., Rouvinskaya, E. A., and Pelinovsky, E. N. (2015). Propagation of Solitary Internal Waves in Two–Layer Ocean of Variable Depth. *Izvestiya, Atmospheric and Oceanic Physics*, **51**(1), 89–97.

Theiler, Q. and Franca, M. J. (2016). Contained density currents with high volume of release. *Sedimentology*, **63**(6), 1820–1842.

Thorpe, S. A. (1977). Turbulence and mixing in a Scottish Loch. *Philosophical Transactions of Royal Society A*, **286**, 125–181.

Thorpe, S. A. (2005). *The Turbulent Ocean*. Cambridge University Press.

Tian, Z., Zhang, S., Guo, X., Yu, L., and Jia, Y. (2019). Experimental investigation of sediment dynamics in response to breaking high-frequency internal solitary wave packets over a steep slope. *Journal of Marine Systems*, **199**(103191).

Turkington, B., Eydeland, A., and Wang, S. (1991). A Computational Method for Solitary Internal Waves in a Continuously Stratified Fluid. *Studies in Applied Mathematics*, **85**, 93–127.

Vallis, G. K. (2017). *Atmospheric and Oceanic Fluid Dynamics*. Cambridge University Press.

Venayagamoorthy, S. K. and Fringer, O. B. (2007). On the formation and propagation of nonlinear internal boluses across a shelf break. *Journal of Fluid Mechanics*, **577**, 137–159.

Vercelli, E. (1925). *Il regime delle correnti e delle maree nello Stretto di Messina*. Venezia.

Vlasenko, V. and Hutter, K. (2002). Numerical experiments on the breaking of solitary internal wavesover a slope–shelf topography. *Journal of Physical Oceanography*, **32**(6), 1779–1793.

Vlasenko, V. and Stashchuk, N. (2007a). Nonlinear internal waves, internal bores, and turbulent mixing in the nearshore coastal environment. *Journal of Geophysical Research*, **112**, C11018.

Vlasenko, V. and Stashchuk, N. (2007b). Three–dimensional shoaling of large–amplitude internal waves. *Journal Of Geophysical Research*, **112**(C11018).

Wallace, B. C. and Wilkinson, D. L. (1988). Run-up of internal waves on a gentle slope in a two-layered system. *Journal of Fluid Mechanics*, **191**, 419–442.

Walter, R. K., Woodson, C. B., Arthur, R. S., Fringer, O. B., and Monismith, S. G. (2012). Nearshore internal bores and turbulent mixing in southern Monterey Bay. *Journal of Geophysical Research*, **117**, C07017.

Wang, C. and Pawlowicz, R. (2012). Oblique wave-wave interactions of nonlinear near-surface internal waves in the Strait of Georgia. *Journal of Geophysical Research*, **117**(C6).

Whitham, G. B. (1974). *Linear and Nonlinear Waves*. Wiley.

Winters, K., Lombard, P., Riley, J., and D'Asaro, E. (1995). Available potential energy and mixing in density-stratified fluids. *J. Fluid Mech.*, **289**, 115–128.

Woodson, C. (2018). The Fate and Impact of Internal Waves in Nearshore Ecosystems. *Annual Reviews of Marine Sciences*, **10**, 421–441.

Wunsch, C. and Ferrari, R. (2004). Vertical Mixing, Energy, and the General Circulation of the Oceans. *Annual Reviews of Fluid Dynamics*, **36**, 281–314.

Xie, J., He, Y.and Chen, Z., Xu, J., and Cai, S. (2015). Simulations of Internal Solitary Wave Interactions with Mesoscale Eddies in the Northeastern South China Sea. *Journal of Physical Oceanography*, **45**, 2959–2978.

Xie, J., He, Y., Lü, H., Chen, Z., Xu, J., and Cai, S. (2016). Distortion and broadening of internal solitary wavefront in the northeastern South China Sea deep basin. *Geophysical Research Letters*, **43**, 7617–7624.

Xue, J., Graber, H. C., Romeiser, R., and Lund, B. (2014). Understanding internal wave–wave interaction patterns observed in satellite images of the Mid-Atlantic Bight. *EEE Trans. Geosci. Remote Sens.*, **52**, 3211–3219.

Yuan, C., Grimshaw, R., Johnson, E., and Chen, X. (2018a). The Propagation of Internal Solitary Waves over Variable Topography in a Horizontally Two–Dimensional Framework. *Journal of Physical Oceanography*, **48**(2).

Yuan, C., Grimshaw, R., Johnson, E., and Wang, Z. (2018b). Topographic effect on oblique internal wave–wave interactions. *Journal of Fluid Mechanics*, **856**, 36–60.

Zabusky, N. J. and Kruskal, M. D. (1965). Interaction of solitons in a collisionless plasma and the recurrence of initial states. *Physical Review Letters*, **15**, 240–243.

Zhou, X. and Grimshaw, R. (1989). The effect of variable currents on internal solitary waves. *Dynamics of Atmospheres and Oceans*, **14**, 17–39.